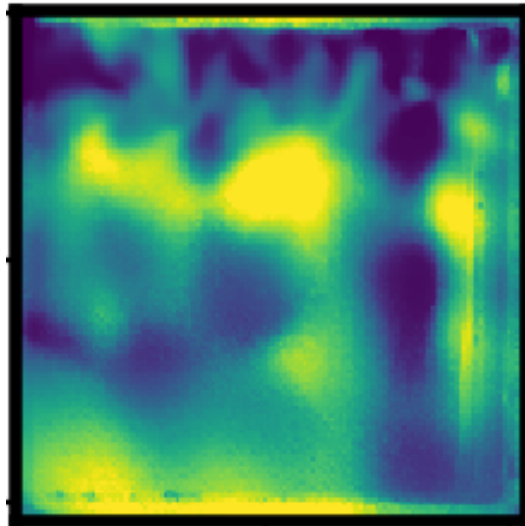DEPARTMENT OF AEROSPACE
ENGINEERING
INDIAN INSTITUTE OF TECHNOLOGY
MADRAS
CHENNAI - 600036

Dynamical systems and complex systems approach to study transition to thermoacoustic instability in a model multi-element rocket combustor

A Thesis

Submitted by

K. PRAVEEN

For the award of the degree

Of

DOCTOR OF PHILOSOPHY

Feb, 2022

QUOTATIONS

यदा यदा हि धर्मस्य ग्लानिर्भवति भारत ।

अभ्युत्थानमधर्मस्य तदात्मानं सृजाम्यहम् ॥७॥

परित्राणाय साधूनां विनाशाय च दुष्कृताम् ।

धर्मसंस्थापनार्थाय सम्भवामि युगे युगे ॥८॥

Whenever virtue subsides and wickedness prevails,
I manifest myself.
To establish virtue, to destroy evil,
to save the good I come from eon to eon.

BHAGAVAD GITA (chapter 4, verses - 7 and 8)

DEDICATION

Dedicated to my parents and sister, for their constant love and unflinching support.

THESIS CERTIFICATE

This is to undertake that the Thesis (or Project report) titled **DYNAMICAL SYSTEMS AND COMPLEX SYSTEMS APPROACH TO STUDY TRANSITION TO THERMOACOUSTIC INSTABILITY IN A MODEL MULTI-ELEMENT ROCKET COMBUSTOR**, submitted by me to the Indian Institute of Technology Madras, for the award of Ph.D., is a bona fide record of the research work done by me under the supervision of Prof. R. I. Sujith. The contents of this Thesis, in full or in parts, have not been submitted to any other Institute or University for the award of any degree or diploma.

In order to effectively convey the idea presented in this thesis, the following work of other authors was reprinted in the thesis with their permission.

- Figure. 1.2, page 3: Reproduced with permission from Sutton & Biblarz and John Wiley & Sons, Inc.

- Figure. 1.1, page 2: Images reproduced from: a) Bloomer, H.E., Conrad, E.W., Vincent, D.W. and Wanhainen, J.P., 1968. Liquid rocket acoustic-mode-instability studies at a nominal thrust of 20000 pounds, NASA-TN-D-4968 (allowed for public use) b) https://www1.grc.nasa.gov/historic-facilities/rocket-enginetest-facility/apollo-era-testing/ c) Goetz, O.K. and Monk, J.C., 2005, January. Combustion device failures during space shuttle main engine development. In Fifth International Symposium on Liquid Space Propulsion, https://ntrs.nasa.gov/api/citations/20050217132/downloads/20050217132.pdf (allowed for public use)

- Figure. 1.3, page 9: Image reproduced from Harrje, D.T. and Reardon, F.H., 1972. Liquid propellant rocket combustion instability. nasa sp-194. NASA Special Publication, 194. (allowed for public use)

Place: Chennai 600 036

Date: 16th Feb, 2022

K. Praveen

Research Scholar

Prof. R. I. Sujith

Research Guide

LIST OF PUBLICATIONS

I. REFEREED JOURNALS BASED ON THE THESIS

1. **Kasthuri, P., I. Pavithran, S. A. Pawar, R. I. Sujith, R. Gejji,** and **W. E. Anderson** (2019). Dynamical systems approach to study thermoacoustic transitions in a liquid rocket combustor. *Chaos*, **29(10)**, 103115.

2. **Kasthuri, P., I. Pavithran, A. Krishnan, S. A. Pawar, R. I. Sujith, R. Gejji, W. E. Anderson, N. Marwan,** and **J. Kurths** (2020). Recurrence analysis of slow-fast systems. *Chaos*, **30(6)**, 063152.

3. **Kasthuri, P., S. A. Pawar, R. Gejji, W. E. Anderson** and **R. I. Sujith** (2022). Coupled interaction between acoustics and unsteady flame dynamics during the transition to thermoacoustic instability in a multi-element rocket combustor. *Combustion and Flame*, **240**, 112047.

4. **Kasthuri, P., A. Krishnan, R. Gejji, W. E. Anderson, N. Marwan, J. Kurths,** and **R. I. Sujith** (2022). Investigation into the coherence of flame intensity oscillations in a model multi-element rocket combustor using complex networks. *Physics of Fluids*, **34(3)**, 034107.

II. REFEREED JOURNALS (Others)

1. **Kasthuri, P., V. R. Unni,** and **R. I. Sujith** (2019). Bursting and mixed mode oscillations during the transition to limit cycle oscillations in a matrix burner *Chaos*, **29(4)**, 043117.

2. **Godavarthi, V., P. Kasthuri, S. Mondal, R. I. Sujith, N. Marwan,** and **J. Kurths** (2020). Synchronization transition from chaos to limit cycle oscillations when a locally coupled chaotic oscillator grid is coupled globally to another chaotic oscillator *Chaos*, **30(3)**, 033121.

3. **Kushwaha, A., and P. Kasthuri, S. A. Pawar, R. I. Sujith, I. Chterev,** and **I. Boxx** (2021). Dynamical Characterization of Thermoacoustic Oscillations in a Hydrogen-Enriched Partially Premixed Swirl-Stabilized Methane/Air Combustor *Journal of Engineering for Gas Turbines and Power*, **143(12)**, 121022.

4. **Bedard, M. J., R. M. Gejji, W. E. Anderson, B. L. Austin Jr, P. Kasthuri,** and **R. I. Sujith** (2021). Detailed Measurement of Oxidizer-Rich Staged Combustion Injector Dynamics in Model Rocket Combustors *AIAA Journal*, 1-16.

ACKNOWLEDGEMENTS

First and foremost, I am grateful to my parents and my sister for their love and support. They have always stood by my decisions, only questioning them to the necessary extent, with my long-term well-being as their concern. Without such an understanding family, I would not have been able to walk my road.

I sincerely thank Prof. Sujith for showing and sharing his way of doing research and outlook on life in general. His guidance was (and is) instrumental in channeling my attention in the right direction when I first joined the lab. Subsequent time spent with him helped me understand the nuances of research life and streamline my thoughts. Watching and learning from him in close quarters has led to my overall personal development. Over the time I spent in the lab, I not only learned to do quality research, but I am grateful for the various challenges thrown my way. I consider it a big honor to be your student.

I am indebted to my seniors – Vishnu, Samadhan, and Abin, for helping me learn the ropes of research at the beginning of my Ph.D. The atmosphere they created in the lab was conducive to healthy discussions on various topics. Without the advice of such helpful seniors, I would have definitely taken a lot more time to understand and complete the different projects I set out to do.

It was a joy to work on a daily basis with my labmates – Induja and Manikandan. They were the ones I turned to for obtaining my first opinions on my analysis and interpretations. I am also glad to have shared the lab with several kind and jubilant labmates - Vedasri, Alan, Thilagaraj, Syam, Jabasteena, Anand, Midhun, Krishna, Ankit, Shri Vignesh, Jayesh, Abhishek, Samarjeet, Shruti, Ramesh, Siva, and Shanmughapriya. I grew as a person and a researcher through the many interactions with them. I am thankful to Sudha Akka, Nirmala ma'am, Varun sir, and my Masters' classmates for helping me out in their own way on various occasions. Finally, I am grateful to have spent these years in the beautiful campus atmosphere of IIT Madras.

During my time here, I have also gained several interesting friends who helped me keep myself in good spirits.

ABSTRACT

KEYWORDS: thermoacoustic instability; rocket combustion; coupled interaction; dynamical systems theory.

Combustors in modern high-performing rocket engines are prone to transverse thermoacoustic instability characterized by large amplitude high-frequency acoustic pressure and heat release rate oscillations. The occurrence of such thermoacoustic instability can overwhelm the thermal protection mechanisms in the thrust chamber, impart irreparable structural damages, and result in catastrophic explosions. In this thesis, we study the thermoacoustic behavior of an 11-bar self-excited multi-element model rocket combustor operating on an oxidizer-rich staged combustion cycle. We introduce the framework of dynamical systems theory and complex systems theory to analyze the temporal and spatiotemporal dynamics of rocket combustors.

First, we identify the presence of intermittency between the stable state and thermoacoustic instability. We characterize the acoustic pressure oscillations recorded for each dynamical state using tools from nonlinear dynamics, recurrence, multifractal, and network analyses. Given the exorbitant costs involved in a full-scale rocket test, a thorough understanding of the various dynamical behaviors possible in a rocket combustor is mandatory to build accurate models, validate existing models and computational fluid dynamics (CFD) simulations, and importantly avoid developmental setbacks and in-flight jeopardies. We develop measures based on recurrence and multifractal theories which can be used towards characterizing the features present in a signal, which in turn is necessary to stringently validate models and CFD simulations aimed at characterizing the combustion stability of rocket engines. Using recurrence plots and recurrence networks, we identify unique features arising from the slow-fast timescales present in the wave steepened acoustic pressure oscillations during thermoacoustic instability.

Next, we analyze the coupled interaction between acoustic pressure oscillations and methylidyne (CH*) chemiluminescence intensity oscillations for the different dynamical states observed using tools from synchronization theory. We find that only the first few transverse acoustic modes participate in thermoacoustic driving. In the final part of the thesis, using weighted correlation spatial network analysis, we quantified the level of coherence present in the spatiotemporal CH* intensity oscillations in the combustor. The insights gained from the analysis of the coupled interaction between acoustic pressure and CH* intensity oscillations, and the findings from the correlation network analysis, during the transition from stable state to thermoacoustic instability, can be leveraged to build better models and develop compatible control strategies to suppress ruinously large amplitude oscillations in rocket combustors.

TABLE OF CONTENTS

LIST OF TABLES

LIST OF FIGURES

xvi

GLOSSARY

The following are some of the commonly used terms in this thesis:

CFD   A branch of fluid mechanics that uses numerical analysis and data structures to analyze and solve problems that involve fluid flows

LPRE   Liquid propelled rocket engine: Rocket propelled by combustion of energetic liquid or gaseous reactants, generally used in launch vehicles transporting large payloads from earth's surface to orbital and interplanetary space

ABBREVIATIONS

CFD	Computational Fluid Dynamics
CH*	Methylidyne radical
JP-8	Jet Propellant 8
LOx	Liquid oxygen
LH_2	Liquid hydrogen
LPRE	Liquid Propellant Rocket Engine
LNG	Liquefied Natural Gas
OH*	Hydroxyl radical
RN	Recurrence Network
RP	Recurrence Plot

NOTATION

English Symbols

p'	Acoustic pressure fluctuations
I'	CH* intensity fluctuations
f_{nT}	Frequency of nth transverse acoustic mode
nT	n^{th} transverse acoustic mode
$1L$	Fundamental longitudinal acoustic mode
t	Time
V	Volts
d	Embedding dimension
DET	Determinism - a recurrence quantification measure
RR	Recurrence rate - a recurrence quantification measure
$RATIO$	Ratio of determinism to recurrence rate
H	Hurst exponent
AMI	Average Mutual Information
ACF	Auto Correlation Function
CC	Cross correlation
A_{ij}	Adjacency matrix
W_{ij}	Weight matrix
R_p	Pearson correlation coefficient
RI_{nT}	Rayleigh index of nth transverse acoustic mode
XWT	Cross-wavelet transform

Greek Symbols

ϕ	Equivalence ratio
τ	Time delay in seconds
$\langle \phi_{x,y} \rangle$	Relative phase between x and y

CHAPTER 1

INTRODUCTION

Liquid propellant rocket engines (LPREs) are vital for propelling launch vehicles which transport large payloads into orbital and interplanetary space. With the space industry projected to grow in the coming decades (Indian Space Research Organization, 2021; Weinzierl, 2018), a lot of emphasis is placed on the improvement and development of earth and space observation satellite services and manned explorations. Hence, there is an impending need to consistently upgrade existing LPRE families as well as develop new LPREs to meet the diverse requirements of each space mission.

Combustion instability is one of the major challenges while developing LPREs (Anderson and Yang, 1995; Watanabe *et al.*, 2016). Combustion instability (also used interchangeably as thermoacoustic instability) refers to the self-sustained large amplitude oscillations in the pressure and heat release rate in the thrust chamber of LPREs. This phenomenon can occur not only during steady-state operation, but also during startup, shutdown and throttling operation. The incidence of large amplitude oscillations in an LPRE can

(a) impart high amplitude vibrations (acceleration > 300 g) leading to structural failure

(b) engender thrust oscillations resulting in loss of control

(c) cause excessive heat transfer to the thrust chamber walls and injector plates

(d) interfere with the vehicle communication systems

In Fig. 1.1, we show photographs of damage incurred to the different components of LPREs during development. Due to the extremely high power density (> 30 GW/m^3) in the thrust chamber (Culick and Kuentzmann, 2006), the occurrence of combustion instability for just a brief time interval can result in a mission-threatening damage or partial/complete failure of the LPRE. Hence, a lot of emphasis is placed on characterizing thermoacoustic instabilities, understanding the mechanisms behind them
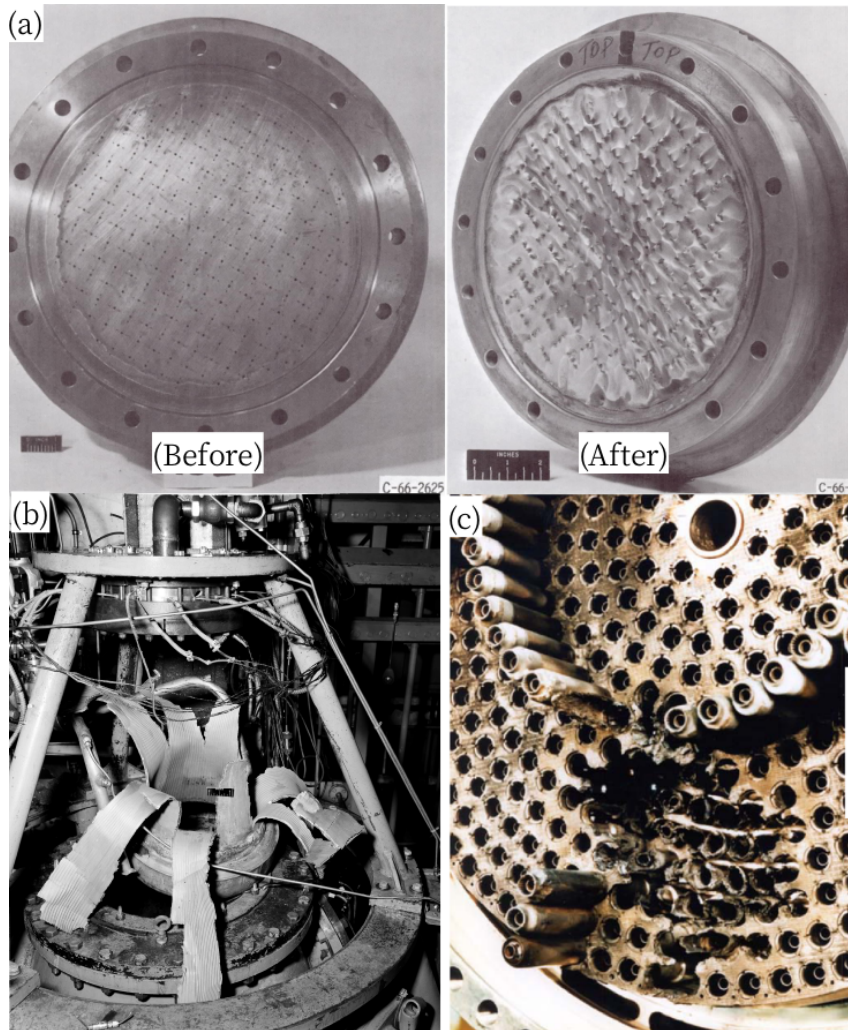
Fig. 1.1: (a) Effect of thermoacoustic oscillations on an LPRE injector before and after a test. Reproduced from Bloomer *et al.* (1968) - (allowed for public use). (b) The thrust chamber exploded during the testing of an LPRE in the rocket engine test facility of NASA in 1958 (Glenn Research Center, 2018). (c) Injector failure during the development of the space shuttle main engine. Reproduced from Goetz and Monk (2005) - (allowed for public use).

and also on the modifications necessary to bring down the amplitudes to acceptable levels. As a result, all LPREs must be proven to be free of thermoacoustic instabilities before mission flight. These extensive tests usually lead to large cost overruns and delays in schedule.

Combustion instability is not only observed in LPREs, but also widely reported in solid rocket motors (Culick and Kuentzmann, 2006), aero - gas turbine engines (Poinsot, 2017), power - producing gas turbine engines (Lieuwen and Yang, 2005), afterburners

(Henderson and Lewis, 1989), industrial furnaces and boilers (Flynn *et al.*, 2017). Therefore, combustion instability is extensively studied by a variety of researchers affiliated with combustion and acoustic sciences.

1.1 BACKGROUND ON LIQUID ROCKET PROPULSION

The main components of an LPRE are shown in Fig. 1.2. Propellants (fuel and oxidizer) are stored in pressurized tanks which form the bulk of the launch vehicle's volume and mass. The propellants are transported to the injectors through a circuit of feed lines, control valves, pumps and manifolds. The pumps in high thrust generating LPREs usually are powered by a turbo assembly (one or more turbopumps). A gear assembly helps to operate the turbo assemblies at different speeds to obtain the desired fuel and oxidizer flow rates. A small proportion of the main propellant flow is usually sufficient to run the gas generator which powers the turbo assemblies. Then, a series of injectors
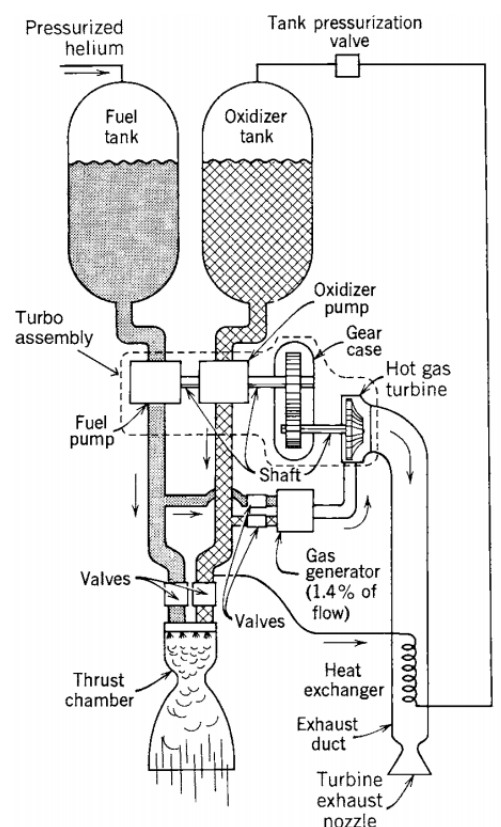
Fig. 1.2: Schematic diagram of the main components of a liquid propellant rocket engine. Reproduced with permission from Sutton and Biblarz (2016).

shower the propellants into the head end of the thrust chamber. Carefully designed injectors ensure that the liquid propellants are atomized into small droplets using a liquid spray jet. Then, the droplets vaporize, diffuse and mix to achieve the desired mixture ratio necessary for efficient combustion. The converging – diverging bell nozzle at the end of the thrust chamber accelerates the combustion products to high velocities. The hot gases exhausted out of the nozzles impart a reactive thrust force on the launch vehicle. Due to the high pressure and temperature environment in the thrust chamber, active thermal management is required to dissipate the heat from the walls of the thrust chamber.

The performance of an LPRE is usually judged by the thrust generated and its specific impulse (Sutton and Biblarz, 2016). Specific impulse (I_{sp}) indicates the efficiency with which propulsive energy is extracted from the propellants. Specific impulse can be defined as the total impulse per unit weight of the propellant.

$$I_{sp} = \frac{\int_0^t F\, dt}{g_0 \int_0^t \dot{m}\, dt} \tag{1.1}$$

Equation. 1.1 gives a time-averaged value of I_{sp}. Here, F, $\dot{m}$ and g_0 are the instantaneous thrust, propellant mass flow rate, and standard acceleration of gravity (9.8 m/s^2 at sea level) respectively. Under constant thrust and propellant flow rates, Eq. 1.1 reduces to

$$I_{sp} = \frac{F}{\dot{m} g_0} \tag{1.2}$$

Higher I_{sp} implies proper utilization of the propellants, which in turn is a reflection of the efficiency of the LPRE. Therefore, I_{sp} is used to compare different rocket engines. The I_{sp} of LPREs lies between 250 – 450 s while that of solid rocket motors are in the range 150 - 300 s (Sutton and Biblarz, 2016). Non-chemical rocket propulsion such as electric, ion and nuclear propulsion have even higher I_{sp}. However, they only can be applied for low-thrust applications currently. Apart from high I_{sp}, LPREs offer significant advantages over other rocket propulsion methods. By controlling the

oxidizer and fuel flow rates, LPREs offer multiple restarts, shutdowns and throttling capabilities. As a result, LPREs are also preferred for planetary descent, attitude control, station-keeping, orbit change maneuvers (Sutton and Biblarz, 2016).

Depending on the manner in which the propellants are introduced into the thrust chamber, several engine cycles exist (Sutton and Biblarz, 2016; Manski *et al.*, 1998). Early LPREs were based on pressure-fed cycle in which the propellants are forced into the thrust chamber using just the pressure head from the pressurized propellant tanks. The tanks of LPREs based on pressure-fed cycle need to have thick walls to withstand high pressures and therefore weigh more. For high thrust requirements, pressure fed cycle imposes a huge weight penalty. To reduce the weight, it is essential to get rid of the pressurized tanks. This led to the development of LPREs based on the gas generator cycle.

In a gas generator cycle, a small percentage of the propellants are burnt in a gas generator to power turbopump(s) which drive the propellant from the tanks to the thrust chamber (Sutton and Biblarz, 2016). The exhausts from the gas generator are exhausted through a separate nozzle, or blown down along the main nozzle. However, the gas-generator contribution to the thrust is infinitesimal, the efficiency is reduced while allowing higher chamber pressures. Tap-off cycle is another engine cycle in which the hot combustion products from the thrust chamber are re-routed upstream to drive the turbopump (Sutton and Biblarz, 2016).

Expander cycles are sometimes preferred for upper stage LPREs with cryogenic propellants (Sutton, 2005). Propellants at cryogenic temperatures are used to cool the walls of the thrust chamber. In the process, the propellants absorbs heat, vaporize, expand and are used to drive the turbopump(s). In this cycle, the limited heat absorption constrains the operational envelope of the engine.

To maximize the I_{sp} of LPREs, staged combustion cycles are sought. In staged combustion cycles, fuel or oxidizer rich mixture is burned in a preburner to drive the turbopumps at high pressures (Sutton and Biblarz, 2016). The entire fuel or oxidizer

rich exhaust is fed directly into the main combustion chamber where the balance fuel or oxidizer undergoes combustion. Staged cycles permit very high chamber pressures and efficiency. Another variant of staged combustion cycle is the full flow staged combustion cycles where both the fuel rich and oxidizer rich mixtures are burned separately in two preburners to drive the fuel and oxygen turbopumps, respectively. This cycle guarantees a slightly higher efficiency than the partially staged combustion cycle. Generally, developing LPREs based on staged combustion cycles are more challenging when compared to other engine cycles because it warrants specific expertise in high temperature metallurgy and turbomachinery. Moreover, thermal management becomes more difficult in staged combustion LPREs.

Several other advanced engine cycles exist for LPREs (Manski *et al.*, 1998). The selection of a proper engine cycle is based on a variety of factors such as the thrust desired, the propellant combination, the weight limitations etc. Irrespective of the engine cycle chosen, the risk of occurrence of thermoacoustic instability is ever-present.

1.2 CLASSIFICATION OF COMBUSTION INSTABILITY

Combustion instabilities are known to occur in a wide variety of forms and arises from the interaction between the acoustic, hydrodynamic and combustion processes in the engine. The mechanism behind combustion instabilities can be related to the acoustics, coherent structures in the flow field, hydrodynamic instabilities, shocks, intrinsic flame instabilities, flame blowout and flame blowoff[1] (Williams, 2018; Lieuwen, 2012). Sometimes, the interaction between more than one of the aforementioned factors might lead to the emergence of combustion instability. Apart from these factors, system induced behaviors such as feed system and structure interactions can also result in combustion instability.

The conventional practice in the LPRE industry is to classify combustion instabilities

---

[1]Flame blowout occurs when the flame cannot be stabilized as a result of the equivalence ratio being varied beyond the flammability limits. Flame blowoff is referred to the extinguishment of flame as a result of the high-speed flow quenching the flame.

into two types - smooth and rough combustion (Heister *et al.*, 2019). When the ratio of the amplitude of the chamber pressure fluctuations to the mean chamber pressure exceed 5%, it is termed as rough combustion. If the obtained ratio is under 5%, combustion is considered smooth. General practice states that smooth combustion is acceptable whereas rough combustion necessitates dedicated tests on the LPRE stability. There are instances of the amplitude of the chamber pressure fluctuations exceeding even the mean chamber pressure (which is generally of the order of tens to hundreds of bars) (Anderson and Yang, 1995; Harrje and Reardon, 1972). Hence, analyzing combustion instability during the development of an LPRE became a norm for the rocket industry. Depending on the frequency of the oscillations in the LPRE, combustion instability can be classified into three types (Sutton and Biblarz, 2016).

(a) Chug or POGO instability: This instability is generally associated with oscillation frequencies between 10 and 300 Hz. The interaction of the bulk propellant flow with the structural modes of the propellant feed system (or even the entire launch vehicle) leads to self-excited longitudinal oscillations in the propellant flow rates. In turn, large thrust variations are produced imparting dangerous cyclic loads on the launch vehicle structure. Such vibrational loads on the launch vehicle can exceed the permissible level and lead to failures. Propellant pump cavitation, gas entrapment in the feed lines and fluctuations in the propellant tank pressurization systems can also exacerbate chug instability. Due to its striking similarity with the oscillatory motion of a POGO jumping stick, it is also referred to as POGO instability. These oscillations are usually suppressed either by incorporating bellows or POGO damping devices in the propellant feed lines (Sutton and Biblarz, 2016).

(b) Buzz: This type of instability is characterized by frequencies lying between 300 Hz and 1000 Hz. It arises from the establishment of acoustic resonances with the injector manifold, thrust chamber assembly and underlying flow turbulence rendering its characteristic buzzing sound. Buzz is overcome by incorporating minor modifications to the injector geometry and arrangement, thrust chamber geometry, changing stiffness of the affected components in the LPRE.

(c) Screech or scream: The oscillation frequencies of this type of instability ranges from 1 kHz to 20 kHz. Nearly all LPREs encounter screech instability during their development stage. The emergence of screech instability is attributed to the interaction between the combustion process, shock waves and chamber acoustics. The occurrence of screech rapidly increases the heat transfer and causes high-frequency chamber pressure oscillations. In certain cases, the amplitude of these high-frequency oscillations even exceed the mean chamber pressure (Oefelein and Yang, 1993). Since the vibrational energy is proportional to the frequency

of oscillations, the occurrence of screech for even a small time interval can lead to disastrous explosions and engine failure. Therefore, screech is not desirable during any mode of engine operation including the startup and shutdown sequences. Out of the three types, screech instability is the most difficult to diagnose and solve. As a result, a number of static tests have to be performed before qualifying the LPRE for flight. Suppression of screech instability involves major modifications of the thrust chamber geometry, cooling jackets, change of oxidizer and fuel combination, changes to the temperature of propellants prior to entering combustion chamber, incorporating baffles, Helmholtz resonators etc.

It must be noted that the frequency range might overlap for the aforementioned three types. Moreover, more than one of these instabilities can coexist (Lorente *et al.*, 2018). The understanding of high-frequency thermoacoustic instabilities is of interest in this thesis.

Depending on the direction of acoustic wave propagation, the obtained high-frequency thermoacoustic instability can be further classified into at least two modes – longitudinal and transverse. In the longitudinal mode, the acoustic wave propagates along the flow direction and reflects off the boundaries imposed by the converging nozzle section and the injector face. Variations in thrust generated by the LPRE is the main problem associated with the occurrence of high-frequency thermoacoustic instability at longitudinal modes.

Transverse acoustic waves propagate perpendicular to the main flow direction (i.e., perpendicular to the chamber injector face). Transverse modes can occur in three forms – radial, tangential or their combination. The acoustic pressure and velocity profiles for the common transverse modes are shown in Fig. 1.3. In a radial mode, the acoustic waves are reflected off the walls of the thrust chamber. However, in a tangential mode, the acoustic waveform can be either a standing wave or a traveling wave. A standing tangential wave mode remains fixed in space while the amplitude of the wave fluctuates (in time). In a spinning tangential wave, both the amplitude as well as the position of the nodes (and antinodes) vary. Transverse thermoacoustic instability entails excessive heat transfer to the thrust chamber walls and are particularly damaging to the injector (Govaert *et al.*, 2021). Accounts of melting of the injector heads due to enhanced heat

transfer from the transverse thermoacoustic instabilities in the space shuttle main engine (SSME) and its consequences are well-known in LPRE literature (Anderson and Yang, 1995; Oefelein and Yang, 1993).

High-frequency thermoacoustic instability can also materialize as a combination of the longitudinal and transverse modes. The expected frequencies associated with each of these various modes can be calculated theoretically. However, the calculated frequencies and the observed frequencies might be off by a few hundred Hz due to the complex boundary conditions (Poinsot, 2017), temperature gradients (Sujith *et al.*, 1995), and acoustic losses (Poinsot, 2017) in the LPRE.

1.3   HISTORICAL OVERVIEW OF THERMOACOUSTIC INSTABILITY

The first known occurrence of thermoacoustic instability dates back to the late eighteenth century. In 1777, Higgins observed the production of sound identified by
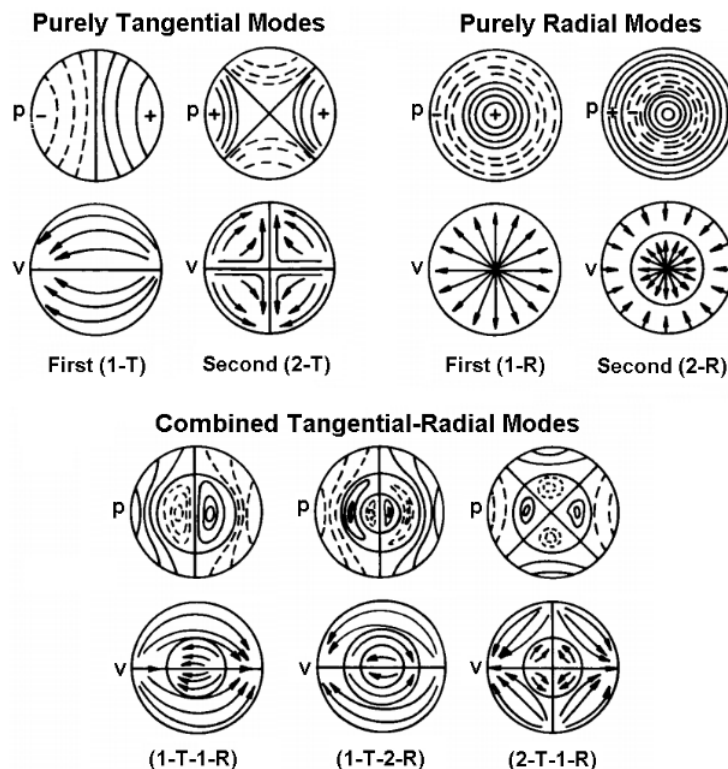
Fig. 1.3: Schematic diagrams of the acoustic pressure and velocity mode shapes for the common transverse modes found in LPREs. Reproduced from Harrje and Reardon (1972) (allowed for public use).

a clear tonal frequency when a vertical glass tube, closed at the upper end, was lowered into a hydrogen flame. In 1850, Sondhauss conjectured a relation between the time period of oscillations and the geometry of the apparatus. However, he could not provide a convincing explanation for the production of sound. Soon, in 1859, Rijke performed experiments in a vertical tube containing a metallic gauze in its lower end. Both the ends of the vertical tube were open to the atmosphere. When, the gauze was heated from below, he heard a clearly distinguishable tonal sound. He conceived that the production of sound was related to the upward draught created by the buoyant forces acting on the air flow within the duct. This explanation also failed to be convincing. Finally, Rayleigh (1878) proposed the following criteria which is necessary for the establishment of thermoacoustic instability.

"If the heat be periodically communicated to, and abstracted from, a mass of air vibrating (for example) in a cylinder bounded by a piston, the effect produced will depend upon the phase of the vibration at which the transfer of heat takes place. If heat be given to the air at the moment of greatest condensation, or taken from it at the moment of greatest rarefaction, the vibration is encouraged. On the other hand, if heat be given at the moment of greatest rarefaction, or abstracted at the moment of greatest condensation, the vibration is discouraged. "

This criteria has stood the test of time and has been the mantra for researchers studying thermoacoustic instability. Putnam and Dennis (1956), and Chu (1965) mathematically expressed the condition for the growth or decay of the oscillations according to Rayleigh criterion as,

$$\int_{V} \int_{0}^{T} p' \dot{q}' \, dt \begin{cases} > \text{acoustic losses,} & \text{oscillations grow} \\ < \text{acoustic losses,} & \text{oscillations decay} \\ = \text{acoustic losses,} & \text{no effect on the oscillations.} \end{cases} \tag{1.3}$$

Here, p' is the acoustic pressure fluctuation as measured at the flame, $\dot{q}'$ is the heat release rate fluctuations, T is the time period of oscillation, and V is the integration

volume over the combustion zone. It is important to note that the oscillations grow only when the thermoacoustic driving exceeds the losses through acoustic damping. Addition or removal of heat at the point of mean pressure will change only the frequency of the oscillation. For example, adding (or removing) heat a quarter-period before a pressure peak will increase (or decrease) the oscillation frequency. However, adding (or removing) sufficient heat a quarter-period after a pressure peak will decrease (or increase) the oscillation frequency. Heat addition (or removal) at any other phase will cause a combination of amplitude and frequency change on the oscillations.

However, the Rayleigh criterion does not account for the mean flow which plays a crucial role in determining the extent of coupling between the acoustic and combustion processes. As a result, other general criteria have been developed considering the effect of mean flow (Cantrell and Hart, 1964; Morfey, 1971; Myers, 1991), and fluctuations in temperature (Chu, 1965; Nicoud and Poinsot, 2005) and concentration (Brear *et al.*, 2012). Despite such progress, an accurate criterion for the occurrence of thermoacoustic instability remains unaccomplished.

1.3.1 Thermoacoustic instabilities in LPREs

The breathtaking advances in the first half of the twentieth century ushered the age of jet and rocket propulsion. Until 1940s, LPREs development was led by amateur rocket societies, some well-funded teams located mostly in the Germany, Soviet Union and the United States (Sutton, 2005). The development of LPREs was strife with spectacular failures. Some of these failures were attributed to the occurrence of thermoacoustic instability. Soon, the development of LPREs were considered a national priority and became an industrial effort with substantial funding. Special expert committees were assigned to investigate the causes and means to overcome these failures (Sutton, 2005). The LPRE which powered the V-2 missile developed by the Germans during the second world war was originally devised for a liquid oxygen (LOx) and alcohol combination. Due to the notorious combustion instability encountered during

the development, the Germans switched the fuel to a mixture of kerosene and unsymmetrical dimethylhydrazine (Sutton, 2005).

In the erstwhile Soviet Union, from the 1940s, high-frequency thermoacoustic instability was encountered during the development of LPREs such as NK-33, RD-107, RD-108, RD-110, RD-111, RD-170 and RD-270 (Dranovsky, 2007; Natanzon, 2008; Anderson and Yang, 1995). Significant efforts were required to control the thermoacoustic instabilities resulting in development delays and project revisions. It even led to the cancellation of several projects and planned missions.

The United States encountered high-frequency thermoacoustic instability during the development of H-1 LPRE, booster engines (Thor, Atlas), lunar ascent LPREs and space shuttle main engine (Sutton, 2005; Anderson and Yang, 1995). Perhaps, the most famous history related to thermoacoustic instability is attributed to the development of the F-1 engine which powered the Apollo missions.

In mid 1962, an F-1 engine was destroyed during the course of a test planned under the Apollo manned lunar mission (Oefelein and Yang, 1993). Saverio "Sonny" F. Morea, the F-1 engine development project manager remarked "It was a disaster because once we had that instability, it would burn through the thrust chamber in milliseconds. The hardware went all over the place", "combustion instability was the biggest problem I ever had in my entire career" and "if we didn't come up with a solution, we weren't going to the Moon" (NASA's Marshall Space Flight Center, 2019).

The catastrophic failure was quickly identified to be a direct consequence of high-frequency thermoacoustic instability inside the combustion chamber. The timing of this setback and the political pressure associated with the space race at that time set of a series of events which propelled combustion instability into popular usage. Special committees were formed to investigate thermoacoustic instability. The committee studied previous recorded occurrences of thermoacoustic instability on large LPREs. It took 1332 full-scale hot-fire tests, 108 injector design changes, close to forty million dollars, and a better part of four years to suppress this thermoacoustic instability
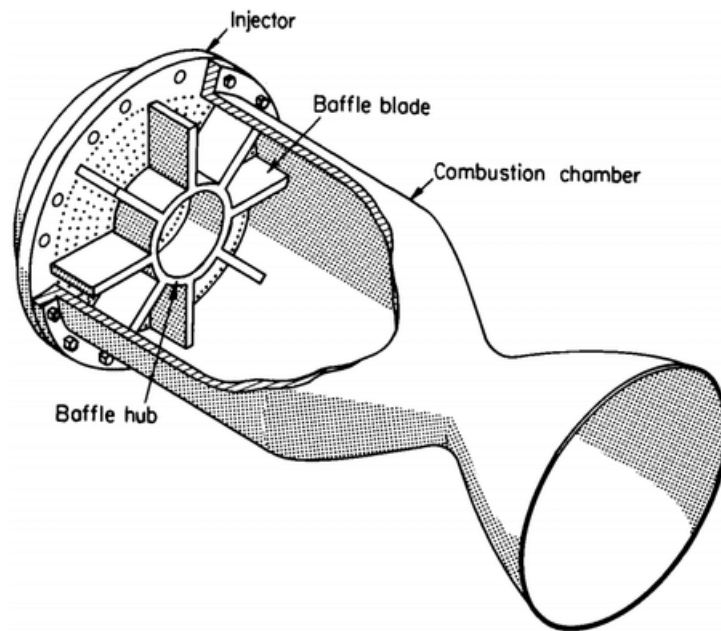
Fig. 1.4: Cutaway sketch of a thrust chamber with baffles installed at the injector face.
Reproduced from Harrje and Reardon (1972) (allowed for public use).

(Oefelein and Yang, 1993; Morea and Johnson, 2012). The stability fix involved a
baffle and a revised injector distribution. However, this improvement in stability came
at a 4% reduction in combustion efficiency (Oefelein and Yang, 1993).

A cutaway sketch of a thrust chamber with baffles installed in the injector face is shown
in Fig. 1.4. The baffle is usually a set of protruding element from the injector face
designed to arrest tangential thermoacoustic oscillations. Some of the injector holes
are present on the baffle plate. Essentially, the baffle compartmentalizes combustion
oscillations and arrests the growth of tangential oscillations. Nearly 14 different
baffle configurations were studied. The selected configuration was so stable that it
would damp out the artificially induced thermoacoustic instability within one-tenth of
a second. Since the understanding of high-frequency thermoacoustic instabilities was
incomplete at that time, this whole process involved exorbitant amounts of money and
significantly delayed the mission. The development of RS-25 LPRE (popularly known
as the space shuttle main engine) was also marred by issues pertaining to combustion
instability.

Shortly after liftoff in May 1980, one of the Viking engines in the first stage of

13

the Ariane 1 launch vehicle encountered combustion instability leading to explosive mission failure. Modifications to the injector geometry and change of fuel were necessary to remedy the thermoacoustic instability (Souchier *et al.*, 1999). During the development of Aestus LPRE which powered the upper stages of the Ariane 5 launch vehicle, high-frequency thermoacoustic instability was encountered during startup, full thrust and shutdown operations (Langel *et al.*, 1991). Laborious changes to the injector design and ignition characteristics were necessary to manage the thermoacoustic instability.

The Japanese LE-5B and LE-9 LPREs suffered from combustion instability (Fukushima *et al.*, 2002; Watanabe *et al.*, 2016). China also faced problems due to combustion instability in its YF-1, YF-2, YF-20 and YF - 100 (Sutton, 2005). For India's SCE-200 engine, which is under development, combustion stability assessment is one of the crucial evaluations (Kanthasamy *et al.*, 2014). Even now, it is challenging to identify the root causes behind the emergence of thermoacoustic instabilities and fixes required to suppress them in modern LPREs.

1.3.2 Measurements in an LPRE

In the early days, accelerometers and fast-response pressure transducers have been used to sense the high-frequency thermoacoustic instability (Harrje and Reardon, 1972). Acceloremeters capture the acceleration originating from the vibrations of the combustion chamber walls. Since the obtained measurements are coupled with the structural resonances of the LPRE, accelerometer data need not match with the pressure measurements. Moreover, the complex nature of the structural coupling makes it difficult to determine the extent of combustion oscillations in the LPRE and at best can be only considered as an indirect measurement of thermoacoustic instability. Thermocouples can monitor the temperature at the chamber walls and of the working fluid. However, due to the slow (relative to the acoustics and combustion) heat transfer process, temperature data from thermocouples can only be acquired at lower

sampling rates. As a result, thermocouple measurements do not provide meaningful measurements to interpret the high-frequency thermoacoustic instability.

Therefore, fast response pressure sensors are preferred to characterize the nature of combustion oscillations in an LPRE. The pressure sensors come in two types - piezoresistive and piezoelectric. The piezoresistive type transducers provides the absolute pressure unlike the piezoelectric type transducers which sense only the fluctuations about the mean pressure. Therefore, piezoresistive pressure transducers remain the first choice measurements in rocket combustors.

1.3.3   Rating techniques to quantify stability of LPREs

To quantify the stability of an LPRE, several combustion stability rating techniques were considered. The popular method involved forced excitation of pressure oscillations using directional explosive charges (Anderson and Yang, 1995; Harrje and Reardon, 1972). Directional explosive charges ensure that only the specific longitudinal or transverse mode gets excited. Detonating the explosive charge produces large amplitude pressure surges in the intended direction. Then, using precise high-frequency pressure measurements, the time taken to damp out the excited perturbation is quantified. Stability of the LPRE was guaranteed by a rapid decay in the amplitude of the oscillation. The rate of decay was roughly used as measure to quantify the inherent stability of the LPRE.

Another popular rating method in Russia is the method of oscillation decrement. It was a mandatory method to characterize injector configurations in the RD-170 and RD-180 LPREs (Dranovsky, 2007). Oscillation decrement is essentially the autocorrelation of the signal. In this method, the signal is compared to its time delayed copies. The rate of decay of autocorrelation is then used to define a damping rate which quantified the stability of the LPRE. The advantage of this method is that it is a passive method and does not require artificially induced disturbances.

For any LPRE, the stability rating techniques can then be used to map the stability

boundaries. A typical stability boundary map is compiled for a range of testable control parameters such as chamber pressure, mixture (i.e., oxidizer to fuel) ratio, and throttling level. Such a stability map enables quantification of the stability margin (i.e., the proximity to thermoacoustic instability) for any given combination of operating conditions. An LPRE prone to thermoacoustic instability has large portions of the stability map deemed unstable. In such scenarios, it is desirable to understand the root cause of thermoacoustic instability and then perform appropriate modifications.

1.4 WHAT CAUSES HIGH-FREQUENCY THERMOACOUSTIC INSTABILITY IN ROCKET ENGINES?

Understanding the mechanisms that drive and sustain thermoacoustic instabilities will be helpful in several ways. It would greatly reduce the expensive testing, help in modelling and validating high-fidelity simulations, and may even prescribe design methodologies. Moreover, tailored control strategies can be engineered into the LPRE which inhibit the mechanisms driving high-frequency thermoacoustic instability.

The understanding of high-frequency thermoacoustic instability in LPREs requires a thorough knowledge of the combustion processes, the turbulent flow and the acoustics of the thrust chamber. The fundamental steps for combustion in an LPRE is governed by atomization, vaporization, mixing and diffusion, reaction processes. The injection pattern, chamber pressure, geometry of the thrust chamber, level of turbulence, the mixture ratio, film cooling, thermal and the acoustic boundary conditions determine the combustion stability characteristics of the LPRE.

One of the first authoritative works on the understanding of the high-frequency thermoacoustic instabilities in LPREs is the compilation by Harrje and Reardon (1972). The influence of thrust chamber and injector geometry, propellant evaporation and mixing characteristics, and their connection to the occurrence of thermoacoustic instabilities were summarized. Analytical methods to model high-frequency thermoacoustic instabilities, methodologies to characterize the stability of

16

LPREs, and design philosophies to ensure the stability of LPREs are also described. In another landmark compilation by Anderson and Yang (1995), the sensitive dependence of mixture ratio (i.e., the ratio of fuel and oxidizer mass flow rates), momentum flux ratio, temperature of propellants, and chamber pressure on the combustion stability characteristics were understood. Case studies of thermoacoustic instability phenomena in several flight-proven LPREs were also discussed. Later, Culick and Kuentzmann (2006) summarized the mechanisms exciting thermoacoustic instabilities and bulk flow instabilities and the numerical models used.

The unique Soviet practices followed in the diagnosis and management of thermoacoustic instabilities have been summarized by Dranovsky (2007) and Natanzon (2008). Recently, Sirignano (2015) reviewed the driving mechanisms leading to thermoacoustic instabilities in LPREs. First, he elaborately summarized the literature of analytical models used in rocket combustors. Then, he developed a nonlinear wave equation model for handling two-phase flows typical in combustors of LPREs. The role of shock wave in determining the amplitude during limit cycle oscillations was also shown to be related to the mean-flow Mach number.

1.4.1 Theoretical and analytical studies on high-frequency thermoacoustic instability

Until the late twentieth century, high-speed sophisticated instrumentation on LPREs were not possible. As a result, engineers relied mainly on limited data acquired from tests and empirical relationships between variables to characterize the high-frequency thermoacoustic instabilities.

Sensitive time lag theory

After the introduction of the Rayleigh criterion, the subsequent exciting development on the understanding of thermoacoustic phenomena came in the 1950s. It is well-known that combustion oscillations are affected by the acoustic pressure perturbations in the combustor through various chemical and fluid mechanical pathways. Since the

combustion processes encompass multiple time and length scales arising from injection, atomization, vaporization, transport, and turbulence, it is essentially impractical to model each of these individual processes accurately to understand the interaction between combustion, acoustic, and flow processes in an LPRE. Professor Luigi Crocco (1951, 1952) introduced the classic sensitive time-lag theory (also known as n-τ model), which essentially bypassed the treatment of the various length and time scales involved in the combustion processes. This theory was concurrently developed by several others as reflected in the works of Summerfield (1951); Tsien (1952); Marble and Cox Jr (1953); Crocco and Cheng (1956).

Here, all the combustion and fluid mechanical processes are encapsulated in two parameters: a positive amplification factor (n) and a time delay (τ), which are selected based on the propellant, injector design, and oscillation frequency in the LPRE. The time delay τ dictated whether the oscillations would grow or decay, while n dictated the growth (or decay) rate. Then, the heat release rate oscillations ($\dot{q}'$) and acoustic pressure perturbations (p') are related as $\dot{q}' = np'(t - \tau)$. Under certain conditions, the perturbations in the heat release rate oscillations could feedback into the pressure, thus strengthening the positive feedback loop. In turn, this led to the emergence of self-sustaining high amplitude periodic pressure oscillations in the combustion chamber. The n-τ model was first shown to work reasonably well for longitudinal thermoacoustic instability (Crocco and Cheng, 1956). Later, for transverse thermoacoustic instability, Reardon *et al.* (1964) showed that flow velocity had a stronger effect on the atomization, vaporization, and mixing processes. Therefore, the heat release rate and subsequent time lag need to be coupled with both the acoustic pressure and flow velocity for the n-τ model to work. In essence, the n-τ model paved the way of simple reduced order models which do not deal explicitly with each physical processes in the LPRE.

Reduced order models based on linear theory

Studies based on linearized wave equations for simplified geometries allow reduced computational effort. Combustion is incorporated into the wave equation as a source term either using response functions or variants of n-τ model or empirical relations (Harrje and Reardon, 1972). The acoustic pressure is extracted directly by solving the wave equation for its eigenmodes and eigenfrequencies. Further, if the analytical mode shapes are known a priori, the spatial and temporal solution can be split using separation of variables. Then, the wave equation can be written as an ordinary differential equation in time and can be solved using the Euler or the Runge – Kutta methods (Harrje and Reardon, 1972). Following this linear stability analysis is effective to predict only the initial growth rate. Beyond the initial growth phase, thermoacoustic instability is predicted to have an unbounded growth. However, in reality, the growth rate of oscillations beyond a certain amplitude is limited by nonlinear processes.

Nonlinear effects

Rocket combustion is essentially a highly nonlinear and dynamic process. The nonlinearities may arise out of gas dynamic processes, flame interactions, boundary interactions, high thermal energy density (O $\sim 30~GW/m^3$), and the turbulent base flow (Culick and Kuentzmann, 2006; Lieuwen, 2012). Further, extreme rates of heat addition in rockets is a major source of nonlinearities in rockets. The magnitudes of the oscillations of the system variables and acoustic variables approach the order of magnitude of the mean variables. As a consequence, the nonlinearities in the system become significant and promote the transfer of energy across higher modes. The turbulent base flow induces wrinkles along the flame boundaries which are smoothed out at different rates depending on their length scales. The presence of flow separation at sharp edges, rapid flow expansions and interaction of the acoustic oscillations with the coherent structures in the reactive flow-field add upon the nonlinearities in the system (Fabignon *et al.*, 2003; Messineo *et al.*, 2016). Further, the wave steepening mechanism

causes acoustic waves to turn into shock waves (Hirschberg *et al.*, 1996; Flandro *et al.*, 2007). The usage of nonlinear theory correctly predicts the saw-tooth wave profiles in pressure for cases containing shock discontinuities, while linear theory predicts smooth sinusoidal waveforms (Tyagi and Sujith, 2003*a,b*; Sirignano, 2015).

Chester (1964) investigated the conditions required for the occurrence of flow discontinuities in the form of shock waves in a closed duct using a rigorous gas dynamics framework. Inspired by the experimental work of Saenger and Hudson (1960), he showed that the shock waves arise as the natural solution for frequencies close to the resonant frequency since the nonlinear terms from acoustics, viscosity and heat conduction become significant. Further, he showed the effects of bulk viscosity of the fluid and boundary layer on the oscillations at near resonant frequencies.

On top of all these events, there exist several interactions across various subsystems such as injector hydrodynamics and flame dynamics, rendering the system complex (Rubin, 1966; Price, 1984; Blomshield *et al.*, 1997; Gröning *et al.*, 2016; Messineo *et al.*, 2016). Several processes occurring in rocket engines are artifacts of the nonlinearities in the system (Blomshield *et al.*, 1997; Flandro *et al.*, 2007). Limit cycle oscillations could arise due to the balance between the acoustic driving and damping mechanisms in the system along with other limiting mechanisms like propellant flow.

A stable combustor can be excited with a finite amplitude disturbance to trigger self-sustained oscillations of considerable amplitudes. This phenomenon is known as triggering instabilities in rockets. During triggering, the system transitions to a state of high amplitude oscillations through a finite amplitude perturbation above a threshold amplitude, called triggering amplitude. When the amplitude of the initial condition is less than the triggering amplitude, the system behavior decays asymptotically to a stable state. The phenomenon of triggering is observed when the system is operating in the bistable zone (Jegadeesan and Sujith, 2013).

In rocket engines, the time history of acoustic pressure oscillations is usually accompanied by a rise in the mean pressure levels. This phenomenon, known as DC

shift (etymology is linked with the analogy with electrical science) exposes the rocket to dangerous amplitudes (Flandro *et al.*, 2007). As a result of these nonlinear behaviors, it is vital to understand the dynamics exhibited by a rocket combustor from the perspective of nonlinear dynamics.

In order to understand limit cycle and triggering behaviors, it is essential to overcome the shortcomings of the linear methods. The deficiencies of linear methods for studying thermoacoustic instability was identified by the early pioneers. They presciently predicted that a true understanding of the onset and sustenance of thermoacoustic instability is possible by embracing the nonlinear analysis methods.

The sensitive time lag theory was extended to nonlinear analyses using a perturbation series in amplitude (Sirignano, 1964; Mitchell *et al.*, 1969; Zinn, 1968). Zinn and Powell (1971); Zinn and Lores (1971) introduced the Galerkin method for nonlinear oscillations into the time-lag theory. They were able to achieve a reasonable agreement with the experimental data limited to low Mach number flows.

Later, Jahnke and Culick (1994) introduced dynamical systems theory to study the limit cycle behavior and estimated the stability boundaries using time averaging methods. The complexities of the nonlinear equations necessitated the usage of several approximations and assumptions. The chosen approximations, assumptions, number of modes and the degree of nonlinearity considered had a large impact on the prediction (Culick, 1994). So far, most of the studies have emphasised only the acoustic nonlinearities. It is difficult to faithfully capture the nonlinear aspects of combustion processes. This problem has been circumvent largely by relying on time-lag models.

1.4.2 Experimental studies on high-frequency thermoacoustic instability

From the turn of this century, the ability to perform sophisticated experiments at high-pressure and high-temperature environments along with the advances in high-speed instrumentation and imaging technology have enabled us to focus on understanding the fundamental processes controlling thermoacoustic instabilities in LPREs. Experiments

in model combustors comprising a single or an array of injection elements have provided great insights into the combustion and flow processes. These experiments have enhanced our knowledge of the influence of injector geometry (specifically, shear coaxial versus pintle injector types), and the coupled interaction between the combustion processes and the acoustic field under longitudinal and transverse excitation. Moreover, such configurations are amenable to high-fidelity simulations and reduced-order modeling. The thermoacoustic instabilities in these experiments are either forced through external means or self-excited.

Further, if the pressure or temperature of the propellant exceeds the critical point, their properties vary substantially. In an LPRE, the propellants can be injected into the combustor in either the subcritical or transcritical or supercritical states (Heister *et al.*, 2019; Sardeshmukh *et al.*, 2020). Most of the first stage LPREs operate in the supercritical or transcritical regimes whereas upper stage LPREs operate under subcritical conditions. Therefore, it is important to understand the dynamics across all these pressures and temperatures. Performing experiments at transcritical and supercritical conditions became feasible only recently (Davis and Chehroudi, 2007).

Forced systems

Even though combustion instability is often encountered in full-scale LPREs, it is difficult to spontaneously excite thermoacoustic oscillations in subscale laboratory combustors. As a result, we have to artificially initiate thermoacoustic instability using devices which impart sufficient amplitude perturbations into the combustor. So far, acoustic speakers, directional explosive charges (or bombs), pulse guns, sirens and rotary actuators have been used. Out of these methods, explosive charges and pulse guns can be scaled to be used to excite only the natural acoustic modes of the combustor. Moreover, these two methods can be scaled and installed in even full-scale combustors. However, sirens and rotary actuators cannot be used in full-scale combustors but can be used to sweep through a range of frequencies apart from the natural acoustic modes of

the combustor.

In a 9 bar LOx/CH_4 combustor, Richecoeur *et al.* (2006) continuously forced the flow rate at the transverse frequencies of the combustor with a periodically obstructed secondary nozzle. They suggested that at certain operating conditions, the shear regions of neighboring jet flames collide to enhance the atomization and mixing of propellants, leading to an increase in the intensity of heat release rate oscillations. Further, they reported a strong coupling between the high-frequency transverse acoustic pressure and the OH* chemiluminescence with a concomitant increase in flame-spread and flame intensities. However, the excited pressure amplitudes from this flame-flame interactions were only about 8% of the mean chamber pressure.

Later, Méry *et al.* (2013) increased the mean chamber pressure to ~ 60 bar and excited higher amplitudes by modulating the entire flow rate through two nozzles at the exit of the same combustor to obtain oscillation amplitudes close to 20% of the mean chamber pressure. For high levels of oscillation amplitudes, they reported that the smaller droplets closely follow the transverse acoustic velocity while their vaporization and eventual heat release rate follows the transverse acoustic pressure.

In a warm oxygen/kerosene model rocket combustor with a single coaxial injector, Miller *et al.* (2007) varied the length of the combustion chamber to excite longitudinal thermoacoustic instabilities. Since thermoacoustic instability was observed only for a range of lengths, they hypothesized that the spatiotemporally varying heat release rate couples with the acoustics to select the most amplified mode.

Successive studies were performed in DLR's 40-60 bar BKH combustor based on LOx/H_2 propellants by modulating the exhaust through the secondary nozzle in the combustor (Hardi *et al.*, 2014*a*). The length of the LOx core length as well as its fluctuations were shown to decrease for increasing oscillation amplitudes (Hardi *et al.*, 2014*b*). The transverse acoustic velocity was reported to play a primary role in the shortening of the flame jet. The transverse acoustic pressure oscillations was found to be in-phase with the OH* emission intensity (Hardi *et al.*, 2014*a*).

Continuously varying the length of the oxidizer post, Yu *et al.* (2012) observed stable to unstable to stable transitions in a single-element $H_2O_2/JP-8$ combustor. Later, they detected that the relative timing between the vortex pulse determined by the compression wave in the post and its interaction with the chamber acoustic compression wave controlled the occurrence of thermoacoustic instability (Harvazinski *et al.*, 2015).

Self-excited systems

Self-excited thermoacoustic instabilities are observed in several full-scale LPREs and some carefully designed subscale rocket combustors. Studying thermoacoustic instabilities in such spontaneously self-excited combustors is desirable since the actual mechanisms exciting the high amplitudes will be revealed without any artifact from the external forcing.

In a 14 bar $LOx/kersone$ combustor with triplet impinging jet injectors, Sohn *et al.* (2007) showed that the onset of self-excited oscillations depend on the correlation between the characteristic burning or mixing timescale with the acoustic timescale. Nunome *et al.* (2011) studied the effect of cryogenic hydrogen injection temperature on the stability of a LOx/LH_2 combustor for five different coaxial injector configurations. They reported the occurrence of unstable combustion when the hydrogen injection temperature was lowered below 50 K.

In DLR's 42 injector LOx/H_2 BKD combustor, a series of investigations were performed to study self-excited thermoacoustic instabilities. It was shown that the ratio of oxidizer to fuel flow rate and hydrogen injection temperature had a stronger effect on the chamber acoustic frequencies than the chamber pressure (Gröning *et al.*, 2013, 2014). Later, the length of the oxidizer posts was varied to study its effect on the combustion stability. They observed that the heat release rate oscillations were determined by the injector resonances. Maximum oscillation levels were achieved only when the dominant acoustic pressure and the OH* intensity frequencies coincided. Moreover, two types of thermoacoustic instability were identified. The first type is

an injector-driven thermoacoustic instability characterized by amplitude levels around $\sim 40\%$ of the mean chamber pressure (Gröning *et al.*, 2016). In the second type, amplitude levels reached up to $\sim 80\%$ of the mean chamber pressure due to enhanced interaction between chamber acoustics and the injector's fundamental longitudinal mode (Armbruster *et al.*, 2018). Later, using dynamic mode decomposition, they showed that the flame dynamics are strongly influenced by the LOx injector acoustics only beyond a certain chamber pressure (Armbruster *et al.*, 2019). They also suggested that the periodic vortex shedding in the LOx post orifice to be the source of this injector-driven thermoacoustic instability. Using LOx/LNG in the same combustor, they hypothesized that the rapid displacement of the lifted jet flame might trigger thermoacoustic instability (Martin *et al.*, 2021).

Simultaneously at Purdue University, several studies were performed to understand self-excited thermoacoustic instabilities in single-element and multi-element subscale rocket combustors. In a 22 bar single-element longitudinal thermoacoustic instability combustor, Sisco *et al.* (2011) concluded that injector boundary conditions had a superior influence over the stability than other parameters such as the oxidizer tube geometry which affected the phase lag.

In a $9 - 11$ bar 2D subscale rocket combustor fed by $H_2O_2/(JP - 8 \text{ or } CH_4)$ and featuring an array of gas-centered shear coaxial injectors, Pomeroy and Anderson (2016) investigated the stability characteristics for different injector flow configurations and reported thermoacoustic amplitudes ranging from about 5% to even 100% of the mean chamber pressure. In a 12 bar O_2/CH_4 single-coaxial element combustor, Lorente *et al.* (2018) showed that low-frequency bulk mode oscillations can coexist with high-frequency longitudinal oscillations depending on the oxidizer temperature.

Coupling mechanisms driving thermoacoustic instabilities

Based on the location at which the highest heat release rate oscillations are recorded during the occurrence of thermoacoustic instability, the instability sustaining

mechanism could be velocity coupled or pressure coupled with the resulting heat release rate oscillations. In the velocity coupled mechanism, the jet flames near the acoustic velocity antinode are perturbed more than the jet flames at other locations (Rey *et al.*, 2004; Sliphorst *et al.*, 2011). These perturbations leads to a nonuniform distribution of the vortices across the combustor. Eventually, a collective interaction between the neighboring jet flames results in high heat release rate oscillations leading to thermoacoustic instability. In the pressure coupled mechanism, the largest heat release rate oscillations are observed at the acoustic pressure antinodes (Knapp *et al.*, 2007).

Probably, the injector coupling is the most commonly observed coupling mechanism in liquid rocket engine combustors (Bazarov and Yang, 1998; Gröning *et al.*, 2016). While delivering propellants is the primary job of injectors, any perturbation developed upstream of the combustor (i.e., in the feedlines, turbopumps etc.) can interact with the dynamics in the combustion chamber. When a feedback loop is established between the injector resonant modes and the chamber acoustics, the engine can experience an undesirable growth in the amplitude of pressure oscillations. This leads to the state of thermoacoustic instability.

In a continuously variable resonant combustor where the oxidizer post length can be varied to obtain stable or unstable behavior, Harvazinski *et al.* (2015) showed the coincidence in the arrival times of acoustic pressure pulses in the oxidizer post and the combustion chamber to sustain strong cyclic variations of heat release rate oscillations during thermoacoustic instability. Morgan *et al.* (2015) used dynamic mode decomposition obtained from chemiluminescence images to show the presence of velocity coupling for the first transverse mode and a pressure coupling for the second transverse mode near the center of a 2D combustion chamber. Recently, Méry (2017) showed that the transverse flame displacement mechanism is a significant contributor to the heat release oscillations.

Apart from these aforementioned mechanisms, several other mechanisms pertaining to

atomization and vaporization of liquid propellants (Anderson and Yang, 1995; Harrje and Reardon, 1972), and flame-flame interactions (Richecoeur *et al.*, 2006) have also been reported to initiate and sustain high-frequency thermoacoustic instability in the combustor of rocket engines.

1.4.3 State of the art - high fidelity simulations

In last two decades, the breakthroughs in computing power allowed computational fluid dynamics (CFD) simulations to investigate combustion instability of LPREs (Heister *et al.*, 2019). High-fidelity simulations using unsteady Reynolds-Navier Stokes (URANS), large eddy simulations (LES), direct numerical simulations (DNS) and hybrid LES-RANS have been attempted. Out of these approaches, DNS provides the most accurate simulation but is currently limited by the extensive computational costs. It is cumbersome to compute the dynamics in each subsystem of an LPRE. Hence, simulations based on the joint usage of a baseline flow field with an acoustic solver and a suitable flame-response model is used (Urbano *et al.*, 2016). Such simulations have yielded acceptable predictions of stability maps and estimates of unstable modes in atmospheric pressure simulations (Urbano *et al.*, 2017). For higher pressures approaching the critical point of the reactants, the physical properties of the reactants vary substantially making it is difficult to predict accurately (Sardeshmukh *et al.*, 2020). Moreover, these simulations are reasonably accurate only when the appropriate flame response model is known beforehand. Therefore, it would be desirable to perform high-fidelity simulations which do not require the prior knowledge of flame response to understand the physical mechanisms driving thermoacoustic instability (Selle *et al.*, 2014; Matsuyama *et al.*, 2016). The major challenges while simulating thermoacoustic instability in LPREs are the modeling of thermoacoustic interaction, compressibility effects (including shock waves), resolving the wide range of spatial and temporal scales related to the acoustic, combustion, and turbulent flow processes (Popov and Sirignano, 2016; Urbano *et al.*, 2016), detailed chemical kinetics (Sardeshmukh *et al.*, 2015;

Bedard *et al.*, 2020), turbulence-chemistry interactions (Pant *et al.*, 2019).

Due to the coupled nonlinear interaction between the acoustic, reactive, hydrodynamic and gas dynamic processes, any small deviation from the experiment in the CFD simulation results in big differences in the resultant thermodynamic, chemical kinetic, acoustic and flow variables, and therefore the resultant combustion dynamics. Hence, it is of paramount importance to tightly validate the CFD simulation with the available experimental data. So far, the following methodologies have been used to validate the numerical simulations from the experimental data.

(a) Pressure signals are quantitatively compared for correct amplitudes and spectral content (Feldman *et al.*, 2012; Harvazinski *et al.*, 2013*b*). In some cases, the use of a three-dimensional simulation over axisymmetric simulations has improved the match in amplitudes and frequencies (Harvazinski *et al.*, 2013*a*; Garby *et al.*, 2013). The differences in the dominant frequencies are attributed to the improper modeling of the boundary conditions. In experiments, the heat loss from the walls renders non-adiabatic boundary conditions. During high-frequency thermoacoustic instability, several harmonics are also observed along with the fundamental dominant frequency. All the harmonics and their amplitudes are seldom captured in simulations. Further, the sharp or broadband nature of the peaks is compared from the width of the corresponding peak in the power spectral density plots.

(b) Time-averaged distributions of heat release rate oscillations from chemiluminescent radicals such as hydroxyl (OH*) and methylidyne (CH*) are compared during stable and unstable operation. The OH*/CH* emission intensity is measured in experiments while the simulations predict the heat release rate. Therefore, the differences arising from the chemical kinetics model and turbulence-chemistry interaction can be substantial during thermoacoustic instability (Xia *et al.*, 2011; Bedard *et al.*, 2014; Sardeshmukh *et al.*, 2015; Pant *et al.*, 2019; Hardi *et al.*, 2016*b*).

(c) A dynamic comparison of the heat release rate oscillations can be performed during stable and unstable operations (Hardi *et al.*, 2016*b*; Huang *et al.*, 2016). Instantaneous and phase averaged images can provide suggestions on how the deviations emerge during the course of a thermoacoustic cycle. Moreover, proper orthogonal decomposition (POD) and dynamic mode decomposition (DMD) techniques can be implemented to identify and compare the most energetic modes (Huang *et al.*, 2018). The comparison of the spatial modes from POD and DMD might provide crucial information on the coupling between the acoustics and the combustion processes.

The joint advances in computational power and our improved understanding of thermoacoustic phenomenon have improved the capability to simulate combustion

dynamics at high pressures. Simulations have also pointed out the possible mechanisms initiating and sustaining thermoacoustic instabilities (Harvazinski *et al.*, 2015; Urbano *et al.*, 2017; Pant *et al.*, 2019).

Despite such progress, current simulations fail to capture several intricate features of the combustion dynamics inside the combustor. As an example, consider the following two scenarios.

(a) Two simulations might predict the same amplitudes. However, their frequency content (i.e., the spectrum), signal waveform and associated multi-scale features might be vastly different. As a result, one simulation might correspond to a variant of thermoacoustic instability which can potentially be severely dangerous whereas the other simulation might correspond to a milder variant of thermoacoustic instability.

(b) Simulation might predict low amplitude oscillations. However, a slight perturbation in the propellant flow rate or the acoustic pressure might tip the system to harmful large-amplitude thermoacoustic instabilities. Therefore, it is essential to estimate the proximity to the onset of thermoacoustic instability for both the simulations and the experiments. Analysis of the detailed features of the signal enables us to estimate the proximity to the onset of thermoacoustic instability and therefore quantify the stability margin of the LPRE.

Therefore, it is imperative that the high-fidelity simulations also capture intricate features of the steepened pressure and heat release rate waveforms, their multifractal nature etc. Currently, there is a dearth of tools to validate such features in the numerical datasets.

1.5 CONTROL OF THERMOACOUSTIC INSTABILITY

Thrust chambers of LPREs are designed primarily for high performance (i.e., high combustion efficiency). Therefore, the inherent natural damping mechanisms are normally insufficient to arrest the growth of oscillations during the onset of thermoacoustic instability. So far, control of thermoacoustic instability in LPREs is largely an acquired art, leveraging on prior experiences and inherited company knowledge amassed over years of LPRE development and testing. Once a failure due to thermoacoustic instability is recorded during the testing of an LPRE, a series of steps are usually performed before performing a modification to the LPRE (Kitsche, 2010).

The engineer analyzes the recorded pressure and temperature data acquired from various locations within the LPRE. Simultaneously, high-speed video data of the rocket exhaust plume out of the nozzle obtained from the test stand is also analyzed. Post the test, the LPRE is disassembled. Then, the engineer(s) performs a visual inspection of the various components of the LPRE, comparing it with the images of the corresponding component obtained prior to the test. This exercise helps us to identify the component or subsystem which led to the failure. Based on the obtained knowledge from the visual inspection as well as the analysis of the acquired measurements from the LPRE, the engineer evaluates different ways to suppress the amplitude during thermoacoustic instability.

Early investigators used to suppress the ruinously large amplitude oscillations by making elaborate changes to the geometry of the thrust chamber (length or diameter) which significantly hampered the LPRE performance. Advances in computer modelling enables a fairly accurate estimation of the natural acoustic frequencies (fundamental modes and its harmonics) for a given geometry. This allows the design of the LPRE to be modified so that the natural acoustic frequencies of the thrust chamber do not coincide with that of the injector and other combustion specific frequencies. In some cases, the change in propellant combination was found to reduce the amplitude of the high-frequency thermoacoustic oscillations (Sutton, 2005). When thermoacoustic instabilities are identified late into the development, such comprehensive changes to the LPRE are not feasible.

The size, type and arrangement of the injector elements on the injector plate are found to play a significant role in the combustion dynamics (Harrje and Reardon, 1972). American and Soviet LPREs followed different philosophies while designing injector elements (Sutton, 2005). American designs relied heavily on jet impingement to atomize and achieve the desired mixture ratio, whereas Soviet designs used spray nozzle elements. Combined modifications to the flow, swirl and the placement of injectors in the thrust chamber in combination with the injector type were necessary to suppress

the oscillations. In some cases, an increase in the injection pressure or the injection velocity have helped to manage the amplitude found during thermoacoustic instability. In certain situations, an increase or decrease in the depth of the injection holes have found to work (Sutton, 2005).

When the encountered thermoacoustic instability corresponds to a tangential or radial mode, using metal baffles is found to be a reliable solution. First developed by Soviets (Sutton, 2005), this method allows retrofitting of baffles on top of the injector plate (see Fig. 1.4). Further modifications such as injecting cold propellants to reduce the thermal damage imposed by transverse oscillations and using step baffles to distribute the regions exhibiting intense heat release rate oscillations have also been performed. The usage of baffles reduces the usable volume for combustion in the thrust chamber. So, the stability enhancement from baffles usually comes with a slight performance penalty. However, there have been records of cases in which the baffles have aggravated or not affected the combustion stability (Oefelein and Yang, 1993).

Another solution developed by the Americans is the usage of acoustic resonance cavities near the head end of the thrust chamber. These carefully designed cavities absorb the acoustic oscillations at certain acoustic frequencies, thus continuously suppressing the pressure oscillations in the thrust chamber. Many Soviet LPREs do not use either baffles or acoustic resonance cavities, but rely on proven shear coaxial injection elements to ensure stable combustion operation. Usually, a combination of the above solutions is implemented to control the thermoacoustic oscillations in the LPRE. In some cases, implementing some of these control solutions have been found to be counterproductive and have even exacerbated the thermoacoustic instabilities (Armbruster *et al.*, 2020).

Further, depending on whether the thermoacoustic instability is encountered during startup, shutdown, throttling or full thrust operation, specific control solutions are devised. If the thermoacoustic instability is encountered only during the start transience, a change in the start sequence or usage of a crucible baffle is found to be a good remedy. The crucible baffle melts away after the start transience. In spite of the knowledge of

31

these control remedies, there exists no handbook or universally adopted prescription or methodology to make the changes to LPRE operation.

Recently, the development of high-speed measurement techniques has enabled simultaneous experimental works concerning control methods to suppress thermoacoustic instabilities. For example, Armbruster *et al.* (2020) devised a novel damping method to suppress injector-driven thermoacoustic oscillations. In this method, acoustic resonators tuned to injector acoustic modes can be retrofitted to existing LPREs.

In recent years, the progress of high fidelity simulations has served as an intermediate step to validate changes to the LPRE and predetermine the associated performance loss or gains. Once a design modification is approved, a series of tests at transient, steady-state, and mission-specific operating conditions must be carried out on subscale and subsequently full-scale versions of the LPRE. Our improved knowledge of thermoacoustic instability in an LPRE, amassed over the last century, has helped reduce the number of tests for certifying an LPRE.

Apart from the aforementioned passive control strategies, active control methods have also been developed. Active control techniques uses a feedback loop to nullify unstable perturbations in the combustor (Bennewitz and Frederick, 2013; Zhao *et al.*, 2018; Thannickal *et al.*, 2021). However, proper sensing of the disturbance and compact fast-response actuators need to be developed to realize active control solutions to operate in the harsh environments of an LPRE. Therefore, active control techniques have not been deployed in full-scale LPREs.

Ideally, LPRE combustors should be designed for stability along with performance. However, at present, this design methodology is not feasible. Since the methods used to impede high-frequency thermoacoustic instabilities are evolved by trial and error approaches, a comprehensive understanding of the physics behind initiating and sustaining these instabilities is lacking. Hence, there is an impetus for understanding thermoacoustic instabilities through experiments, high-fidelity

simulations and theoretical approaches.

1.6 RECENT ADVANCES

In this century, the phenomenon of thermoacoustic instability is being analyzed adopting a variety of novel methods inspired from dynamical systems theory (Sujith and Unni, 2020*b*; Juniper and Sujith, 2018) and complex systems theory (Sujith and Pawar, 2021). These approaches have been successful in explaining the temporal evolution of combustion dynamics, coupling behavior between acoustics and heat release rate, and elucidating the mechanisms which generate and sustain thermoacoustic instabilities. Moreover, an array of early warning measures to forewarn the occurrence of thermoacoustic instability have been unearthed (Pavithran *et al.*, 2021). However, the bulk of the recent research efforts applying these methods have been focused on understanding thermoacoustic instabilities in gas turbine engines. Here, we briefly describe the advances made using each of these methods.

1.6.1 Dynamical systems approach

Any system whose behavior changes with time is called a dynamical system (Strogatz, 2018). In an experimental setting, one does not have access to all the state variables which enables us to understand the temporal behavior of the system. The tools from dynamical systems theory allows one to characterize the long-term temporal behavior of a dynamical system even with the limited variables acquirable from experiments. Further, this approach have helped us make great strides towards understanding the nonlinear characteristics of thermoacoustic instability (Sujith and Pawar, 2021).

Dynamical states

In solid propellant rocket motors, Culick and co-workers used nonlinear acoustics to theoretically explain the saturation of amplitude leading to limit cycle oscillations (Culick, 1994; Jahnke and Culick, 1994; Burnley and Culick, 2000). Later, in gas

turbine combustors, limit cycle oscillations were shown to arise from the nonlinearities in the flame dynamics (Peracchio and Proscia, 1999; Lieuwen, 2002).

Applying numerical continuation methods, Jahnke and Culick (1994) showed that a thermoacoustic system can undergo pitchfork and torus bifurcations to exhibit quasiperiodic oscillations from limit cycle oscillations characterized by the presence of more than one incommensurate frequency. Chaotic oscillations were discovered first in models for premixed combustor (Sterling, 1993) and experiments on a laboratory gas turbine type combustor (Fichera *et al.*, 2001). Recently, chaotic oscillations have been reported in the solid propellant rocket motors (Guan *et al.*, 2018) and model rocket combustors (Aoki *et al.*, 2020).

Using bifurcation studies, different routes to chaos in a laminar thermoacoustic system were established (Kabiraj *et al.*, 2012; Guan *et al.*, 2020). The presence of a variety of dynamical states such as intermittency, frequency-locked, chaos, and quasiperiodicity were reported. Each dynamical state was characterized using phase space trajectories, recurrence plots, and return maps. The flame dynamics were remarkably different for each of these dynamical states. Understanding the difference in the flame dynamics for each state is crucial since each state would impose different thermal loading on the combustor.

In a turbulent combustor, Nair *et al.* (2013) proved that the aperiodic oscillations during stable operation of the combustor was chaotic. However, during thermoacoustic instability, this chaotic behavior was lost, paving way to ordered periodic oscillations. Nair *et al.* (2014) showed the presence of intermittency in between combustion noise (i.e., the stable state) and thermoacoustic instability. This intermittent state is characterized by bursts of high amplitude periodic oscillations interspersed between epochs of low amplitude aperiodic oscillations in an apparently random manner. Subsequent studies have confirmed the presence of intermittency prior to thermoacoustic instability (Gotoda *et al.*, 2014; Kheirkhah *et al.*, 2017; Ebi *et al.*, 2018). It was revealed that the state of combustion noise is actually not stochastic

but deterministic (Tony *et al.*, 2015). The flame dynamics during intermittency was found to be drastically different to that observed during stable state and thermoacoustic instability (Unni and Sujith, 2017; George *et al.*, 2018).

Performing multifractal analysis, Nair *et al.* (2014) showed that the acoustic pressure signal observed during combustion noise is multifractal, wherein the magnified views of the signal encompass the features of the entire signal. They attributed the existence of multiple time scales in the system to this multifractal nature. However, during the onset of thermoacoustic instability, this multifractal nature in the combustion dynamics is lost. Exploiting this disappearance, several precursors to thermoacoustic instability were devised.

Synchronization

Several studies have focused on the coupled interaction between the acoustic pressure and heat release rate fields during stable and unstable operations (Rogers and Marble, 1956; Zukoski, 1985; Poinsot *et al.*, 1987). However, only recently, Pawar *et al.* (2017) investigated this coupled behavior during the transition from stable state to thermoacoustic instability using techniques from synchronization theory. They observed desynchronized chaos during stable state. However, during thermoacoustic instability, they observed synchronized periodicity. In the intermediate state of intermittency, they observed synchronization during epochs of periodic oscillations punctuated by desynchronization during epochs of aperiodic oscillations, resulting in intermittent phase synchronization. Furthermore, they distinguished two different (strong and weak) synchronization behaviors during thermoacoustic instability. The weaker state is referred to as phase synchronization where the phases of acoustic pressure and heat release rate oscillations are synchronized. For a different operating condition also corresponding to thermoacoustic instability, they reported a stronger form of synchronization known as generalized synchronization where both the phase and the amplitude of acoustic pressure and heat release rate oscillations are also

synchronized.

Mondal *et al.* (2017*b*) investigated the spatiotemporal synchronization behavior between the local heat release rate and the global acoustic field in the same turbulent combustor. During intermittency, they discovered the coexistence of patches of synchronized periodic oscillations and desynchronized aperiodic oscillations coexisting in the reaction zone. Since these patterns of spatial synchrony and spatial desynchrony interchange as the flow convects downstream, they called the synchronization state a breathing chimera-like state. Chiocchini *et al.* (2018) built an interdependence index based on synchronization to forewarn an impending thermoacoustic instability. Borrowing concepts from synchronization theory, there have been several studies which used open-loop forcing to suppress the amplitude of thermoacoustic oscillations (Guan *et al.*, 2019*a*; Mondal *et al.*, 2017*a*; Roy *et al.*, 2020; Sahay *et al.*, 2021).

Evidently, most of these works barring a few, have been performed for understanding the dynamical behavior in Rijke tubes, laminar burners, and gas turbine-inspired turbulent combustors. In this thesis, we advocate adopting this approach to study the dynamical behavior in rocket combustors.

1.6.2 Complex systems approach

The dynamics of many natural and man-made systems are composed of a large number of interacting units. The interactions between these units (or subsystems) leads to the emergence of an aggregate nonlinear system behavior. This 'whole' system behavior cannot be understood by the reductionist approach of 'sum of its parts'. Besides, the system can self-organize under different stimuli as a result of this complex nonlinear behavior. Such systems which encapsulate all such traits can be regarded as a complex system (Bar-Yam *et al.*, 1998).

An LPRE combustor can be considered as one such complex system whose behavior is determined by a variety of intricate interactions between the spatially spread flame, turbulent flow, and acoustic subsystems. Moreover, these interactions are spread out

over a wide range of spatial and temporal scales determined by the combustion, flow, and thrust chamber geometry (acoustics).

Complex networks

The framework of complex networks is one of the favored approaches to study the dynamics of complex systems (Barabási *et al.*, 2016; Newman, 2018). Deriving its roots from graph theory, sociology and statistical physics, complex networks exploded into a popular science in the beginning of this century. Since its inception, complex networks has been widely used in a variety of sciences including reactive flows (Sujith and Unni, 2020*a*; Shima *et al.*, 2021). Complex networks affords the unique prospect of being constructed in any user-defined manner to study a specific aspect of the system dynamics. Complex networks can be built solely from the temporal or spatiotemporal data acquired from experiments (Zou *et al.*, 2018; Iacobello *et al.*, 2020).

Using visibility algorithm, Murugesan and Sujith (2015) constructed complex networks corresponding to the time series of local pressure maxima in a turbulent combustor. They identified that the resulting network during the state of combustion noise exhibited a scale-free topology. During the transition to thermoacoustic instability, this scale-free nature is lost, leading up to a regular network. In the same combustor, Tandon and Sujith (2021) studied the emergence of order during thermoacoustic instability from disorder during combustion noise in the same combustor using cycle networks. Constructing recurrence networks, Godavarthi *et al.* (2017) studied the topology of the phase space of the pressure fluctuations during the transition from combustion noise to thermoacoustic instability. Using cycle networks, Okuno *et al.* (2015) showed the existence of pseudo-periodicity and high-dimensionality in the dynamics during thermoacoustic instability. Unni *et al.* (2018) studied the flow dynamics for the stable, intermittent and unstable regimes of a turbulent combustor by analyzing the topology of a time-averaged spatial network derived from the velocity field. They discerned that the spatial regions exhibiting extreme values of network centrality measures are the 'critical

regions' in the flow-field where control actions need to be targeted. Krishnan *et al.* (2019*b*) investigated the spatiotemporal dynamics of acoustic power sources for the different operational regimes of the same combustor by constructing time-varying spatial networks. They suggested that small fragments of acoustic power sources which exist during combustion noise nucleate, coalesce, and grow to form large clusters during thermoacoustic instability. Later, they suppressed thermoacoustic instability by targeted secondary air-jets on the 'hub' regions highlighted by the network measures (Krishnan *et al.*, 2019*a*). They also quantified the vorticity interactions using spatial weighted turbulent networks constructed from Biot-Savart law (Krishnan *et al.*, 2021).

Marrying synchronization and vorticity networks, Hashimoto *et al.* (2019) studied the spatiotemporal dynamics during thermoacoustic instability in the large eddy simulations of a O_2/H_2 rocket combustor featuring a single coaxial injector element. Recently, using thermoacoustic power networks, Shima *et al.* (2021) elucidated the formation mechanism of high-frequency thermoacoustic oscillations in the same combustor. Using symbolic transfer entropy, they identified causality relationships between acoustic pressure and heat release rate fluctuations during the transition to thermoacoustic instability. Aoki *et al.* (2020) characterized the intermittent behavior in the experimental single-element O_2/H_2 combustor using a combination of ordinal partition transition networks and symbolic dynamics.

1.6.3   Machine learning

Over the last few years, rapid advances made in machine learning algorithms have pervaded all fields of science and engineering (Bishop, 2006; Brunton *et al.*, 2020). Specific applications to LPREs include combustion instability analysis (Waxenegger-Wilfing *et al.*, 2021*b*), health monitoring (Schwabacher, 2005), and control (Dresia *et al.*, 2021; Waxenegger-Wilfing *et al.*, 2021*a*). Novel machine learning algorithms mated with other recently developed methods have been realized to precurse thermoacoustic instability (Kobayashi *et al.*, 2019; Gangopadhyay *et al.*, 2020; Ruiz

et al., 2021; Cellier *et al.*, 2021; Sengupta *et al.*, 2021; Bury *et al.*, 2021; Dhadphale *et al.*, 2021). In the future, machine learning methods are likely to play a major role in the modeling of LPRE development, and in LPRE control and monitoring applications.

1.7   INTERIM SUMMARY AND MOTIVATION

The presence of complex nonlinear interactions between the acoustic and the reactive flow subsystems in the LPREs leads to thermoacoustic instability. Conventionally, the stability of the combustion chambers in LPREs has been either classified as stable or unstable. However, in practice, there exist intermediate states. The dynamical behavior during these intermediate states is significantly different from the stable state and thermoacoustic instability. Hence, it is vital to understand the combustion dynamics during the entire transition from stable state to full-blown thermoacoustic instability via intermediate states.

Furthermore, contemporary LPREs are developed based on computational fluid dynamics (CFD) simulations and phenomenological models before subjecting to subscale tests, cold flow tests, and hot flow tests. Due to the exorbitant costs and lengthy development timelines involved, it is critical that the simulations and models capture all the required physical aspects of the system. A failure to do so would lead to a mismatch between simulation data and real data. Such a failure might potentially delay the development of rocket engines for their respective applications. Given this scenario, parallel research efforts to match the amplitude levels seen in experiments with those obtained in the models are being undertaken (Sardeshmukh *et al.*, 2015).

The current state of the art of such high fidelity simulations has not progressed to fill the gap between experiments and numerical results. In many simulations, it is very difficult to obtain a good match in the amplitudes and the frequencies. Even if this is achieved, the resultant waveforms of the pressure oscillations are dissimilar and do not capture important features such as wave steepening (Saenger and Hudson, 1960). The failure to capture these behaviors can lead to significant departures in determining the

combustion stability of LPREs. Therefore, future modeling efforts must go beyond the quantitative comparisons of pressure and heat release rate amplitudes and frequencies, and try to capture other intricate features such as steepened pressure and heat release rate waveforms, multi-scale nature of the time series, etc.

Tools from the nonlinear theory have made substantial progress in characterizing the dynamics in laboratory-scale burners to gas turbine combustors (Juniper and Sujith, 2018). Despite this progress, there is a dearth of similar studies focused on rocket engines apart from a handful of studies. Given the critical consequences of nonlinearities in LPREs, we need to apply tools from dynamical systems theory and complex systems theory to characterize combustion dynamics in LPREs. Suitable measures developed following such an approach can be used to augment existing tools to tightly validate high-fidelity simulations aimed at developing stable LPREs. This approach would help us understand and characterize several nonlinear behaviors exhibited by LPREs, which are otherwise not feasible from the viewpoint of linear theory. Further, the characterization of the signal features following dynamical systems and complex systems theory provide an alternative method to accurately quantify the stability margin of LPREs based on both simulations and experiments.

Moreover, much of the literature on the stability of LPREs is focused only on the state of thermoacoustic instability. We intend to study not only thermoacoustic instability but the transition to thermoacoustic instability from the stable state as well. Furthermore, the self-excited nature of the combustor used in this study preserves the natural coupling mechanisms between the subsystems, providing us an edge over other studies pertaining to the forced response of external transverse acoustic oscillations. Sufficient knowledge about the coupled interaction between the spatiotemporal acoustic pressure and the heat release rate oscillations along with the flame dynamics subject to a transverse acoustic field would vastly improve the accuracy of modeling efforts and accelerate the development of stable LPREs. Furthermore, a comparative study of the flame dynamics near the wall and the center of the combustor would illuminate the non-local nature of

the coupling in the combustor.

1.8 OBJECTIVES

The primary aim of the thesis is to establish the frameworks of dynamical systems theory and complex systems theory to study the temporal and spatiotemporal dynamics in rocket combustors. In this thesis, we investigate the dynamics during the transition to self-excited transverse thermoacoustic instability in a model multi-element rocket combustor operating at elevated pressure conditions. The specific objectives are:

(a) Identify and characterize the dynamical states that occur during the transition to thermoacoustic instability.

(b) Characterize the slow-fast timescales present in the wave steepened acoustic pressure oscillations during thermoacoustic instability and provide methods to distinguish such signals from other time series signals.

(c) Using tools from synchronization theory, characterize the temporal and spatiotemporal coupled interaction between the acoustic pressure and methylidyne (CH*) chemiluminescence intensity oscillations (representative of heat release rate) during the transition from stable state to thermoacoustic instability via intermittency.

(d) Compare the local CH* intensity oscillations near the end wall and the center regions of the combustor during the transition to thermoacoustic instability.

(e) Estimate the contribution of each transverse acoustic modes to the spatial distribution of acoustic power during thermoacoustic instability at different transverse locations in the combustor.

(f) Quantify the extent of coherence in the CH* intensity oscillations for each dynamical state at different transverse locations of the combustor using the approach of weighted correlation networks.

1.9 OVERVIEW AND SCOPE OF THE THESIS

We study the transition to thermoacoustic instability in a multi-element subscale combustor of a rocket engine based on the oxidizer-rich staged combustion cycle. This oxidizer-rich staged combustion cycle pioneered by the erstwhile Soviet Union (Katorgin *et al.*, 1995) is sought actively along with other staged combustion cycles by different countries due to its performance advantage (i.e., higher specific impulse)

(Bedard *et al.*, 2021; Suresh, 2021). The experimental datasets were made available by Prof. William Anderson at Purdue University. This experimental dataset has been extensively analyzed at Purdue (Orth *et al.*, 2018; Gejji *et al.*, 2019, 2020) and Air Force Research Laboratory, USA (Harvazinski *et al.*, 2019). In Chapter 2, we describe the experimental setup of the rocket combustor and the measurement techniques utilized. This combustor exhibits self-excited high-frequency transverse instabilities. In Chapter 3, we characterize the various dynamical states during the transition to thermoacoustic instability using tools from dynamical systems theory along with the traditional tools. Then, in Chapter 4, we show the presence of slow and fast timescales in the wave steepened limit cycle oscillations during thermoacoustic instability and characterize the corresponding dynamics using recurrence networks.

Inspired by the progress in elucidating the different synchronization states of thermoacoustic instability in gas turbine type combustors, we differentiate the coupling between the acoustic pressure and heat release rate oscillations at the wall and the center of the combustor in the rocket engines in Chapter 5. We also devise a methodology to quantify the contribution of each acoustic mode towards the spatiotemporal acoustic power sources and sinks during thermoacoustic instability. In Chapter 6, we construct complex networks to study the coherent and incoherent spatiotemporal heat release rate oscillations during the transition to thermoacoustic instability. We highlight the differences in the flame dynamics at the wall and the center regions of the combustor for each dynamical state. Throughout the thesis, we utilize the frameworks of dynamical systems theory and complex systems theory for our temporal and spatiotemporal analyses. Such an approach has been largely unexplored in the case of rocket engines. Finally, we summarize our conclusions, describe the direct implications of our findings, and suggest future directions in Chapter 7.

CHAPTER 2

Experimental setup and measurement techniques

All the experiments are performed in a multi-element self-excited subscale rocket combustor based on an oxidizer-rich staged combustion cycle. This combustor is an evolution of combustors designed over the last decade to excite transverse mode thermoacoustic instabilities at Maurice J. Zucrow Laboratories, Purdue University. The experimental rig was designed, built and tested under the guidance of Prof. William Anderson (Orth *et al.*, 2018). We obtained the datasets corresponding to the pressure measurements acquired at various locations in the combustor and the methylidyne (CH*) chemiluminescence measurements acquired from the optically accessible windows of this combustor for our analysis.

2.1 EXPERIMENTAL SETUP

Known as the transverse instability combustor (TIC), the experimental rig consists of an oxidizer-rich preburner and a rectangular combustion chamber intended to produce self-excited transverse thermoacoustic instabilities (see Fig. 2.1). Since the main focus was to study transverse instabilities, the combustor consists of a long converging section intended to damp out the longitudinal modes.

The preburner is used to raise the temperature of gaseous oxygen. The preburner uses gaseous oxygen as oxidizer and hydrogen as fuel. The preburner feeds oxygen with 4%-5% mass fraction of water vapor to the combustor at a mean chamber pressure of 6.55 MPa, and mean temperature of 635 K. The combustor houses a linear array of nine oxidizer centered gas-gas shear coaxial injectors located at the entry to the combustion chamber. The injectors are designed based on the heritage Soviet designs used in oxidizer rich staged LPREs such as RD-170/180. A similar injector design is being tested for the semi-cryogenic engine under development in India (Rohit *et al.*, 2013).

An oxidizer manifold feeds the hot oxidizer (oxygen with 4% - 5% mass fraction of water vapor) uniformly to each of the coaxial injectors. The fuel, methane at 297 K, is injected through each of the shear coaxial injectors downstream of the oxidizer posts through a manifold with a choked inlet. In turn, nine non-premixed turbulent jet flames are established in the combustor. The propellant flow rates were chosen to maintain an equivalence ratio of approximately 1.24, which is typical for oxidizer-rich staged combustion cycle rocket engines. A mean Mach number of 0.265 is established in the oxidizer posts at nominal operating conditions. A mean pressure level of $\sim$1.14 MPa is maintained over the course of a test.

The combustor walls are coated with a protective layer of thermal barrier coating to minimize the wall heat loss during the test interval. The cumulative mass flow rate of oxidizer is 0.71 kg/s, while the mass flow rate of methane is maintained at 0.22 kg/s. Propellant flows are metered using critical flow venturi nozzles placed upstream of the choked inlets to the propellant manifolds (American Society of Mechanical Engineers, 2016; International Standards Organization, 2005). Uncertainty of mass flow rates, and subsequently operating conditions, were evaluated using the Kline-McClintock method of uncertainty propagation (Kline and McClintock, 1953) and following the procedure presented by Walters et al. (Walters *et al.*, 2020). The typical uncertainty in mass flow rate of propellants was $\leq$1% with a 95% confidence interval.

A summary of operating conditions are provided in Table. 2.1.

Table 2.1: Summary of operating conditions

$\dot{m}_{Ox}$ [kg/s]	$\dot{m}_{fuel}$ [kg/s]	ϕ [-]	P_c [MPa]	T_{Ox} [K]	T_{fuel} [K]	f_{1T} [kHz]
0.71	0.22	1.24	1.14	620	297	2.65

Geometry

The geometry and operating conditions are devised such that only transverse modes (1T mode frequency at 2650 Hz) are excited in the combustor. The combustion chamber is 240 mm wide and 30.5 mm deep. The 200 mm long combustion chamber is split into a
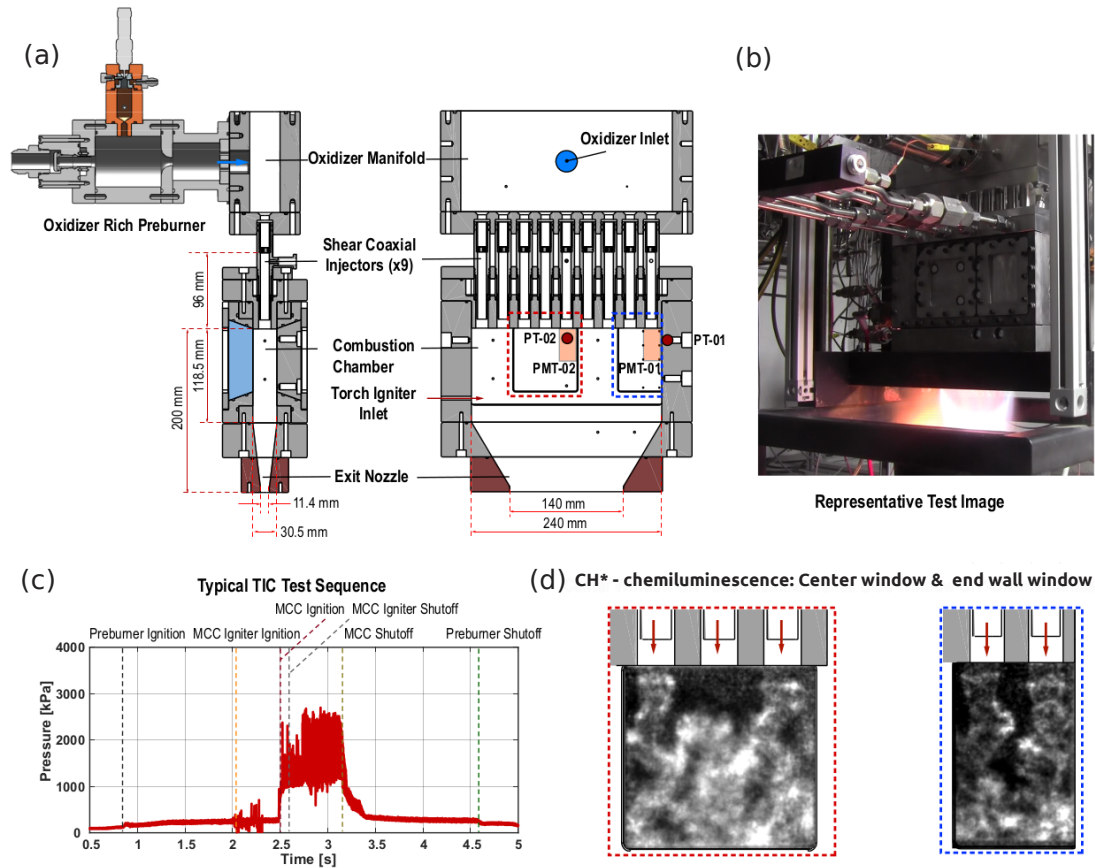
Fig. 2.1: (a) Schematic of the multi-element rocket engine combustor. The high-frequency pressure transducer and photomultiplier tube measurement locations are labeled as PT and PMT, respectively. (b) Image of the combustor during a hot-fire test. (c) Pressure time trace with time stamps of the various test stages. (d) Representative CH*-chemiluminescence images as observed from the optically accessible windows located near the center and the end wall of the combustor are shown.

118.5 mm straight section and 81.5 mm converging section. The combustion chamber is terminated with a converging section designed to preempt longitudinal modes and ensure acoustic decoupling from the downstream locations. The length of the chamber is designed for a fundamental longitudinal (1L) mode of 3475 Hz. This choice of length ensures that the harmonics of the transverse modes do not coincide with the 1L mode or its harmonics. A nozzle at the end of the converging section provides a choked boundary condition at the exit of the combustor.

All the injectors are uniformly spaced out by an injector centerline-centerline distance of 25.7 mm. The exit diameter of the injector element is 15.7 mm. The geometry of the

oxidizer manifold is tuned to minimize dynamic pressure losses and provide uniform flow to each of the injection elements downstream of it. A choke plate located upstream of each injector helped to decouple any feed system dynamics from the experiment and vice versa.

2.2 MEASUREMENT TECHNIQUES

Two spatial regions of interest are analyzed separately through tests - A and B performed under the same set of operating conditions. For test A, the optically accessible region is located towards the right end of the combustor, while for test B, this region is located near the center. Thus, we observe two jet flames for test A and three jet flames for test B (see Fig. 2.1d).

2.2.1 Pressure measurement

The acoustic pressure oscillations are acquired at the right-side end wall (PT-01) and the center of the combustor (PT-02) using piezoresistive Kulite WCT-312M sensors, at a rate of 250 kHz. The pressure sensors are installed in a recessed Helmholtz cavity to provide thermal isolation from the hot combustion exhaust. The resonance frequency (22.4 kHz) of the cavity is designed to be higher than any frequencies of interest in the experiment ($\sim$22 kHz) (Fugger $et\ al.$, 2017). This installation enables accurate measurement of dynamic pressure fluctuations in the chamber while reducing thermal load on the sensor element. The location of the pressure transducers used for the analysis are labeled in Fig. 2.1a.

2.2.2 Chemiluminescence measurement

Based on simulations and experiments performed for similar pressures and operating conditions, Bedard et al. (Bedard $et\ al.$, 2020) and Sardeshmukh et al. (Sardeshmukh $et\ al.$, 2017) compared heat release rate to chemiluminescence from CH*, OH* and CO2* radicals in the flame. They concluded that the CH* chemiluminescence provided a better qualitative representation of the heat release rate dynamics even though a phase

difference was reported between the experimentally obtained CH* emissions and the heat release obtained from the computations.

A Hamamatsu photomultiplier tube module (H11903-210) attached to a fiber optic probe gathered line of sight light emissions from a volume in the optically accessible window (PMT-01 and PMT-02) accessible in the combustor. The light emissions are filtered using an optical filter (Semrock FF01-427/10) to obtain CH* chemiluminescence signals at the same rate of 250 kHz synchronous with the acoustic pressure measurements (Bedard, 2017).

Line-of-sight integrated high speed CH* chemiluminescence images are simultaneously recorded at a rate of 100 kHz through the optically accessible windows in the combustion chamber. An optical filter (Semrock 434/14 Brightline Bandpass) of 14 nm bandwidth centered at 434 nm isolated the CH* emissions from the background luminosity. The emissions are collected through a 200 mm focal length, $f/4.0$ objective (Nikon AF Micro NIKKOR) and then amplified by a Lambert HiCATT 25 intensifier with 1:1 relay lens, and recorded with a Phantom v2512 high speed CMOS camera with a spatial resolution of 0.214 mm/pixel. The intensifier gain was set at 750 V with an exposure of 1 μs. The same camera and intensifier settings were used for both the tests. The CH* chemiluminescence measurements from the high speed imaging are representative of the local heat release rate dynamics. However, the photomultiplier measurement is representative of the cumulative heat release rate measurement since the obtained emissions emanates from a probe volume rather than just a point. The probe volume covered by the photomultiplier is shaded in orange in Fig. 2.1a. Further details of the operating conditions, hardware, design, measurement, and data acquisition techniques can be found in studies performed at Purdue University (Orth *et al.*, 2018; Harvazinski *et al.*, 2019).

2.3 TEST RUN

Ignition of preburner and main combustion chamber is achieved using hydrogen-oxygen torch igniters. A representative time series of acoustic pressure oscillations obtained from the pressure transducer located at the right side wall of the combustor is shown in Fig. 2.1c. The time interval in region I corresponds to starting of the preburner and the ignition of the main chamber. The first jump in the pressure signal close to 1 s corresponds to the start of the preburner and the second jump around 2.5 s corresponds to the ignition of the main chamber. Region III pertains to the shutdown of the engine. The acoustic pressure oscillations in region II are of prime interest in this study, as this interval of the signal represents the actual dynamical transitions from stable state to thermoacoustic instability in the rocket combustor. Therefore, a test run comprising approximately 1 s of steady inflow provides sufficient time to acquire data exhibiting transition to thermoacoustic instability at the frequencies of interest with negligible effects of heat loss (Orth *et al.*, 2018).

CHAPTER 3

Dynamical characterization of acoustic pressure oscillations during the transition to thermoacoustic instability

Combustion at elevated pressures and temperatures typical in rocket combustors is a highly nonlinear and dynamic process. As described in Sec. 1.4.1, the nonlinearities may emerge either from the flame, flow (turbulence and gas dynamic), the acoustics, and their interactions. As a result, rocket combustors exhibit a variety of dynamic behaviors attributed to nonlinear effects such as limit cycle oscillations, triggering, shifts in mean pressure levels, and shock waves. Adopting the framework of dynamical systems and complex systems theory, recent studies in gas turbine literature have shown immense progress towards understanding several dynamical states of combustor operation such as chaos, period-n limit cycle, and quasiperiodicity (Kabiraj *et al.*, 2012; Juniper and Sujith, 2018). Several measures such as Hurst exponent and recurrence quantification measures have been deployed to detect the proximity to the onset of thermoacoustic instability (Sujith and Pawar, 2021). In light of these advancements, it is enticing to apply this framework to understand the combustion dynamics in rocket combustors.

In this chapter, we apply various tools from nonlinear time series analysis to detect the different dynamical states and also characterize the dynamical transitions observed in acoustic pressure oscillations of the combustor. First, we briefly discuss the various tools used in our analysis. Next, we perform time series analysis of pressure oscillations for the different dynamical states. Then, we perform recurrence quantification analysis and multifractal analysis. Finally, we describe several measures that can be used to detect the dynamical transitions across different dynamical states in the combustor.

3.1 NONLINEAR TIME SERIES ANALYSIS

In order to study the dynamics inside combustion chambers of rocket engines, we need access to a wide variety of system variables. However, it is difficult to obtain data of all the independent variables that govern the dynamics of a rocket combustor. Usually only a handful of system variables (in the limiting case, at least one) are available to be acquired by an experimentalist. From such a limited dataset, applying techniques based on nonlinear time series analysis allows us to study the nontrivial underlying mechanisms (Ambika and Harikrishnan, 2020). Next, we will briefly describe the methodology used to perform the nonlinear time series analysis.

3.1.1 Takens' delay embedding

The dynamics of a rocket combustor in the higher dimensional phase space can be reconstructed from a state variable (for example, acoustic pressure: p') by Takens' delay embedding theorem (Takens, 1981). Such a reconstruction involves converting the univariate time series data into a set of delayed vectors from the appropriate choices of time delay (τ_{opt}) and embedding dimension (d). We construct the vectors $x'(t) = [(p'(t), p'(t + \tau_{opt}), p'(t + 2\tau_{opt}), \ldots, p'(t + (d-1)\tau_{opt}))]$ from the measured pressure signal, $p'(t)$. Here, t is varied from 1 to $n - (d-1)\tau_{opt}$, where n is the total number of data points in the signal. Each delay vector corresponds to a state point in the phase space and the combination of all these vectors constitute a phase space trajectory. To perform an appropriate phase space reconstruction for a particular state of the system, we need to obtain the optimum time delay (τ_{opt}) and the minimum embedding dimension (d) for the given signal. Here, τ_{opt} can be estimated using average mutual information (Fraser and Swinney, 1986) or autocorrelation function (Nayfeh and Balachandran, 2008). The minimum embedding dimension (d) can be obtained using false nearest neighbor method (Nayfeh and Balachandran, 2008) or alternately Cao's method (Cao, 1997) which we use in this study.

3.1.2 Recurrence analysis

Recurrence of state points in the phase space is a fundamental property of bounded dynamical systems. Recurrence plots are used to visually identify the time instants at which the phase-space trajectory of the system re-visits roughly the same area in the phase space (Eckmann *et al.*, 1995). The patterns present in a recurrence plot allow us to characterize the features of the signal embedded in the d-dimensional phase space. The construction of the recurrence plot requires a prior knowledge of the optimum time delay (τ_{opt}) and minimum embedding dimension (d). The recurrence plot of any time series is constructed by computing the pairwise distances between the state points of the reconstructed phase space. For a time series of n time instants, we can obtain the phase space trajectory $\vec{x'}(t)$ made of $n - (d-1)\tau_{opt}$ time instants. Then, the pairwise distances between all state points in the phase space can be accommodated in a distance matrix (PD_{ij}), as formulated below,

$$PD_{ij} = \left\| \vec{x'_i} - \vec{x'_j} \right\| \quad i,j = 1,2,\ldots,n - (d-1)\tau_{opt}. \tag{3.1}$$

Here, $\left\| \vec{x'_i} - \vec{x'_j} \right\|$ is the Euclidean distance between the two state points, i and j, on the phase space trajectory. Then, PD_{ij} is binarized by applying a suitable threshold (ϵ_r) to obtain the recurrence matrix (R_{ij}).

$$R_{ij} = \Theta(\epsilon_r - PD_{ij}), \tag{3.2}$$

where Θ is the Heaviside step function and ϵ_r is the threshold defining the neighborhood around the state point. The threshold (ϵ_r) can be fixed as a certain fraction of the size of the phase space attractor. Whenever a state point in the phase space recurs in the predefined threshold, it is marked as a black point. Non-recurring points are marked as white points in the recurrence plot. R_{ij} is one for a black point and zero for a white point. Thus, a recurrence plot is a two-dimensional arrangement of black and white

points that exhibits different patterns characterizing different dynamics of the signal. Several statistical measures can be derived from the organization of such black and white points in the recurrence plots. Such an analysis is known as the recurrence quantification analysis of a measured signal. One of the prime advantages of this analysis is that it can be applied to short and even nonstationary data, making it apt for data analysis from rocket combustors. Measures such as determinism, recurrence rate, trapping time, entropy, laminarity, and average diagonal length can be used to study the recurrence behaviour of the phase space trajectory (Marwan, 2003; Webber Jr and Marwan, 2015). These measures could further be used to distinguish between the various dynamical states exhibited by the system. Here, we discuss the usage of determinism (DET), recurrence rate (RR), and the ratio between these quantities ($RATIO$) in the analysis of acoustic pressure data obtained experimentally from the model rocket combustor.

Recurrence rate measures the density of black points in a recurrence plot and can be obtained as:

$$RR = \frac{1}{N^2} \sum_{i,j=1}^{N} R_{ij} \tag{3.3}$$

where $N = n - (d - 1)\tau_{opt}$ is the number of state vectors in the reconstructed phase space.

Determinism measures the percentage of black points in a recurrence matrix which form diagonal lines of minimum length l_{min}.

$$DET = \frac{\sum_{l=l_{min}}^{N} lP(l)}{\sum_{l=1}^{N} lP(l)} \tag{3.4}$$

where, $P(l)$ is the probability distribution of diagonal lines having length l and $l_{min} = 2$.

The ratio of determinism and recurrence rate ($RATIO = DET/RR$) has been introduced by Webber Jr and Zbilut (1995) to discover transitions in physiological systems.

52

3.1.3 Multifractal analysis

Classical Euclidean geometry deals with smooth objects which have an integer dimension. However, many things in nature contain wrinkles when observed at different levels of magnification. Such objects or signals are classified as fractals and they exhibit self-similar features at various observational scales (Feder, 2013). Measures such as length, area, and volume for such objects are dependent on the scale at which the measurements are performed. The logarithmic plot of the measure of the object versus the scale at which the object is measured would give a straight line with an inverse power law (Feder, 2013). The absolute value of the slope of this line is known as fractal dimension (D). Fractal dimension can then be used to describe a fractal time series which exhibits self-similarity at various timescales (Mandelbrot, 1967). For a fractal time series signal, the Hurst exponent (H) quantifies the amount of correlation in the signal and is related to the fractal dimension of the time series as $D = 2 - H$ (Mandelbrot, 1983). If $p(t)$ is a fractal time signal, then $p(ct) = p(t)/c^H$ is another fractal signal preserving the same statistics (Nair and Sujith, 2014).

Certain complex signals cannot be described using a single fractal dimension. These signals can be described with a range of fractal dimensions and such signals are classified as multifractals. In this thesis, we use multifractal detrended fluctuation analysis (MFDFA) (Kantelhardt *et al.*, 2002) to study the multifractal characteristics of the time series of acoustic pressure oscillations. To estimate the Hurst exponent, the time series [$p(t)$] is mean [$\langle p(t) \rangle$] adjusted to get a cumulative deviate series y_i as:

$$y_i = \sum_{t=1}^{i} (p(t) - \langle p(t) \rangle) \quad i = 1, 2, \ldots, n \tag{3.5}$$

$$\langle p(t) \rangle = \frac{\sum_{t=1}^{n} p(t)}{n}. \tag{3.6}$$

The deviate series is then separated into an integer number n_w non-overlapping segments of equal span w. To look for trends in the segments, a local polynomial

fit $(\overline{y}_i)$ is made to the deviate series y_i and the fluctuations about the trend are obtained by subtracting the polynomial fit from the deviate series. Next, a quantity known as structure function (F_w^q) of order q and span w, can then be obtained from the fluctuations for $q \neq 0$ as:

$$F_w^q = \left[\frac{1}{n_w} \sum_{i=1}^{n_w} \left(\sqrt{\frac{1}{w} \sum_{t=1}^{w} (y_i(t) - \overline{y}_i)^2} \right)^q \right]^{1/q}.$$

(3.7)

For $q = 0$, F_w^q diverges. Therefore, a logarithmic averaging is performed to obtain the value of F_w^q as $q \Rightarrow 0$ (see Appendix. C). Finally, we obtain for $q = 0$, we obtain

$$F_w^q = \exp \left[\frac{1}{2n_w} \sum_{i=1}^{n_w} \log \left(\frac{1}{w} \sum_{t=1}^{w} (y_i(t) - \overline{y}_i)^2 \right) \right].$$

(3.8)

The generalized Hurst exponents $[H(q)]$ is then obtained from the slope (Ihlen, 2012) of the linear regime in a log-log plot of F_w^q, for a range of span sizes, w. We obtain this linear regime for 2 to 10 cycles of the acoustic oscillations corresponding to the frequency of 2650 Hz during thermoacoustic instability, as described in Appendix. A. Thenceforth, the generalized Hurst exponents can be represented as a spectrum of singularities, $f(\alpha)$, via a Legendre transform (Zia *et al.*, 2009).

$$\tau_q = qH^q - 1$$

(3.9)

$$\alpha = \frac{\partial \tau_q}{\partial q}$$

(3.10)

$$f(\alpha) = q\alpha - \tau_q.$$

(3.11)

This spectrum, represented in the form of a plot of $f(\alpha)$ against α, is known as the multifractal spectrum. The multifractal spectrum provides information on the fractal characteristics of the data. Further details regarding MFDFA can be found in the work of Kantelhardt *et al.* (2002) and Ihlen (2012).

In literature, the generalized Hurst exponent $H(q)$ for $q = 2$ is popularly known as the Hurst exponent (H). For $q = 2$, H becomes the scaling of the root mean square of the standard deviation of the fluctuations with the window size. Since its introduction, H has been used for various applications (Grech and Mazur, 2013; Suyal *et al.*, 2009). In thermoacoustics, Nair and Sujith (2014) have used H to capture the transition from stable state to thermoacoustic instability via intermittency in a laboratory-scale turbulent combustor. Also, Unni and Sujith (2016) have used H as a precursor to detect blowout in a turbulent combustor.

3.2 CLASSIFICATION OF DYNAMICAL STATES

In this section, we characterize the temporal behavior of acoustic pressure oscillations observed during the onset of thermoacoustic instability in the rocket combustor. Towards this purpose, we examine the time series of the chamber acoustic pressure oscillations, as shown in Fig. 3.1, acquired for the same operating conditions (working fluids, flow rates, upstream pressures, and temperatures) and the injector configurations. However, we notice that although the operating conditions are the same during experiments, the dynamics arising out of the combustor is different during each trial. The data-sets chosen for the analysis along with the dynamical transitions observed are summarized in Table. 3.1. Throughout the rest of this thesis, overline and prime are used to denote mean and fluctuations of the concerned quantity, respectively.

For Test - A (Fig. 3.1a), we observe that the time series is entirely composed of stable state, exhibiting low amplitude aperiodic oscillations. For Test - B (Fig. 3.1b), we observe small epochs of marginally large amplitude periodic oscillations interspersed within the aperiodic oscillations of the signal. We refer to this dynamical state as intermittency. In general, intermittency refers to a dynamical state composed of high amplitude bursts of periodic oscillations amidst epochs of low amplitude aperiodic oscillations in an apparently random manner (Nair *et al.*, 2014). Next, we obtain a transition from stable state to thermoacoustic instability via intermittency for Test - C
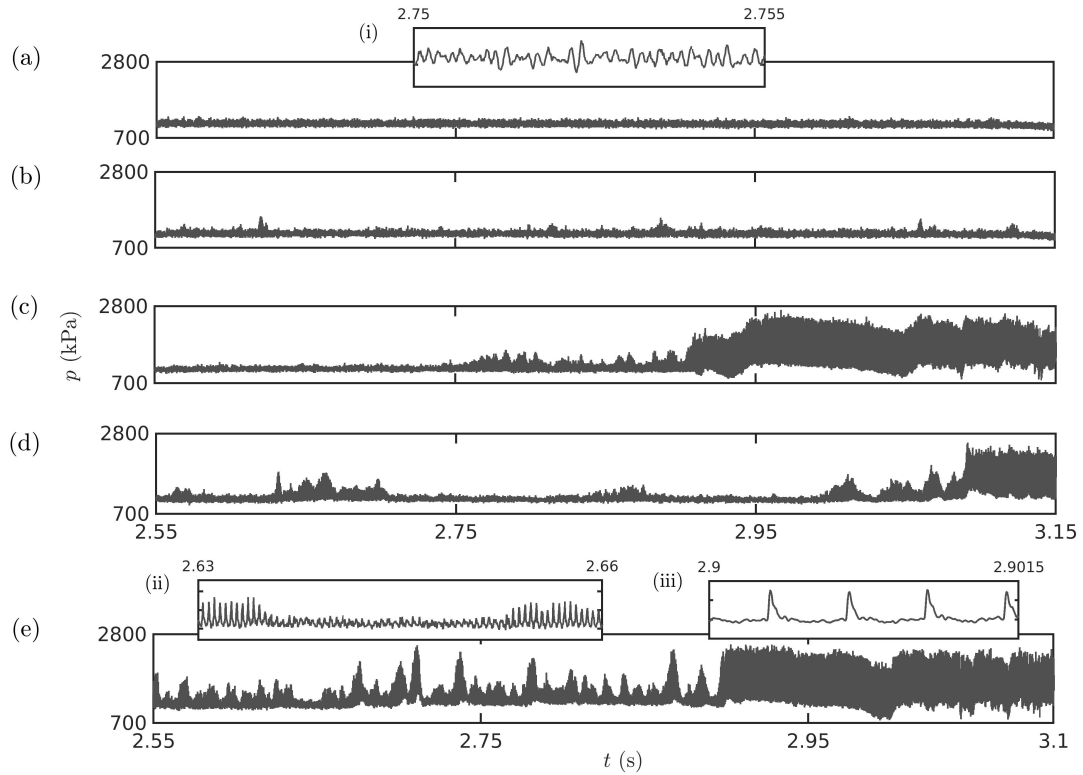
Fig. 3.1: Time series of acoustic pressure fluctuations acquired at the right side wall of the combustion chamber in the interval of interest marked II in Fig. 1c for tests: (a) Test - A (stable state), (b) Test - B (intermittency), (c) Test - C (stable state - intermittency - thermoacoustic instability), (d) Test - D (intermittency - thermoacoustic instability), and (e) Test - E (intermittency - thermoacoustic instability). The representative portions of the various dynamical states are zoomed and shown in the insets: (i) stable state, (ii) intermittency, and (iii) thermoacoustic instability.

(Fig. 3.1c). Here, thermoacoustic instability is comprised of large amplitude periodic oscillations. For Test - D (Fig. 3.1d) and Test - E (Fig. 3.1e), we detect only two dynamical states: intermittency followed by thermoacoustic instability without the occurrence of a stable combustor operation. However, the time spent in the periodic epoch of intermittency is higher during Test - E than that for Test - D. The reasons behind such a difference in the dynamics of the combustor behaviour for the same operating conditions remain unanswered.

A careful observation of the dynamics of the rocket combustor shows the existence of three primary dynamical states in the acoustic pressure oscillations. These states are stable state (low amplitude aperiodicity), intermittency (epochs of periodicity

Data-set	Dynamical transitions observed
Test - A	Stable state
Test - B	Intermittency
Test - C	Stable state $\Rightarrow$ Intermittency $\Rightarrow$ Thermoacoustic instability
Test - D	Intermittency $\Rightarrow$ Thermoacoustic instability
Test - E	Intermittency $\Rightarrow$ Thermoacoustic instability

Table 3.1: The list of data-sets chosen for analysis and the corresponding dynamical transitions observed in each test.

interspersed between epochs of aperiodicity in an apparently random manner), and thermoacoustic instability (epochs of sustained periodicity). During the periodic epochs of intermittency and thermoacoustic instability, we observe that the periodic waveform nearly takes the shape of a saw tooth wave profile. Further, we notice that the state of intermittency always precedes the onset of thermoacoustic instability. Such an observation is different from previous descriptions of the onset of thermoacoustic instability in rocket combustors where the transition from small amplitudes to large amplitudes is reported to occur through an exponential growth (Hart and McClure, 1959; Hart *et al.*, 1964; Culick, 1966, 1970; Bloxsidge *et al.*, 1988). Recently, Orth *et al.* (2018) band-pass filtered the time series of acoustic pressure oscillations in the same model multi-element combustor, analyzed in this thesis. When the frequencies pertaining to the fundamental mode are band-passed, they observed the presence of an exponential growth rate in the amplitude of oscillations. They also observed a similar exponential growth rate when the harmonic frequencies are band-passed. However, we analyze the time series with its entire frequency content preserved. We characterize the dynamical features of the representative portions of the time series pertaining to these three dynamical states observed during different trials of experiments. We choose stable state of Test - A, intermittency from Test - E, and thermoacoustic instability from Test - E. Next, we will look into the frequency content present in these three dynamical states. The amplitude spectrum with a frequency resolution of 12 Hz generated out of the fast Fourier Transform (FFT) algorithm is plotted in Fig. 3.2. For stable state (Fig. 3.2a), we observe that the amplitude spectrum is broadband, containing a wide range of
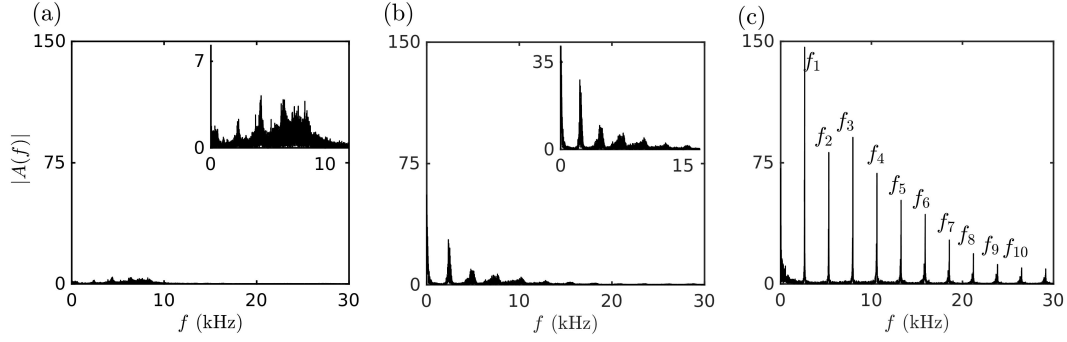
Fig. 3.2: The amplitude spectrum obtained through fast Fourier transform (FFT) with a frequency resolution of 12 Hz for (a) stable state of Test - A, (b) intermittency of Test - E, and (c) thermoacoustic instability of Test - E. The zoomed insets are shown for (a) and (b).

frequencies at smaller amplitudes. During intermittency (Fig. 3.2b), we observe a dominant peak emerging around 2500 Hz amidst the neighbouring band of frequencies. During thermoacoustic instability (Fig. 3.2c), we notice a sharp peak at $f_1 = 2650$ Hz along with several of its harmonics (nf_1) of considerable amplitudes. We have marked only the first ten harmonics ($f_2 = 2f_1$ to $f_{10} = 10f_1$) for conciseness. The presence of several harmonics of considerable amplitudes during thermoacoustic instability is due to the spiky nature of the signal caused by the steepening of the compression wave front into a shock wave (Tyagi and Sujith, 2003*b*; Flandro *et al.*, 2007). The shift in the dominant frequency in time is attributed to the increase in mean temperature during the transition.

3.2.1 Phase space reconstruction

To probe the hidden features of the dynamics during each state, we reconstruct the phase space traced by the acoustic pressure oscillations. Towards this purpose, we need to evaluate the optimum time delay and minimum embedding dimension for each state. Further, to estimate the optimum time delay, we plot the average mutual information (AMI) for different time lags (Fraser and Swinney, 1986) as shown in the first column of Fig. 3.3. AMI measures the mutual dependence of the signal and its delayed version at two different time instants. The first minima of the AMI can be used as the optimum

58

time delay for the construction of the phase space. However, we observe that the optimum time delay cannot be unambiguously determined using AMI (Fig. 3.3a-c), due to the difficulty in clearly identifying the first local minima, especially in Fig. 3.3b,c. Hence, we turn to the autocorrelation function (ACF) to estimate the optimum time delay (Nayfeh and Balachandran, 2008).
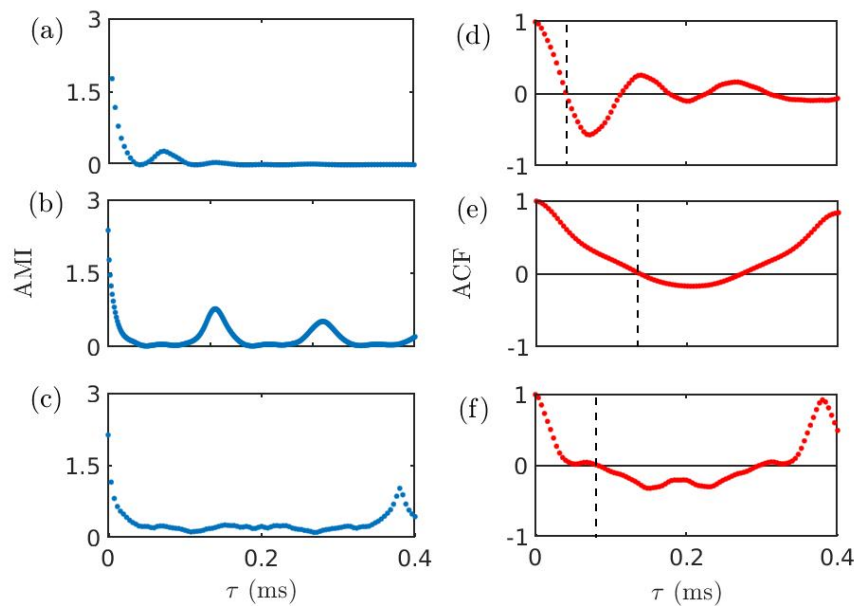
Fig. 3.3: (a-c) Average mutual information (AMI) and (d-f) autocorrelation function (ACF) are evaluated to estimate the optimum time delay required for the construction of phase portrait during (a, d) stable state of Test - A, (b, e) intermittency in Test - E, and (c, f) thermoacoustic instability of Test - E. The dashed line in (d, e, f) indicate the zero crossing delay, selected as the optimum time delay.

Autocorrelation function (ACF) calculates the linear correlation between a time series and its delayed copy of the same time series. The value of ACF ranges between -1 to 1. The optimum time delays obtained from ACF corresponds to the first zero crossing in the plot, which are denoted by dashed lines in (Fig. 3.3d-f). The corresponding optimum time delays for stable state, intermittency, and thermoacoustic instability are 0.04 ms, 0.136 ms and 0.084 ms, respectively.

Further, we need to estimate the minimum embedding dimension required for phase space reconstruction. We rely on Cao's method (Cao, 1997) to identify the minimum embedding dimension. The two parameters: $E1$ and $E2$ are evaluated for a range
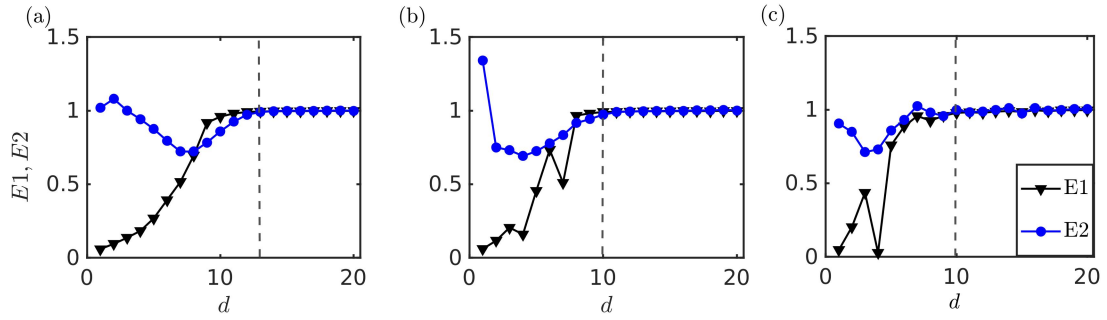
Fig. 3.4: (a-c) The optimum embedding dimension required for phase space reconstruction is obtained by Cao's method, evaluating quantities, $E1$ (▼) and $E2$ (●), during (a) stable state of Test - A, (b) intermittency in Test - E, and (c) thermoacoustic instability for Test - E, respectively. The optimum embedding dimension are denoted by dashed lines.

of embedding dimensions from 1 to 20. $E1$ measures the ratio of mean distances between two points in the phase space in two successive embedding dimensions. When a sufficient embedding dimension is attained, $E1$ attains a value close to 1 and remains constant for further increments in embedding dimension. $E2$ is a quantity which can distinguish between deterministic and stochastic signals. For a completely random signal, $E2$ remains nearly unity for any embedding dimension. For deterministic signals, $E2$ varies for lower embedding dimensions and saturates beyond a certain embedding dimension.

The optimum embedding dimension is the dimension, denoted by dashed lines in Fig. 3.4a-c, for which $E1$ and $E2$ starts to become invariant with further increase in dimension (d). In addition, we observe that $E2$ is not unity for some embedding dimensions, denoting that the dynamics during stable state are not completely stochastic. The minimum embedding dimension chosen is 13 for stable state (Fig. 3.4a), and 10 for both intermittency (Fig. 3.4b) and thermoacoustic instability (Fig. 3.4c).

With the optimum time delay obtained for each state, we plot the three-dimensional phase portraits for stable state, intermittency, and thermoacoustic instability in Fig. 3.5a-c, respectively. We observe that the phase portraits during stable state in Fig. 3.5a is cluttered and has no distinct repeating pattern corresponding to the low amplitude aperiodic oscillations. However, during thermoacoustic instability in
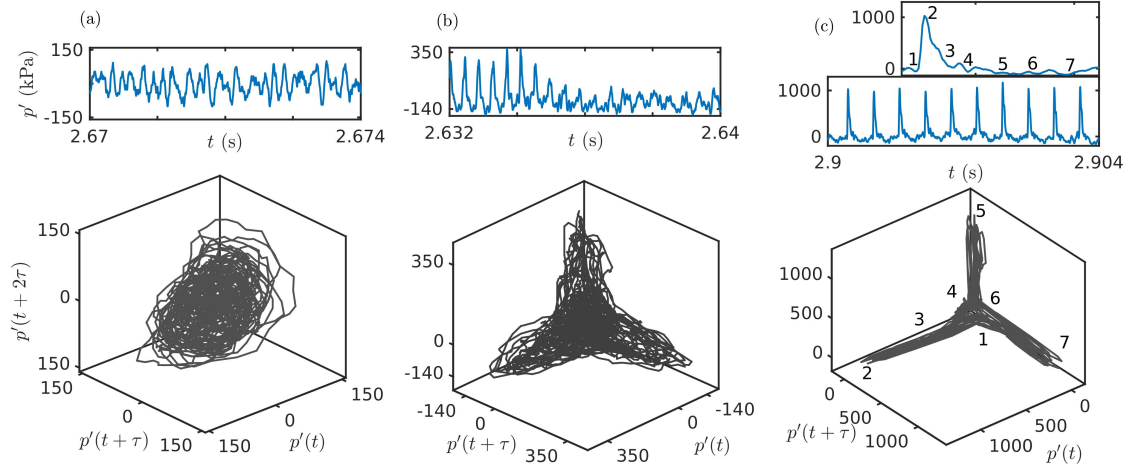
Fig. 3.5: The reconstructed phase portraits for (a) stable state of Test - A, (b) intermittency in Test - E, and (c) thermoacoustic instability in Test - E. The phase portraits are reconstructed using the corresponding time interval depicted for each dynamical state. The trajectory traced out by the phase portrait for one cycle of oscillation during thermoacoustic instability is enumerated from 1-7 in the corresponding waveform shown in the inset.

Fig. 3.5c, we obtain a pattern (marked 1-7 in order) which repeats at equal intervals of time. The phase portrait of this state shows a stretched trefoil-knot like structure, similar to that observed in gas phase detonations(Abderrahmane *et al.*, 2011). This structure is radically different from the phase portrait of thermoacoustic instability observed for gas turbine combustors, which mostly trace out a ring or elliptical orbit (Kabiraj *et al.*, 2012; Pawar *et al.*, 2016). During thermoacoustic instability in this rocket combustor, due to an increase in the speed of sound because of rising temperature and convective effects in the compression phase, the waveform tends to catch up with the expansion front(Hirschberg *et al.*, 1996; Tyagi and Sujith, 2003*a*). This leads to the steepening of the compression wave front into a shock wave. As a result, the pressure wave front has a faster growth in the amplitude during the compression phase compared to the slow decay of the oscillation in the expansion phase. This characteristic behavior is captured faithfully in the corresponding phase portrait wherein the phase space trajectory spends relatively shorter times during the compression phase (points 1-2 in Fig. 3.5c) compared to the expansion phase (points 2-7 in Fig. 3.5c) of the signal. During intermittency in Fig. 3.5b, we obtain a phase portrait bearing some resemblance

to the phase portrait during thermoacoustic instability. The presence of amplitude modulation during periodic oscillations and the aperiodic oscillations corrugates the phase portrait of intermittency.

3.2.2 Return maps

A Poincare map or the first return map preserves many properties of periodic, quasi-periodic and chaotic orbits(Nayfeh and Balachandran, 2008). Hence, we use a return map, tracking the successive local maxima of the signal, to probe the dynamics. In Fig. 3.6, the first return map tracking the local maxima of the acoustic pressure oscillations during stable state, intermittency: aperiodic and periodic epochs, and thermoacoustic instability are plotted.

The trajectory traced by the return map helps us in identifying the precise dynamical state which is sometimes not apparent from the visual inspection of the three-
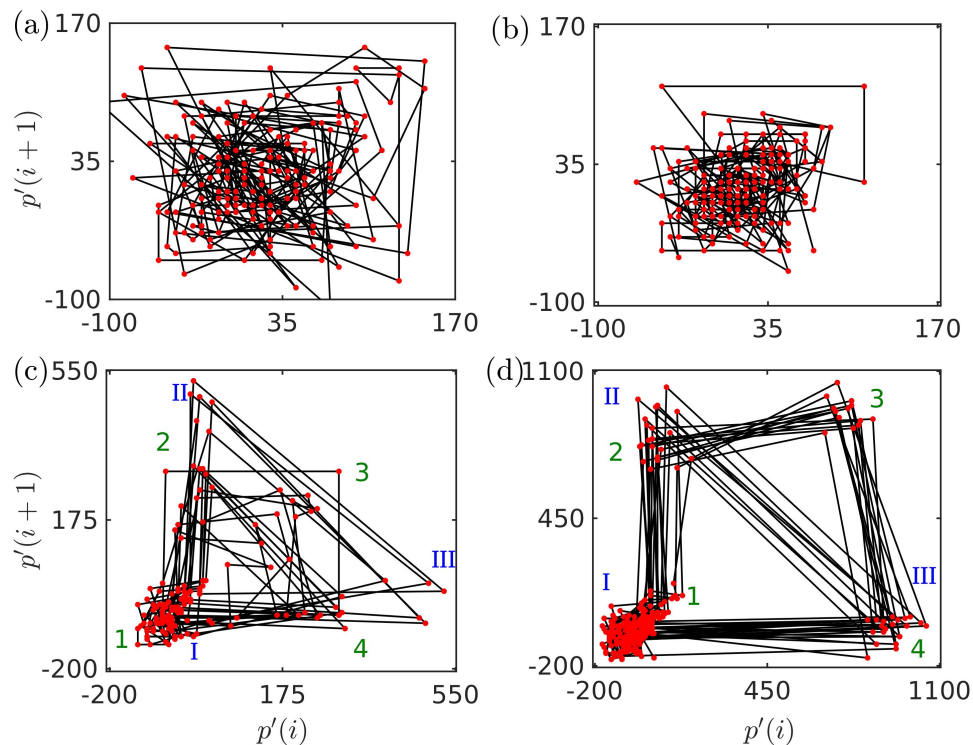
Fig. 3.6: Poincare sections or first return maps of the acoustic pressure oscillations during (a) stable state in Test - A, (b) aperiodic portion of intermittency in Test - D, (c) periodic portion of intermittency in Test - E, and (d) thermoacoustic instability of Test - E.

dimensional phase portrait. In a first return map, a point is observed for limit cycle oscillations with period-1, a ring is observed for the quasiperiodic oscillations, and a clutter of points is observed for a chaotic signal(Hilborn *et al.*, 2000). Also, if the consecutive dots traced in the return map of period-n oscillations are joined, it results in the trajectory of a n-sided polygon.

The aperiodic oscillations (see Fig. 3.6a,b) during stable state and intermittency show a clutter of trajectories without exhibiting any specific pattern. However, for periodic oscillations (Fig. 3.6c,d) during both intermittency and thermoacoustic instability, we observe the random occurrence of period-3 and period-4 oscillations as shown by triangles (I-II-III) and quadrilaterals (1-2-3-4), respectively, in their first return maps. This further suggests that the state of thermoacoustic instability is non-trivial and is not the same as the period-1 limit cycle oscillations which is usually observed for gas turbine engines. It is particularly interesting to note that a similar switching between period-2 and period-3 limit cycle dynamics have been reported recently for a full-scale solid rocket motor (Guan *et al.*, 2018). At this juncture, we must note that caution must be exercised while applying tools designed to detect conventional period-1 limit cycle oscillations as they might fail for such complex period-3 and period-4 oscillations.

3.2.3 Recurrence plots

The phase portraits of high-dimensional attractors are usually visualized by projecting them into the lower dimensions. However, a lot of information will be lost when the phase space is condensed into lower dimenisons. Eckmann *et al.* (1995) proposed a visual representation tool, known as recurrence plot that enables us to investigate the behavior of n-dimensional phase space trajectory through a two-dimensional representation of its recurrences. The recurrence plot contains unique patterns for each kind of oscillation. For example, periodic oscillations are represented by continuous diagonal lines, because the trajectory of such signals revisits roughly the same region of phase space in equal intervals of time. For random signals, we obtain a grainy structure
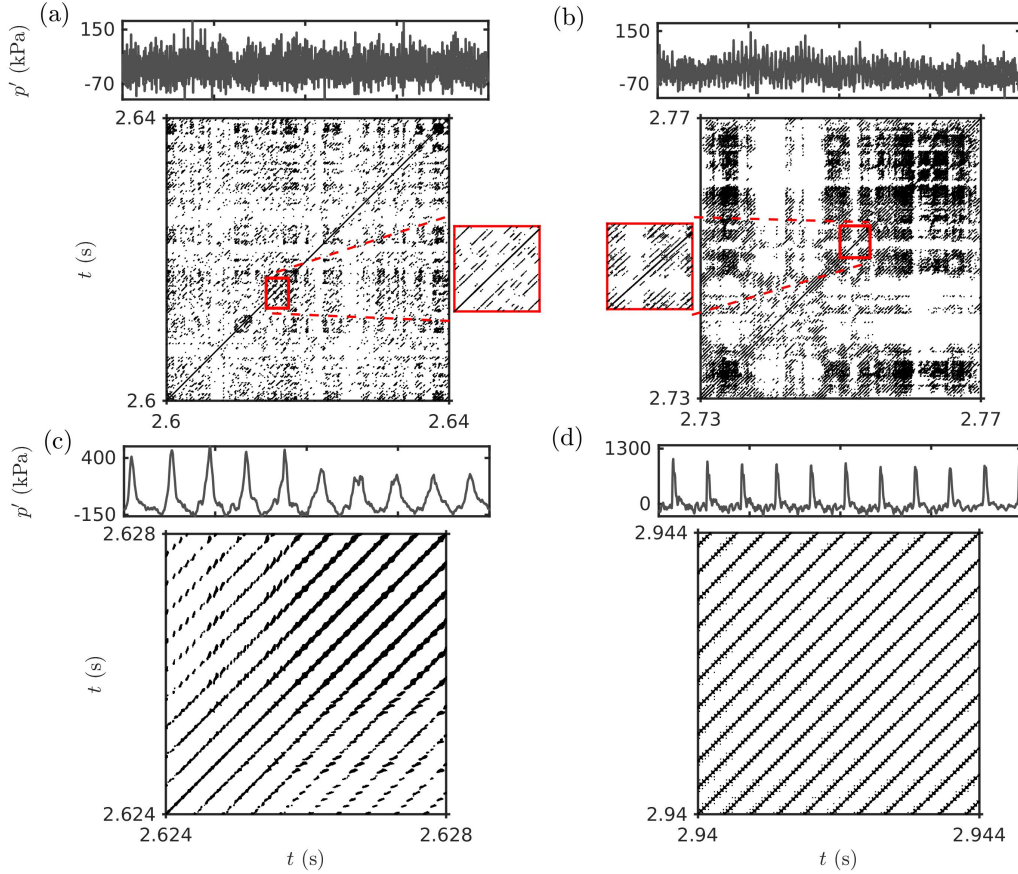
Fig. 3.7: Recurrence plots (RP) for the dynamics of (a) stable state (along with a zoomed inset) in Test - A, (b) aperiodic epoch of intermittency (along with its zoomed inset) in Test - D, (c) periodic epoch of intermittency in Test - E, and (d) thermoacoustic instability of Test - E. The recurrence plots are obtained for the corresponding time interval depicted for each dynamical state (a-d) to appropriately detect the patterns. A threshold of 20% of the maximum size of the corresponding attractor is utilized. The parameters such as time delay and embedding dimension are the same as that discussed in Section IVB.

in the recurrence plot. For chaotic signals, unlike random signal, one would obtain isolated short lines parallel to the main diagonal line (Hołyst *et al.*, 2001). Therefore, the pattern in a recurrence plot enables us to quantify the temporal dynamics of chaotic, quasiperiodic, intermittent, periodic, and stochastic signals (Webber Jr and Marwan, 2015). For a detailed description on recurrence plots, we encourage the reader to see Marwan *et al.* (2007).

Recurrence plots (RP) for the acoustic pressure oscillations during the stable state, intermittency (both aperiodic and periodic epochs), and thermoacoustic instability are

shown in Fig. 3.7. The black patches during the occurrence of aperiodic oscillations in Fig. 3.7a,b correspond to the trajectory trapped within a small region in the phase space. The short (or broken) lengths of diagonal lines in RP (see zoomed inset in Fig. 3.7a,b) during both stable state and aperiodic region of intermittency imply deterministic behavior, and could possibly suggest chaotic dynamics for the aperiodic oscillations. However, dedicated tests have to be performed before confirming chaotic dynamics. The recurrence plots during periodic oscillations of intermittency (Fig. 3.7c) and that of thermoacoustic instability (Fig. 3.7d) show continuous diagonal lines, indicating strong deterministic characteristics in the dynamics. However, during the periodic portion of intermittency, the diagonal lines are relatively broken due to the gradual decrease in the amplitude of oscillations in the signal.

3.2.4   Multifractal analysis

Many complex signals exhibiting aperiodic oscillations contain certain structural characteristics, which are difficult to be captured by various tools discussed so far. Fractal theory can be used to describe such complex signals that are composed of multiple time scales. By applying fractal analysis to thermoacoustic systems, Nair and Sujith (2014) showed that the stable state (*i.e.*, a state of combustion noise) in a turbulent combustor has multifractal features and these multifractal signatures vanish at the onset of thermoacoustic instability. By following their approach, we study the multifractal behavior of acoustic pressure oscillations observed in the model rocket combustor.

In Fig. 3.8a, we plot the variation of generalized Hurst exponents with the variation in the order-q for different dynamical states observed during the onset of thermoacoustic instability. We notice that, during stable state and intermittency, the large scale fluctuations and small scale fluctuations scale differently as the variation of $H(q)$ shows a different trend for both the states. Contrary to this, $H(q)$ shows a negligible change with variation in q during thermoacoustic instability, indicating the existence of a single scale during this state.
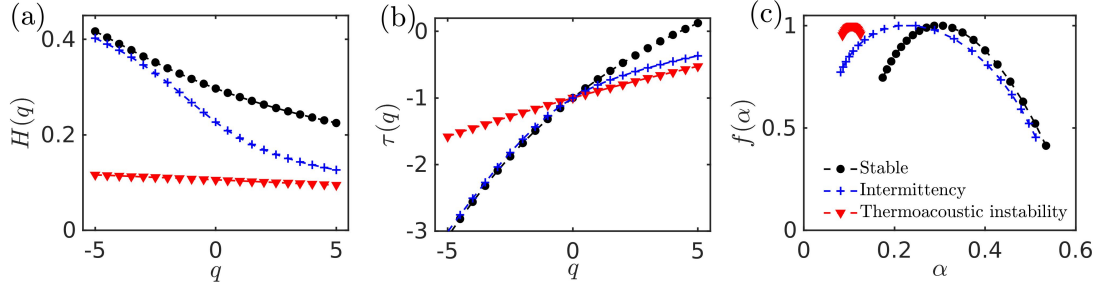
Fig. 3.8: Multifractal analysis is performed on the stable state (●) in Test - A, intermittency (+) in Test - E, and thermoacoustic instability (▼) of Test - E. (a) Generalized Hurst exponents, (b) mass exponents, and (c) multifractal spectrum are plotted to characterize the multifractal features of the various dynamics observed in the rocket combustor. The MFDFA method of a third order polynomial fit and a q range of -5 to 5 is used. The window size of 2 - 10 cycles of 2650 Hz oscillations is used, as described in Section IIC.

Further, we observe a nonlinear variation of the mass exponents, $\tau(q)$, with scaling order q in Fig. 3.8b for all the states except thermoacoustic instability. Generally, a linear and nonlinear variation of $\tau(q)$ represents monofractal and multifractal behavior of the signal, respectively(Ihlen, 2012). This indicates that the states of stable state and intermittency exhibit multifractal behavior which reduces to a monofractal-like behavior during thermoacoustic instability. Also, the resulting multifractal spectra shown in Fig. 3.8c for stable state and intermittency exhibits a wide spectrum spanning several values of singularity exponents (α). Thus, the variation of generalized Hurst exponents, mass exponents, and the multifractal spectrum strongly point out to the presence of multifractal nature in these oscillations.

During thermoacoustic instability, this multifractality is lost. This loss of multifractality is evident from the invariant nature of $H(q)$, the linear variation of $\tau(q)$ with q, and the collapse of the multifractal spectrum to a shorter arc centred around a non-zero α. This non-zero value of α, and the non-integer value of the $H(q)$ further confirms the monofractal-like behavior of acoustic pressure signals during thermoacoustic instability.

Additionally, the multifractal spectra during stable state and intermittency display a right skewed behavior (Fig. 3.8c). This right skewness suggests that the multifractal

dynamics of the pressure oscillations is determined predominantly by the small scale fluctuations. It is also reflected in the reduction in the slope of generalized Hurst exponents for positive order q, indicating that the qth-order root mean square values are insensitive to the local fluctuations with large magnitudes (Ihlen, 2012). Having studied the dynamical features of acoustic pressure oscillations during the onset of thermoacoustic instability, we now proceed to characterize the dynamical transitions observed in the system dynamics of rocket combustor quantitatively.

3.3 MEASURES TO DISTINGUISH DIFFERENT DYNAMICAL STATES

We have shown that a thermoacoustic system can exhibit different dynamical states such as stable state, intermittency, and thermoacoustic instability. A measure which can distinguish between these different dynamical states would be an ideal tool for engineers and simulators to help in assessing the stability of a rocket combustor.

In Fig. 3.9, we show several measures which exhibit a quantitative change during the transition from stable state to thermoacoustic instability. In Fig. 3.9a, we plot the time series of acoustic pressure without removing the mean pressure, during Test - C containing the transition from stable state to thermoacoustic instability via intermittency, for which the measures are evaluated. The variation of conventional measures employed to detect the transition to thermoacoustic instability such as root mean square value (Fig. 3.9b), the variance of the oscillations (Fig. 3.9c), and magnitude of the dominant frequency from the amplitude spectrum (Fig. 3.9d) are plotted. The entire time series is split into 100 segments of 6 ms interval each for plotting Fig. 3.9b and Fig. 3.9c. Due to the compromise in the frequency resolution with shorter window size, we use a relatively larger window interval of 55.6 ms, which resulted in 8 segments of the actual time series, for plotting Fig. 3.9d.

The variation of both root mean square and variance of the acoustic pressure oscillations increases progressively as the system dynamics approaches thermoacoustic instability. The non-monotonic trend in the variation of these measures prior to thermoacoustic
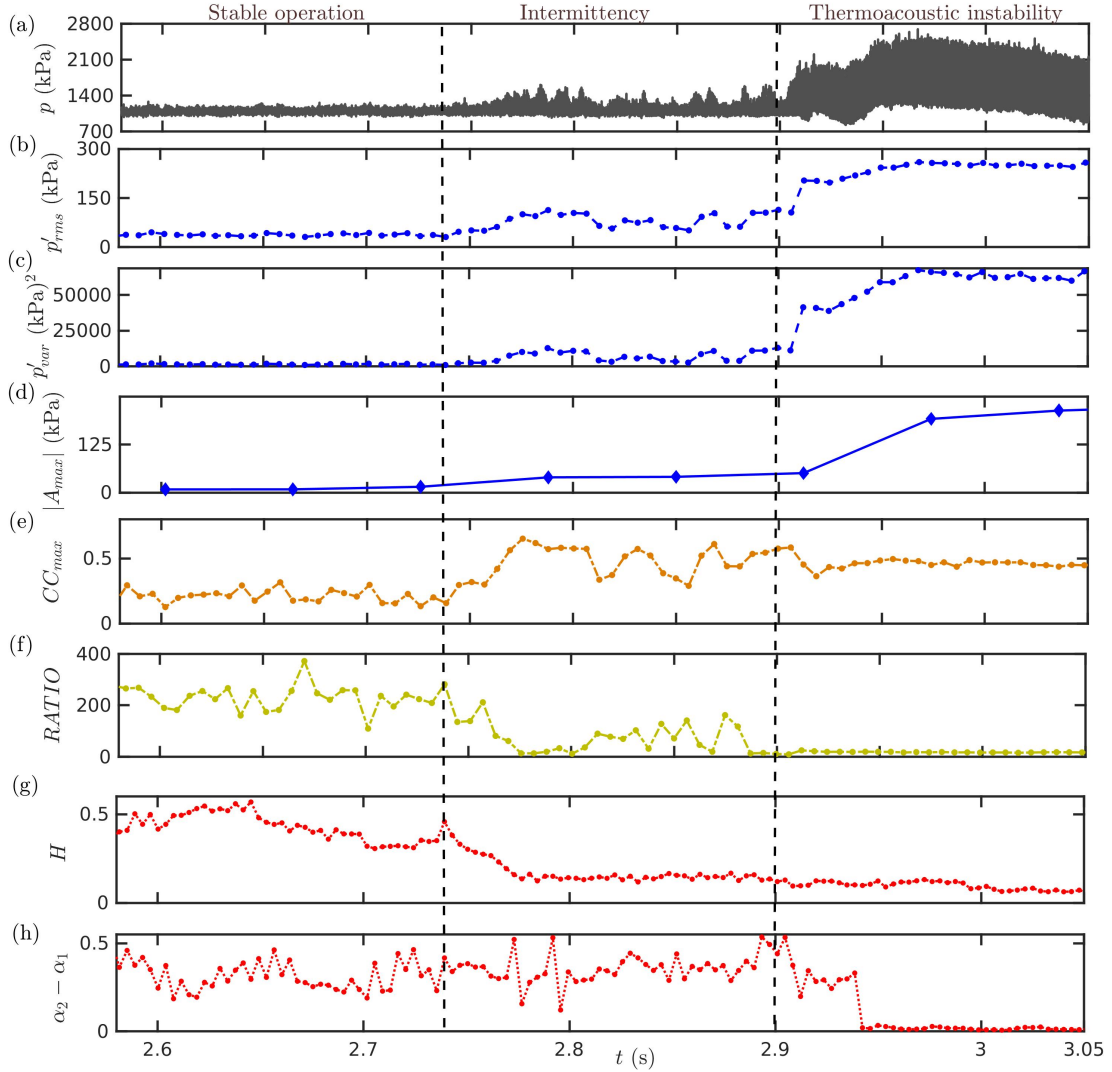
Fig. 3.9: (a) The time series of acoustic pressure (p) during Test - C containing the transition from stable state to thermoacoustic instability via intermittency. The variation of (b) root mean square value (p'_{rms}), (c) the variance of the oscillations (p'_{var}), (d) the magnitude of the dominant frequency from the amplitude spectrum ($|A_{max}|$), (e) maximum of cross correlation (CC_{max}), (f) ratio of determinism to recurrence rate ($RATIO$), (g) Hurst exponent (H), and (h) multifractal spectrum width ($\alpha_2 - \alpha_1$) are plotted to distinguish the dynamical transitions across stable state, intermittency, and thermoacoustic instability. The measures are based on the fluctuations (p') about the mean pressure, rather than p itself. The dashed vertical lines demarcating the three dynamical states are marked by visual inspection. The end times of the time windows for each measure considered are used to mark their respective abscissas.

68

instability is due to the presence of intermittency. The magnitude of the dominant frequency in the amplitude spectrum calculated with a frequency resolution of 18 Hz exhibits a gradual variation from stable state to thermoacoustic instability. However, to determine the onset of thermoacoustic instability from these measures, an apriori knowledge of the expected amplitude levels out of the combustor is required. Armed with the knowledge of the amplitude levels during the onset of thermoacoustic instability in a combustor, one can determine whether thermoacoustic instability is attained or not. However, in most scenarios, the amplitude levels in a combustor are difficult to predict as they depend highly on the operating conditions, working fluids *etc*. Even if this is overlooked, using these measures, we cannot robustly distinguish the transition between the states of stable state, intermittency, and thermoacoustic instability.

In an attempt to overcome the shortcomings of these conventional measures, Orth *et al.* (2018) introduced the maximum of cross correlation (CC_{max}) as a measure to distinguish between stable state and thermoacoustic instability. CC_{max}, bounded between -1 to 1, captures the highest similarity between two time series. In Fig. 3.9e, we show the variation of the maximum value of the cross correlation (CC_{max}) between the acoustic pressure signals acquired at two different locations in the combustor (labelled as 'Fuel Manifold Pressure' and 'Right Wall Pressure' in Fig. 3.1b). We observe that CC_{max} is unable to distinguish between intermittency and thermoacoustic instability as the values of CC_{max} are nearly the same during intermittency and thermoacoustic instability. Next, we show the variation in the recurrence based measure: the ratio of determinism to recurrence rate ($RATIO$) in Fig. 3.9f. We note that the value of $RATIO$ starts decreasing with the onset of intermittency and decays to almost zero during thermoacoustic instability. CC_{max} and $RATIO$ are plotted for a window size of 7.5 ms corresponding to 20 cycles of oscillations. The robustness of $RATIO$ in distinguishing the different dynamical states for a range of recurrence thresholds is discussed in Appendix. A.

Finally, the variation of fractal measures, Hurst exponent (H) in Fig. 3.9g and multifractal spectrum width (α_2 - α_1) in Fig. 3.9h are plotted to distinguish the dynamical transitions across stable state, intermittency, and thermoacoustic instability. Here, α_2 and α_1 are the extreme values of the singularity exponents covered by the multifractal spectrum. The multifractal spectrum width (α_2 - α_1) is calculated by measuring the range of singularity exponents covered by the spectrum. For the multifractal measures, a window size of 37.6 ms corresponding to 100 cycles of oscillations with an overlap of 90 cycles is used. The multifractal spectrum width drops from near 0.4 to lower than 0.02 during the onset of thermoacoustic instability. However, the presence of intermittency cannot be detected by this measure. The value of Hurst exponent (H) varies from around 0.5 during stable state to less than 0.1 during the onset of thermoacoustic instability. During intermittency, if the value of H drops below 0.1, this model rocket combustor can be considered to be in the proximity of an impending thermoacoustic instability. However, the critical Hurst exponent below which thermoacoustic instability is imminent may vary from system to system. Hence, $RATIO$, Hurst exponent, and multifractal spectrum width collectively can be used to distinguish the combustor operation across all three states for a rocket combustor, as they possess fixed values for a particular type of dynamics, unlike traditional measures such as rms value, amplitude of frequency peaks, and variance of the oscillations. The statistical significance and robustness of the multifractal measures for different parameters are described in Appendix. A.

Next, in Fig. 3.10, we show that the same measure $RATIO$ can also be used to detect the transitions from aperiodic to periodic oscillations, and vice versa, in a signal (see Fig. 3.10a). We compare the efficacy of $RATIO$ as compared to CC_{max} in detecting such transitions. We also show the variation of DET and RR in Fig. 3.10c,d, respectively. We observe that through a windowed variation of CC_{max} (Fig. 3.10b) and $RATIO$ (Fig. 3.10e), we can detect the switching between periodic and aperiodic behavior during intermittency. Here, CC_{max} is obtained by cross correlating the same
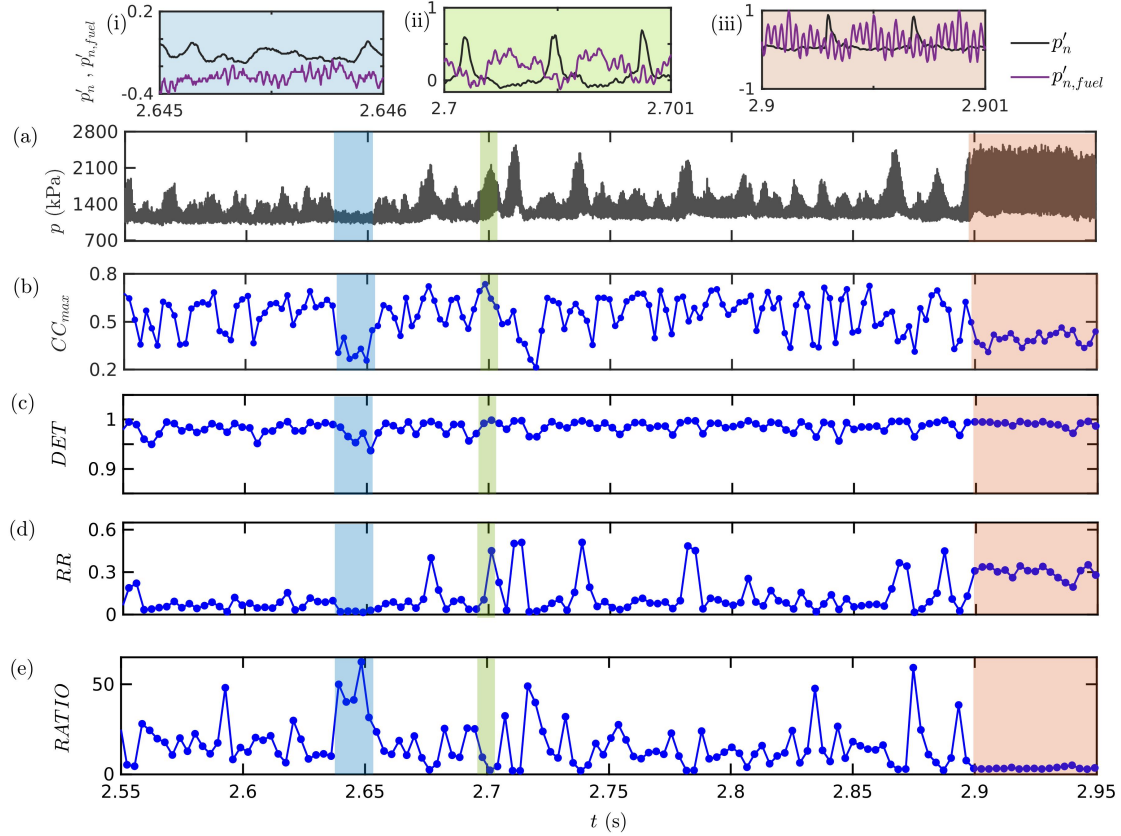
Fig. 3.10: The time series of (a) acoustic pressure (p) is plotted during the transition from intermittency to thermoacoustic instability for Test - E. The variation of (b) maximum of cross correlation (CC_{max}), (c) determisim (DET), (d) recurrence rate (RR), and (e) ratio of determinism and recurrence rate ($RATIO$) to detect the aperiodic to periodic transitions, and vice versa. The blue shaded region corresponds to the long aperiodic epoch of intermittency, the greeen shaded region corresponds to the periodic epoch of intermittency, and the red shaded region corresponds to the epoch of thermoacoustic instability. Zoomed views of normalized pressure signals at the right wall (p'_n) and fuel manifold ($p'_{n,fuel}$) locations are shown for (i) aperiodic epoch of intermittency, (ii) periodic epoch of intermittency, and (iii) thermoacoustic instability, respectively. The end times of the time windows for each measure considered are used to mark their respective abscissas.

two pressure signals used to calculate CC_{max} plotted in Fig. 3.9. Zoomed views of the normalized pressure time series of the two signals ($p'_{n,fuel}$ and p'_n) are plotted for an aperiodic epoch of intermittency, a periodic epoch of intermittency, and thermoacoustic instability in Fig. 3.10i-iii. A window size of 2.3 ms corresponding to two hundred slices of the actual time series is used to calculate all measures in Fig. 3.10. A smaller window size is necessary to detect the aperiodic-periodic transitions. DET, RR and subsequently, $RATIO$ are obtained by calculating the recurrences of the phase trajectories within a threshold of 20% of the maximum size of the corresponding attractor. The time delay and embedding dimension are calculated for the entire time series and are found to be 0.196 ms and 10, respectively.

We observe an uncharacteristically higher value of DET for the aperiodic oscillations, compared to other combustors (Pawar and Sujith, 2018). The value of DET for both aperiodic and periodic dynamics in this data (see Fig. 3.10c) remains nearly the same. The value of $DET \sim 1$ suggests the possibility of high deterministic features (Marwan *et al.*, 2007) in the aperiodic oscillations of the rocket combustor dynamics. This high determinism value could be a result of the dynamics of the flame front, arising from the globally unstable hydrodynamic field (Emerson *et al.*, 2012).

On the other hand, the value of RR exhibits a significant increase during the transition from aperiodic to periodic oscillations (see Fig. 3.10d). Hence, $RATIO$ exhibits a higher value for aperiodic oscillations and a lower value for periodic oscillations. On the other hand, for CC_{max}, we expect a value close to 0 for aperiodic oscillations with low similarity and a higher value close to 1 for periodic oscillations with large similarity. The blue and green shaded regions in Fig. 3.10a-e represents an aperiodic epoch and a periodic epoch, respectively, during intermittency. During the aperiodic epoch, we observe that CC_{max} shows lower values while $RATIO$ exhibits larger values. We observe the opposite behavior in both $RATIO$ and CC_{max} during the periodic epoch of intermittency. During thermoacoustic instability (see red shaded region in Fig. 3.10a-e), the values of both these measures are largely invariant, denoting sustained periodic

behavior in the system. For this state, we observe that the values of both CC_{max} and $RATIO$ are low. The lower value of CC_{max} is unexpected during thermoacoustic instability as the dynamics during this state is periodic.

The reason behind the lower value of CC_{max} for both periodic and aperiodic oscillations can be understood from the overlapped plot of the two pressure signals used for the calculation of CC_{max} (see Fig. 11i-iii). To aid us in detecting the similarity, the two time series ($p'_{n,fuel}$ and p'_n) are normalized. For the aperiodic epoch of intermittency, we do not observe any similarity between the two signals (Fig. 3.10i). During the periodic epoch of intermittency (Fig. 3.10ii), we observe that the two signals follow a nearly similar trend at a finite non-zero time lag, leading to higher values in CC_{max}. On the contrary, during the state of thermoacoustic instability (Fig. 3.10iii), we notice that the time series of $p'_{n,fuel}$ contains significantly higher frequencies, whereas that of p'_n contains lower frequency corresponding to fundamental mode of the combustor (2650 Hz). This difference in the oscillations of acoustic pressure at different locations contribute to lower the value of CC_{max}. Unlike CC_{max}, we observe that the lower values of $RATIO$ correctly captures the periodic oscillations during thermoacoustic instability as well as during intermittency. This suggests that using $RATIO$ is better than CC_{max} to unambiguously determine the periodic-aperiodic-periodic transitions in the acoustic pressure signal observed during the onset of thermoacoustic instability. We also remark that RR can be a good candidate to distinguish the aperiodic-periodic transitions if there is a significant variation in RR during the aperiodic-periodic transitions.

3.4 CONCLUDING REMARKS

In this chapter, the dynamics of acoustics pressure oscillations during the transition from stable state to thermoacoustic instability in a model multi-element rocket combustor is analyzed. We observe that the transition from small amplitude stable state to large amplitude thermoacoustic instability occurs through intermittency. Intermittency is a

dynamical state wherein bursts of high amplitude periodic oscillations appear amidst epochs of low amplitude aperiodic oscillations, distributed in a seemingly random manner.

The waveform during thermoacoustic instability is highly nonlinear, consisting of typically steepened pressure wavefronts leading to the formation of shock waves, and is significantly different from the sinusoidal limit cycle oscillations typically seen in gas turbine combustors. As a result, we obtain a characteristic trefoil knot-like shape of the phase space attractor during thermoacoustic instability. Further, we detect the dynamical switching between possibly period-3 and period-4 oscillations in an apparently random manner during thermoacoustic instability and the periodic epochs of intermittency. Such complex limit cycle dynamics are seldom seen in gas turbine combustors.

Through a suitable multifractal analysis, we detect the collapse of multifractality during the onset of thermoacoustic instability. We present a recurrence based measure ($RATIO$) and two fractal based measures (multifractal spectrum width and the Hurst exponent), that can be used to distinguish between different states of combustor operation. We found that these measures are more robust than the existing measures such as root mean square of the oscillations, spectral amplitude, maximum of cross correlation *etc.* in distinguishing the dynamical state of a rocket engine. The measures illustrated in this chapter can be used to validate the CFD multi-fidelity simulations used for optimizing the stability and performance metrics of the rocket combustor. Summarizing, the signals pertaining to rocket combustors are different from their gas turbine counterparts and other derived laboratory combustors due to the significant contribution of nonlinearities in the rocket combustor. Hence, extreme care must be exercised while extending the results obtained for gas turbine combustors to rocket combustors.

CHAPTER 4

Slow-fast time scales in the wave steepened limit cycle oscillations

Many complex systems exhibit periodic oscillations comprising slow-fast timescales. In such slow-fast systems, the slow and fast timescales compete to determine the dynamics. In this chapter, we perform a recurrence analysis on simulated signals from paradigmatic model systems as well as signals obtained from experimental data of a gas turbine-type combustor and the model rocket combustor, each of which exhibit slow-fast oscillations. We find that slow-fast systems exhibit characteristic patterns along the diagonal lines in the corresponding recurrence plot (RP). We discern that the hairpin trajectories in the phase space leads to the formation of line segments perpendicular to the diagonal line in the RP for a periodic signal. Next, we compute the recurrence networks (RNs) of these slow-fast systems and uncover that they contain additional features such as clustering and protrusions on top of the closed ring structure. We show that slow-fast systems and single timescale systems can be distinguished by computing the distance between consecutive state points on the phase space trajectory and the degree of the nodes in the RNs. Such a recurrence analysis substantially strengthens our understanding of slow-fast systems which do not have any accepted functional forms.

4.1 SLOW-FAST TIMESCALES IN DIVERSE PHYSICAL SYSTEMS

The rhythmic beating of the heart (Glass, 2001), periodic firing of neurons (Izhikevich, 2007), spontaneous oscillations of chemical reactions (Zhabotinsky, 1991), dangerous self-excited oscillations in suspension bridges (Lazer and McKenna, 1990), glacial oscillations (Dansgaard *et al.*, 1984), high amplitude oscillations in aircraft engines and rocket engines (Lieuwen and Yang, 2005) are a few examples of the various periodic phenomena we come across in our lives. Most of these phenomena exhibit oscillations

at a preferred timescale known as the time period of the oscillation. However, many periodic phenomena are inherently made up of more than one timescale in an oscillation (Bertram and Rubin, 2017). Such periodic phenomena are popularly classified as slow-fast oscillations (Bertram and Rubin, 2017). Such systems are found across a wide range of applications ranging from medicine (Kantz and Schreiber, 1998), economics (Lordon, 1997), physical sciences (Leeman *et al.*, 2016), earth sciences (Vettoretti and Peltier, 2018) to engineering (Johnson and Sutin, 2005; Vallaitis *et al.*, 2008; Bruun *et al.*, 2012).

For example, let us consider the electrocardiogram (ECG) signal, wherein the electrical activity in the heart is recorded using a set of electrodes. A typical cycle of an ECG signal is defined by different processes such as atrial depolarization, ventricular depolarization, and ventricular repolarization (Chen *et al.*, 2014). Each of these processes (designated as P wave, QRS complex, and T wave in one cycle of the ECG signal) have an intrinsic timescale. A characteristic feature of slow-fast systems is that their periodic waveforms are radically different from those of harmonic oscillators. For the most simple case of a slow-fast system containing two timescales, a slow growth/decay is accompanied by a fast decay/growth. As a result, a slow-fast system could spend more time in the growth or decay phase. To present an example in electrical engineering, the charge and discharge of a capacitor (Millman, 2010) is characterized by a slow and fast timescale, respectively. In a similar manner, the periodic stick-slip motion of a bowed violin string exhibits more than one timescale (Schumacher *et al.*, 2005). Recently, Kasthuri *et al.* (2019) showed the presence of bursting and mixed-mode oscillations in a premixed matrix burner with several interacting laminar flames. They demonstrated that these oscillations occurred due to the interaction of slow timescale associated with temperature fluctuations and fast timescale with acoustic pressure fluctuations.

In nonlinear dynamics literature, the term slow-fast systems have also been used to describe multiple timescales that cause periodic amplitude modulations, bursting
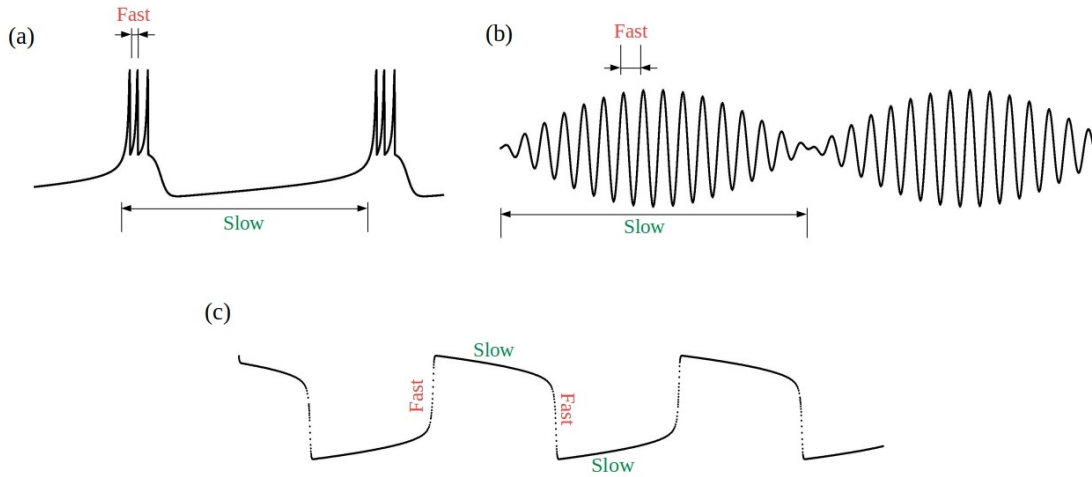
Fig. 4.1: The slow and fast timescales during (a) periodic bursting in the Izhikevich neuronal model (Izhikevich, 2003) and (b) amplitude modulated sine wave. (c) The slow and fast regions within a cycle of oscillation in the Van der Pol oscillator. We study slow-fast signals akin to (c) in this chapter.

oscillations, and mixed-mode oscillations (Desroches *et al.*, 2012). Hence, we illustrate the slow-fast systems that we discuss in this chapter along with other slow-fast systems in Fig. 4.1. Bursting oscillations (Fig. 4.1a) are characterized by epochs of large amplitude periodic oscillations followed by quiescence (Kuehn, 2015). Mixed-mode oscillations are another class of periodic oscillations that exhibit amplitude switching between two or more amplitude states in the signal. In periodically modulated waves (Fig. 4.1b), the amplitude envelope of the signal oscillates at a slow timescale over a fast oscillating signal. In these types of slow-fast systems, the slow timescale corresponds to the modulation of the envelope of the signal, while the fast timescale pertains to the high frequency oscillation in the signal.

However, unlike all these types of periodic oscillations, the slow-fast systems described in this chapter contain all the slow and fast timescales within one period of oscillation (Fig. 4.1c). Such slow-fast systems have been long studied under the guise of relaxation oscillators. These oscillators are a class of limit cycle oscillators which are characterized by a non-sinusoidal periodic waveform (Van der Pol, 1926). Relaxation oscillations have been modelled using several models such as the Van der Pol oscillator (Van der Pol, 1926), Fitz-Hugh-Nagumo oscillator (FitzHugh, 1961), and LEGION

(Wang and Terman, 1995).

Traditionally, slow-fast systems with a pre-established set of governing equations have been solved using conventional methods from linear theory. A classical technique is to reduce the set of governing equations to the weak or the strong nonlinear limit (Strogatz, 2018), whenever the two timescales are widely separated. Then, the system of equations is solved to obtain the resultant amplitudes and phases of the signal. Apart from this method, various other techniques such as perturbation theory, method of multiple timescales, and the method of averaging exist (Nayfeh and Balachandran, 2008). However, experimental and other real-world signals rarely have any well-defined functional forms, which can be solved using these methods. Moreover, the timescales in practical systems are seldom widely separated. All these obstacles render the analysis of such signals intractable. Despite the abundance of slow-fast periodic signals and their known association with nonlinear dynamics, they have not been viewed under the microscope of recurrence theory to obtain insights. Such an analysis would potentially pave way to detect the presence of multiple timescales in the system and its accompanying effects on the dynamics of the system. Armed with this knowledge, recurrence plots and recurrence networks can be used to extract hidden features of high dimensional systems.

In this chapter, we first characterize the dynamics of prototypical slow-fast signals obtained from well-established models, i.e., Van der Pol (VDP) model, a modified form of Izhikevich model, and the Hodgkin-Huxley model. We use nonlinear time series methods based on recurrence analysis of the phase space trajectory such as recurrence plot (RP) (Marwan *et al.*, 2007) and recurrence network (RN) (Zou *et al.*, 2018) to distinguish the properties of these signals. Following the same methodology, we analyze two high-dimensional slow-fast signals of thermoacoustic oscillations from experiments - the time series of unsteady heat release rate signal from a model gas turbine combustor (Pawar *et al.*, 2017), and the acoustic pressure signal obtained from a model rocket combustor (Orth *et al.*, 2018).

4.2 RECURRENCE NETWORKS

Using the method of phase space reconstruction, we can visually unravel the dynamics of nonlinear systems from its phase space attractor only in low dimensions ($d \leq 3$). However, a vast number of real-world signals tend to have higher dimensions ($d > 3$). As a result, the fundamental property of recurrence of a phase space trajectory is exploited to understand the underlying hidden features of high-dimensional nonlinear systems (Eckmann *et al.*, 1995; Marwan *et al.*, 2007). As described in Chapter. 3, we obtain different patterns in the recurrence plot (RP) dependent on the characteristics of the signal. The patterns in RPs have garnered the attention of physicists in many instances (Marwan, 2008). However, understanding such patterns in the RPs of slow-fast systems have not yet been probed, to the best of our knowledge.

One of the methods to select a recurrence threshold (ϵ_r) is to fix the recurrence rate (Marwan *et al.*, 2007; Kraemer *et al.*, 2018) (RR). RR is defined as $RR = \frac{1}{n^2} \sum_{i,j=1}^{n} R_{ij}$. It estimates the percentage of recurring points in a RP. We observe that a value lower than the optimum RR fails to completely capture the periodicity in the signal and is reflected as broken diagonal lines in the RP. In this chapter, an optimum value of RR is selected after careful consideration for each slow-fast systems.

Recurrence networks (Marwan *et al.*, 2009) are a class of networks through which high-dimensional systems can be understood. A recurrence network (RN) comprises of phase space points in time as nodes whose links are based on recurrences of these state points in the phase space. Similar to the RPs, we can create a ϵ_r - recurrence network (Marwan *et al.*, 2009; Donner *et al.*, 2010; Zou *et al.*, 2018), where ϵ_r is the optimal recurrence threshold. A value higher than the optimum value results in superfluous connections in the RN, distorting the network topology. Whereas a lower ϵ_r would not capture the recurrence of trajectories in the phase space, leading to an underdeveloped network topology. The topology of the RN has been found to preserve the phase space of the high-dimensional nonlinear system (Godavarthi *et al.*, 2017). We also show the effect of embedding dimension on the RN in Appendix. B.

To construct a RN, we require an adjacency matrix A, to be computed from the recurrence matrix R for an ϵ_r - threshold,

$$A_{ij} = R_{ij} - \delta_{ij} \qquad (4.1)$$

where δ is the identity matrix of the same size as R and is used to remove self-connections. If the distance between the state space points is within the ϵ_r - threshold, then, A_{ij} = 1, and the corresponding two nodes are connected. Else, the two nodes remain disconnected, and A_{ij} = 0. Once the adjacency matrix is constructed for all pairs of nodes, several network measures can be computed from the RN, quantifying the geometrical structure of the phase space attractor (Donner *et al.*, 2010, 2011). Using the network properties obtained from the RN, a number of studies have used RN to study the dynamical features of diverse systems (Gao *et al.*, 2013; Godavarthi *et al.*, 2017; Gotoda *et al.*, 2014; George *et al.*, 2019).

We visualize the RN using the open-source network analysis platform, Gephi (Bastian *et al.*, 2009). The geometric feature of RN is attributed by a force directed algorithm known as 'Force Atlas' in Gephi, where the connected nodes are attracted to each other, while the disconnected nodes are repelled from each other. An appropriate RN visualization is achieved when the forces are balanced, leading to a static RN. Each node in the RN is color coded based on degree, a network property (Barabási *et al.*, 2016). Degree of a node i (K_i) refers to the number of connections node i has to all other nodes in the network and is calculated as,

$$K_i = \sum_{j=1}^{n} A_{ij}. \qquad (4.2)$$

Using recurrence plots and recurrence networks, we progressively investigate the recurrence properties of slow-fast systems from low-dimensional systems to high-dimensional systems. As case studies for low-dimensional systems, we consider the Van der Pol (VDP) oscillator and the modified signal derived out of Izhikevich's spiking

neuron model (Izhikevich, 2003). We consider the Hodgkin-Huxley model (Izhikevich, 2007; Díaz *et al.*, 2016) as a case for studying high-dimensional prototypical slow-fast signals. We, then, analyze the time series of heat release rate oscillations obtained from experiments in a laboratory-scale gas turbine type turbulent combustor (Pawar *et al.*, 2017) and the acoustic pressure signal from a laboratory-scale model multi-element model rocket combustor (Orth *et al.*, 2018), during the state of thermoacoustic instability, to understand the recurrence dynamics of slow-fast signals in higher dimensional physical systems.

4.3   RECURRENCE ANALYSIS OF LOW-DIMENSIONAL PROTOTYPICAL SIGNALS

Prior to understanding slow-fast systems, we analyze a harmonic signal, namely a sine wave of unit amplitude and time period of 2π (see Fig. 4.2a), which is definitely a single timescale system. The phase space of the sine wave is a circular loop structure (Fig. 4.2b), wherein the phase space trajectory evolves at a uniform speed. Here, the uniform speed of the phase space trajectory is attributed to successive state points on the trajectory separated by equal distances in the phase space. In the corresponding RP (Fig. 4.2c), we observe only equally spaced, non-interrupted diagonal lines with spacing equal to the time period of the oscillation. The corresponding RN topology of the sine wave (Fig. 4.2d) shows a circular loop filled up with same degree nodes.

Now, we start analyzing slow-fast systems where we first consider the VDP system (Van der Pol, 1926), which is perhaps the most studied slow-fast system. Its governing equations are

$$
\begin{aligned}
\dot{x} &= \mu(y + x - \tfrac{x^3}{3}), \\
\dot{y} &= -\tfrac{1}{\mu}x,
\end{aligned}
\tag{4.3}
$$

where μ is referred to as the nonlinearity parameter to obtain relaxation type oscillations. We fix $\mu = 2$ for the current analysis. The time series of variables, $x(t)$ and $y(t)$ of Eq. 4.3, are plotted in Fig. 4.3a. The corresponding phase portrait exhibits a
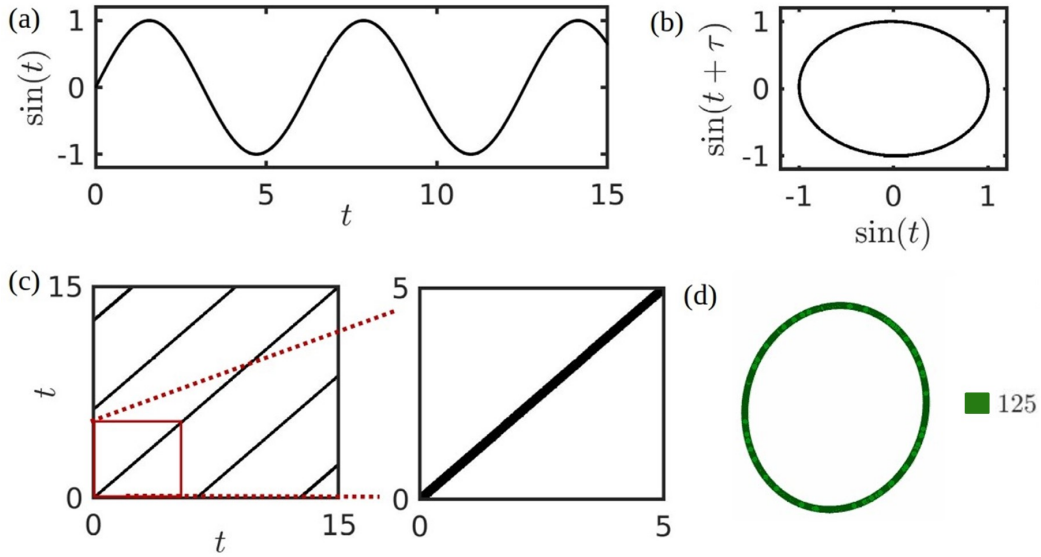
Fig. 4.2: (a) The time series of a sine wave of unit amplitude and time period 2π, sampled at 100 Hz. (b) The corresponding reconstructed phase space calculated for $\tau_{opt} = 157$ time steps and $d = 2$, (c) RP along with a zoomed view, and (d) RN.

closed-loop, confirming the periodicity of the time series (Fig. 4.3b). However, unlike the phase space of the harmonic signal (Fig. 4.2b), we observe that the phase space trajectory evolves at different speeds, giving rise to the slow and fast timescales. The separation between successive state points on the phase space trajectory during the fast epoch is large as compared to that of the slow epoch. As a result, the fast epoch can be visually discriminated from the slow epoch in the phase space. For the VDP system, we observe two epochs of slow oscillations (marked as S) and two epochs of fast oscillations (marked as F) within a cycle in the original phase space (i.e. a plot between the variables x and y of the system).

In Fig. 4.3c, we show the time series of the variable $x(t)$ and its delayed copy $x(t + \tau)$. Here, the delay τ_{opt} is obtained by the first zero crossing in the autocorrelation function (ACF). Unlike the original phase space (Fig. 4.3b), in the reconstructed phase space of x (see Fig. 4.3d), we obtain four epochs of slow and fast oscillations (marked as S and F, respectively) within a cycle of oscillation. This exercise shows that systems containing slow-fast timescales need to be interpreted carefully based on the technique of phase space reconstruction, since the number of slow/fast regions could be exaggerated with
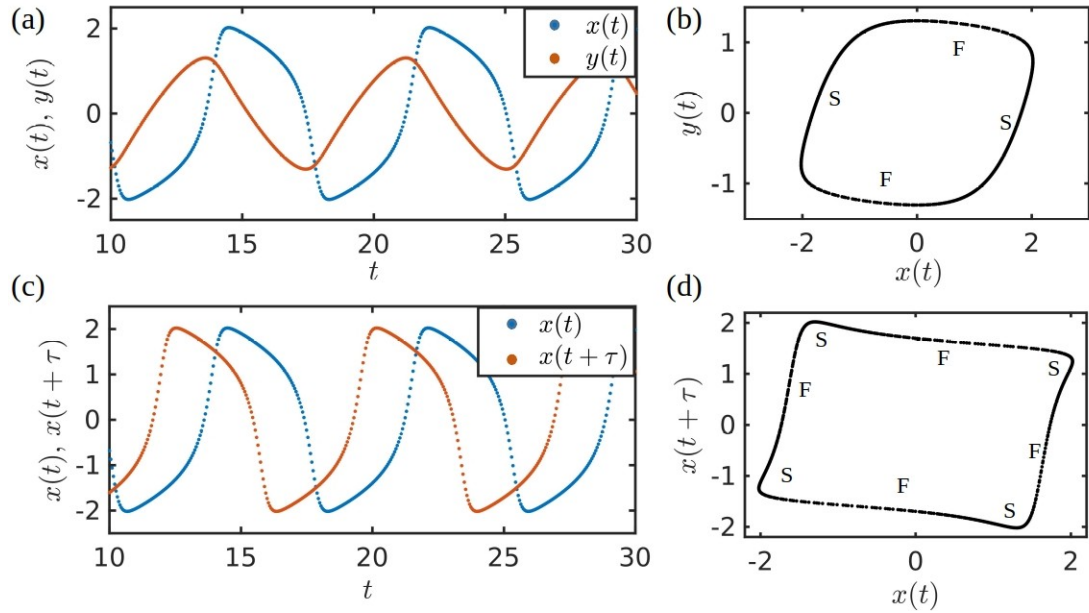
Fig. 4.3: (a) The time series of x and y of the VDP system for $\mu = 2$. (b) The original phase space between x and y. (c) The time series of x and its delayed copy, $x(t + \tau)$. (d) The reconstructed phase space of x using Takens' delay embedding theorem with $\tau_{opt} = 39$ time steps and $d = 2$. The slow and fast motions in the phase space are marked by S and F, respectively.

respect to that present in the original phase space. We remark that the reconstructed phase space trajectory of $y(t)$ evolves at a single timescale (not shown here for brevity) and hence, does not exhibit any slow-fast features. Hence, we must be wary of slow-fast oscillations in practical scenarios going unnoticed when we are not tracking the appropriate system parameter.

Further, we plot the RP and the corresponding RN for the VDP system from the original phase space and from the reconstructed phase space (see Fig. 4.4). The recurrence matrix is constructed by fixing $RR = 0.05$. For both RPs, (shown in Fig. 4.4a,c, respectively), at a first glance, we observe only diagonal lines, indicating periodic behavior of the system. However, in the corresponding zoomed view of the RP in Fig. 4.4(a,c), we identify the presence of momentary thick regions along the diagonal lines of a RP. We attribute these thick regions to slow epochs and the thin regions to the fast epochs in the evolution of the phase space trajectory. We refer to the presence of such distinct black patterns on the diagonal lines in a RP of the periodic signal as micro-
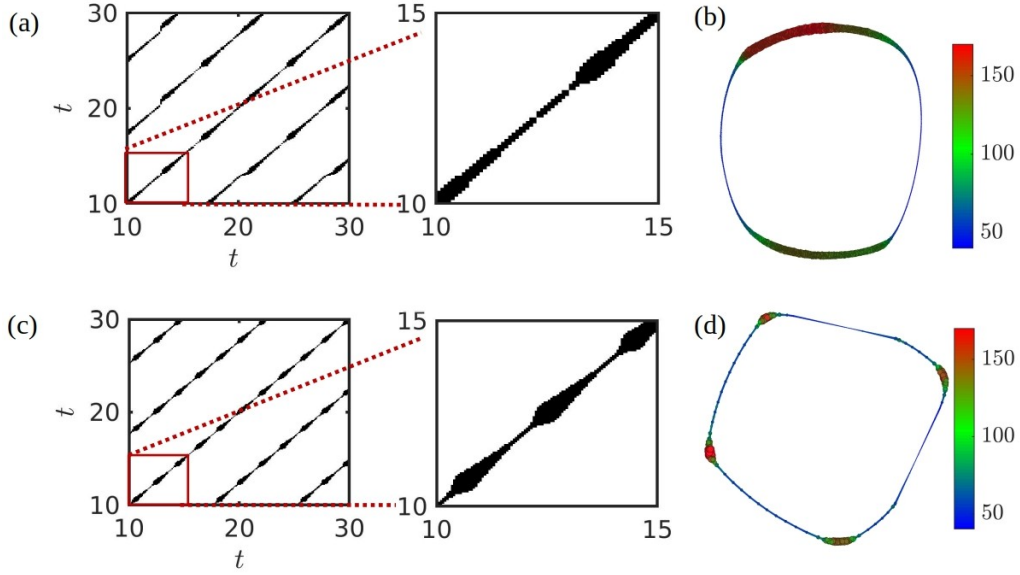
Fig. 4.4: (a) RP along with its zoomed view and (b) the corresponding RN constructed using the original variables x and y of the VDP oscillator (Eq. 4.3), shown in Fig. 4.3. (c,d) - The same plots are shown for the phase space reconstructed using time delay embedding for the variable, $x(t)$. The nodes in RN are color coded based on their degree. A recurrence threshold of $RR = 0.05$, $d = 2$, and $\tau_{opt} = 39$ time steps are used. We observe that the number of slow-fast regions in the phase space could be exaggerated by time delay embedding.

patterns of RP. Thus, with the analysis of such micro-patterns, we can distinguish the time instances corresponding to slow regions from the fast regions in the phase space. The reason behind the occurrence of such a micro-pattern in the RP can be understood from the evolution of the phase space trajectory at slow and fast timescales. When the phase space trajectory evolves at a slower rate in the phase space, it spends relatively more time within an ϵ_r - threshold as compared to the phase space trajectory for the fast motion. This leads to the thickening of the diagonal lines in the RP. A similar argument can be given to explain the thinning of the diagonal lines whenever the phase space trajectory exhibits fast motion.

Recently, Kraemer and Marwan (2019) reported a tangential motion of phase space trajectories leading to uneven thickening along diagonal lines. They identified the temporal correlations (i.e. preceding and succeeding state points fall within the recurrence threshold) in the data, the presence of noise, and the usage of insufficient embedding dimension as reasons for this effect. Here, we observe thickening of

diagonal lines in the RP for the slow epochs in the phase space of the prototypical slow-fast signal (with no noise) embedded using an optimum embedding dimension. As a result, we can attribute the thickening of diagonal lines with the temporal correlations in the slow epoch in the phase space of the slow-fast system.

We observe that the network topologies of both the original and the reconstructed VDP system are similar to the corresponding phase space observed in Fig. 4.3(b,d). Thenceforth, the nodes represented in the RNs are color-coded based on the increasing order of their respective degrees. In the corresponding RNs (see Fig. 4.4b,d, respectively), we identify distinct regions which exhibit spatial clustering of high degree (red) nodes amongst the almost uniform distribution of the low degree (blue) nodes. The spatial clusters of high degree nodes within a cycle represent the region in which the trajectory moves slowly in the phase space, resulting in a higher number of connections in the RN. There are two such regions in the RN constructed from the original phase space (see Fig. 4.4b) and four slow regions in the RN from the reconstructed phase space (Fig. 4.4d); exactly matching their number in the respective phase spaces shown in Fig. 4.3(b,d).

Next, we consider another slow-fast signal (see Fig. 4.5a) obtained by modifying the time series of the variable x from the Izhikevich's spiking neuron model (Izhikevich, 2003). First, we solve for the variable x in the set of Eqs. 4.4. The dimensionless parameters $a = 0.1$, $b = 0.2$, $c = -60$, $d = 8$, and $I = 110$ are used to obtain spiking behavior in $x(t)$.

$$
\begin{aligned}
\dot{x} &= 0.04x^2 + 5x + 140 - y + I \\
\dot{y} &= a(bx - y)
\end{aligned}
\tag{4.4}
$$

The parameters a, b, c and d retain the same meaning as described originally in Izhikevich (Izhikevich, 2003). Then, the resulting time series is modified, so that enough number of points are present both during the growth and decay phase of the oscillations, to get a connected RN.

We observe that one oscillation in this signal is almost symmetric about the growth

and the decay phase (Fig. 4.5a). The three-dimensional phase space by using $\tau_{opt} =$ 102 time steps (obtained from ACF) for this signal is visualized in Fig. 4.5b. We find that the three-dimensional phase space attractor is stretched along the three axes, while maintaining a closed-loop structure in the evolution of the phase space trajectory for one cycle of oscillation.

We observe that the RP exhibits continuous equi-spaced diagonal lines, signifying the periodic dynamics of the signal (Fig. 4.5c). Superimposed on this RP, the micro-patterns exhibit intricate features unique to this slow-fast system. Similar to the VDP system, the thickened portions of the diagonal line (see Fig. 4.5c) correspond to the slow motions in the phase space. A perpendicular line segment occurs amidst two thickened regions along the diagonal line in the RP, whenever the phase space trajectories traversing in opposite directions are spaced within the ϵ_r-threshold. This is also confirmed by the fast motions of the phase space trajectory at the extremities (or corners) of the phase space in Fig. 4.5b, where the phase space trajectory reverses its direction abruptly, akin to a hairpin turn in a mountainous road. Thenceforth, we shall refer to such abrupt reversal in the trajectory leading to the formation of line segments perpendicular to the main diagonal line as the *hairpin trajectory*. It is important to emphasize that there is no such occurrence of two neighboring phase space trajectories traversing in opposite directions in the VDP system (see Fig. 4.3c,d). As a result, we do not obtain any perpendicular lines in the RP of the VDP system.

In Fig. 4.5d, the RN for this signal is plotted. Within one cycle, the trajectory is predominantly slow with many nodes having a very high number of connections (red and green). The fast regions in the phase space are present in the protrusions comprising nodes with low degree (blue). In contrast to the RN of the VDP system, we observe that only nodes with high and medium degree (red and green colors, respectively) occupy the ring-like structure. However, the protrusions on the ring are predominantly occupied by the nodes with low degree (blue). This characteristic behavior must arise out of some fundamental difference in these two slow-fast systems, which is being reflected on their
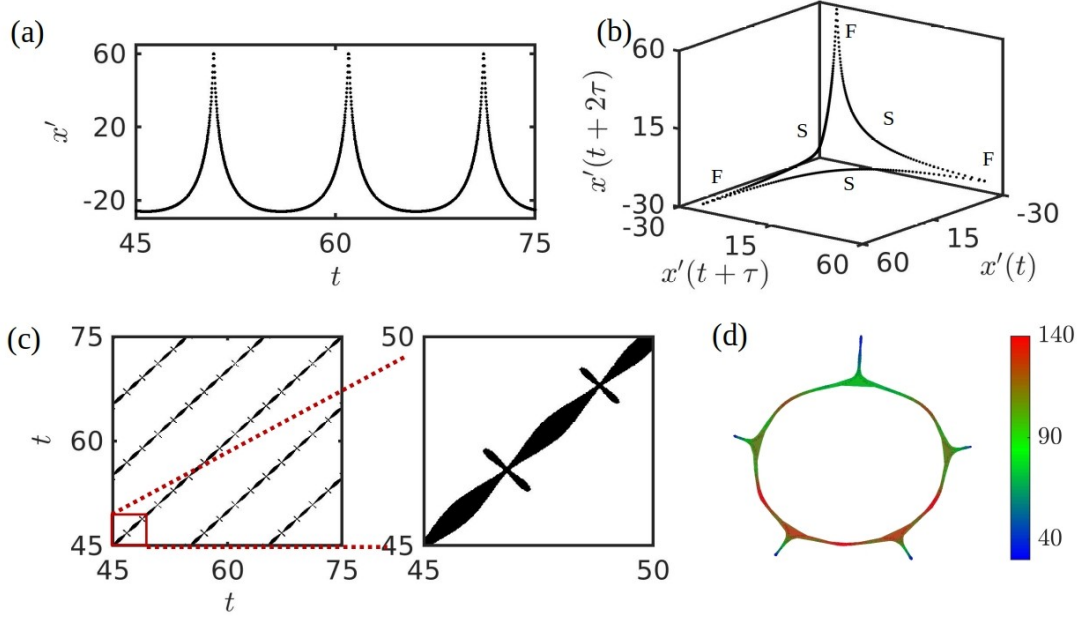
Fig. 4.5: (a) A prototypical periodic spiky signal is derived from a modified output of Izhikevich's neuron spiking model (Eq. 4.4). (b) The reconstructed phase space, (c) RP along with its zoomed view portion, and (d) RN for the signal shown in (a). The parameters fixed for plotting (b)-(d) are τ_{opt} = 102 time steps, $d = 6$, and $RR = 0.05$. Here, we observe characteristic micro-patterns on the RP and protrusions over the ring-shaped RN.

respective recurrence properties. Also, we identify that the micro-patterns in the RP and the RN for this prototypical signal are clearly different from the ones obtained for the VDP system.

4.4 RECURRENCE ANALYSIS OF HIGH-DIMENSIONAL PROTOTYPICAL SIGNALS

We also analyze the recurrence properties of the well-known Hodgkin-Huxley model, which exhibits slow-fast oscillations (Izhikevich, 2007; Díaz *et al.*, 2016). It is represented by,

$$
\dot{V} = \frac{1}{C_m} \left[I - g_{Na} m^3 h (V - E_{Na}) - g_K n^4 (V - E_K) - g_L (V - E_L) \right]
$$
$$
\dot{m} = \alpha_m(V)(1 - m) - \beta_m(V)m
$$
$$
\dot{n} = \alpha_n(V)(1 - n) - \beta_n(V)n
$$
$$
\dot{h} = \alpha_h(V)(1 - h) - \beta_h(V)h.
$$

(4.5)

Here, V is the the potential, I is the current per unit area, and g_i is the maximum value of conductance where i corresponds to either one of potassium (K), sodium (Na), or leak channel (L). The gating variables, α and β, control the activation and inactivation of their respective channels. Variables: m, n, and h are non-dimensional quantities associated with the potassium channel activation, sodium channel activation, and sodium channel inactivation, respectively. These variables acquire values between 0 to 1. In Eq. 4.5, the constant parameters used are: E_{Na} = 115 mV, E_K = -12 mV, E_L = 10.6 mV, g_{Na} = 120 mS/cm^2, g_K = 36 mS/cm^2, g_L = 0.3 mS/cm^2, and C_m = 1 μF/cm^2. The corresponding steady state values for the gating variables, α and β, are related to the potential V as,

$$
\begin{aligned}
\alpha_h &= 0.07 \exp\left[\frac{-(V+65)}{20}\right], & \beta_h &= \left(1 + \exp\left[\frac{-(V+35)}{10}\right]\right)^{-1}, \\
\alpha_m &= 0.1 \frac{V+40}{1 - \exp\left[\frac{-(V+40)}{10}\right]}, & \beta_m &= 4 \exp\left[\frac{-(V+65)}{18}\right], \\
\alpha_n &= 0.01 \frac{V+55}{1 - \exp\left[\frac{-(V+55)}{10}\right]}, & \beta_n &= 0.125 \exp\left[\frac{-(V+65)}{80}\right].
\end{aligned}
\tag{4.6}
$$

The set of equations are solved using Euler's method. In Fig. 4.6a, we plot the time series of the membrane potential, V, obtained for I = 10 nA/cm^2 in Eq. 4.5.

We observe that V exhibits a limit cycle behavior with slow-fast timescales. From the corresponding three-dimensional phase portrait in Fig. 4.6b, we see that certain regions are slow (marked S), while others are fast (marked F). The corresponding RP also exhibits unique micro-patterns on top of the diagonal lines (see Fig. 4.6c). The hairpin trajectory in its phase space renders a sword-like structure similar to the perpendicular lines observed in the RP of the prototypical spiky signal (Fig. 4.5c).

The corresponding RN exhibits a protrusion made up of high degree nodes, and several clusters built of medium degree nodes on top of a ring of low degree nodes (Fig. 4.6d). Here, hairpins consist of slow epochs. Hence, we obtain protrusions containing high degree nodes, in stark contrast to the RN of the modified Izhikevich model. Altogether,
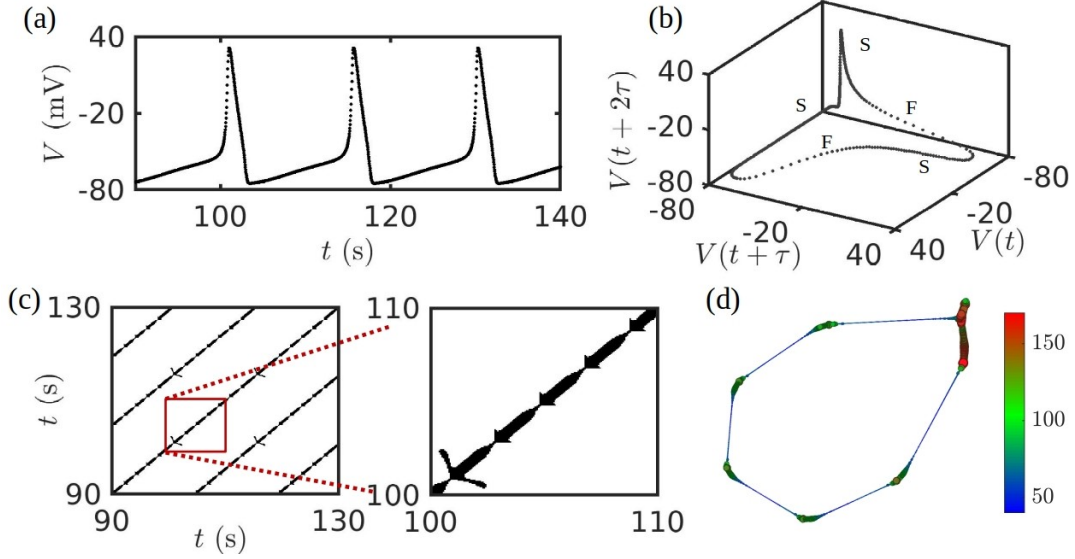
Fig. 4.6: (a) Time series of membrane potential (V) obtained from Hodgkin-Huxley model (Eq. 4.5) for $I = 10$ nA/cm^2. (b) The reconstructed phase space, (c) RP along with its zoomed view portion, and (d) RN, for the signal shown in (a). The parameter fixed for plotting (b)-(d) are $d = 7$, $\tau_{opt} = 66$ time steps, and RR = 0.05. We observe a characteristic sword-like pattern in the RP, and, distinct clusters and protrusion in the RN.

the RN of the Hodgkin-Huxley model contains both features observed in Fig. 4.4b,d and Fig. 4.5d.

After analyzing the phase space dynamics and recurrence properties of these three prototypical slow-fast signals along with a sine wave, we understand that the RN for these slow-fast systems exhibit characteristic features on top of the closed-loop structure, expected for periodic signals. Moreover, the RP of such systems is manifested by unique micro-patterns pertaining to slow-fast dynamics over the diagonal lines.

4.5 RECURRENCE ANALYSIS OF HIGH-DIMENSIONAL EXPERIMENTAL SIGNALS

In order to confirm the aforementioned observations in the slow-fast dynamics of real-world data, we present the results of the investigation of two different time series acquired from experiments in a laboratory scale gas turbine-type turbulent combustor and a model rocket combustor during the state of an oscillatory instability, known as thermoacoustic instability (Juniper and Sujith, 2018). Here, thermoacoustic
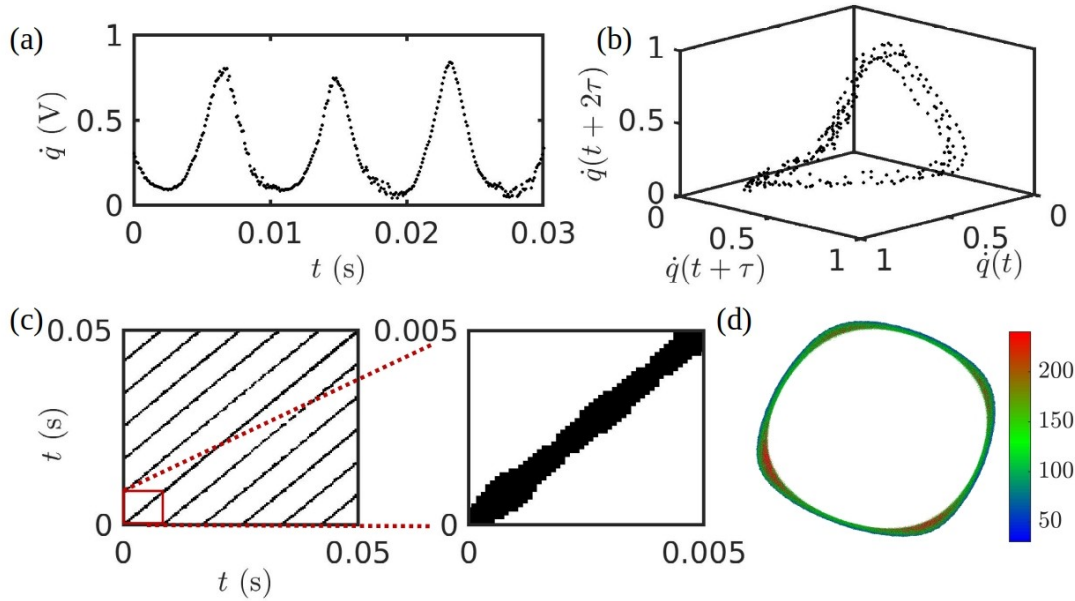
Fig. 4.7: (a) Time series of heat release rate oscillations ($\dot{q}$) during thermoacoustic instability acquired from a laboratory-scale turbulent combustor. (b) The reconstructed phase space, (c) RP along with its zoomed view portion, and (d) RN, plotted for the signal shown in (a). The parameter fixed for plotting (b)-(d) are $d = 12$, $\tau_{opt} = 20$ time steps, and $RR = 0.1$. The RP and RN for this experimental signal resemble those of the VDP model to a great extent. More details regarding this experiment and its operating conditions can be found in Pawar *et al.* (2017)

.

instability is a dynamical regime featured by large amplitude, self-sustained periodic oscillations in the acoustic pressure, $p(t)$, and heat release rate, $\dot{q}(t)$, along with other dynamical variables of the system. The occurrence of this feedback-driven phenomenon overwhelms the thermal protection systems, compromises the controllability and structural stability of gas turbines and rocket engines (Lieuwen, 2012; Juniper and Sujith, 2018).

First, in Fig. 4.7a,b, we consider the time series of heat release rate oscillations ($\dot{q}(t)$) and the corresponding reconstructed phase space obtained during the state of thermoacoustic instability for a gas turbine type turbulent combustor. We observe that the time series is spikier than a sine wave, exhibiting a clear departure from sinusoidal signals. The spikiness in the signal (Pawar *et al.*, 2017) (Fig. 4.7a) is attributed to the near instantaneous heat release rate as a result of the impingement of the large-scale

coherent vortex structure carrying fuel-air mixture against the walls of the combustor (Seshadri *et al.*, 2016).

In the corresponding phase space of the heat release rate ($\dot{q}$) signal in Fig. 4.7b, we observe a distorted closed-loop structure, indicative of the non-uniform evolution of the phase space trajectory due to the presence of slow and fast timescales. However, such slow and fast timescales are not too separated when compared to the earlier phase space of prototypical signals. In the RP of this signal (see Fig. 4.7c), we see the presence of continuous diagonal lines, indicating sustained periodicity in the oscillations. The corrugations along the diagonal lines arise due to the presence of the slow and fast timescales in the phase space. The RN for this signal (Fig. 4.7d) looks similar to that of VDP as there are clusters of high degree nodes (red) on the ring of medium degree (green) nodes. The clusters pertain to the slow regions in the phase space.

Finally, we investigate the time series of acoustic pressure oscillations ($p'(t)$) in a multi-element model rocket combustor during the state of thermoacoustic instability (Orth *et al.*, 2018) (Fig. 4.8a). We observe that a major portion of the cycle is spent in the slow relaxation phase with a momentary jump in the pressure due to the fast compression phase of the signal. Physically, due to an increase in the speed of sound during the compression phase, the compression side catches up with the expansion side of the pressure wave. This phenomena, known as wave steepening, results in an abrupt increase in the amplitude of the pressure oscillations (Tyagi and Sujith, 2003*a*). Under favorable conditions, the steepened wave manifests as a shock wave in the flow-field. Such wave steepened shock waves are commonly observed in the pressure oscillations in the combustion chambers of rockets (Saenger and Hudson, 1960; Chester, 1964).

The reconstructed phase space of this pressure signal, shown in Fig. 4.8b, is similar to the phase portrait shown in Figs. 4.5b & 4.6b, wherein the trajectory moves along the three axes to complete one oscillation cycle. Unlike the usual closed-loop structure of the phase space trajectory of periodic signals observed in the previous slow-fast systems, the phase space of the pressure signal exhibits a peculiar shape like a trefoil-
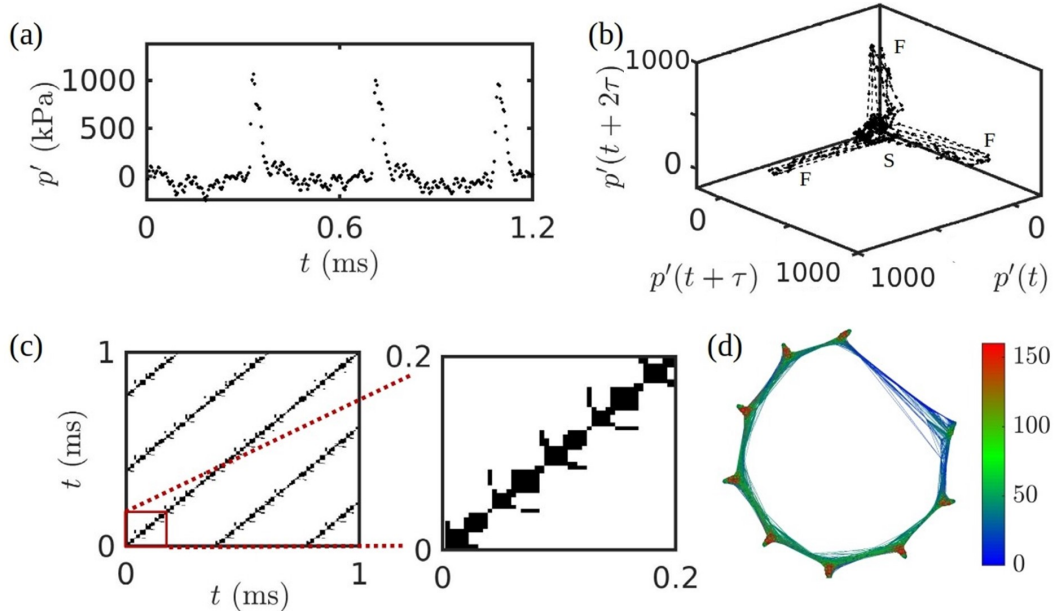
Fig. 4.8: (a) Time series of acoustic pressure oscillations (p') during thermoacoustic instability acquired from a multi-element rocket combustor. (b) The reconstructed phase space, (c) RP along with its zoomed view portion, and (d) RN, for the signal shown in (a). The parameter fixed for plotting (b)-(d) are $d = 10$, $\tau_{opt} = 21$ time steps, and $RR = 0.05$. The RN and RP of this signal resembles those of neuron spiking models.

knot. The geometrical difference of the phase space attractor is attributed to the vast divergence in the slow and fast timescales in the rocket system.

The RP and the RN for the pressure oscillations are plotted in Fig. 4.8c,d, respectively. The RP contains unique micro-patterns arising due to the presence of spikes. On top of the diagonal lines that indicate periodicity of the signal, we observe thick regions divided by a thin region. The thick regions emerge due to the increased trapping of the phase space trajectory in the slow epoch, while the thin regions correspond to the fast spike in the phase space. Due to the hairpin trajectories at the extremities in the reconstructed phase space, the RP of this signal exhibits line segments protruding away from each diagonal line in a periodic manner.

The RN of this signal looks similar to Fig. 4.5d, based on its topological similarity. The protrusions in the RN in Fig. 4.8d are made up of high degree (red) nodes, unlike the RN in Fig. 4.5d where the protrusions are made up of low degree (blue) nodes. Suitable measures characterizing the RN can be used to benchmark simulations that

predict thermoacoustic instability in combustion chambers of rocket engines.

4.6 QUANTITATIVE   ANALYSIS   OF   RECURRENCE   NETWORK   PROPERTIES

Next, we quantitatively characterize the recurrence network topology obtained from the reconstructed phase space to unravel the differences between the slow-fast system and a single timescale system such as a sine wave. The conventional approach in networks built from time series is to compute the global network measures such as the mean degree of a network (Barabási *et al.*, 2016).
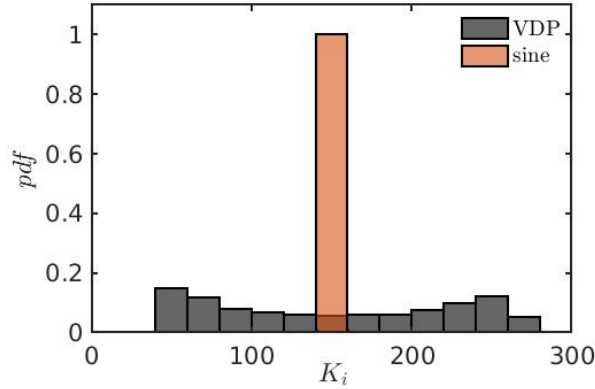
Fig. 4.9: Histogram of the probability distribution function of the degree of each node for a sine wave (brown) and the VDP model (black). A bin size of 20 is used for the representation. The time series of sine wave and VDP model ($\mu = 2$) are built with a temporal step size of 0.01 s and time period 7.63 s to ensure same number of points in both the signals. We observe that the degree distribution is wider in the VDP model as opposed to that of the sine wave.

To ensure that no disparity arises due to the length of the time series and the frequency of oscillations, we ensure that both the sine wave and the VDP signals are of the same frequency and amplitude. We find that the mean degree ($K_{mean} = \sum_{i=1}^{n} K_i/n$) remains the same for both the sine wave and the VDP model ($K_{mean} = 152$). In Fig. 4.9, we plot the histogram of the probability distribution function of the K_i of each node in the RN of sine wave and the RN of VDP model. We observe that the distribution for the VDP model has a broader spread compared to a unique value for the sine wave, justifying the presence of multiple timescales in spite of its periodic behavior of both models.
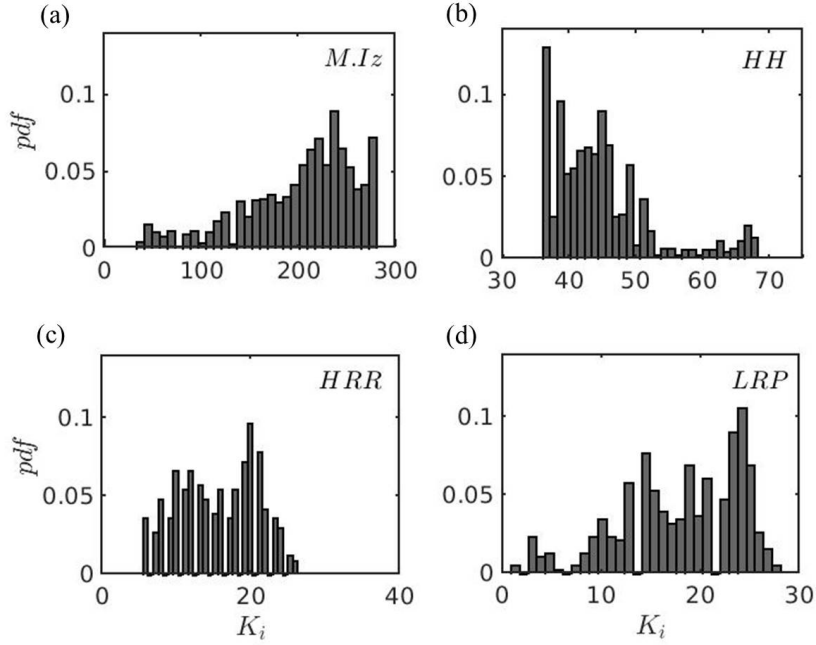
Fig. 4.10: Probability distribution of the degree of each node in the RN of (a) modified Izhikevich model ($M.Iz$), (b) Hodgkin-Huxley model (HH), (c) heat release rate oscillations of a gas turbine-type combustor (HRR), and (d) acoustic pressure oscillations from a laboratory-scale liquid rocket combustor (LRP). Similar to the VDP model, the probability distribution of degree of nodes in the RN of slow-fast systems exhibit a wider spread.

In Fig. 4.10, we show the probability distribution of degrees for the RN constructed for the modified Izhikevich model ($M.Iz$), Hodgkin-Huxley model (HH), the heat release rate oscillations of a gas turbine-type turbulent combustor, and the acoustic pressure oscillations from the laboratory-scale liquid rocket combustor (LRP). We observe that the degree (K_i) has a broad distribution for each slow-fast, in stark contrast to the unique degree of a sine wave.

Further, the degree distribution for the VDP model is clearly a bimodal distribution (Fig. 4.9). The degree distributions obtained for both the experimental and synthetic slow-fast systems are not only broad but also seem to display multimodality. Recently, Kachhara and Ambika (2019) demonstrated the presence of bimodality in the degree distributions of the RNs constructed from ECG signals obtained from healthy and unhealthy subjects. They reported that the presence of both small-scale and large-scale structures in the phase space to be the reason behind the bimodality. Further,

the topology of the RNs from ECG signals also exhibited protrusions and clusters of high/low degree nodes. To unravel the variation of degree of each node (K_i) in the RN, we again first demonstrate by comparing VDP model and the sine wave. In Fig. 4.11, we show the variation of K_i along with the distance (PD_i) between consecutive points ($\vec{x}$) in the reconstructed phase space for the VDP model and sine wave. Here, the nodes are labeled according to their temporal appearance in their corresponding phase spaces. PD_i is calculated using Euclidean norm as,

$$PD_i = \|\vec{x}_i - \vec{x}_{i+1}\| \quad i = 1, 2, \ldots, n - 1. \tag{4.7}$$

For every cycle of oscillation in the sine wave, we see that both PD_i (Fig. 4.11b) and K_i (Fig. 4.11c) remain invariant. However, for every cycle of oscillation in the VDP model, we observe four oscillations in both PD_i and K_i, since there are four slow epochs and four fast epochs in the phase space of the reconstructed signal of the VDP model (see Fig. 4.3d). Moreover, we see the simultaneous occurrence of lower values in
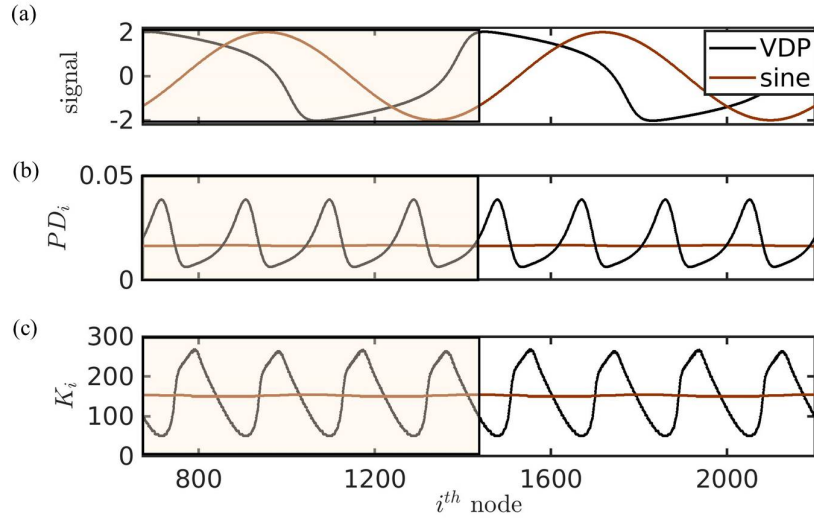
Fig. 4.11: (a) Time series of variable x of the VDP model (VDP - black curve) for $\mu = 2$, time period of 7.63 s and a temporal step size of 0.01 s. The time series of the sine wave (brown curve) of same time period, amplitude and sampling rate is also shown. The temporal variation of (b) PD_i and (c) K_i are plotted. The shaded rectangle highlights one cycle of oscillation in (a) - (c). Note that the nodes in a RN are representative of the phase space points in time.

PD_i and higher values in K_i, whenever the phase space exhibits slow motion. During slow motion, the consecutive points in the phase space are located nearby and hence, PD_i is low and K_i is high. Correspondingly for epochs of fast motion in the phase space, we obtain higher values in PD_i and lower values in K_i. The four oscillations within a cycle of oscillation manifests as four clusters in the RN, as seen in Fig. 4.4d.
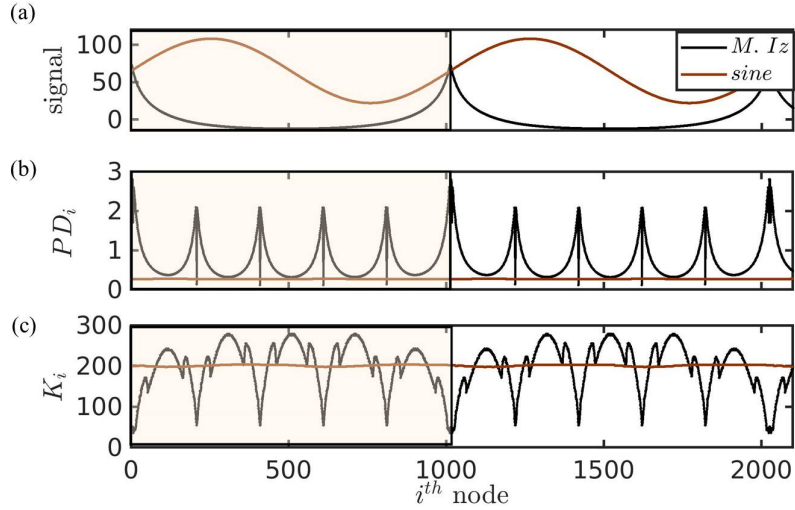
Fig. 4.12: (a) Time series of x' of the modified Izhikevich model (black curve) for a time period of 10.11 s and a temporal step size of 0.01 s. The time series of a sine wave (brown curve) of the same time period, amplitude and sampling rate is also shown. The temporal variation of (b) PD_i and (c) K_i are plotted. The shaded rectangle highlights one cycle of oscillation in (a) - (c). Note that the nodes in a RN are representative of phase space points in time.

In Fig. 4.12, we plot the variation of PD_i and K_i for the time series obtained from the modified Izhikevich ($M.\,Iz$) model and a sine wave, both of which contain periodic oscillations with a time period of 10.11 s sampled at a temporal step size of 0.01 s. Similarly, we observe significant temporal variations in both PD_i and K_i for the slow-fast system while that of the sine wave remains constant. Also, we find higher values in K_i, whenever PD_i is low and vice versa. There are five oscillations in PD_i and K_i within a cycle of oscillation of the prototypical slow-fast signal. This manifests as five protrusions of low degree nodes in the RN shown in Fig. 4.5d.

For the other systems described in this chapter, we show the temporal variation of

the distance between consecutive state points in the phase space trajectory (PD_i) and the degree of each node (equivalently time instant) in the recurrence network for the Hodgkin-Huxley model (HH), heat release rate oscillations (HRR), and acoustic pressure oscillations (LRP), respectively, in Fig. 4.13.

For every cycle of oscillation in the sine wave, we know that both PD_i and K_i (Fig. 4.13c) remain invariant. However, for the slow-fast systems, we see the simultaneous occurrence of lower values in PD_i and higher values in K_i whenever the phase space exhibits slow motion. During slow motion, the consecutive points in the phase space are located nearby and hence, PD_i is low and K_i is high. Correspondingly for epochs of fast motion in the phase space, we obtain higher values in PD_i and lower values in K_i.
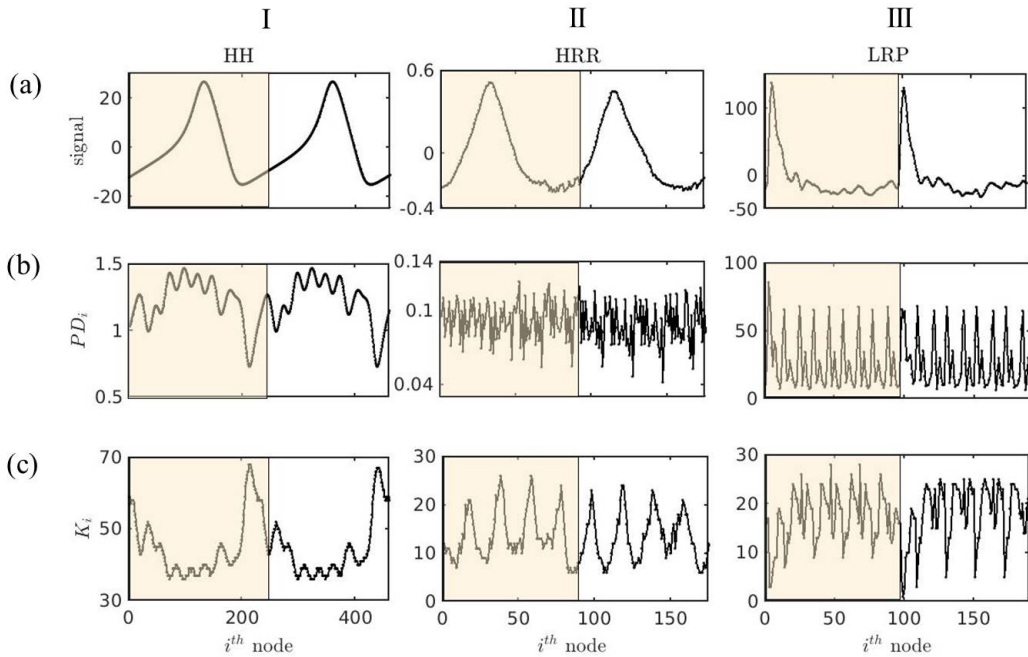
Fig. 4.13: (a) Time series of the periodic slow-fast system and temporal variation of (b) PD_i and (c) K_i are plotted for (I) Hodgkin-Huxley model (HH), (II) heat release rate oscillations of a gas turbine-type combustor (HRR), and (III) acoustic pressure oscillations from a laboratory-scale liquid rocket combustor (LRP). The shaded rectangle highlights one cycle of oscillation in (a) - (c). Here, we observe that the PD_i and K_i oscillates even within a single period of oscillation of the slow-fast system.

We observe six clusters along with a protrusion in the corresponding RN of HH model.

The six clusters arise from the six cycles of small amplitude oscillations in PD_i and K_i (see Fig. 4.13Ib,c). These six cycles could reflect six pairs of slow-fast epochs in the corresponding phase space of this signal. There exists a single large oscillation in both PD_i and K_i which gives rise to the protrusion with high degree nodes in the corresponding RN.

Next, in the HRR system, we can clearly observe the four oscillations from the K_i (see Fig. 4.13IIc), while it is difficult to discern this information from the PD_i (see Fig. 4.13IIb). Furthermore, these four oscillations manifest as four clusters in the corresponding RN.

Finally, in the RN of LRP system, we observe nine protrusions ensuing from the nine pairs of slow-fast epochs in its phase space and is reflected in the nine oscillations within a cycle of the LRP in both PD_i and K_i (see Fig. 4.13IIIb,c).

With the understanding gained from analyzing the various prototypical and experimental systems in this chapter, we noticed that the dynamics of slow-fast systems can be understood based on their recurrence properties. From the RNs, we observed that some slow-fast systems exhibit protrusions, while other systems display clustering. Each slow-fast system imparts a signature micro-pattern over the diagonal lines in their corresponding RP. It is also interesting to note that even though both real-world systems discussed here operate in a regime of thermoacoustic instability, both systems exhibit different RN topology due to a difference in their underlying mechanisms that generate such oscillations. Finally, we interpret the RN topology using the temporal variation in the distance between consecutive points in the phase space and the degree of each node in the RN of slow-fast systems.

4.7 CONCLUDING REMARKS

In this chapter, the recurrence properties of slow-fast systems are studied by means of recurrence plots and recurrence networks are explored. A systematic approach is adopted by first performing the analysis on prototypical signals before analyzing

high-dimensional signals obtained from experiments. We find that slow-fast systems exhibit different recurrence properties compared to periodic systems which operate on a single timescale. We observe that unique features about the slow-fast system can be obtained from the micro-patterns along the diagonal line in the RPs, unlike mere straight lines observed in the RP for harmonic signals. Especially, we find that hairpin trajectories in the phase space lead to the occurrence of line segments perpendicular to the main diagonal line in the RP. These findings help to improve the understanding of the various patterns evident in the RP. Further, we identify characteristic features in the corresponding RN topologies for slow-fast systems. In addition to the closed-ring structure of periodic signals, we also observe protrusions and clustering in the RN for slow-fast systems. Such additional features in the RN result from the temporal variation in the distance between consecutive points in the phase space and the degree of nodes in the RN of slow-fast systems. These variations are absent in single timescale systems. Understanding the slow-fast time scales and their universality in diverse systems across natural sciences, medicine, econometrics, and engineering, would be crucial in the future. Specifically for rocket engines, we believe that suitable quantifiers derived from the RN can be used to benchmark simulations that predict thermoacoustic instability in combustion chambers of rocket engines.

CHAPTER 5

Coupled interaction between acoustic pressure and flame intensities during the transition to thermoacoustic instability

.

During thermoacoustic instabilities characterized by transverse acoustic mode oscillations, the large amplitude oscillations in the heat release rate may lead to undesirable melting of components of the combustion chamber. Therefore, it is important to understand the onset of these large amplitude heat release rate oscillations. Despite decades of active research, a deeper understanding of the coupled interaction between the acoustic and the heat release rate oscillations in rocket engine combustors has been missing (Harrje and Reardon, 1972; Hardi, 2012; Sardeshmukh *et al.*, 2019). Moreover, past studies have focused mostly on the state of thermoacoustic instability. Hence, the coupled interaction between the acoustic pressure and the heat release rate oscillations in the combustors of rocket engines during the transition from stable state to thermoacoustic instability is not completely understood.

The analysis of coupled interaction between the acoustics and the flame in transverse-excited combustors operating under elevated pressure conditions are notoriously difficult. First, the nonlinear interactions between acoustics, multiple jet flames, and flow processes in rocket engine combustors introduce additional features such as steep fronted waves (Saenger and Hudson, 1960) and rise in mean pressure (Flandro *et al.*, 2007). Further, due to the high-frequency acoustics typically seen in combustors of rocket engines, the flame and the acoustic length scales are comparable. Such an environment is termed 'acoustically non-compact' where the acoustic perturbations vary significantly even across a single jet flame in the combustor. These effects makes

it challenging to study of the coupled interaction between the acoustics and heat release rate in the combustors prone to transverse thermoacoustic instability.

In this chapter, we adopt the framework of synchronization theory (Lakshmanan and Senthilkumar, 2011; Pawar *et al.*, 2017) and recurrence theory (Marwan *et al.*, 2007; Gotoda *et al.*, 2014) to analyze the coupled dynamics of acoustic pressure and CH* intensity (representative of heat release rate) oscillations during this transition in the 2D multi-element self-excited model rocket combustor. First, we perform a temporal analysis of the coupling between the acoustic pressure and the CH* intensity (representative of heat release rate) oscillations during the transition to thermoacoustic instability.

Then, we study the spatiotemporal dynamics of the jet flames near the end wall and the center of the combustor for each dynamical state. We discuss the effect of the transverse propagating shock wave on the flame dynamics. Then, we devise a novel methodology to reconstruct the spatiotemporal variation of the acoustic pressure in such 'acoustically non-compact' environments, and extend our reconstruction to spatiotemporally resolved CH* chemiluminescence measurements. From the reconstructed data, we estimate the contribution of each transverse mode to the generation of acoustic power using the spatial distribution of Rayleigh index. Finally, using recurrence quantification analysis, we quantify the extent of determinism in the dynamics of local CH* intensity oscillations at both the end wall and center locations of the combustor.

5.1 OSCILLATORS OF THE THERMOACOUSTIC SYSTEM

In this chapter, we study the coupled interaction between the turbulent reacting flow field and acoustic field during the transition to transverse thermoacoustic instability. We define the acoustic field and the turbulent reacting field as the two oscillators and use the framework of synchronization theory to understand the interacting between these two subsystems.

For the study of synchronization, the oscillators should be self-sustained and exhibit a coupling (weak/strong) between them (Pikovsky *et al.*, 2003). In turbulent combustors, due to the inherent hydrodynamic fluctuations, the heat release rate and the acoustic pressure exhibit self-sustained chaotic oscillations during stable operation of the combustor (Pawar *et al.*, 2017). The acoustic field in a cold turbulent flow has been reported to exhibit self-sustained chaotic oscillations at broadband frequencies (Godavarthi *et al.*, 2018). In our study, the underlying flow field is highly turbulent (Reynolds number $\sim$ 393000 at the injector exit), and as the oxidizer is preheated to 635 K, the jet flames inherently oscillate even during stable operation due to density-stratification (Emerson *et al.*, 2012) and also due to inherent turbulent fluctuations. Therefore, in the presence of turbulent reactive flow, the acoustic field and the turbulent reacting flow in our combustor can indeed be considered as self-sustained aperiodic oscillators.

Note that each of these oscillators behave as a damped oscillator in the absence of turbulent flow. However, the presence of continuous disturbances from the inherent turbulent hydrodynamic flow makes them self-sustained oscillators. Therefore, we can apply the framework of synchronization to study the coupled behavior between acoustic pressure and CH* intensity (representative of heat release rate) oscillations during the transition to thermoacoustic instability. Studying such synchronization behaviors between different subsystems (through different variables that represent these subsystems) of the same system is well-established in nonlinear dynamics; examples include thermoacoustic systems (Pawar *et al.*, 2017; Chiocchini *et al.*, 2018; Murayama and Gotoda, 2019; Guan *et al.*, 2019*b*), biological systems (Schäfer *et al.*, 1999), psychology (Scherer, 2000), neuroscience (Siapas *et al.*, 2005; Nikulin and Brismar, 2006), and network systems (Pecora and Carroll, 2015).

We study the data obtained from two test cases - E and C, as described earlier in Chapter. 3. Since both the tests are performed for the same set of operating conditions, we will utilize test E and test C for comparing the dynamics near the end wall and the

center of the combustor, respectively. Due to the continuous presence of hydrodynamic fluctuations inherent in the turbulent flow (Reynolds number ~ 393000 at the injector exit), both the CH* intensity and the acoustic pressure exhibit self-sustained oscillations (Pawar *et al.*, 2017; Godavarthi *et al.*, 2018). Hence, we consider the acoustic pressure and the CH* intensity as the two oscillators of the system.

5.2 TEMPORAL ANALYSIS OF THE COUPLED ACOUSTIC PRESSURE AND CH* INTENSITY FLUCTUATIONS

In Fig. 5.1, we show the pressure (i.e., $p = \bar{p} + p'$) and the normalized CH* intensity (I) measured at both the locations in the combustor during the transition to thermoacoustic instability. The pressure and photomultiplier signals acquired near the end wall (PT-01 and PMT-01) and the center of the combustor (PT-02 and PMT-02) are used to capture this dynamical transition in tests - E and C, respectively as described in Chapter. 2. To visually compare the qualitative behavior of the two signals, we show the waveforms of the acoustic pressure (p') and the CH* intensity fluctuations (I') normalized with their respective maximum values in the zoomed insets.

Although both the tests are performed for the same set of operating conditions, interestingly, they exhibit different sets of dynamical states. In test E, we observe intermittency, characterized by epochs of low amplitude aperiodic oscillations ($p'/\bar{p} \sim 10\%$) and high amplitude periodic oscillations ($p'/\bar{p} \sim 90\%$) interspersed in a random manner. This intermittency is succeeded by thermoacoustic instability, characterized by large amplitude ($p'/\bar{p} \sim 100\%$) high frequency (~ 2650 Hz) limit cycle oscillations at the first transverse mode (1T) of the combustor. At the beginning of test C, we observe a stable state, characterized by low amplitude aperiodic oscillations ($p'/\bar{p} < 10\%$). This stable state is followed by intermittency and thermoacoustic instability. During this transition from stable state to thermoacoustic instability in both the tests, the presence of DC shift can be clearly discernible from significant increase in the mean pressures.
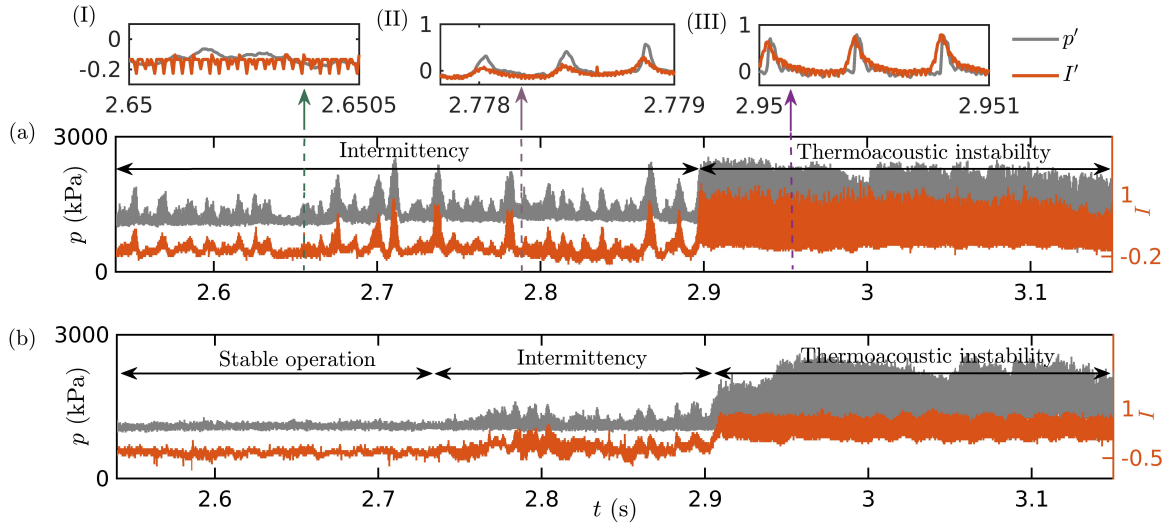
Fig. 5.1: Time series of the pressure (p) and the normalized CH* intensity (I) oscillations for (a) test E and (b) test C. The zoomed insets represent the normalized waveforms of p' and I' during (I) aperiodic epoch of intermittency, (II) periodic epoch of intermittency, and (III) thermoacoustic instability.

Next, we qualitatively analyze the coupled behavior of the p' and I' during the onset of thermoacoustic instability. At the outset, we observe that the oscillations are either aperiodic or periodic during each dynamical state en route to thermoacoustic instability. During thermoacoustic instability (Fig. 5.1III), we observe that both p' and I' are periodic and nearly in-phase with each other. The p' signal exhibits a spiky wave form where the amplitude of the signal rises sharply to a high value, then decays gradually and stays near the minimum amplitude for a long epoch in the oscillation cycle, as described in Chapter. 4. Such a waveform is typical of steep fronted pressure wave. While the waveform of I' is also spiky and stays near the minima for a long epoch in the oscillation cycle, the rise in its amplitude is not as rapid as that of the p'.

During intermittency, we observe alternate occurrences of bursts of periodic oscillations in between epochs of low amplitude aperiodic oscillations. The wave steepening effect is not as pronounced during the periodic part of intermittency when compared to thermoacoustic instability (compare zoomed insets - II and III in Fig. 5.1). During the periodic part of intermittency (Fig. 5.1II), the oscillations of both p' and I' match in their rhythms with nearly zero phase difference. Conversely, during epochs of aperiodic

104

oscillations in the intermittency signal (Fig. 5.1I), the temporal locking of oscillations in p' and I' appears to be absent. The waveform of the oscillations in each dynamical state of p' and I' during test C is nearly akin to that seen in test E. This test exhibits the stable state before intermittency. During the stable state, we observe sustained desynchronized aperiodic oscillations in both p' and I' signals.

5.2.1 Cross wavelet analysis of the acoustic pressure and the CH* intensity oscillations

To understand the synchronization characteristics between p' and I' signals during the onset of thermoacoustic instability quantitatively and also to identify the locking of their dominant modes, we perform a cross wavelet transform (XWT) (Grinsted *et al.*, 2004) between these signals. The XWT indicates the regions in the time-frequency space where the two time series simultaneously exhibit high spectral powers. The complex Morlet wavelet shown in Eq. (5.1) is used as the mother wavelet (ψ_0). Here, η and ω are dimensionless time and frequency, respectively. The Morlet wavelet, ψ_0, can be dilated and translated in time-frequency space following a continuous wavelet transform (Grinsted *et al.*, 2004).

$$
\begin{aligned}
\psi_0(\eta) &= \pi^{-1/4} e^{i\omega_o \eta} e^{(-1/2)\eta^2}, \\
W(u,s) &= \frac{1}{\sqrt{s}} \int_{-\infty}^{+\infty} x(t)\psi_0\left(\frac{t-u}{s}\right) \mathrm{d}t.
\end{aligned}
\tag{5.1}
$$

Here, $x(t)$ is the time series analyzed, whereas s and u are the scale and translation parameters of ψ_0, respectively. The XWT for the two time series, $x(t)$ and $y(t)$ is obtained by $W_{xy} = W_x W_y^*$ (* denotes complex conjugate). The magnitude of the common spectral power is obtained as $|W_{xy}|$. The instantaneous relative phase between the two time series is given by $\arg(W_{xy})$. This information can be illustrated in a time-frequency plot.

Desynchrony between acoustic pressure and CH* intensity oscillations during stable state
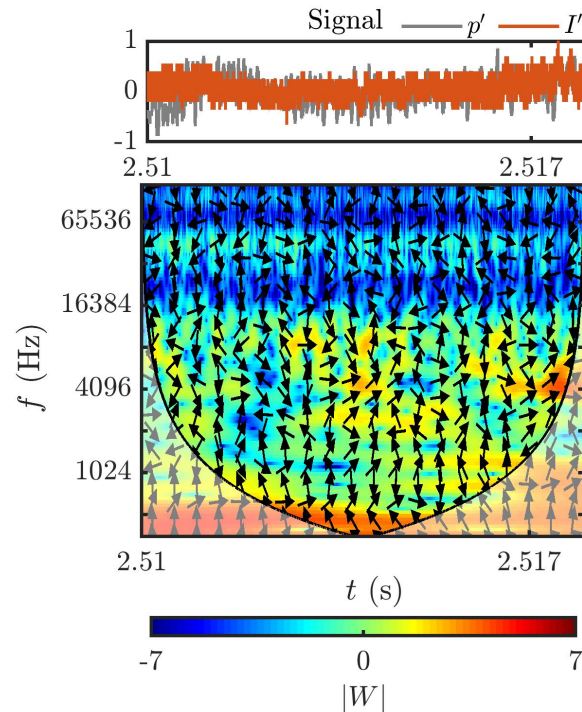
Fig. 5.2: The normalized time series of acoustic pressure (p') and CH* intensity (I') oscillations, along with the corresponding XWT plot during the stable state. The pressure and CH* intensity oscillations measured near the center of the combustor are used.

Both p' and I' are aperiodic throughout the stable state (see Fig. 5.1I). From the XWT plot of p' and I' shown in Fig. 5.2 for a time interval of 30 ms, we observe a non-homogeneous distribution of common spectral power along with a random alignment of the relative phase arrows at the 1T mode or its harmonics. Therefore, the coupled behavior between p' and I' during stable state corresponds to that of desynchronization.

Evolution of synchrony between acoustic pressure and CH8 intensity oscillations during intermittency and thermoacoustic instability

In Fig. 5.3a, we show the XWT of p' and I' signals for an epoch of intermittency comprising the transition from periodic to aperiodic oscillations. The region outside the shaded area in the XWT is called the 'cone of influence'. In the shaded region, the

106

estimates of power of cross wavelet transform between the p' and I' signals cannot be ascertained above a 95% confidence level, due to the finiteness of the data and temporal sampling (Grinsted *et al.*, 2004). Henceforth, we utilize the information inside the 'cone of influence' to understand the time-frequency behavior. When the signal is periodic, we observe a strong amplitude content at a band of frequencies centered around 2650 Hz (1T mode) in the plot of XWT. The common spectral power of this mode decays as soon as the oscillations in the signal become aperiodic. In the aperiodic epoch of the intermittency signal acquired at the end wall, we observe the absence of any common power between the p' and I' oscillations.

On the other hand, during the state of thermoacoustic instability (Fig. 5.3b,c), we observe that a common band of frequencies around 1T mode sustains their high magnitude throughout the signal. Moreover, the presence of steepened shock wave results in the occurrence of several harmonics of considerable amplitudes. During thermoacoustic instability, near the end wall (see Fig. 5.3b), we observe that the common spectral power gradually decreases from 1T to 10T modes. However, for thermoacoustic instability, near the center of the combustor (see Fig. 5.3c), we only observe high common spectral power for the 2T mode followed by the 1T mode. Performing a simulation based on the same combustor, Harvazinski *et al.* (2019) had reported that the pressure at the center of the chamber has a frequency that is double the frequency observed at the end wall. The results from XWT plots in Fig. 5.3b,c are in agreement with their study. Further, our result indicates that only the first two modes dominate the coupled behavior of p' and I' in the center of the combustor.

Additionally, the instantaneous phase difference between p' and I' signals at each frequency is represented by arrows distributed all over the plot of XWT. The alignment of these arrows in the same direction in time, for a frequency having high common spectral power indicates the presence of synchrony between the signals at that frequency. Further, the orientation of arrows indicates the value of the relative phase between these synchronized oscillations at the frequency they are locked and enables
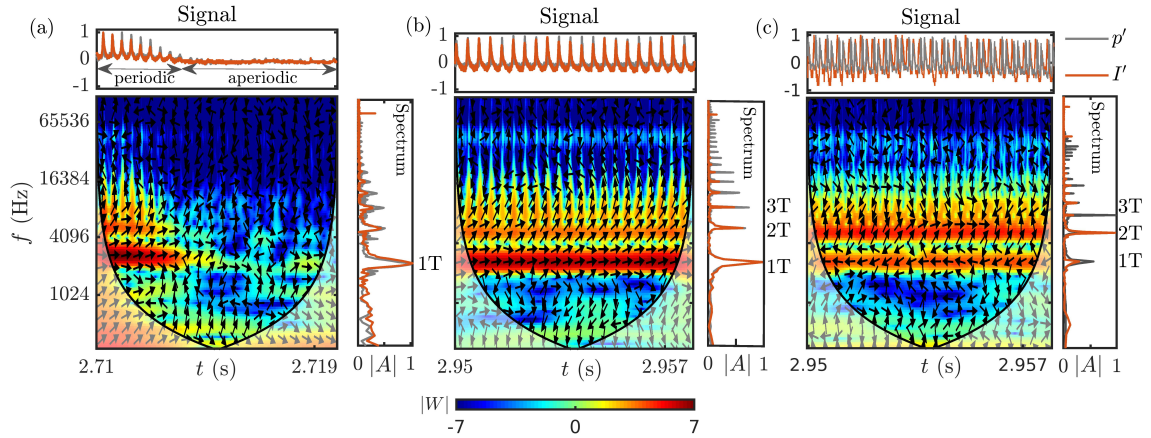
Fig. 5.3: The normalized time series of the acoustic pressure oscillations (p') and the CH* intensity oscillations (I') for (a) periodic to aperiodic transition observed during intermittency, and (b) thermoacoustic instability measured near the end wall, and (c) thermoacoustic instability near the center of the combustor. We also show the corresponding XWT and the normalized amplitude spectrum from FFT. PT-01 and PMT-01 are used in (a,b), while PT-02 and PMT-02 are used in (c). The orientation of the arrows in the XWT represent the relative phase angle between p' and I'. A statistically sufficient time interval of around 21 oscillation cycles is used to evaluate the XWT plots. Note that the frequency scale used is nonlinear.

us to identify lead-lag behavior. During thermoacoustic instability (Fig. 5.3b,c), the arrows are aligned at the same angle at the frequencies corresponding to the first few transverse modes. Near the end wall (Fig. 5.3b), during thermoacoustic instability, the arrows are nearly horizontal and pointing rightward for the 1T mode. This suggests the presence of in-phase synchronization between the p' and I' signals with a relative phase difference around $-6°$.

Near the center of the combustor (Fig. 5.3c), during thermoacoustic instability, we observe that the arrows are almost horizontal but point leftwards at the frequency corresponding to 1T mode. This indicates that the p' at the center of the combustor and the I' are anti-phase synchronized with a relative phase difference of 170°. Near the center of the combustor, we observe that the 2T mode is the most dominant followed by the 1T mode in the spectrum of I' (see spectrum in Fig. 5.3c). In the corresponding XWT plot, the arrows corresponding to the 2T mode are aligned at 45°. This indicates that I' near the center of the combustor leads p' and is driven by both the acoustic

velocity and pressure oscillations. The type of synchronization existing between p' and I' at both the locations in the combustor during thermoacoustic instability is detected using recurrence measures in Sec. 5.2.2.

In Fig. 5.3a, during periodic epochs of intermittency, the arrows are aligned at the same angle for the 1T mode. However, during the aperiodic epoch of intermittency (Fig. 5.3a), the arrows are almost randomly oriented in all directions, indicating desynchrony between p' and I' signals. Thus, both p' and I' signals are phase synchronized during thermoacoustic instability and are intermittently phase synchronized during intermittency. A similar synchronization transition to longitudinal thermoacoustic instability in a gas turbine type combustor was reported in Pawar *et al.* (2018).

Further, the amplitude spectra of p' and I' (shown on the right side of the each XWT in Fig. 5.3b,c) during thermoacoustic instability show the presence of several harmonics (up to 10T). However, the XWT of these signals (Fig. 5.3b,c) indicates that the spectral power in the common frequency bands gradually diminishes beyond the first few harmonics of the p' and I' signals.

We plot the approximate mode shapes for the first four transverse acoustic pressure modes in Fig. 5.4a. For the nth mode, its mode shape is calculated as $\cos(2\pi \frac{x}{W} n)$ with W being the width of the combustor. The presence of temperature and density gradients, shock wave, reactants and product species would significantly alter the mode shapes (Sujith *et al.*, 1995). In spite of these deficiencies, some features of the acoustic pressure mode shapes remain unchanged from Fig. 5.4a. The end wall region houses the acoustic pressure anti-node for all the transverse modes. Further, the inherent flow and geometric symmetry of the combustor will ensure transverse symmetry in temperature. Therefore, the location of the pressure node for the first transverse mode will remain approximately at the center of the combustor.

Using the XWT, we plot the variation of the mean of the relative phase ($\langle\phi\rangle_{p',I'}$) between p' and I' obtained near the end wall (Fig. 5.4b) and center (Fig. 5.4c) of the combustor
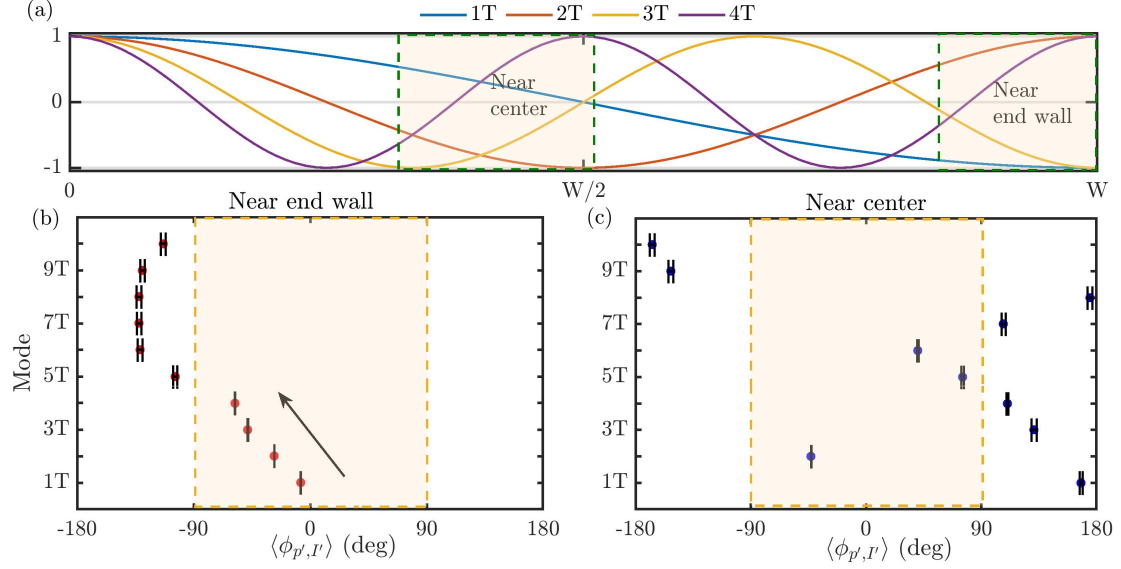
Fig. 5.4: (a) The mode shapes for the first four transverse acoustic pressure modes in the combustor. The mode shapes are derived from a cosine approximation. The mean relative phase ($\langle\phi\rangle_{p',I'}$) between the acoustic pressure and the CH* intensity oscillations for each transverse mode observed near the (b) end wall and (c) center of the combustor. The standard deviation of $\langle\phi\rangle_{p',I'}$ is captured by the span of the horizontal error bars.

for each of the first ten transverse modes. Close to the end wall, $\langle\phi\rangle_{p',I'}$ is close to zero (albeit with the I' leading p' slightly) for the 1T mode indicating the presence of strong coupling. However, beyond 1T mode, we observe a gradual change in $\langle\phi\rangle_{p',I'}$ from 0° to beyond 90°, denoting weaker coupling. For 2T to 4T modes, we observe that the I' leads p'. When the angle exceeds −90° (upward oriented arrows), we notice the absence of common power between these signals at those modes (see blue regions in Fig. 5.3b). This suggests that the two signals are desynchronized for harmonics greater than the 4T mode (see Fig. 5.4a).

The coupling behavior between p' and I' at the center of the combustor is different from that near the end wall, due to the presence of the pressure node at the center for the 1T mode (which is the dominant mode near end wall). We observe strongest coupling for the 2T mode for which $\langle\phi\rangle_{p',I'}$ is around 45° (Fig. 5.4c). High power in the 2T mode is attributed to the center of the combustor being a pressure antinode for the 2T mode (see Fig. 5.4a). For other modes, $\langle\phi\rangle_{p',I'}$ is far off from 0° and also the common spectral

power is diminished. Therefore, we observe a weaker coupling for these modes. From these observations, we can surmise that the higher harmonics in p' beyond the first few modes are solely due to the wave steepening effects (Saenger and Hudson, 1960; Chester, 1964) and do not arise from coupling between the acoustic and the heat release rate oscillations.

5.2.2 Recurrence analysis of acoustic pressure and CH* intensity oscillations

The temporal dynamics of a measured signal can be understood by tracking its recurrence in a certain neighborhood in the phase space (Marwan *et al.*, 2007). The recurrence plot (RP) allows one to visually identify the time instants at which the trajectory of the system visits roughly the same region in its phase space (Marwan *et al.*, 2007). The pattern in the RP enables us to categorize and quantify the temporal dynamics of chaotic, quasiperiodic, intermittent, periodic, and stochastic signals (Webber Jr and Marwan, 2015). We follow the same methodology described in Sec. 3.1.2 to construct the recurrence matrix (R_{ij}).

For the RPs in this chapter, we visualize values of one and zero by colored and white points, respectively. Thus, the RP is a two-dimensional arrangement of colored and white points that exhibits different patterns based on the underlying dynamics of the system. We reiterate that for a periodic signal of constant amplitude, we obtain uninterrupted equally spaced diagonal lines in the RP. For random signals, we obtain a grainy structure made up by isolated points in the RP. The different dynamical states during the transition to thermoacoustic instability have been distinguished for the same subscale rocket combustor in Chapter. 3.

Following the described methodology, we construct the RP for p' and I' to compare the dynamics during the state of thermoacoustic instability observed from both the locations in the combustor. We employ a threshold (ϵ_r) of 20% of the attractor size, and fix the embedding parameters (i.e., the embedding dimension and the time delay) appropriately for each signal. In Fig. 5.5a,b, we plot the RP for both p' and I' measured near the end
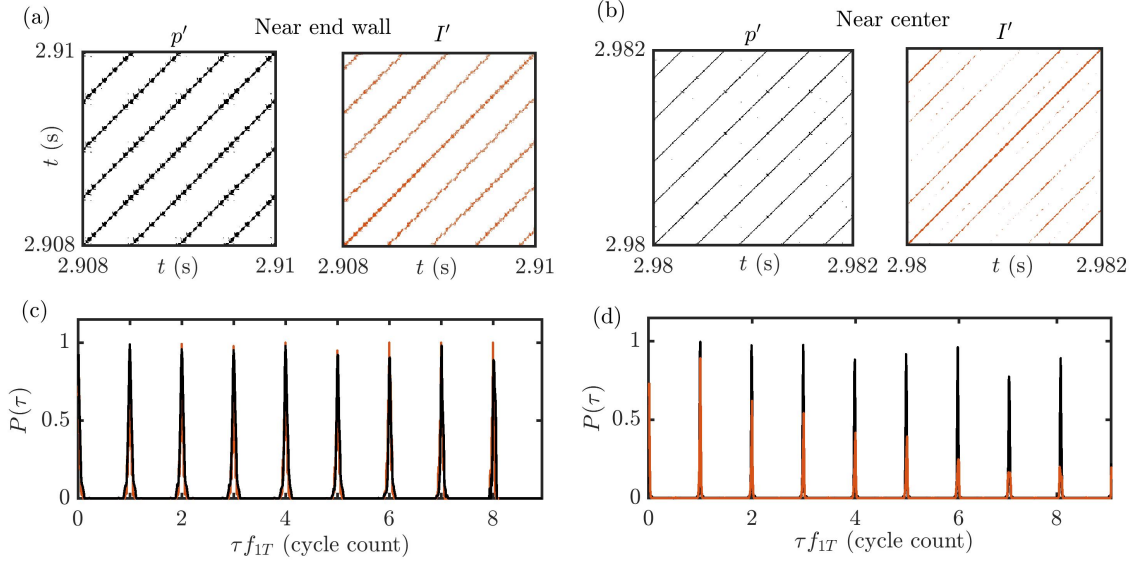
Fig. 5.5: The recurrence plots of the acoustic pressure (p') and CH* intensity fluctuations (I') during thermoacoustic instability near the (a) end wall and (b) center of the combustor. (c, d) The probability of recurrence $P(\tau)$ is plotted against τf_{1T} (i.e., the cycle count) for the end wall and center locations, respectively. The recurrence threshold is fixed as 20% of the attractor size for each case.

wall and center of the combustor, respectively. Near the end wall, the RPs of p' and I' during the state of thermoacoustic instability are nearly identical. Both the RPs are manifested by diagonal lines implying periodicity in the dynamics. Moreover, the RP of p' near the end wall features micropatterns over its diagonal lines as a result of the interplay between slow and fast timescales in the system (as described in Chapter. 4). Such micropatterns are not easily discernible in the RPs of p' and I' measurements near the center of the combustor. Compared to the RPs near the end wall, the RPs of p' and I' near the center of the combustor are not identical. The corresponding RPs can be distinguished by the broken diagonal lines in the RP of I' which are not seen in the RP of p'.

Next, we exploit the quantitative information on the recurrence of p' and I' signals to qualitatively assess their coupled behavior at both locations in the combustor. We compute the probability of recurrence $P(\tau)$ (Romano *et al.*, 2005) which measures the probability with which a trajectory in phase space ($\vec{x'}(t)$) revisits the same neighborhood

after a time lag τ and is given as,

$$P(\tau) = \frac{1}{n - (d-1)\tau_{opt}} \sum_{i=1}^{n-(d-1)\tau_{opt}} \Theta(\epsilon_r - \left\|\vec{x'}_i - \vec{x'}_{i+\tau}\right\|). \qquad (5.2)$$

$P(\tau)$ can be used to capture the type of synchronization existing between p' and I' oscillations from their recurrent behaviors. The type of synchronization is inferred based on the locking of the location of the peaks as well as their heights in the plots of $P(\tau)$ of p' and I' (Romano *et al.*, 2005).

Using $P(\tau)$, we can detect the presence of phase synchronization or generalized synchronization amongst the p' and I' signals. During phase synchronization, both the signals show a perfect locking in their instantaneous phases but their instantaneous amplitudes are uncorrelated (Romano *et al.*, 2005). During generalized synchronization, both the instantaneous phases and amplitudes of the signals are perfectly locked. Therefore, we can express the properties of both signals using a functional relationship (i.e., I' can be modeled as $f(p')$) (Romano *et al.*, 2005).

In Fig. 5.5c,d, we show the plots of $P(\tau)$ calculated for p' and I' as a function of the lag non-dimensionalized by the time period of the cycle (i.e., τf_{1T}) at both the locations near the end wall and the center of the combustor. Near the end wall, we observe that the locations and the heights of the peaks of $P(\tau)$ for both p' and I' coincide with each other and attain a value close to 1 periodically for each cycle of oscillation. However, near the center of the combustor, $P(\tau)$ of both p' and I' do not have identical heights of their peaks. Moreover, their $P(\tau)$ magnitudes gradually decay for increasing τ. Thus, all these observations in the RPs and the plots of $P(\tau)$ indicate that the dynamics of p' and I' near the end wall is in a state of generalized synchronization. However, near the center of the combustor, we observe a state of phase synchronization between the p' and I' signals. Here, both p' and I' are perfectly phase locked but exhibit a weak correlation between their amplitudes. Thus, the state of generalized synchronization represents a stronger synchronization than phase synchronization since the amplitudes lock to each

other in addition to the phase locking between the two signals (Romano *et al.*, 2005; Pawar *et al.*, 2017).

To summarize, we observe a transition from a state of desynchronization (during stable state) to intermittent phase synchronization (during intermittency) to phase synchronization (during thermoacoustic instability) in the coupled behavior between p' and I' near the center of the combustor. Due to the stronger coupling between the p' and I' near the end wall of the combustor, we observe generalized synchronization between them. From the mean relative phase information from the XWT plots, we inferred the individual contribution of each of the transverse modes to the coupling between p' and I' near the end wall and the center of the combustor. Near the end wall, the mean relative phase between p' and I' gradually changes from near in-phase for the 1T mode to out-of-phase for the 5T mode. However, near the center of the combustor, we do not observe any such discernible trend in the corresponding mean relative phase.

5.3 SPATIAL ANALYSIS OF THE JET FLAMES AND THEIR COUPLED INTERACTION WITH THE TRANSVERSE ACOUSTICS DURING THE TRANSITION TO THERMOACOUSTIC INSTABILITY

Next, we will study the spatiotemporal behavior of the jet flames observed at the two locations in the combustor during the stable state, intermittency, and thermoacoustic instability. The behavior of the jet flames near the center of the combustor during the stable state is represented by four representative instantaneous CH* chemiluminescence snapshots in Fig. 5.6. We observe that the jet flames propagate longitudinally in the direction of the flow. The three flames can be clearly distinguished from one another. Only the central flame is lifted off from the injector recess, while its neighboring flames are anchored to the injector recess. Moreover, the central flame has a shorter jet core and burns rapidly. As a result, we observe higher intensities in the central flame compared to its neighbors. The dynamics of the central lifted flame for low amplitude periodic oscillations during intermittency and high amplitude periodic oscillations

during thermoacoustic instability is discussed elaborately with the supporting schlieren images by Gejji *et al.* (2020).

5.3.1 Phase-averaged flame images during periodic epochs of intermittency and thermoacoustic instability

The flame behavior during the periodic epochs of intermittency and thermoacoustic instability at the two locations in the combustor are studied by adopting the method of phase averaging. In this method, only the images pertaining to the phase selected for each cycle of oscillations are averaged over 25 cycles. We cannot apply phase averaging during the stable state and for aperiodic epochs of intermittency since the phase for aperiodic oscillations cannot be properly defined. Four phase-averaged CH* chemiluminescence images during periodic parts of intermittency for the two locations in the combustor are shown in Fig. 5.7. The four phases (A - D) indicated over the pressure waveform in Fig. 5.7a are selected to describe the dynamic behavior of the jet flames.

During the periodic epochs of intermittency, at both the locations in the combustor (see Fig. 5.7c,d), we observe that all the jet flames exhibit higher intensities than that observed during the stable state (Fig. 5.6). Each jet core remains intact throughout the periodic oscillations observed during intermittency. As a result, the jet flames continue
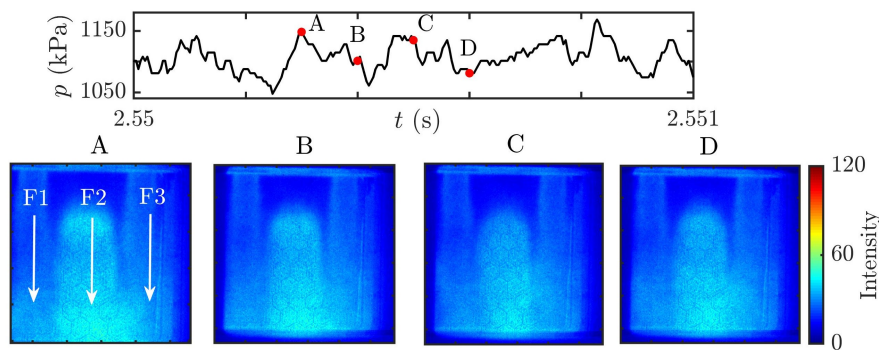
Fig. 5.6: Four representative snapshots of the three jet flames at the center of the combustor during stable state. Apart from the central flame, all other flames are anchored to the injector recess. The three flames are represented by arrows in the first instantaneous image (A).
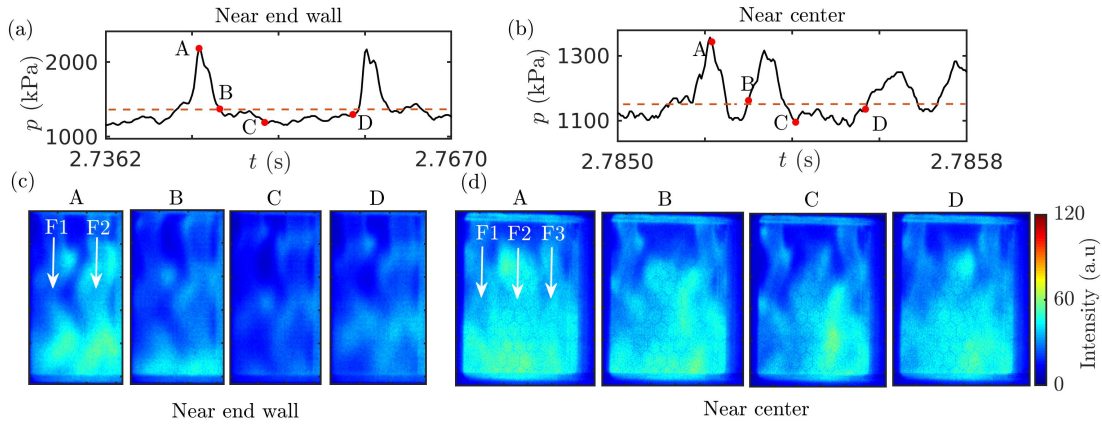
Fig. 5.7: Time series of pressure during intermittency at the (a) end wall (PT-01) and (b) the center of the combustor (PT-02). The four phases (A - D) at which the CH* chemiluminescence images are averaged are indicated over the time series. The phase-averaged images during intermittency near (c) the end wall and (d) the center of the combustor are shown. The flames visible through the optically accessible windows are marked in the phase averaged image (at A) for both the locations in the combustor.

to be distinguishable from each other. Compared to the near steady flames observed during stable state (see Fig. 5.6), we observe the presence of periodic transverse displacement of each jet flame during the periodic epochs of intermittency as the steep fronted shock wave sweeps through it. Therefore, we observe that each jet flame exhibits substantial asymmetric oscillations due to the asymmetric vortex shedding from the gaps between the neighboring injector recesses (Gejji *et al.*, 2020).

Comparing the phase-averaged images during periodic epoch of intermittency near the end wall (Fig. 5.7c) and center (Fig. 5.7d) of the combustor, we observe that the jet flames near the end wall exhibit higher intensities when the passage of the shock wave coincides with the peak pressure (captured by phase at A). The jet flames near the end wall exhibit their minimum intensity at pressure minima (captured by phase at C) during which the shock wave is far away from the optical window. The images corresponding to phases - B and D show intermediate flame intensities. In contrast to the behavior at the end wall, the shock wave passes through the center of the combustor twice for each reflection off the end wall (Harvazinski *et al.*, 2019). Furthermore, the 2T mode is dominant in the center of the combustor, as evidenced from the XWT plot in Fig. 5.3c.
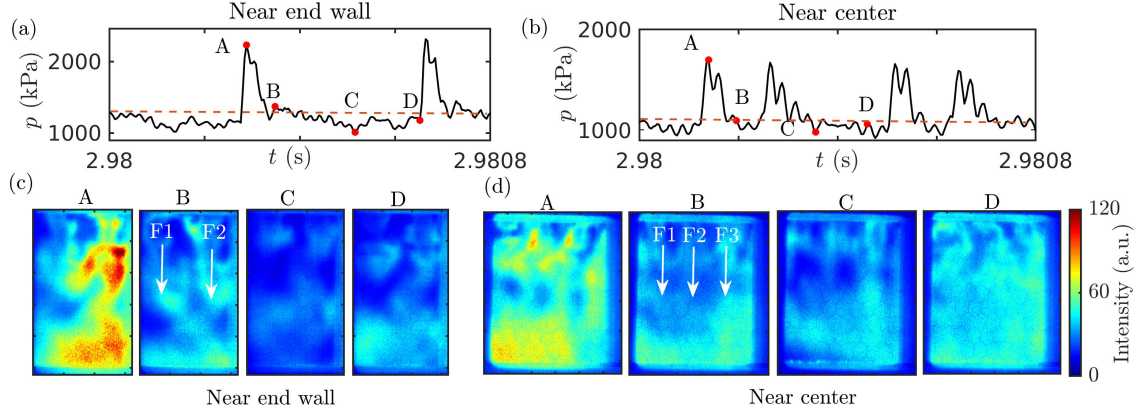
Fig. 5.8: Time series of pressure during thermoacoustic instability at the (a) end wall (PT-01) and (b) the center of the combustor (PT-02). The four phases (A - D) at which the CH* chemiluminescence images are indicated over the time series. The phase-averaged images during thermoacoustic instability near (c) the end wall and (d) the center of the combustor are shown. The flames visible through the optically accessible windows are marked in the phase averaged image (at B) for both the locations in the combustor.

As a result, the jet flames near the center of the combustor during the periodic part of intermittency exhibit nearly the same intensities for the four phases considered. We also observe that the central jet flame (indicated as F2 in Fig. 5.7d) continues to be lifted off during intermittency.

In a similar manner, we present the phase-averaged images during thermoacoustic instability at the four phases indicated over the acoustic pressure signal for both the locations in the combustor in Fig. 5.8a,b. Here, we observe significantly higher intensities coinciding with the local pressure maxima (phase A) at both the end wall (Fig. 5.8c) and the center (Fig. 5.8d) of the combustor. Equivalently, the intensities are at their lowest during the pressure minima (phase C). Due to the large transverse oscillations during this state, we observe that the jet cores are no more intact and the jet flames can no more be distinguished from its neighbors. As the shock wave passes through the jet flame, it imparts a large transverse displacement and substantially displaces the jet core, and momentarily results in a spike in the local heat release rate. This spike can be identified from the high intensities observed in the longitudinal location where the jet flames impinge on the end wall (phase - A in Fig. 5.8c). After

117

the shock wave passes through the jet flame, there is a longer relaxation period (phases - B to D). This longer interval allows the fuel and oxidizer to mix and the jet core to regain its original shape. Harvazinski et al. (Harvazinski *et al.*, 2019) performed hybrid LES/RANS simulations based on the same combustor and operating conditions. From the spatial distribution of methane mass fraction, they found large amounts of methane trapped around the end wall injectors during thermoacoustic instability. The passage of the shock wave rapidly combusts these accumulated reactants, resulting in the enhanced burn rate.

As opposed to the flame behavior near the end wall, the continued presence of hot combustion products at the center of the combustor sustains a higher temperature. As a result, there is no excess reactant mixture to be burnt and the jet flames near the center (Fig. 5.8c) are less intense compared to those near the end wall. Moreover, during thermoacoustic instability, the jet flames which are compact near the injector spread out at the downstream locations. Eventually, the propellants auto-ignite leading to higher heat release rate, well downstream of the injector (Gejji *et al.*, 2020).

Thus, during the transition from the stable state to thermoacoustic instability via intermittency, the jet flames exhibit a transition from low intensities to high intensities. This transition is accompanied by a change from a nearly steady longitudinally propagating jet flame during the stable state to a highly unsteady jet flame with significant transverse motion during thermoacoustic instability. The jet flames which are distinct during the periodic part of intermittency exhibit large transverse oscillations during thermoacoustic instability. This results in merging of neighboring jet flames rendering each jet flame indistinguishable from its neighbors. We also established that the jet flames near the end wall exhibit high intensities during the periodic epochs of intermittency and thermoacoustic instability compared to that near the center of the combustor. This difference in the flame behavior across the combustor is attributed to the combination of the end wall housing the pressure antinode and the enhanced combustion from the accumulated unburnt reactants near the end wall.
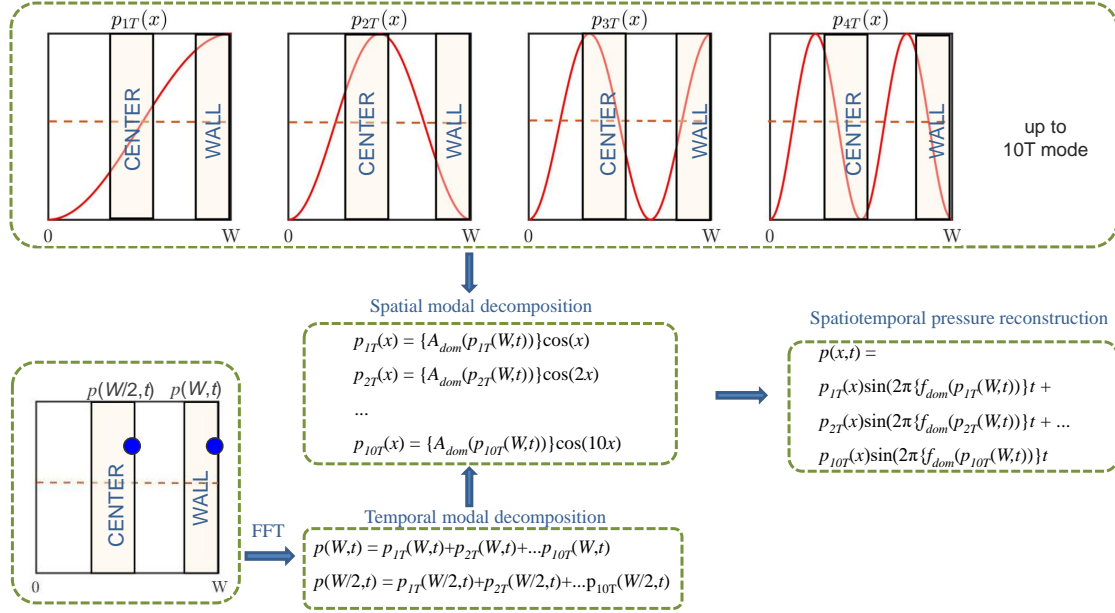
Fig. 5.9: Flowchart of spatiotemporal pressure reconstruction based on spatial (only transverse direction) and temporal modal decomposition. The optically accessible windows at the center and end wall of the combustor are shaded for reference. The location of pressure measurements at both these locations are shown using blue circles. Functions f_{dom} and A_{dom} computes the dominant frequency and its corresponding amplitude, respectively.

5.4 ACOUSTIC POWER SOURCES AND SINKS USING LOCAL RAYLEIGH INDEX

Thermoacoustic driving and damping in the combustor can be better understood in terms of acoustic power sources and sinks. The local Rayleigh index (RI) is a measure which quantifies the local thermoacoustic driving/damping over a spatial domain (Culick *et al.*, 2012). Since our combustor is receptive to several transverse acoustic modes, we compute the RI for each transverse mode. We define the RI_{nT} for each mode as,

$$RI_{nT} = \frac{1}{TP} \int_0^{TP} \frac{p'_{nT}(\vec{x},t)I'_{nT}(\vec{x},t)dt}{\overline{p}_{nT}(\vec{x},t)\overline{I}_{nT}(\vec{x},t)} \tag{5.3}$$

Here, TP is the time period of acoustic pressure oscillation, nT is the nth transverse mode and $\vec{x}$ refers to the location in the two dimensional space of the combustor. The mean of a variable is denoted by overline.

119

The requirement of an unambiguous time period allows us to compute RI_{nT} only during the state of thermoacoustic instability. The local Rayleigh index will allow us to estimate the acoustic driving from each transverse mode in the combustor. However, we need the spatiotemporal pressure and heat release rate variation for each mode. Since the pressure is measured only at specific locations at the center and right side end wall of the combustor (see Fig. 2.1a), we extract the pressure variation over time and the transverse direction using a spatial and temporal modal decomposition, as depicted in the flowchart shown in Fig. 5.9.

The local CH* intensity oscillations (representative of local heat release rate oscillations) are decomposed into the individual modes by performing FFT of the CH* chemiluminescence images at each spatial location (i.e., at each pixel). Then, the Rayleigh index for each mode (RI_{nT}) is computed over a time interval of 25 cycles of oscillations during thermoacoustic instability. The spatial distribution of RI_{nT} at both the locations considered are presented in Fig. 5.10. Only the first five acoustic modes are selected since only these modes exhibit significant coupling behavior (as confirmed by the XWT plots in Fig. 5.3).

Near the end wall (Fig. 5.10a), we do not observe any significant contribution to acoustic driving beyond the first two modes. We do not observe sufficiently strong acoustic power sources (i.e., $RI \sim 0$) corresponding to the higher harmonics since these modes are largely out of phase with I' as seen in Fig. 5.4b,c. For the 1T and 2T modes, almost the entire window has a uniform distribution of acoustic power sources. Moreover, the distribution of RI_{1T} indicates that the 1T mode provides the highest contribution to acoustic power. Earlier, from Fig. 5.4b, we had seen that only the first two modes have $\langle \phi \rangle_{p',I'}$ close to $0°$.

From Fig. 5.10b, we see that the region near the center derives most of its acoustic power from the 2T mode. We had established that $\langle \phi \rangle_{p',I'}$ at the center of the combustor is closest to $0°$ only for the 2T mode (Fig. 5.4d). In fact, the 1T mode actually houses strong acoustic power sinks that counter the acoustic power contribution from the other
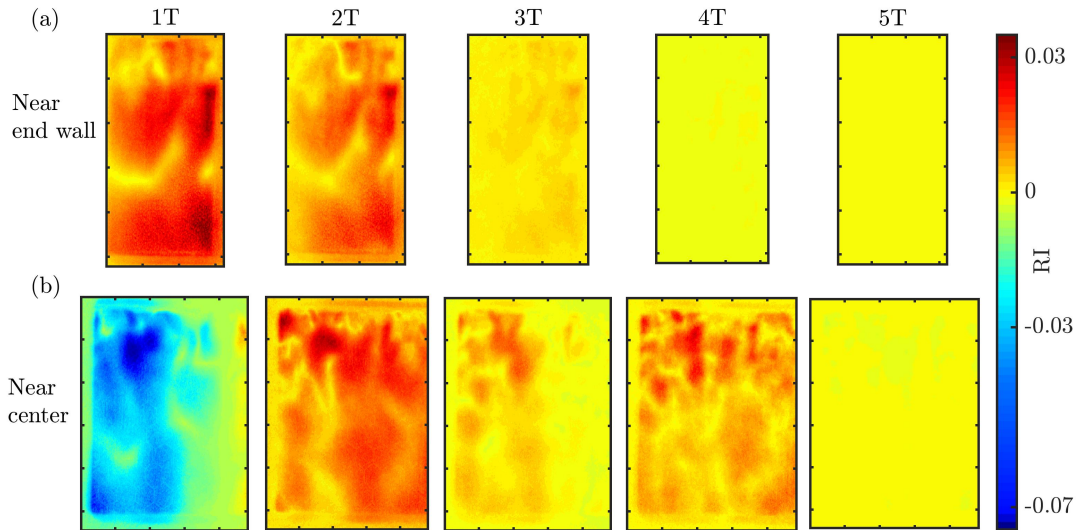
Fig. 5.10: The spatial distribution of Rayleigh index (RI) is plotted for the first five transverse acoustic modes for near (a) end wall and (b) the center of the combustor during thermoacoustic instability.

harmonics. The damping effect of 1T mode at the center is supported by the anti-phase coupling between p' and I' (see Fig. 5.4d). It is interesting to note that the regions occupied by the jet flames offset from the central jet flame in this window has the strongest acoustic sinks (see blue regions in the distribution corresponding to 1T mode in Fig. 5.10b). The cumulative effect of the contribution of acoustic power sources/sinks from the 1T to 4T acoustic modes is reflected in the weak coupling near the center of the combustor. For thermoacoustic oscillations exhibiting numerous harmonics, we believe this procedure would be useful to quantify the acoustic power sources/sinks from each acoustic mode.

5.5 RECURRENCE QUANTIFICATION ANALYSIS OF LOCAL CH* INTENSITY OSCILLATIONS

Next, we perform a recurrence analysis on the local CH* intensity oscillations observed at both spatial locations of the combustor. Such an analysis would reveal temporal features about the CH* intensity oscillations, and enable a comparison of the flame dynamics at the two spatial locations. Towards this purpose, we use determinism
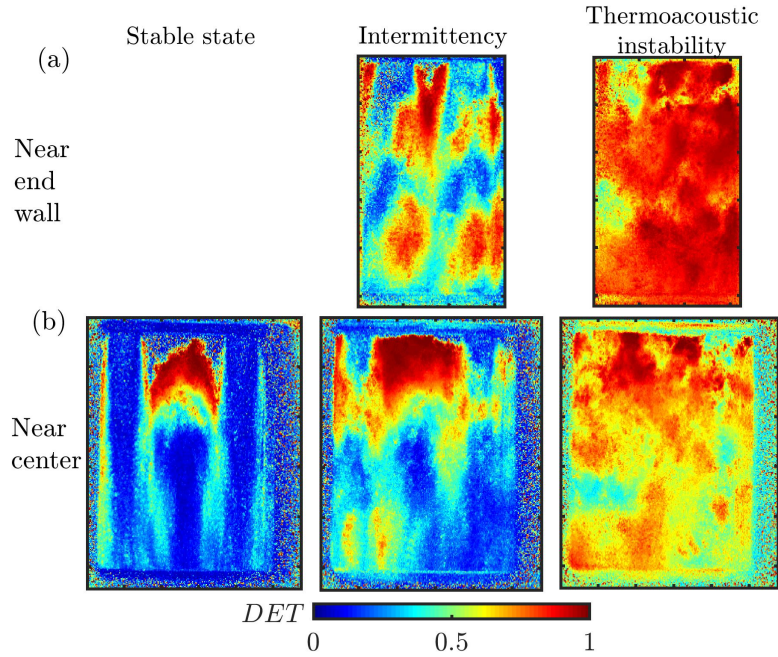
Fig. 5.11: The spatial distributions of DET for the local CH* intensity oscillations measured near the (a) end wall and (b) center of the combustor are plotted for stable state, intermittency, and thermoacoustic instability. A recurrence threshold of 20% of the attractor size is used to estimate the recurrence measures. Note that stable state is not observed near the end wall of the combustor.

(DET) which quantifies the predictability of CH* intensity oscillation acquired at a given spatial location. We compute DET following Eq. 3.4 in Chapter. 3. A purely uncorrelated stochastic signal would have DET extremely close to 0, while a completely deterministic (correlated) signal would have DET = 1. A high value of DET approaching 1 is indicative of a well-correlated dynamics which can be found in either perfectly periodic and quasiperiodic systems (Zou *et al.*, 2010). All other signals exhibit DET values between 0 and 1. Hence, DET can be used to distinguish the stochastic or deterministic nature of the signal (Marwan *et al.*, 2007).

In Fig. 5.11, we show the spatial distribution of DET for the different dynamical states observed in the combustor. Here, we evaluate DET considering the time series of CH* intensity oscillations obtained from each pixel within the image. From Fig. 5.11, we observe that the overall spatial distribution of high values of DET increases as the dynamics evolves from the stable state to thermoacoustic instability. During the stable

state, we observe low DET for the spatial locations occupied by the jet cores and higher DET values at the flame edges. This high value of DET arises from the correlated nature of the vortex shedding dynamics along the flame surface. For the central lifted flame (Fig. 5.11b), we observe that the region between the recess and the flame tip has a very high DET, indicating the presence of deterministic fluctuations in the flame anchoring region. Such deterministic behavior in the local CH* intensity oscillations in the central lifted flame is not easily apparent from the raw CH* chemiluminescence images. During intermittency, with the advent of transverse oscillations, the jet flames get displaced laterally. Correspondingly, we observe patches of high values of DET spread over the window. The locations occupied by the flame just after the entry to the combustor exhibits high DET at both the center and the end wall. Further, we obtain high DET values at locations exhibiting large CH* intensity oscillations near the end wall (see Fig. 5.7c). As the dynamics transition to thermoacoustic instability, the jet flames are no more intact and spread over the entire window (see Fig. 5.8c,d). Consequently, almost the entire region near the end wall exhibits DET close to 1, indicating widespread periodicity in the local CH* intensity oscillations. Compared to the end wall (Fig. 5.11a), the DET near the center (Fig. 5.11b) varies from 0.5 to 1. This indicates that the CH* intensity oscillations and, in turn, the heat release rate oscillations during thermoacoustic instability are more deterministic near the end wall than that near the center of the combustor.

Thus, the spatial distribution of DET is able to capture the deterministic features present in the dynamics of local heat release rate oscillations during each dynamical state. Regions exhibiting high/low DET during thermoacoustic instability at the end wall of the combustor coincide with those of high/low RI_{1T}, respectively (see the corresponding distribution in Fig. 5.10a). However, this qualitative similarity in the distributions of DET and RI_{2T} is not seen at the center of the combustor.

From this spatial analysis, we have shown that the dynamics of local CH* intensity oscillations change drastically during the transition from the stable state to intermittency

to thermoacoustic instability. Specifically during thermoacoustic instability, the oscillating jet flames in conjunction with the shock wave alters the distribution of the local CH* intensity oscillations in a significantly different manner at the end wall compared to the center of the combustor. Furthermore, we showed that contribution of local CH* intensity fluctuations in driving unstable acoustic modes during thermoacoustic instability is significantly dependent on the location within the combustor.

5.6 CONCLUDING REMARKS

In this chapter, we analyzed the coupled interaction between the acoustic pressure oscillations (p') and the CH* intensity oscillations (I') in the presence of self-excited transverse thermoacoustic oscillations developed in a multi-element rocket combustor. Specifically, we compared the coupled behavior of these oscillations in the center and the end wall regions of the combustor. During the transition to thermoacoustic instability, we observe a synchronization transition in the coupled behavior of p' and I' oscillations. These oscillations which are desynchronized during stable state and aperiodic epochs of intermittency become phase synchronized during periodic epochs of intermittency. During the state of thermoacoustic instability, we also find that p' and I' exhibit phase synchronization at the center of the combustor and generalized synchronization near the end wall of the combustor. From the increasing trend of the relative mean phase between the modes of p' and I', we discern that only the first few modes contribute to the coupling between the p' and I' oscillations. The higher harmonics seen in the spectrum of p' arise from the nonlinear wave steepening effect and do not contribute to the coupling between p' and I'.

Performing a spatial analysis, we found that the local CH* intensity oscillations near the end wall are higher compared to that near the center of the combustor. This difference in the flame behavior is ascribed to a combination of the presence of pressure antinode and spike in heat release rate due to rapid reaction resulting from wall impingement of

premixed pockets of reactants. From the spatial distribution of the Rayleigh index, the contribution of each transverse mode to the generation of acoustic driving is computed during thermoacoustic instability. The superior acoustic driving from the 1T mode near the end wall and the 2T mode near the center of the combustor is revealed. Using recurrence quantification analysis of the local CH* intensity oscillations, we quantified the transition from stochasticity to widespread determinism in the local CH* intensity oscillations during the onset of thermoacoustic instability. We also found that the local CH* intensity oscillations near the end wall are more deterministic (correlated) compared to the center of the combustor during thermoacoustic instability.

CHAPTER 6

Quantifying coherence in the flame intensity oscillations using correlation networks

Understanding the flame dynamics in conjunction with the acoustic pressure oscillations forms the fundamental part of understanding the driving processes in rocket combustors. (Harrje and Reardon, 1972; Anderson and Yang, 1995; Urbano *et al.*, 2017; Hardi *et al.*, 2014*a*). The jet flame dynamics is controlled by the local acoustic perturbations, turbulent flow, non-premixed combustion, hydrodynamic instabilities, and the geometry of the combustor. Since coherent flame oscillations can generate and sustain thermoacoustic instability (Lieuwen, 2012; Karmarkar *et al.*, 2021), it is of utmost importance to characterize the coherence in the flame oscillations. Therefore, the heat release rate oscillations can be separated into two components: coherent and incoherent fluctuations (Lieuwen, 2012).

A jet flame usually exhibits intrinsic incoherent oscillations in response to the turbulent flow fluctuations (Lieuwen, 2012). Based on the flame density ratio, the jet flame may exhibit coherent oscillations (Emerson *et al.*, 2012). Further, when the jet flames are sensitive to the local transverse acoustic pressure and acoustic velocity fluctuations, they are laterally displaced and oscillate vigorously (Oschwald and Knapp, 2009; Sliphorst *et al.*, 2011; Morgan *et al.*, 2015). In a rocket combustor susceptible to transverse thermoacoustic instability, the neighboring jet flames might merge and even exhibit strong collective interaction (Rey *et al.*, 2004). Such flame-flame interactions have been proposed to be a possible driving mechanism for thermoacoustic instability (Richecoeur *et al.*, 2006; Armbruster *et al.*, 2021). Furthermore, the presence of atomization, vortex shedding, shear layers, coherent structures, and shock waves in the flow field imparts heterogeneity to the local flame dynamics. Therefore, the jet flame dynamics in a

rocket combustor is heavily influenced by the nonlinear interactions between acoustic, combustion and fluid mechanic processes.

Inspired by the advances in thermoacoustics using complex network theory (see Sec.1.6.2), in this chapter, we construct positively and negatively correlated spatial networks to identify different regions of coherent and incoherent heat release rate oscillations in the turbulent reactive flow field of the 2D subscale rocket combustor during the onset of thermoacoustic instability. First, we describe the methodology behind network construction in Sec. 6.1. Then, using the network measures described in Sec. 6.2, we quantify the extent of coherence and incoherence in the flame intensity oscillations at different regions in the combustor in the remainder of the chapter.

6.1 METHODOLOGY OF CORRELATED SPATIAL NETWORK CONSTRUCTION

In the network, each spatial location (i.e., each pixel) in the region of interest is considered as a node. The interactions between any two nodes is captured by the links connecting them. To quantify the interaction between two such nodes, various measures such as Pearson correlation, average mutual information, and event synchronization between two time series have been used to construct relevant spatial networks (Zou *et al.*, 2018).

Here, we construct weighted networks based on the Pearson correlation (Eq. (6.1)) between the time series of intensity fluctuations obtained from the CH* chemiluminescence images acquired near the end wall of the combustor. Pearson correlation (R_p) is a linear measure computed between two time series. A positive R_p suggests that the two time series increase and decrease together, whereas a negative R_p indicates that one time series increases while the other decreases and vice versa. The case of $R_p = 0$ means that there is no linear relationship between the two time series over the time interval considered. In Eq. (6.1), x_i^t and x_j^t are the elements of the two time series at their corresponding grid points whose arithmetic mean is given by $\bar{x}_i$ and

$\bar{x}_j$, respectively.

$$R_p(i,j) = \frac{\sum_{t=1}^n \left(x_i^t - \bar{x}_i\right)\left(x_j^t - \bar{x}_j\right)}{\sqrt{\sum_{t=1}^n \left(x_i^t - \bar{x}_i\right)^2}\sqrt{\sum_{i=1}^t \left(x_j^t - \bar{x}_j\right)^2}}. \qquad (6.1)$$

Here, n is the total number of time instants used to evaluate the time-averaged correlation (R_p). We have a total of $N = 9828$ (126 px $\times$ 78 px) nodes with $i, j \in [0, N]$. We compute the pairwise correlation values (R_p) for all the nodes and encapsulate this information in a correlation matrix of size $N \times N$. Then, we construct positively ($R_p > 0$) and negatively ($R_p < 0$) correlated weighted networks from the correlation matrix made up of R_p for all pairwise combinations of the available spatial locations. For the positively correlated network, we set all negative correlation coefficients to zero. While analyzing the negatively correlated network, we set all positive correlation coefficients to zero and then, take the absolute value of the correlation matrix to obtain the negatively correlated network. Then, we can proceed to set the appropriate positive threshold (ϵ) to disregard weaker correlations and build the relevant adjacency matrix. The rationale behind the selection of ϵ followed in this chapter is described in Sec. 6.4.

The adjacency matrix, A_{ij} ($N \times N$) encodes the connections between all the grid points in the network. Two nodes, i and j, are connected and $R_p(i, j)$ is assigned as the corresponding weight (W_{ij}) of their link, only when $R_p(i, j)$ exceeds a predefined threshold, ϵ. The positively (A_{ij}^+) and negatively (A_{ij}^-) correlated adjacency matrices are generated following Eq. (6.2). We do not consider self-connections rendering $A_{ii} = 0$. In this manner, we construct a spatial network for each of the dynamical states observed in the combustor.

$$A_{ij}^{+} = \begin{cases} W_{ij} = R_p(i,j), & \text{if } R_p(i,j) \geq \epsilon \\ W_{ij} = 0, & \text{otherwise.} \end{cases} \qquad (6.2.1)$$

$$A_{ij}^{-} = \begin{cases} W_{ij} = -R_p(i,j), & \text{if } -R_p(i,j) \geq \epsilon \\ W_{ij} = 0, & \text{otherwise.} \end{cases} \qquad (6.2.2)$$

6.2 NETWORK MEASURES TO QUANTIFY THE SPATIAL DYNAMICS FOR EACH DYNAMICAL STATE

We use network measures such as degree, node strength, and average nearest neighbors' degree, to compare the topology of networks for each dynamical state. The degree, k_i (Eq. (6.3)), quantifies the number of grid points (nodes) connected to a particular grid point i in the network (Barabási *et al.*, 2016).

$$k_i = nnz(A_{ij}). \qquad (6.3)$$

Here, the nnz function counts the number of non-zero elements present in each row in the adjacency matrix. The degree distribution, $P(k)$ versus k, represents the probability that a node in a network has degree k. If n_k represents the number of nodes having degree k, $P(k)$ is defined as $P(k) = n_k/N$.

The node strength s_i for a node i, captures the sum of the weights of all its links.

$$s_i = \sum_{j \in N} W_{ij}. \qquad (6.4)$$

Both k_i and s_i quantify the relative importance of node i in the network. However, s distinguishes nodes based on the weight of the links, rather than on the number of links. The behavior of a node can be significantly influenced by its spatial location. The interactions amongst neighboring nodes result in degree correlations in the network. To

probe the presence of degree correlations, it is important to analyze the neighbors of a node. We quantify the effect of neighboring nodes by the average degree of the nearest neighbors (Barrat *et al.*, 2005) of a node i, which is evaluated as,

$$k_{nn,i} = \frac{1}{k_i} \sum_{j \in \nu(i)} k_j. \qquad (6.5)$$

Here, ν_i covers only the nearest neighbors (nn) of the node i. Then, the degree correlation function ($k_{nn}(k)$) is evaluated from k_{nn} as,

$$k_{nn}(k) = \sum_{k'} k' P(k'|k), \qquad (6.6)$$

where $P(k'|k)$ is the conditional probability that a k-degree node is connected to a k'-degree node (Barabási *et al.*, 2016). Thus, $k_{nn}(k)$ is the average degree of the neighbors of all k-degree nodes.

The variation of $k_{nn}(k)$ with k unearths correlations between the neighbors (Newman, 2002). An increasing trend of $k_{nn}(k)$ is termed as assortative and suggests that high degree nodes tend to be surrounded by other high degree nodes. In simple words, it quantifies the 'rich gets richer' effect (Barabási *et al.*, 2016). In contrast, a decreasing trend is termed as disassortative (Barabási *et al.*, 2016). Networks exhibiting no clear distinguishable trend in the distribution of $k_{nn}(k)$ are called neutral networks (Barabási *et al.*, 2016). Using the aforementioned measures, we characterize the spatial weighted positively and negatively correlated networks during the onset of thermoacoustic instability.

Since the acoustic pressure and heat release rate oscillations are the highest, we are interested in the flame dynamics near the wall. As a result, we analyze the CH* intensity oscillations emanating from the two turbulent jet flames located towards one end of the combustor through an optically accessible window.

6.3 JET FLAME RESPONSE TO TRANSVERSE ACOUSTIC OSCILLATIONS ALONG THE LONGITUDINAL DIRECTION

It is well-known from past studies that a flame in the presence of transverse thermoacoustic oscillations respond differently than that observed for the longitudinal oscillations (O'Connor *et al.*, 2015). In this combustor, the turbulent jet flames are largely in the longitudinal direction and are susceptible to transverse velocity perturbations whenever an acoustic wave passes through them. Hence, it is interesting to examine the response of the flames to self-excited transverse oscillations in the longitudinal direction.
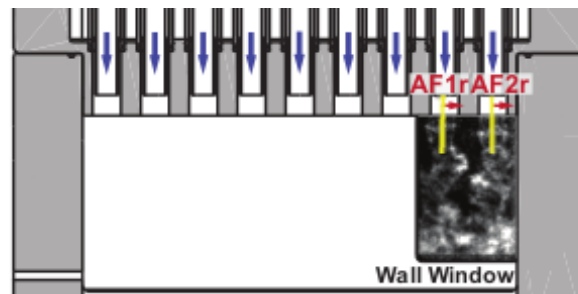
Fig. 6.1: The selected portion of the jet flame (i.e., half of the width of the jet flame) overlaid on the representative CH* chemiluminescence image obtained from the end wall window.

Across the width of the jet flame, a varicose or sinuous mode of the jet flame would exhibit in-phase or out-of-phase oscillations, respectively, in the flame intensity fluctuations obtained from both halves of the jet flame. We found that each jet flame exhibits sinuous oscillations. When we select the entire width of the jet flame for the local flame intensity calculations, we were not able to make this distinction between the oscillatory motion of the flame due to superposition effects along both halves of the jet flame. Hence, we selected just a half of the jet flame (see Fig. 6.1) to detect the type of vortex shedding (sinuous or varicose) exhibited by the flame front. The time series of the local flame intensity fluctuations is obtained by summing up the flame intensities at each pixel across half-width of the jet flame for the right half of left jet flame (AF1r) and right half of right jet flame (AF2r) as shown in Fig. 6.1.
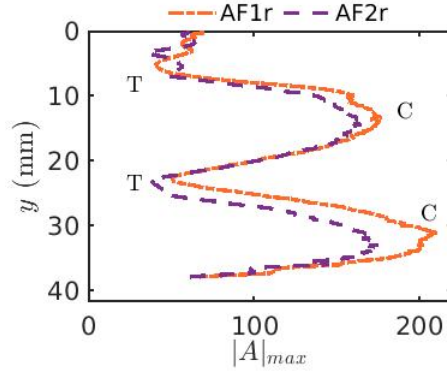
Fig. 6.2: The flame response along the longitudinal direction characterized by the amplitude of dominant mode of the oscillations of pixel intensities summed across the transverse direction for the half width of the left flame (AF1r) and right flame (AF2r). The crests and troughs in the flame response are indicated with C and T respectively.

In Fig. 6.2, we plot the variation of the amplitude of the dominant mode of the local flame intensity oscillations obtained from the half-width of the flame in the longitudinal direction (see Fig. 6.1). From Fig. 6.2, we observe that the spectral amplitude of the dominant mode through FFT of such local flame intensity fluctuations shows oscillatory response with the presence of multiple crests (C) and troughs (T) along the flame length. Such an oscillatory response of the flame is a combined result of the globally unstable nature of the preheated reacting flow-field (Suresha *et al.*, 2016) in the presence of transverse acoustic field in the combustor. Near the injector, the flame response is controlled by flame anchoring while at the downstream locations, the flame response is largely controlled by the dissipation of vortical disturbances and other secondary flows along the boundary of the flame surfaces (Shanbhogue *et al.*, 2009). Thus, each flame exhibits varying dominant amplitudes along its length.

We notice a similar response for the AF1r and AF2r jet flames with two crests. The first crest in the flame responses occurs around 14 mm downstream of the injector head. In addition to the flame anchoring effects, the flame response at this location is supplemented from the strong interactions from the transverse acoustic wave and the neighboring sides of the flames through merging effects, and the resulting impingement with the wall. The flame which is compact near the injector spreads out at the

downstream locations. This leads to enhanced mixing and subsequently higher flame intensities. Conversely, the second crest around 32 mm downstream of the injector is a consequence of the secondary flows caused by vortical dissipation along the flame surfaces leading to better mixing and autoignition of propellants (Blacker, 2019). Downstream of the second crest, boundary effects of the converging nozzle section dominate (Gejji *et al.*, 2019). Thus, the response of the flame to transverse acoustic perturbations is non-uniform along the longitudinal direction of the combustor.

Next, we will evaluate the correlation between all the node pairs and build suitable weighted networks to study the coherence in the flame intensity oscillations.

6.4   COHERENCE IN THE FLAME INTENSITY OSCILLATIONS

The extent of coherence (or incoherence) present in the flame intensity oscillations is quantified by the Pearson correlation (see Eq. (6.1)). It is necessary to know the range of correlation values computed between the pairwise local intensity oscillations (i.e., node pairs) before network construction. With this aim, the empirical probability distribution of the correlation values, $P(R_p)$, observed for each dynamical state is presented in Fig. 6.3. During both the dynamical states, the range of values spanning positive correlation is wider than that of negative correlation. This observation suggests that most of the node pairs are positively correlated in the dynamics of flame intensity oscillations. The magnitude of the mean correlation increases from 0.25 during intermittency to 0.46 during thermoacoustic instability.

The distribution of the correlation values changes its form from a unimodal distribution (with peak R_p at 0.18) during intermittency to a bimodal distribution during thermoacoustic instability. We obtain a bimodal distribution (with two R_p peaks at 0.38 and 0.68) during thermoacoustic instability since the jet flames responds both to the incident and reflected shock wave for each cycle.

Since the selection of a suitable correlation threshold is non-trivial, we compute the positively and negatively correlated networks for different correlation thresholds (ϵ) to
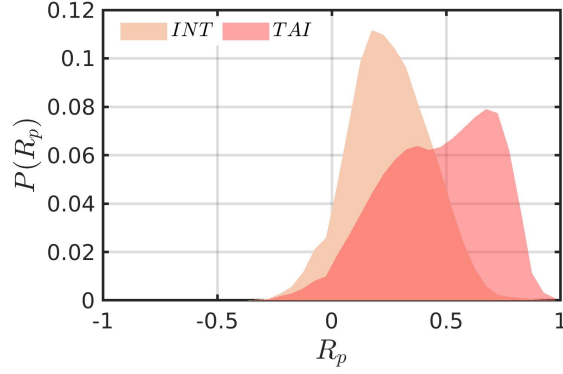
Fig. 6.3: Empirical probability distribution of correlation values observed during intermittency (INT) and thermoacoustic instability (TAI). The mean of the distribution increases during the transition to thermoacoustic instability indicative of the emergence of more coherent flame intensity oscillations.

understand the varying levels of coherence in the flame intensity oscillations.

Selecting $\epsilon = 0$ would allow us to examine either the effect of all positive or negative correlations for the positively or negatively correlated networks, respectively. Successive increments in ϵ would remove the weak correlations and reveal the effect of strong correlations in the dynamics of flame intensity oscillations in the combustor.

Next, we study the effect of short-range and long-range links on the extent of positive and negative correlations. In Fig. 6.4, we show all possible link weights (W_{ij}) for each Euclidean distance of the link (D_{ij}) during each dynamical state for the positively and negatively correlated networks. This plot reveals all the possible W_{ij} for a given D_{ij}. Hence, W_{ij} is multi-valued for a given D_{ij}. At this point, we reiterate that there are no self-connections and therefore, for all $D_{ij} = 0$, $W_{ij} = 0$.

At the outset, we observe that the distributions of W_{ij} are similar during both intermittency and thermoacoustic instability. From the plots for the positively correlated network (Fig. 6.4a,b), we observe that the highest W_{ij} belong to the links connecting the nearest neighbors (i.e., the smallest D_{ij}). The presence of high W_{ij} at lower D_{ij} indicates strong local interactions resulting in higher correlation amongst nodes over a neighborhood. Interestingly, during thermoacoustic instability, we observe high values of W_{ij} that are greater than 0.8, even at larger D_{ij}. This observation suggests the presence of long-range widespread interactions amongst different local regions near
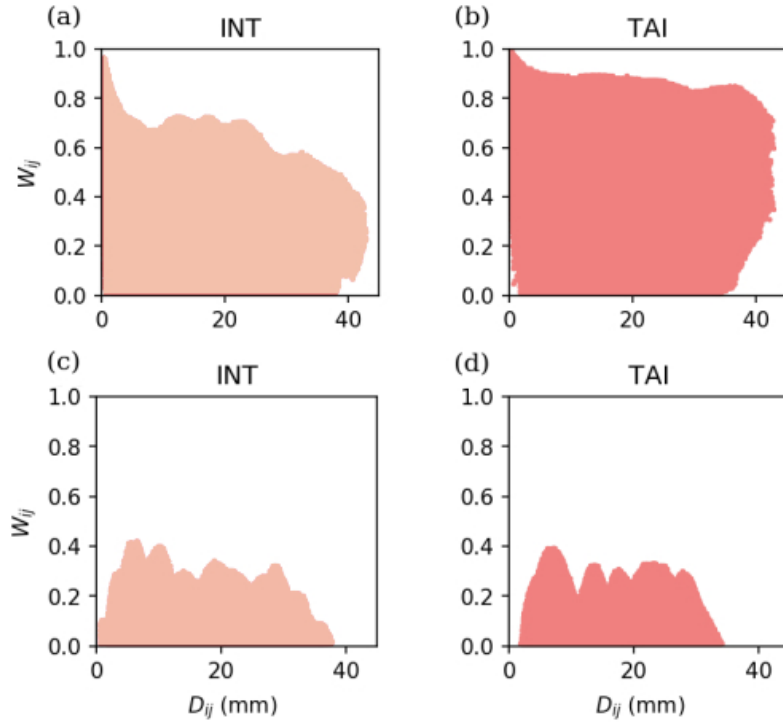
Fig. 6.4: Link weight (W_{ij}) versus the Euclidean link distance (D_{ij}) as obtained for the positively correlated network during (a) intermittency (INT), (b) thermoacoustic instability (TAI), and the negatively correlated network during (c) intermittency, and (d) thermoacoustic instability. Positively correlated networks have strong long-range correlations which are absent in negatively correlated networks.

the end wall of the combustor.

In a similar manner, all possible W_{ij} for each D_{ij} for the negatively correlated network corresponding to each dynamical state are plotted in Fig. 6.4c,d. Here, across both the dynamical states, we observe that there are no connections to the nearest neighbors. Possibly, the presence of convection in the flow induces only positive correlations within the local neighborhood of a node. Maximum W_{ij} is observed not in the local neighborhood of the nodes but for links having intermediate D_{ij} values. The absence of negative correlation in the immediate neighborhood of a node suggests that convection induces only positive correlations. This reveals a fundamental difference in the connectivity of the positively and negatively correlated spatial networks. Hereon, we will discuss the distribution of network measures for each dynamical state observed in the combustor.

6.4.1   Positively correlated networks

We begin by analyzing the positively correlated networks of the flame intensity oscillations near the end wall of the combustor during the dynamical states of intermittency and thermoacoustic instability. We show the spatial distributions of degree (k) and node strength (s) for different thresholds in Fig. 6.5.

For $\epsilon = 0$, we observe that almost all nodes exhibit high k for both intermittency and thermoacoustic instability due to the ubiquitous presence of positive correlations across the window. Hence, both intermittency and thermoacoustic instability display a similar k distribution for $\epsilon = 0$. On increasing ϵ to 0.3, weaker correlations are cut-off from the network, revealing regions with stronger interactions. From the k distribution for intermittency, we observe a distinct pattern in the location of nodes with high k. This pattern shows two distinct clusters (found at y = 10 - 19 mm and y = 20 - 34 mm) which exhibit large intensity oscillations during intermittency. These two longitudinal locations correspond to the crests formed by the asymmetrically oscillating jet flames, where heightened flame responses to the acoustic perturbations are recorded.

During thermoacoustic instability, the nodes over the jet flame closest to the end wall along with the aforementioned two clusters exhibit high k. Due to the even larger transverse displacement of the jet flames imparted by the high amplitude shock wave during thermoacoustic instability, the rightmost jet flame impinges with the end wall, resulting in a spike in the local flame intensity. Thus, the nodes lying over the entire jet flame closest to the end wall become highly correlated and possess high k during thermoacoustic instability. For ϵ beyond 0, high k is observed only during thermoacoustic instability. This difference in k distributions suggest that the majority of the nodes are weakly and strongly coherent during intermittency and thermoacoustic instability, respectively.

The corresponding s distributions show striking differences between intermittency and thermoacoustic instability right from $\epsilon = 0$. We observe maximum s only during thermoacoustic instability. Furthermore, the pattern of s is nearly the same as the
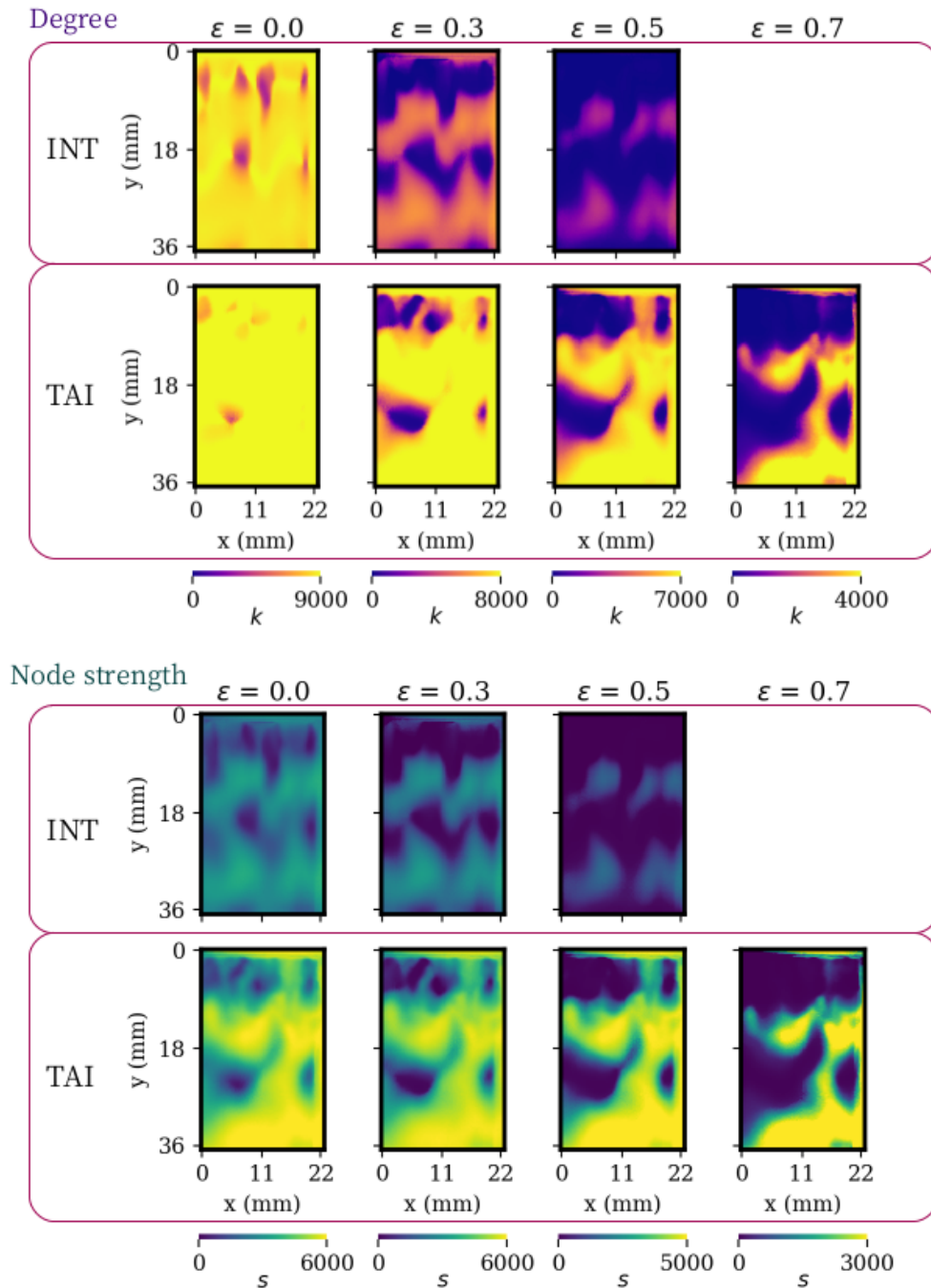
Fig. 6.5: The spatial distribution of degree (k) and node strength (s) for the positively correlated network during the dynamical states of intermittency (INT) and thermoacoustic instability (TAI) for various correlation thresholds. The patterns in the distributions of k and s across different ϵ reveal the locations exhibiting varying levels of coherent oscillations. Beyond $\epsilon = 0.5$, no patterns are visible from the spatial distributions of k and s during intermittency.

corresponding phase averaged image of CH* chemiluminescence observed at phase A (see Fig. 5.7c in Chapter. 5). Compared to the distribution of k for $\epsilon = 0$ which seems

to capture all the locations covered by the jet flames, the distribution of s captures only the locations housing the highest flame intensity oscillations near the end wall. For successive increments in ϵ, the spatial locations responsible for the highest flame intensity oscillations are revealed. These spatial locations also happen to exhibit the highest flame intensity oscillations.

In order to examine the size and strength of coherent clusters in the positively correlated networks, we visualize the adjacency matrices.

Visualization of adjacency matrix
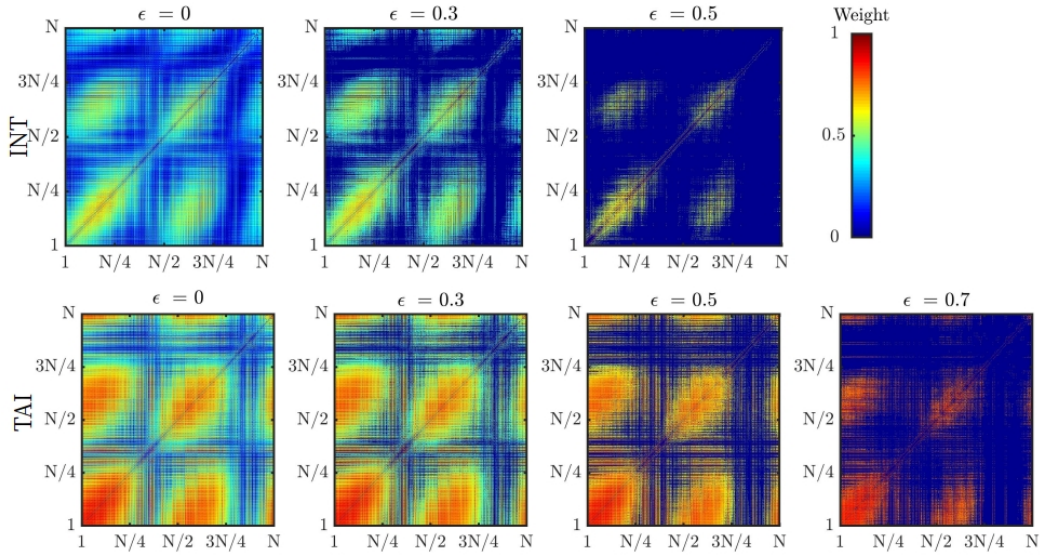
Fig. 6.6: Visualization of the adjacency matrix for the positively correlated networks during intermittency (INT) and thermoacoustic instability (TAI) for the different thresholds considered. Large weights amongst neighboring nodes are indicative of the presence of clusters.

We visualize the corresponding adjacency matrices (of size $N \times N = 9828 \times 9828$) for the positively correlated networks during intermittency and thermoacoustic instability in Fig. 6.6. Throughout all the adjacency matrices, we can observe the strong linkages amongst the neighboring nodes identified by the spots carrying high weights. The weights of these spots increase during the transition from intermittency to thermoacoustic instability. The size and color of these characteristic spots depict the extent of coherence in the clusters identified in the spatial distributions in Fig. 6.5.

Partial degree analysis
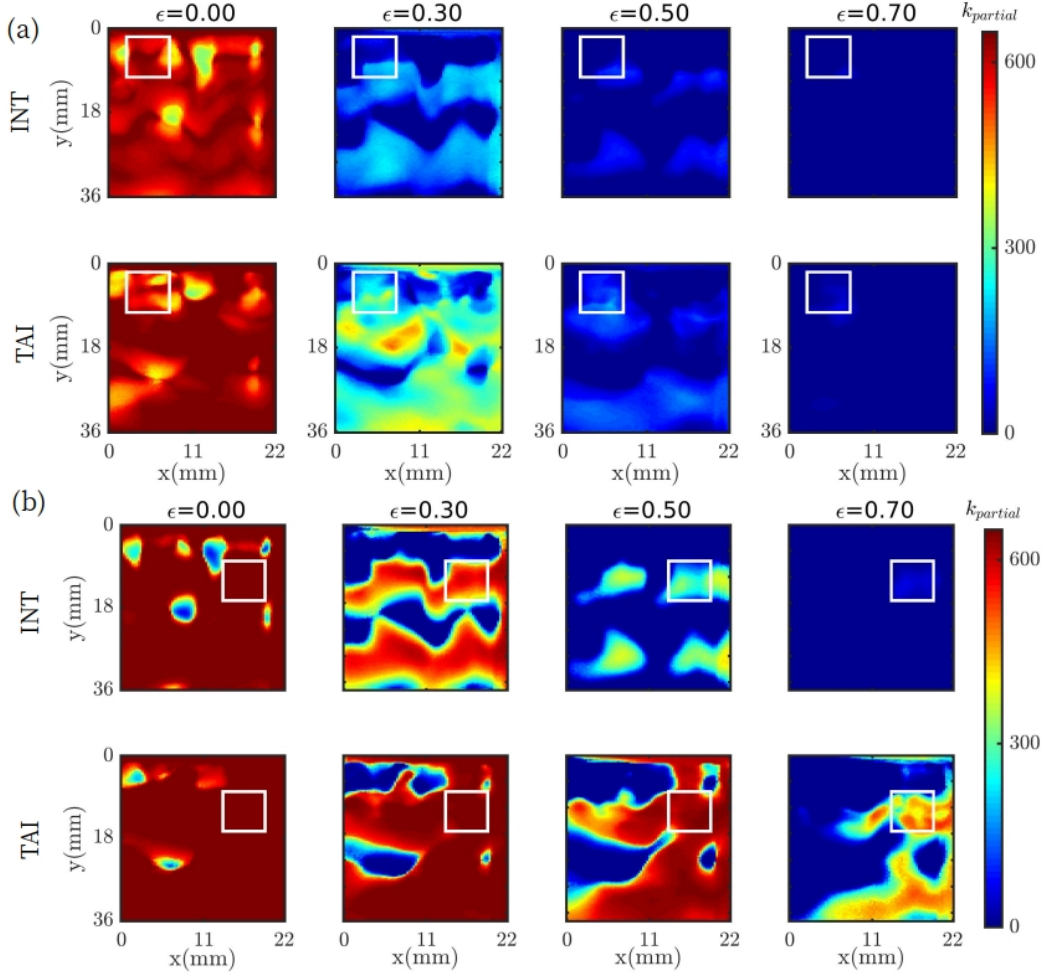
Fig. 6.7: Spatial distribution of the partial degree ($k_{partial}$) evaluated for the connections originating from the nodes located inside the (a) box 1 and (b) box 2 for the positively correlated networks during intermittency (INT) and thermoacoustic instability (TAI) for the different thresholds considered. Boxes 1 and 2 are chosen to be representative of an incoherent and coherent region in the flow field, respectively.

In order to demonstrate the enhanced connectivity of nodes belonging to a coherent cluster, we repeat the network analysis for small localized regions in the flow-field. Only the connections from the localized region (boxes 1 and 2) are considered. The boxes 1 and 2 are chosen to be representative of an incoherent and coherent region respectively. The size of the box is chosen to approximately span the width of one of the jet flames in the window. Then, we evaluated the partial degree, i.e., the number

links connected to the selected region housing a small fraction of nodes in the entire network.

In Fig. 6.7, we show the obtained partial degree distribution ($k_{partial}$) for the connections emerging from two boxes (box 1 and 2) from the positively correlated networks constructed during intermittency and thermoacoustic instability. For $\epsilon = 0$, all the distributions of $k_{partial}$ are nearly similar. However, upon increasing the ϵ to 0.3 and above, we observe that only the distributions of $k_{partial}$ associated with box 2 show large number of connections. This analysis is further proof of the box 2 region belonging to a coherent cluster whereas box 1 belongs to an incoherent region. In summary, the two boxes chosen demonstrate the presence (or lack of) strong clustering behavior and widespread connectivity due to high (or low) coherence in the flame intensity oscillations.

6.4.2 Negatively correlated networks

Now, we study the effect of negative correlations found in the flame intensity oscillations during intermittency and thermoacoustic instability. Negatively correlated networks are constructed following the methodology explained in Sec. 6.1. The distribution of the network measures in the negatively correlated networks enables us to quantify the extent of negative correlations in the flame intensity oscillations. In turn, the regions exhibiting negative correlations might indicate local regions which serve as acoustic power sinks, inhibiting the growth of thermoacoustic oscillations.

As seen in Fig. 6.3, the range of negative correlations are comparatively lower than the range of positive correlations. As a result, we show the distribution of network measures only for $\epsilon = 0$ in Fig. 6.8. For both intermittency and thermoacoustic instability, we observe small islands filled by nodes with high k. These small islands are surrounded by nodes with low k. For both intermittency and thermoacoustic instability, we discern that the distributions of k and s are similar, even using the lowest $\epsilon = 0$. Furthermore, both network measures only change slightly from intermittency to thermoacoustic instability.
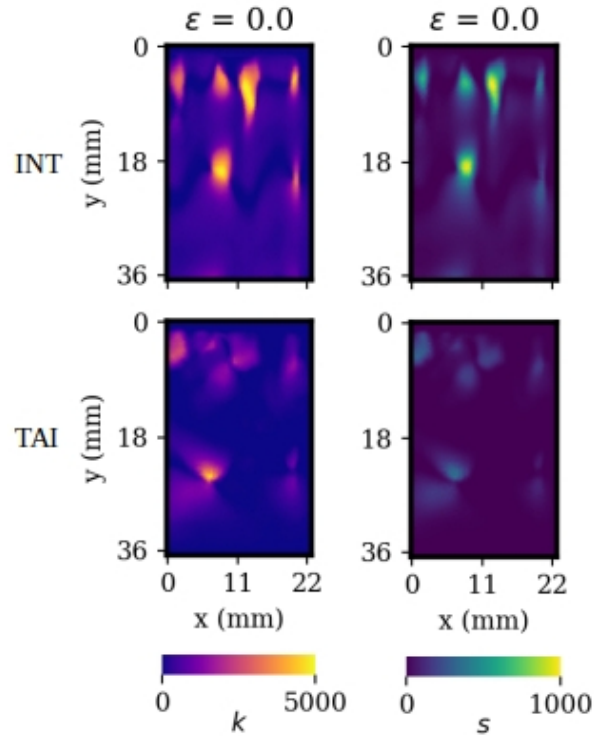
Fig. 6.8: The spatial distribution of degree (k) and node strength (s) for the negatively correlated network during the different dynamical states for the various correlation thresholds investigated. The sparse presence of negative correlations spread over the spatial domain during different dynamical states is captured by the corresponding distributions of k and s.

The distributions for the negatively correlated networks perfectly complement their corresponding distributions from the positively correlated networks. By this, we mean that nodes having low k (or s) in the positively correlated network has a high k (or s) and vice versa.

The variation of s is largely similar to that of k. This indicates that the locations housing anti-correlated flame intensity oscillations interact uniformly across the entire region. Hence, we conjecture that the uniform nature of these incoherent flame intensity oscillations implies that the oscillations are damped uniformly at these locations, whereas coherent flame intensity oscillations are driven at specific spatial locations (clusters).

All these findings suggest that the spatiotemporal dynamics of the flame intensity oscillations significantly change from intermittency to thermoacoustic instability.

Physically, the end wall of the combustor houses the transverse acoustic pressure anti-node. The strong thermoacoustic coupling near the end wall results in higher flame intensities. As a result, the driving of the 1T mode in the end wall region is higher, leading to widespread coherent flame intensity oscillations during the state of thermoacoustic instability.

Identifying the presence of clusters of coherent flame intensity oscillations does not provide information on the source and pathways underlining the mechanisms sustaining thermoacoustic instability. However, enhanced information on the size and structure of such coherent flame intensity oscillations would enable us to appropriately design control solutions to disrupt the size, structure, and strong coherence in the flame intensity oscillations.

6.5 DEGREE CORRELATIONS AND ASSORTATIVE MIXING IN CORRELATED FLAME INTENSITY NETWORKS

Next, we plot the degree distribution ($P(k)$ versus k) for all the positively and negatively correlated networks in Fig. 6.9. At the outset, we notice that $P(k)$ of the positively correlated networks constructed by setting an $\epsilon = 0$ for all dynamical states (Fig. 6.9a) exhibits an increasing trend with k. This implies that there are a large number of spatial locations in the end wall region which are highly connected amongst themselves during both intermittency and thermoacoustic instability.

For $\epsilon > 0$ (Fig. 6.9b-d), we do not see any monotonic behavior in the degree distribution of the positively correlated networks for any dynamical state. We observe that the probability of finding a node having low to intermediate value of k is similar for $\epsilon = 0.3$ and 0.5. However, the probability of obtaining a high k node increases for thermoacoustic instability due to the widespread coherence in the flame intensity oscillations. However, for the highest ϵ of 0.7, this probability decreases since the fraction of highly correlated node pairs reduces.

Unlike the positively correlated networks, we obtain a decreasing trend in $P(k)$ for the
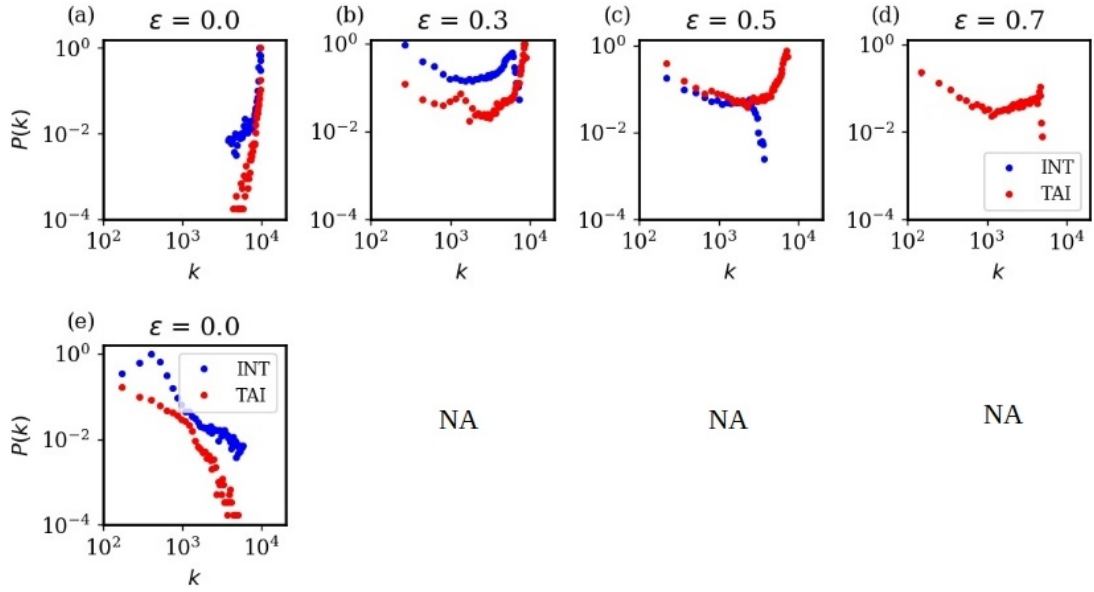
Fig. 6.9: The degree distribution ($P(k)$ versus k) for (a-d) the positively and (e) negatively correlated networks for each correlation threshold investigated. The degree distributions are shown only for the thresholds investigated. The thresholds for which no patterns are visible in the spatial distributions are labeled non-applicable (NA).

negatively correlated networks (Fig. 6.9e) for $\epsilon = 0$. This decreasing trend suggests there exists only a few spatial locations in the flow-field, wherein the flame intensity oscillations are highly negatively correlated amongst themselves.

The stark differences in the degree distributions of positively and negatively correlated networks motivate us to check the presence of degree-degree correlations. We rely on the measures described in Sec. 6.2 to detect these correlations.

In order to verify the presence of degree-degree correlations, we plot the degree correlation function, $k_{nn}(k)$, against the degree (k) for all the networks investigated in Fig. 6.10a-e. We observe that $k_{nn}(k)$ increases with k for both the dynamical states. This trend confirms the presence of degree-degree correlations in the networks, wherein connections are established between nodes of similar degrees. This phenomenon is known as assortative mixing in network theory (Newman, 2002).

Specifically, the high degree nodes are preferentially connected with other high degree nodes. Physically, the presence of assortative mixing implies that regions with highly correlated intensity oscillations tend to interact with other regions containing highly
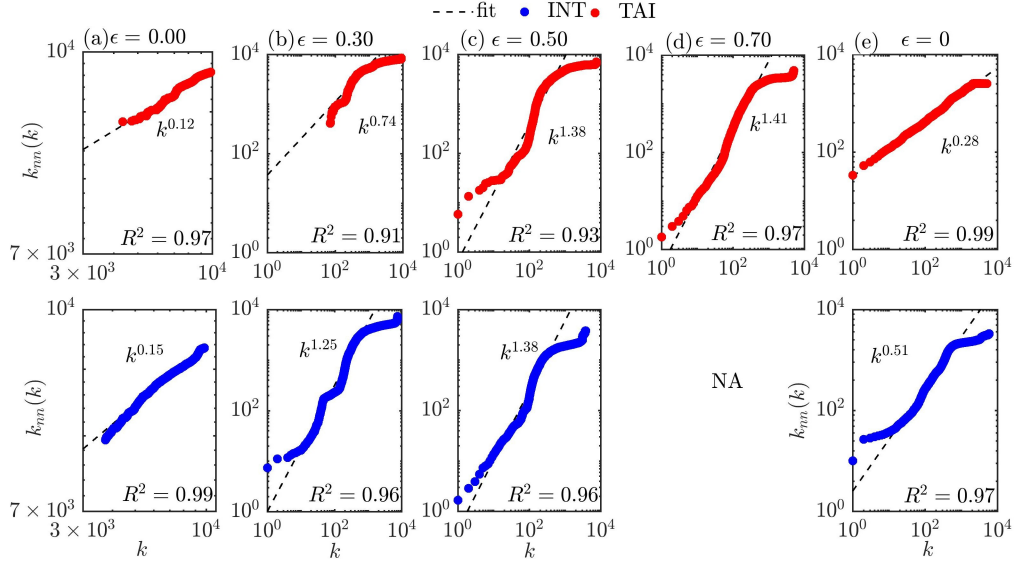
Fig. 6.10: Log-log plot of the degree correlation function ($k_{nn}(k)$) and degree (k) for (a-d) the positively and (e) the negatively correlated networks during intermittency (INT) and thermoacoustic instability (TAI) for the different thresholds considered. The increasing trend in the plots suggest the presence of assortative mixing in the positively correlated networks. The degree correlation exponent (μ) and the goodness of the fit (R^2) are indicated. The thresholds for which no patterns are visible in the spatial distributions are labeled non-applicable (NA).

correlated intensity oscillations (Newman, 2002). This leads to the formation of a core group (a cluster) in the network that acts as a "reservoir" for coherent flame intensity oscillations. These reservoirs manifest in the form of clusters in the spatial distributions of degree and node strength in the positively correlated networks. Near the end wall, we find one reservoir of coherent flame intensity oscillations which spans the majority of the window (see Fig. 6.5).

To quantify the assortativity in the networks, one can check the presence of scaling relation (Barabási *et al.*, 2016; Pastor-Satorras *et al.*, 2001) between $k_{nn}(k)$ and k such that $k_{nn}(k) \sim k^{\mu}$. In the log-log plot of $k_{nn}(k)$ and k shown in Fig. 6.10, we have fitted $k_{nn}(k)$ as k^{μ}. All the fits are obtained by linear regression characterized by a goodness of the fit (R^2) > 90%. We observe all the networks have a $\mu > 0$, confirming the presence of assortativity. The value of μ ranging from 0.12 to 1.41 indicate the different assortative nature in the networks examined in this chapter. In comparison,

the internet network, mobile phone call network, and science collaboration network have μ values of 0.56, 0.33 and 0.16, respectively (Barabási *et al.*, 2016). The value of $\mu > 1$ is indicative of the stronger assortative nature in some of the positively correlated networks.

The presence of assortativity in the networks indicate that any node is most likely connected to other nodes with similar degree. Newman (2002) reported that the removal of high degree nodes in an assortatively mixed network is an inefficient way to destroy the network connectivity considerably. Hence, we can hypothesize that any passive control strategies targeting the regions with high k in this combustor may be inefficient in suppressing thermoacoustic oscillations. Any successful control action for suppressing the oscillations might warrant overwhelming changes to the engine design and necessitate several full-scale tests. However, dedicated experiments need to be performed to verify this hypothesis.

6.6 CONCLUDING REMARKS

In this chapter, we have performed a weighted spatial network analysis of the local flame intensity oscillations acquired from the CH* chemiluminescence fields during the transition from intermittency to thermoacoustic instability in a multi-element 2D model rocket combustor. The spatiotemporal dynamics has been studied near the end wall region where the flame intensity oscillations are the highest. First, we showed that the response of the jet flame to transverse acoustic oscillations is non-uniform along the longitudinal direction of the combustor.

Our analysis unraveled fundamental differences in the connectivity of positively and negatively correlated spatial networks. The network measures revealed the differences in the coherence in the flame intensity oscillations during intermittency and thermoacoustic instability. We identified that many spatial locations are populated by high degree and high node strength during thermoacoustic instability, translating to highly coherent flame intensity oscillations. Such network measures can be

valuable metrics for testing the validity of computational simulations. Finally, we also discovered the presence of assortative mixing leading to the formation of reservoirs of coherent flame intensities. To the best of our knowledge, this is the first evidence of assortative mixing in turbulent reactive flows.

Validation of computational simulations with experimental data, especially for high-pressure and high power-density devices has traditionally been performed by comparing point measurements of pressure (or other variables) measured in the experiment temporally. In rocket combustors, where large optical access for high-speed imaging or laser-based diagnostics is challenging, very few studies available in open literature have performed comparison of spatiotemporal data (Hardi *et al.*, 2016*b*,*a*; Morgan *et al.*, 2015; Beinke *et al.*, 2021). In these studies, path integrated chemiluminescence measurements were compared with heat release rate from simulations using direct comparison of broad coherent flow features derived from time-averaged or phase-averaged images using broadband or filtered chemiluminescence measurements. Additional comparison was also performed by reconstructing and comparing prominent features in the flow, sorted by highest energy content using proper orthogonal decomposition, using experimental and computational data. This comparison provided valuable insight in the mechanisms promoting combustion instability in the experiments, but the qualitative nature of the comparison was insufficient for verification and validation of the numerical results. Where more quantitative comparisons are available, these are primarily made using temporal history of pressure measurements with wall mounted sensors (Harvazinski *et al.*, 2015). The amplitudes of the experimentally obtained pressure oscillations (and other directly measured quantities from experiments) and their dominant frequencies are compared with that of the numerical simulations. Obtaining a match in only these features might be inadequate and may not replicate or predict the dynamics occurring in experiments correctly. The detailed features of the spatiotemporal data obtained from experiments albeit very useful, are largely neglected in this validation process. We propose using

the spatial variation of network measures (degree and node strength) along with their distributions on the data obtained from experiments and matching numerical simulations to tighten the validation process. Further, the validation of simulations that aim to mimic the experimental observations in rocket or other high-power combustion devices can be augmented by comparing the size, structure, and extent of coherence in the flame intensity oscillations.

CHAPTER 7

Conclusions and future prospects

In this thesis, the framework of dynamical systems theory and complex systems theory to understand the dynamic behavior of signals acquired from a rocket combustor is established. The recent adoption of this framework has resulted in enormous breakthroughs in the field of gas-turbine combustion (Sujith and Pawar, 2021) and has now become a mainstay in the analysis of oscillatory instabilities found in thermoacoustic systems applied to gas turbine engines, aeroelastic, and aeroacoustic systems (Pavithran *et al.*, 2021). Using the tools from dynamical systems theory and complex systems theory, we investigate the temporal and spatiotemporal dynamics during the transition from a stable state to transverse thermoacoustic instability via intermittency. Towards this purpose, we used the experimental datasets from Purdue's transverse instability combustor, a multi-element self-excited model rocket combustor operating at elevated pressures based on an oxidizer-rich staged combustion cycle.

First, the framework of dynamical systems theory is used to understand the various nonlinear behaviors exhibited by the combustor. Since the combustion dynamics is determined by the complex nonlinear feedback interactions between the acoustic and reactive flow subsystems, the combustor is essentially a complex system. As a result, the frameworks of synchronization theory and complex network theory were utilized to understand the behavior of flame intensity oscillations and its coupling with their transverse acoustic field in the combustor.

Examining several test runs of the combustor performed for the same operating conditions, we showed that the transition from the stable state to thermoacoustic instability occurs via intermittency. Much of the literature on rocket combustors has focused only on understanding the dynamics solely during the state of thermoacoustic instability. In order to comprehensively understand the mechanisms and the associated coupling behaviors leading to the onset of thermoacoustic instability, it is essential

to thoroughly analyze also the stable state and other dynamical states exhibited by the rocket combustor. Throughout this thesis, we systematically study the temporal and spatiotemporal dynamics during stable state and intermittency, along with thermoacoustic instability.

Performing multifractal analysis of the acoustic pressure time series, we detected the loss of multifractality during the onset of thermoacoustic instability. Importantly, we devised several measures such as $RATIO$ (ratio of determinism to recurrence rate) from recurrence analysis, Hurst exponent and multifractal spectrum width from multifractal analysis. We demonstrated the superior performance of these measures developed from recurrence theory and multifractal analysis towards detecting the dynamical transitions from the stable state to intermittency to thermoacoustic instability, compared to conventional measures such as root mean square, variance, and spectral amplitude of the acoustic pressure oscillations. Further, we showed that the recurrence measure $RATIO$ can be tuned to detect rapid switching from aperiodic oscillations to periodic oscillations irrespective of the amplitude of the oscillations.

During thermoacoustic instability and periodic epochs of intermittency, we detected the switching between period-3 and period-4 limit cycle oscillations. Further, during thermoacoustic instability, the acoustic pressure oscillations manifested as steepened wavefronts owing to the presence of shock waves. Such a steepened wavefront is in stark contrast to the sinusoidal-looking limit cycle oscillations. This is exemplified in the characteristic shape of the phase space resembling a trefoil knot. Using recurrence analysis, we showed the presence of slow and fast timescales in the steepened waveforms of acoustic pressure oscillations during thermoacoustic instability. The micropatterns in the recurrence plot and the unique topology of the recurrence network constructed from acoustic pressure oscillations during thermoacoustic instability arise as a result of the presence of multiple timescales in the steepened wavefronts. We also showed that such features are absent in the sinusoidal-looking limit cycle oscillations acquired from an experimental gas turbine-type turbulent combustor.

The coupled interaction between the acoustic pressure and CH* intensity (representative of heat release rate) oscillations were studied during the transition from the stable state to intermittency to thermoacoustic instability. Since the transverse mode was self-excited during thermoacoustic instability, we specifically analyzed this coupled behavior at two transverse locations: near the end wall (acoustic pressure antinode for the fundamental transverse mode) and the center (acoustic pressure node for the fundamental transverse mode) of the combustor. We observed desynchrony between the acoustic pressure and CH* intensity oscillations during the stable state, which transitioned to intermittent phase synchronization during intermittency. During thermoacoustic instability, we observed phase synchronization near the center of the combustor while generalized synchronization (both the phase and amplitude are synchronized) near the end wall of the combustor. From the spatial analysis of the local CH* intensity oscillations, we identified that end wall region exhibited higher intensities compared to the center region during intermittency and thermoacoustic instability. We also quantified the transition from stochasticity to widespread determinism (correlation) in the local CH* intensity oscillations during the transition to thermoacoustic instability. Furthermore, we devised a novel method to compute the spatial Rayleigh index and discerned that only the first few transverse modes participated in the driving process to grow the amplitude of thermoacoustic oscillations. The other higher harmonics present in the amplitude spectra correspond to the nonlinear wave steepening phenomenon. The enhanced driving from the 1T mode compared to the 2T mode and other higher harmonics were revealed from the spatial Rayleigh index.

Next, we utilized the framework of complex network analysis to build positively and negatively correlated weighted spatial networks based on the correlation of local CH* intensity oscillations for the different dynamical states as observed from the near end wall region of the combustor. Using the network measures (degree and node strength) in this analysis, we distinguished different spatial regions based on their coherence in the flame intensity oscillations. We also unearthed the presence of assortative mixing

in the networks, leading to the sustenance of reservoirs of coherent flame intensities.

Scope for future work

The recently realized ability to perform high-fidelity CFD simulations over entire three-dimensional domains of an LPRE (Urbano *et al.*, 2016; Harvazinski *et al.*, 2020) has enabled access to investigate the role of several variables such as fuel or oxidizer mass fraction, local heat release rate, temperature, and vorticity fields, during the stable state and thermoacoustic instability. However, the high-fidelity simulations need to be validated tightly prior to such investigation. The measures illustrated in this study to distinguish different dynamical states exhibited by the combustor can be used to validate the temporal and spatiotemporal dynamics in high-fidelity CFD simulations targeted towards optimizing the stability and performance metrics of the rocket combustor. Such an approach can reduce the mismatch between hot-fire tests and high-fidelity simulations of LPREs, resulting in shortened developmental timescales.

We showed that signals acquired from rocket combustors are different from their gas turbine counterparts and other laboratory-scale turbulent combustors due to the presence of gas dynamical nonlinearities in the rocket combustor. Hence, the methodologies developed for laboratory-scale combustors and gas turbine combustors must be tailored appropriately to be applicable to rocket combustors.

Moreover, the methodologies used to probe the spatiotemporally coupled interaction between the acoustic pressure and flame intensity oscillations presented in this thesis can provide novel insights into the mechanisms initiating and sustaining high-frequency thermoacoustic instabilities. Since many real rocket engine combustors experience a combination of longitudinal and transverse modes, it would be interesting to study the coupled interaction between acoustics and heat release rate fields and the behavior of local heat release rate oscillations in such configurations. Besides, a hybrid approach involving experiments and matching high-fidelity simulations can pay great dividends towards understanding the mechanisms behind the onset of thermoacoustic instabilities

in flight-capable LPREs.

The recent advances in machine learning have provided an alternative approach to analyzing thermoacoustic instabilities (Waxenegger-Wilfing *et al.*, 2021*a*). Already, machine learning methods in conjunction with physics-based measures are being developed to devise novel precursors to the onset of thermoacoustic instabilities (Waxenegger-Wilfing *et al.*, 2021*b*; Dhadphale *et al.*, 2021). Several promising techniques from complex systems theory such as multilayer networks (Boccaletti *et al.*, 2014; Kivelä *et al.*, 2014) and wavelet-based multiscale methods (Percival and Walden, 2000) show great promise towards revealing the different intricate interactions between the acoustic, flow, and combustion processes. In summary, the methods present in this thesis are expected to encourage the adoption of tools from dynamical systems and complex systems theory to advance our understanding of the temporal and spatiotemporal dynamics during thermoacoustic instability and other dynamical states in LPREs.

APPENDIX A

Temporal analysis of acoustic pressure oscillations

A.1 ROBUSTNESS OF RECURRENCE MEASURE WITH THE SELECTION OF RECURRENCE THRESHOLD

The temporal variation of the recurrence measure, $RATIO$, for different recurrence thresholds (ϵ) is shown in Fig. A.1. The recurrence thresholds are selected as a proportion of the maximum size (s) of the phase space attractor of acoustic pressure oscillations reconstructed using Takens' delay embedding theorem for Test-C. Owing to the dependence of the magnitudes of the determinism (DET) and recurrence rate (RR), the absolute values of $RATIO$ varies during the transition. However, the underlying trend required to distinguish the different dynamical states remains intact for the all the recurrence thresholds shown.
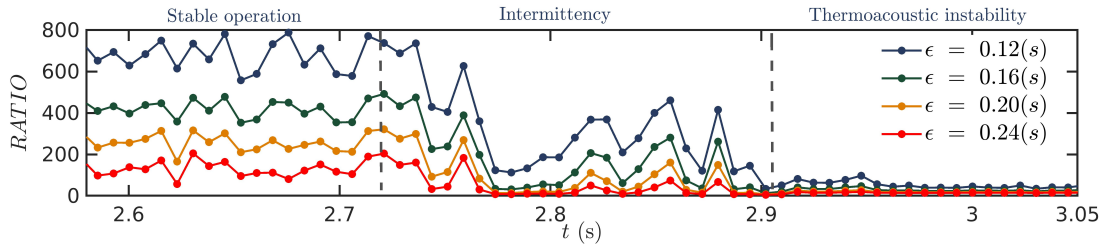
Fig. A.1: The variation of $RATIO$ with time for different recurrence thresholds is shown for Test-C. The selected recurrence thresholds are 12%, 16%, 20% and 24% of the size (s) of the phase space attractor. The dashed lines demarcate stable operation, intermittency and thermoacoustic instability. A non-overlapping window size of 7.5 ms is translated in time.

A.2 STATISTICAL ANALYSIS OF MULTIFRACTAL ANALYSIS

Prior to performing the multifractal analysis, we need to estimate the range of scales necessary to capture the multifractal characteristics of the acoustic pressure oscillations. As explained in Section. IIB, we plot the structure function (see Fig, A.2) against the range of binarized scales necessary to capture the small-scale and large-scale fluctuations. From the plot, we examine the trends for the acoustic pressure fluctuations during the dynamical states of stable operation, intermittency and thermoacoustic instability. We observe a linear regime for the range of scales from 2 to 10 cycles of the dominant instability frequency (2650 Hz) for all the dynamical states. Hence, the multifractal measures such as Hurst exponent (H) and multifractal spectrum width ($\alpha_2 - \alpha_1$) are computed with this range of scales.
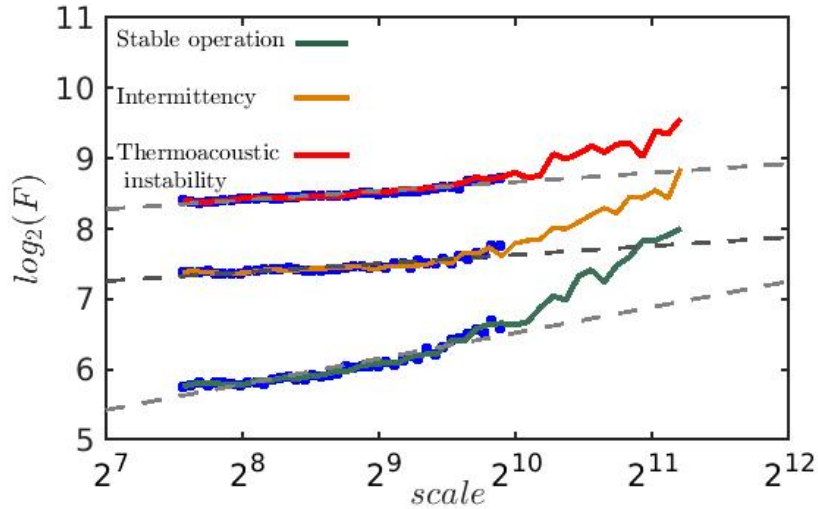
Fig. A.2: The variation of structure function with scale for the acoustic pressure oscillations acquired during Test - C for the dynamical states of stable operation (green curve), intermittency (orange curve) and thermoacoustic instability (red curve). For each dynamical state, the scales ranging from 2 to 10 cycles (blue dots) are fitted with a linear line (grey dashed line).
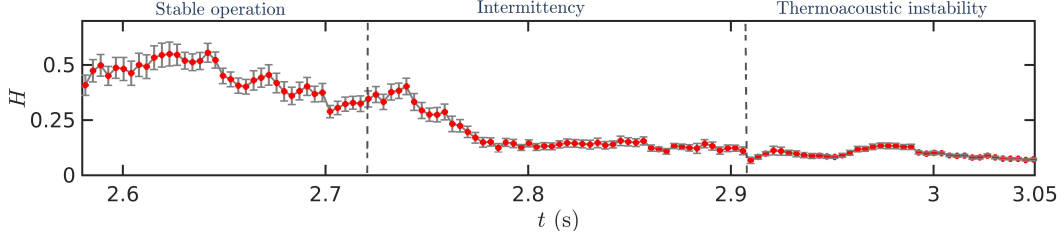
Fig. A.3: The variation of Hurst exponent (H) against time for the Test-C during the transition from stable operation to thermoacoustic instability via intermittency. The error bars indicate 90% confidence in H. A window size of 37.7 ms is varied in time with an overlap of 33.9 ms and q-range of 2 to 10 cycles of 2650 Hz is used.
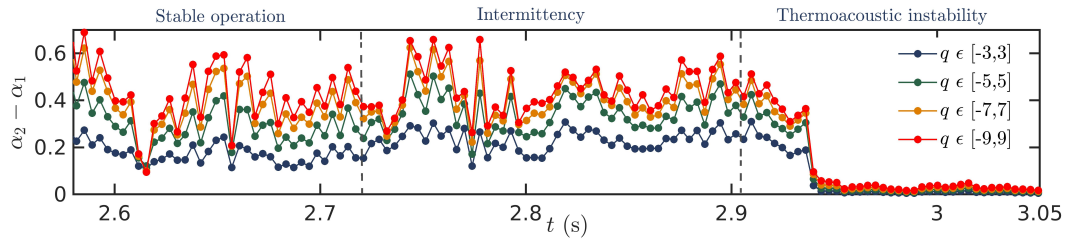
Fig. A.4: The variation of the width of the multifractal spectrum ($\alpha_2 - \alpha_1$) with time for different q-range is shown for Test-C. A window size of 37.7 ms is varied in time with an overlap of 33.9 ms. The dashed lines demarcate stable operation, intermittency and thermoacoustic instability.

In Fig. A.3, we show the temporal variation of Hurst exponent (H) estimated for Test-C. The error bars are estimated with a confidence of 90% based on the goodness of the fit to measure the slope in the plot of structure function. We observe that H can be used to robustly demarcate the onset of thermoacoustic instability from the states of stable operation and intermittency.

The sensitivity of q-range in the computation of the width of the multifractal spectrum ($\alpha_2 - \alpha_1$) is plotted for Test-C in Fig. A.4. Here, we observe that $\alpha_2 - \alpha_1$ is fairly robust in exhibiting similar trends in the variation from stable operation to thermoacoustic instability via intermittency.

155

APPENDIX B

Effect of embedding dimension on the recurrence network of a slow-fast system

We demonstrate the robustness of the topology of the RNs for different embedding dimensions (d) for the modified Izhikevich model (Fig. B.1a) and time series of the acoustic pressure oscillations acquired during the state of thermoacoustic instability in a rocket combustor (Fig. B.1b). The corresponding embedding dimensions selected from the modified false nearest neighbors method for these two cases are $d = 6$ and $d = 10$, respectively.
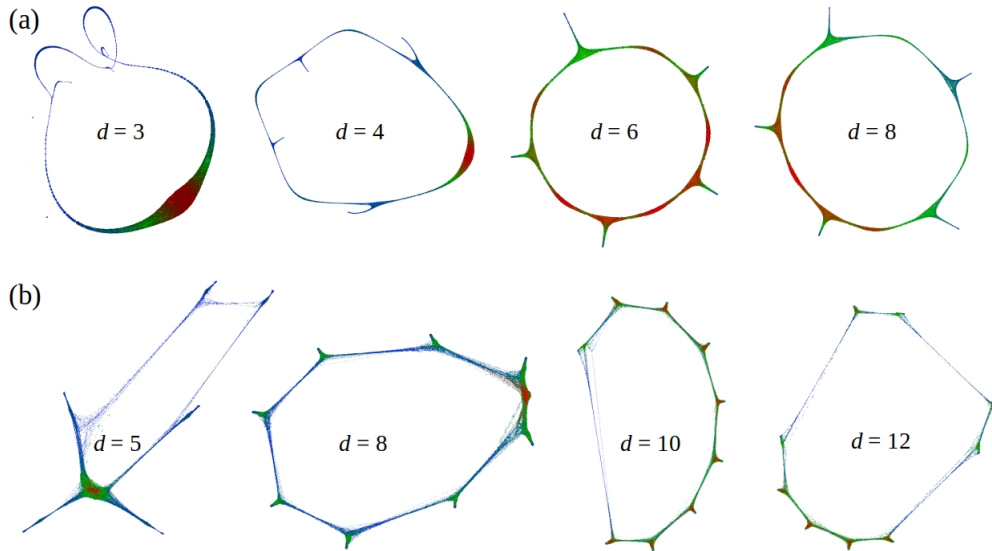
Fig. B.1: The RNs for various embedding dimensions (d) are plotted for (a) modified Izhikevich model (Fig. 4.5) and (b) the acoustic pressure oscillations (p') acquired from a multi-element rocket combustor (Fig. 4.8). We observe that the topology of the RN converges after a certain d.

In general, we observe that the RNs exhibit closed-loop structures characteristic of periodic orbits for the range of d shown. For both cases, the realized RNs for lower embedding dimensions are distorted. With a further increase in d, the topology of RN converges and remains largely the same for further increase in d. In other words, for higher d, we find characteristic features such as the number of protrusions and

clustering of nodes to be nearly the same with increasing d. However, the topology of RN converges at an earlier d for experimental data, than that estimated by the modified false nearest neighbors method. This observed change in the optimal d from the RN and from the modified false nearest neighbors method is not seen in the case of the prototypical signals. We believe that the presence of noise in the experimental data leads to this deviation. The ability of RN to capture the features of the high-dimensional phase space in slow-fast systems can help us to cross-verify the optimum embedding dimension.

APPENDIX C

Derivation of structure function for $q \to 0$

The structure function (F_w^q) of order q and span w is (as in Eq. 3.6),

$$F_w^q = \left[\frac{1}{n_w} \sum_{i=1}^{n_w} \left(\sqrt{\frac{1}{w} \sum_{t=1}^{w} \left(y_i(t) - \overline{y}_i \right)^2} \right)^q \right]^{1/q}.$$

Here, for $q \to 0$, the structure function (F_w^q) would diverge and tend to infinity. Therefore, in order to evaluate the structure function, a logarithmic averaging procedure needs to be applied.

First, we make $f = \frac{1}{w} \sum_{t=1}^{w} \left(y_i(t) - \overline{y}_i \right)^2$.

Then, we can write Eq. 3.6 as,

$$F_w^q = \left\{ \frac{1}{n_w} \sum_{i=1}^{n_w} f^{\frac{q}{2}} \right\}^{\frac{1}{q}}$$

$$F_w^q = \left\{ 1 - 1 + \frac{1}{n_w} \sum_{i=1}^{n_w} f^{\frac{q}{2}} \right\}^{\frac{1}{q}}$$

Then, we use $\lim_{x \to 0} \left\{ 1 + f(x) \right\}^{\frac{1}{g(x)}} = \exp\left[\lim_{x \to 0} \frac{f(x)}{g(x)} \right]$ to get

$$F_w^{q \to 0} = \exp\left[\lim_{q \to 0} \left\{ \frac{-1 + \frac{1}{n_w} \sum_{i=1}^{n_w} f^{\frac{q}{2}}}{q} \right\} \right] \quad F_w^{q \to 0} = \exp\left[\lim_{q \to 0} \left\{ \frac{1}{n_w} \frac{\sum_{i=1}^{n_w} f^{\frac{q}{2}} - 1}{q} \right\} \right]$$

Then, we use the formula: $\lim_{m \to 0} \frac{x^m - 1}{m} = \log x + \frac{m}{2} \log^2 x + \mathcal{O}(m^2) + \ldots$

Omitting the higher order terms, we obtain

$$F_w^{q \to 0} = \exp\left\{ \frac{1}{2n_w} \sum_{i=1}^{n_w} \log f \right\}$$

Substituting for f back into the above equation, we retrieve Eq. 3.7, which is

$$F_w^{q \to 0} = \exp\left\{ \frac{1}{2n_w} \sum_{i=1}^{n_w} \log\left(\frac{1}{w} \sum_{t=1}^{w} \left(y_i(t) - \overline{y}_i \right)^2 \right) \right\}.$$

REFERENCES

1. **Abderrahmane, H. A.**, **F. Paquet**, and **H. D. Ng** (2011). Applying nonlinear dynamic theory to one-dimensional pulsating detonations. *Combustion Theory and Modelling*, **15**(2), 205–225.

2. **Ambika, G.** and **K. Harikrishnan** (2020). Methods of nonlinear time series analysis and applications: A review. *Dynamics and Control of Energy Systems*, 9–27.

3. **American Society of Mechanical Engineers** (2016). Measurement of Gas Flow by Means of Critical Flow Venturis and Critical Flow Nozzles.

4. **Anderson, W. E.** and **V. Yang** (1995). *Liquid rocket engine combustion instability*. AIAA, `doi:10.2514/5.9781600866371`.

5. **Aoki, C.**, **H. Gotoda**, **S. Yoshida**, and **S. Tachibana** (2020). Dynamic behavior of intermittent combustion oscillations in a model rocket engine combustor. *Journal of Applied Physics*, **127**(22), 224903.

6. **Armbruster, W.**, **J. S. Hardi**, **Y. Miene**, **D. Suslov**, and **M. Oschwald** (2020). Damping device to reduce the risk of injection-coupled combustion instabilities in liquid propellant rocket engines. *Acta Astronautica*, **169**, 170–179.

7. **Armbruster, W.**, **J. S. Hardi**, and **M. Oschwald** (2021). Flame-acoustic response measurements in a high-pressure, 42-injector, cryogenic rocket thrust chamber. *Proceedings of the Combustion Institute*, **38**(4), 5963–5970.

8. **Armbruster, W.**, **J. S. Hardi**, **D. Suslov**, and **M. Oschwald** (2018). Experimental investigation of self-excited combustion instabilities with injection coupling in a cryogenic rocket combustor. *Acta Astronautica*, **151**, 655–667, `doi:10.1016/j.actaastro.2018.06.057`.

9. **Armbruster, W.**, **J. S. Hardi**, **D. Suslov**, and **M. Oschwald** (2019). Injector-driven flame dynamics in a high-pressure multi-element oxygen–hydrogen rocket thrust chamber. *Journal of Propulsion and Power*, **35**(3), 632–644.

10. **Bar-Yam, Y.**, **S. R. McKay**, and **W. Christian** (1998). Dynamics of complex systems (studies in nonlinearity). *Computers in Physics*, **12**(4), 335–336.

11. **Barabási, A. L.** *et al.* (2016). *Network science*. Cambridge University Press.

12. **Barrat, A.**, **M. Barthélemy**, and **A. Vespignani** (2005). The effects of spatial constraints on the evolution of weighted complex networks. *Journal of Statistical Mechanics: Theory and Experiment*, **2005**(05), P05003.

13. **Bastian, M.**, **S. Heymann**, and **M. Jacomy** (2009). Gephi: an open source software for exploring and manipulating networks. *In Third international AAAI conference on weblogs and social media*.

14. **Bazarov, V. G.** and **V. Yang** (1998). Liquid-propellant rocket engine injector dynamics. *Journal of Propulsion and Power*, **14**, 797–806.

15. **Bedard, M. J.** (2017). *Detailed Measurement of ORSC Main Chamber Injector Dynamics*. Doctoral thesis, Purdue University.

16. **Bedard, M. J.**, **T. L. Fuller**, **S. Sardeshmukh**, and **W. E. Anderson** (2020). Chemiluminescence as a diagnostic in studying combustion instability in a practical combustor. *Combustion and Flame*, **213**, 211–225.

17. **Bedard, M. J.**, **R. M. Gejji**, **W. E. Anderson**, **B. L. Austin Jr**, **P. Kasthuri**, and **R. I. Sujith** (2021). Detailed measurement of oxidizer-rich staged combustion injector dynamics in model rocket combustors. *AIAA Journal*, 1–16.

18. **Bedard, M. J.**, **S. V. Sardeshmukh**, **T. Fuller**, **W. E. Anderson**, and **M. Tanabe** (2014). Chemiluminescence as a diagnostic in studying combustion instability in a practical combustor. *In 50th AIAA/ASME/SAE/ASEE Joint Propulsion Conference*.

19. **Beinke, S. K.**, **J. S. Hardi**, **D. T. Banuti**, **S. Karl**, **B. B. Dally**, and **M. Oschwald** (2021). Experimental and numerical study of transcritical oxygen-hydrogen rocket flame response to transverse acoustic excitation. *Proceedings of the Combustion Institute*, **38**(4), 5979–5986.

20. **Bennewitz, J. W.** and **R. A. Frederick** (2013). Overview of combustion instabilities in liquid rocket engines-coupling mechanisms & control techniques. *In 49th AIAA/ASME/SAE/ASEE Joint PropulsionConference*, 4106. AIAA.

21. **Bertram, R.** and **J. E. Rubin** (2017). Multi-timescale systems and fast-slow analysis. *Mathematical biosciences*, **287**, 105–121.

22. **Bishop, C. M.** (2006). Pattern recognition. *Machine learning*, **128**(9).

23. **Blacker, A. M.** (2019). *Characterization of Lifted Flame Behavior in a Multi-Element Rocket Combustor*. Doctoral thesis, Purdue University.

24. **Blomshield, F.**, **J. Crump**, **H. Mathes**, **R. A. Stalnaker**, and **M. Beckstead** (1997). Stability testing of full-scale tactical motors. *Journal of Propulsion and Power*, **13**(3), 349–355.

25. **Bloomer, H. E.**, **E. W. Conrad**, **D. W. Vincent**, and **J. P. Wanhainen** (1968). *Liquid rocket acoustic-mode-instability studies at a nominal thrust of 20000 pounds(Liquid rocket acoustic instability for hydrogen-oxygen and earth storable propellant combinations)*. Scientific and Technical Information Office, National Aeronautics and Space Administration. Report: NASA TN D-4968, https://ntrs.nasa.gov/citations/19690005052.

26. **Bloxsidge, G.**, **A. Dowling**, and **P. Langhorne** (1988). Reheat buzz: an acoustically coupled combustion instability. part 2. theory. *Journal of Fluid Mechanics*, **193**, 445–473.

27. **Boccaletti, S.**, **G. Bianconi**, **R. Criado**, **C. I. Del Genio**, **J. Gómez-Gardenes**, **M. Romance**, **I. Sendina-Nadal**, **Z. Wang**, and **M. Zanin** (2014). The structure and dynamics of multilayer networks. *Physics Reports*, **544**(1), 1–122.

28. **Brear, M. J.**, **F. Nicoud**, **M. Talei**, **A. Giauque**, and **E. R. Hawkes** (2012). Disturbance energy transport and sound production in gaseous combustion. *Journal of Fluid Mechanics*, **707**, 53–73.

29. **Brunton, S. L.**, **B. R. Noack**, and **P. Koumoutsakos** (2020). Machine learning for fluid mechanics. *Annual Review of Fluid Mechanics*, **52**, 477–508.

30. **Bruun, E. W.**, **P. Ambus**, **H. Egsgaard**, and **H. Hauggaard-Nielsen** (2012). Effects of slow and fast pyrolysis biochar on soil c and n turnover dynamics. *Soil Biology and Biochemistry*, **46**, 73–79.

31. **Burnley, V.** and **F. Culick** (2000). Influence of random excitations on acoustic instabilities in combustion chambers. *AIAA Journal*, **38**(8), 1403–1410.

32. **Bury, T. M.**, **R. I. Sujith**, **I. Pavithran**, **M. Scheffer**, **T. M. Lenton**, **M. Anand**, and **C. T. Bauch** (2021). Deep learning for early warning signals of tipping points. *Proceedings of the National Academy of Sciences*, **118**(39).

33. **Cantrell, R.** and **R. Hart** (1964). Interaction between sound and flow in acoustic cavities: Mass, momentum, and energy considerations. *The Journal of the Acoustical Society of America*, **36**(4), 697–706.

34. **Cao, L.** (1997). Practical method for determining the minimum embedding dimension of a scalar time series. *Physica D: Nonlinear Phenomena*, **110**(1-2), 43–50.

35. **Cellier, A.**, **C. J. Lapeyre**, **G. Öztarlik**, **T. Poinsot**, **T. Schuller**, and **L. Selle** (2021). Detection of precursors of combustion instability using convolutional recurrent neural networks. *Combustion and Flame*, **233**, 111558.

36. **Chen, S.-T.**, **Y.-J. Guo**, **H.-N. Huang**, **W.-M. Kung**, **K.-K. Tseng**, and **S.-Y. Tu** (2014). Hiding patients confidential datainthe ecg signal viaa transform-domain quantization scheme. *Journal of Medical Systems*, **38**(6), 54.

37. **Chester, W.** (1964). Resonant oscillations in closed tubes. *Journal of Fluid Mechanics*, **18**, 44–64.

38. **Chiocchini, S.**, **T. Pagliaroli**, **R. Camussi**, and **E. Giacomazzi** (2018). Chaotic and linear statistics analysis in thermoacoustic instability detection. *Journal of Propulsion and Power*, **34**(1), 15–26.

39. **Chu, B.-T.** (1965). On the energy transfer to small disturbances in fluid flow (part i). *Acta Mechanica*, **1**(3), 215–234.

40. **Crocco, L.** (1951). Aspects of combustion stability in liquid propellant rocket motors part i: fundamentals. low frequency instability with monopropellants. *Journal of the American Rocket Society*, **21**(6), 163–178.

41. **Crocco, L.** (1952). Aspects of combustion stability in liquid propellant rocket motors part ii: Low frequency instability with bipropellants. high frequency instability. *Journal of the American Rocket Society*, **22**(1), 7–16.

42. **Crocco, L.** and **S. I. Cheng** (1956). *Theory of combustion instability in liquid propellant rocket motors*. Technical report, Princeton University.

43. **Culick, F.** (1970). Stability of longitudinal oscillations with pressure and velocity coupling in a solid propellant rocket. *Combustion Science and Technology*, **2**(4), 179–201.

44. **Culick, F.** (1994). Some recent results for nonlinear acoustics in combustion chambers. *AIAA Journal*, **32**(1), 146–169.

45. **Culick, F.**, **M. V. Heitor**, and **J. H. Whitelaw** (2012). *Unsteady combustion*, volume 306. Springer Science & Business Media.

46. **Culick, F.** and **P. Kuentzmann** (2006). *Unsteady motions in combustion chambers for propulsion systems*. Technical report, NATO Research and Technology Organization Neuilly-Sur-Seine (France).

47. **Culick, F. E.** (1966). Acoustic oscillations in solid propellant rocket chambers. *Astronautica Acta*, **12**(2), 113–126.

48. **Dansgaard, W.**, **S. Johnsen**, **H. Clausen**, **D. Dahl-Jensen**, **N. Gundestrup**, **C. Hammer**, and **H. Oeschger** (1984). North atlantic climatic oscillations revealed by deep greenland ice cores. *Climate processes and climate sensitivity*, **29**, 288–298.

49. **Davis, D. W.** and **B. Chehroudi** (2007). Measurements in an acoustically driven coaxial jet under sub-, near-, and supercritical conditions. *Journal of Propulsion and Power*, **23**(2), 364–374.

50. **Desroches, M.**, **J. Guckenheimer**, **B. Krauskopf**, **C. Kuehn**, **H. M. Osinga**, and **M. Wechselberger** (2012). Mixed-mode oscillations with multiple time scales. *Siam Review*, **54**(2), 211–288.

51. **Dhadphale, J.**, **V. R. Unni**, **A. Saha**, and **R. Sujith** (2021). Neural ode to model and prognose thermoacoustic instability. *arXiv preprint arXiv:2106.12758*.

52. **Díaz, M.**, **A. Jose**, **O. Téquita**, and **F. Naranjo** (2016). Neuronal synchronization of electrical activity, using the hodgkin-huxley model and rclsj circuit. *Ingeniería y Ciencia*, **12**(23), 93–103.

53. **Donner, R. V.**, **M. Small**, **J. F. Donges**, **N. Marwan**, **Y. Zou**, **R. Xiang**, and **J. Kurths** (2011). Recurrence-based time series analysis by means of complex network methods. *International Journal of Bifurcation and Chaos*, **21**(04), 1019–1046.

54. **Donner, R. V.**, **Y. Zou**, **J. F. Donges**, **N. Marwan**, and **J. Kurths** (2010). Recurrence networks—a novel paradigm for nonlinear time series analysis. *New Journal of Physics*, **12**(3), 033025.

55. **Dranovsky, M. L.** (2007). *Combustion instabilities in liquid rocket engines: testing and development practices in Russia*. American Institute of Aeronautics and Astronautics.

56. **Dresia, K.**, **G. Waxenegger-Wilfing**, **R. H. Dos Santos Hahn**, **J. C. Deeken**, and **M. Oschwald** (2021). Nonlinear control of an expander-bleed rocket engine using reinforcement learning. *In Space Propulsion 2020+1*. URL `https://elib.dlr.de/141739/`.

57. **Ebi, D.**, **A. Denisov**, **G. Bonciolini**, **E. Boujo**, and **N. Noiray** (2018). Flame dynamics intermittency in the bistable region near a subcritical hopf bifurcation. *Journal of Engineering for Gas Turbines and Power*, **140**(6), 061504.

58. **Eckmann, J.**, **S. O. Kamphorst**, **D. Ruelle**, *et al.* (1995). Recurrence plots of dynamical systems. *World Scientific Series on Nonlinear Science Series A*, **16**, 441–446.

59. **Emerson, B.**, **J. O'Connor**, **M. Juniper**, and **T. Lieuwen** (2012). Density ratio effects on reacting bluff-body flow field characteristics. *Journal of Fluid Mechanics*, **706**, 219–250, `doi:10.1017/jfm.2012.248`.

60. **Fabignon, Y.**, **J. Dupays**, **G. Avalon**, **F. Vuillot**, **N. Lupoglazoff**, **G. Casalis**, and **M. Prévost** (2003). Instabilities and pressure oscillations in solid rocket motors. *Aerospace science and technology*, **7**(3), 191–200.

61. **Feder, J.** (2013). *Fractals*. Springer Science & Business Media.

62. **Feldman, T.**, **M. Harvazinski**, **C. Merkle**, and **W. Anderson** (2012). Comparison between simulation and measurement of self-excited combustion instability. *In 48th AIAA/ASME/SAE/ASEE Joint Propulsion Conference & Exhibit*.

63. **Fichera, A.**, **C. Losenno**, and **A. Pagano** (2001). Experimental analysis of thermo-acoustic combustion instability. *Applied Energy*, **70**(2), 179–191.

64. **FitzHugh, R.** (1961). Impulses and physiological states in theoretical models of nerve membrane. *Biophysical journal*, **1**(6), 445–466.

65. **Flandro, G. A.**, **S. R. Fischbach**, and **J. Majdalani** (2007). Nonlinear rocket motor stability prediction: limit amplitude, triggering, and mean pressure shift. *Physics of Fluids*, **19**, 094–101, `doi:10.1063/1.2746042`.

66. **Flynn, T.**, **T. Fuller**, **S. Rufener**, **C. E. Finney**, and **C. S. Daw** (2017). Thermoacoustic vibrations in industrial furnaces and boilers. *In Proceedings of AFRC 2017 Industrial Combustion Symposium*.

67. **Fraser, A. M.** and **H. L. Swinney** (1986). Independent coordinates for strange attractors from mutual information. *Physical review A*, **33**(2), 1134.

68. **Fugger, C. A.**, **R. M. Gejji**, **J. E. Portillo**, **Y. Yu**, **R. P. Lucht**, and **W. E. Anderson** (2017). A model combustor for studying a reacting jet in an oscillating crossflow. *Review of Scientific Instruments*, **88**, 065112, `doi:https://doi.org/10.1063/1.4978415`.

69. **Fukushima, Y.**, **H. Nakatsuzi**, **R. Nagao**, **K. Kishimoto**, **K. Hasegawa**, **T. Koganezawa**, and **S. Warashina** (2002). Development status of LE-7A and LE-5B engines for H-IIA family. *Acta Astronautica*, **50**(5), 275–284.

70. **Gangopadhyay, T.**, **A. Locurto**, **J. B. Michael**, and **S. Sarkar** (2020). Deep learning algorithms for detecting combustion instabilities. *In Dynamics and Control of Energy Systems*, 283–300. Springer.

71. **Gao, Z.-K.**, **X.-W. Zhang**, **N.-D. Jin**, **R. V. Donner**, **N. Marwan**, and **J. Kurths** (2013). Recurrence networks from multivariate signals for uncovering dynamic transitions of horizontal oil-water stratified flows. *EPL (Europhysics Letters)*, **103**(5), 50004.

72. **Garby, R.**, **L. Selle**, and **T. Poinsot** (2013). Large-eddy simulation of combustion instabilities in a variable-length combustor. *Comptes Rendus Mécanique*, **341**(1-2), 220–229.

73. **Gejji, R.**, **W. E. Anderson**, and **B. L. Austin** (2019). Transverse combustion instabilities in a high pressure multi-element combustor. *In AIAA Propulsion and Energy 2019 Forum*.

74. **Gejji, R.**, **A. I. Lemcherfi**, **R. Strelau**, **C. D. Slabaugh**, and **W. E. Anderson** (2020). Combustion response of shear coaxial injectors to transverse combustion instabilities. *In AIAA Scitech 2020 Forum*. `doi:10.2514/6.2020-0424`.

75. **George, N. B.**, **V. R. Unni**, **M. Raghunathan**, and **R. I. Sujith** (2018). Pattern formation during transition from combustion noise to thermoacoustic instability via intermittency. *Journal of Fluid Mechanics*, **849**, 615–644.

76. **George, S. V.**, **R. Misra**, and **G. Ambika** (2019). Classification of close binary stars using recurrence networks. *arXiv preprint arXiv:1907.10602*.

77. **Glass, L.** (2001). Synchronization and rhythmic processes in physiology. *Nature*, **410**(6825), 277.

78. **Glenn Research Center** (2018). Apollo Era Testing. URL `https://www1.grc.nasa.gov/historic-facilities/rocket-engine-test-facility/apollo-era-testing/`.

79. **Godavarthi, V.**, **S. A. Pawar**, **V. R. Unni**, **R. I. Sujith**, **N. Marwan**, and **J. Kurths** (2018). Coupled interaction between unsteady flame dynamics and acoustic field in a turbulent combustor. *Chaos*, **28**, 113111.

80. **Godavarthi, V.**, **V. R. Unni**, **E. Gopalakrishnan**, and **R. I. Sujith** (2017). Recurrence networks to study dynamical transitions in a turbulent combustor. *Chaos*, **27**(6), 063113.

81. **Goetz, O. K.** and **J. C. Monk** (2005). Combustion device failures during space shuttle main engine development. *In Fifth International Symposium on Liquid Space Propulsion*.

82. **Gotoda, H.**, **Y. Shinoda**, **M. Kobayashi**, **Y. Okuno**, and **S. Tachibana** (2014). Detection and control of combustion instability based on the concept of dynamical system theory. *Physical Review E*, **89**, 022910.

83. **Govaert, T.**, **W. Armbruster**, **J. S. Hardi**, **D. Suslov**, **M. Oschwald**, and **B. T. Zandbergen** (2021). Wall heat loads in a cryogenic rocket thrust chamber during thermoacoustic instabilities. *Journal of Propulsion and Power*, 1–11.

84. **Grech, D.** and **Z. Mazur** (2013). Scaling range of power laws that originate from fluctuation analysis. *Physical Review E*, **87**(5), 052809.

85. **Grinsted, A.**, **J. C. Moore**, and **S. Jevrejeva** (2004). Application of the cross wavelet transform and wavelet coherence to geophysical time series. *Nonlinear processes in geophysics*, **11**, 561–566.

86. **Gröning, S.**, **J. S. Hardi**, **D. Suslov**, and **M. Oschwald** (2016). Injector-driven combustion instabilities in a hydrogen/oxygen rocket combustor. *Journal of Propulsion and Power*, **32**, 560–573, `doi:10.2514/1.B35768`.

87. **Gröning, S.**, **D. Suslov**, **J. Hardi**, and **M. Oschwald** (2014). Influence of hydrogen temperature on the acoustics of a rocket engine combustion chamber operated with LOx/H$_2$ at representative conditions. *In Space Propulsion 2014*. URL `https://elib.dlr.de/91649/`.

88. **Gröning, S.**, **D. Suslov**, **M. Oschwald**, and **T. Sattelmayer** (2013). Stability behaviour of a cylindrical rocket engine combustion chamber operated with liquid hydrogen and liquid oxygen. *Proceedings 5th EUCASS*.

89. **Guan, Y.**, **V. Gupta**, and **L. K. Li** (2020). Intermittency route to self-excited chaotic thermoacoustic oscillations. *Journal of Fluid Mechanics*, **894**.

90. **Guan, Y.**, **V. Gupta**, **M. Wan**, and **L. K. Li** (2019*a*). Forced synchronization of quasiperiodic oscillations in a thermoacoustic system. *Journal of Fluid Mechanics*, **879**, 390–421.

91. **Guan, Y.**, **L. K. Li**, **B. Ahn**, and **K. T. Kim** (2019*b*). Chaos, synchronization, and desynchronization in a liquid-fueled diffusion-flame combustor with an intrinsic hydrodynamic mode. *Chaos*, **29**(5), 053124.

92. **Guan, Y.**, **P. Liu**, **B. Jin**, **V. Gupta**, and **L. K. Li** (2018). Nonlinear time-series analysis of thermoacoustic oscillations in a solid rocket motor. *Experimental Thermal and Fluid Science*, **98**, 217–226.

93. **Hardi, J.**, **S. Gröning**, **S. Webster**, **S. Beinke**, **D. Suslov**, and **M. Oschwald** (2016*a*). Review of experimental test cases for modelling high frequency combustion instability. *In 52nd AIAA/SAE/ASEE Joint Propulsion Conference*.

94. **Hardi, J. S.** (2012). *Experimental investigation of high frequency combustion instability in cryogenic oxygen-hydrogen rocket engines.*. Doctoral thesis, School of Mechanical Engineering, The University of Adelaide.

95. **Hardi, J. S.**, **S. K. Beinke**, **M. Oschwald**, and **B. B. Dally** (2014*a*). Coupling of cryogenic oxygen–hydrogen flames to longitudinal and transverse acoustic instabilities. *Journal of Propulsion and Power*, **30**(4), 991–1004, `doi:10.2514/1.B35003`.

96. **Hardi, J. S.**, **H. C. G. Martinez**, **M. Oschwald**, and **B. B. Dally** (2014*b*). Lox jet atomization under transverse acoustic oscillations. *Journal of Propulsion and Power*, **30**(2), 337–349.

97. **Hardi, J. S.**, **W. Zach Hallum**, **C. Huang**, and **W. E. Anderson** (2016*b*). Approaches for comparing numerical simulation of combustion instability and flame imaging. *Journal of Propulsion and Power*, **32**(2), 279–294.

98. **Harrje, D. T.** and **F. H. Reardon** (1972). *Liquid propellant rocket combustion instability*. Scientific and Technical Information Office, National Aeronautics and Space Administration. Report: NASA-SP-194, https://ntrs.nasa.gov/citations/19720026079.

99. **Hart, R.**, **J. Bird**, **R. Cantrell**, and **F. McClure** (1964). Nonlinear effects in instability of solid-propellant rocket motors. *AIAA Journal*, **2**(7), 1270–1273.

100. **Hart, R.** and **F. McClure** (1959). Combustion instability: acoustic interaction with a burning propellant surface. *The journal of chemical physics*, **30**(6), 1501–1514.

101. **Harvazinski, M. E.**, **W. E. Anderson**, and **C. L. Merkle** (2013*a*). Analysis of self-excited combustion instabilities using two-and three-dimensional simulations. *Journal of Propulsion and Power*, **29**(2), 396–409.

102. **Harvazinski, M. E.**, **T. L. Fuller**, **W. E. Anderson**, **N. A. Arnold-Medabalimi**, and **C. Huang** (2020). Large eddy simulations of a liquid rocket injector under multiple operating conditions. *In AIAA Scitech 2020 Forum*.

103. **Harvazinski, M. E.**, **R. Gejji**, **D. G. Talley**, **M. R. Orth**, **W. E. Anderson**, and **T. L. Pourpoint** (2019). Modeling of transverse combustion instability. *In AIAA Scitech 2019 Forum*. San Diego, California, USA, `doi:10.2514/6.2019-1732`. Paper 1732.

104. **Harvazinski, M. E.**, **C. Huang**, **V. Sankaran**, **T. Feldman**, **W. Anderson**, **C. Merkle**, and **D. G. Talley** (2013*b*). Combustion instability mechanisms in a pressure-coupled gas-gas coaxial rocket injector. *In 49th AIAA/ASME/SAE/ASEE Joint PropulsionConference*, 3990. American Institute of Aeronautics and Astronautics.

105. **Harvazinski, M. E.**, **C. Huang**, **V. Sankaran**, **T. W. Feldman**, **W. E. Anderson**, **C. L. Merkle**, and **D. G. Talley** (2015). Coupling between hydrodynamics, acoustics, and heat release in a self-excited unstable combustor. *PHYS FLUIDS*, **27**, 045102.

106. **Hashimoto, T.**, **H. Shibuya**, **H. Gotoda**, **Y. Ohmichi**, and **S. Matsuyama** (2019). Spatiotemporal dynamics and early detection of thermoacoustic combustion instability in a model rocket combustor. *Physical Review E*, **99**(3), 032208.

107. **Heister, S. D.**, **W. E. Anderson**, **T. L. Pourpoint**, and **R. J. Cassady** (2019). *Rocket propulsion*, volume 47. Cambridge University Press.

108. **Henderson, B.** and **J. Lewis** (1989). Characteristics of combustion driven pressure oscillations in advanced turbo-fan engines with afterburner. *AGARD, Combustion Instabilities in Liquid-Fuelled Propulsion Systems 8 p(SEE N 90-10191 01-25)*.

109. **Hilborn, R. C.** *et al.* (2000). *Chaos and nonlinear dynamics: an introduction for scientists and engineers*. Oxford University Press.

110. **Hirschberg, A.**, **J. Gilbert**, **R. Msallam**, and **A. Wijnands** (1996). Shock waves in trombones. *The Journal of the Acoustical Society of America*, **99**(3), 1754–1758.

111. **Hołyst, J.**, **M. Żebrowska**, and **K. Urbanowicz** (2001). Observations of deterministic chaos in financial time series by recurrence plots, can one control chaotic economy? *The European Physical Journal B-Condensed Matter and Complex Systems*, **20**(4), 531–535.

112. **Huang, C.**, **W. E. Anderson**, **M. E. Harvazinski**, and **V. Sankaran** (2016). Analysis of self-excited combustion instabilities using decomposition techniques. *AIAA Journal*, **54**(9), 2791–2807.

113. **Huang, C.**, **J. Xu**, **K. Duraisamy**, and **C. Merkle** (2018). Exploration of reduced-order models for rocket combustion applications. *In 2018 AIAA Aerospace Sciences Meeting*.

114. **Iacobello, G.**, **L. Ridolfi**, and **S. Scarsoglio** (2020). A review on turbulent and vortical flow analyses via complex networks. *Physica A: Statistical Mechanics and its Applications*, 125476.

115. **Ihlen, E. A. F. E.** (2012). Introduction to multifractal detrended fluctuation analysis in matlab. *Frontiers in physiology*, **3**, 141.

116. **Indian Space Research Organization** (2021). *Annual Report 2020-21*. Report 2021, ISRO, Indian Space Research Organization. URL `https://www.isro.gov.in/2020-2021-english`.

117. **International Standards Organization** (2005). Measurement of Gas Flow by Means of Critical Flow Venturi Nozzles.

118. **Izhikevich, E. M.** (2003). Simple model of spiking neurons. *IEEE Transactions on neural networks*, **14**(6), 1569–1572.

119. **Izhikevich, E. M.** (2007). *Dynamical systems in neuroscience*. MIT press.

120. **Jahnke, C. C.** and **F. E. Culick** (1994). Application of dynamical systems theory to nonlinear combustion instabilities. *Journal of Propulsion and Power*, **10**(4), 508–517.

121. **Jegadeesan, V.** and **R. Sujith** (2013). Experimental investigation of noise induced triggering in thermoacoustic systems. *Proceedings of the Combustion Institute*, **34**(2), 3175–3183.

122. **Johnson, P.** and **A. Sutin** (2005). Slow dynamics and anomalous nonlinear fast dynamics in diverse solids. *The Journal of the Acoustical Society of America*, **117**(1), 124–130.

123. **Juniper, M. P.** and **R. I. Sujith** (2018). Sensitivity and nonlinearity of thermoacoustic oscillations. *Annual Review of Fluid Mechanics*, **50**, 661–689.

124. **Kabiraj, L.**, **R. I. Sujith**, and **P. Wahi** (2012). Bifurcations of self-excited ducted laminar premixed flames. *Journal of Engineering for Gas Turbines and Power*, **134**(3), 031502.

125. **Kachhara, S.** and **G. Ambika** (2019). Bimodality and scaling in recurrence networks from ecg data. *EPL (Europhysics Letters)*, **127**(6), 60004.

126. **Kantelhardt, J. W.**, **S. A. Zschiegner**, **E. Koscielny-Bunde**, **S. Havlin**, **A. Bunde**, and **H. E. Stanley** (2002). Multifractal detrended fluctuation analysis of nonstationary time series. *Physica A: Statistical Mechanics and its Applications*, **316**(1-4), 87–114.

127. **Kanthasamy, M.**, **G. Remesh**, **V. Narayanan**, **R. P. Thomas**, and **N. Kartha** (2014). Experimental studies for semi-cryo engine development. *Indian Journal of Cryogenics*, **39**(1), 106–116.

128. **Kantz, H.** and **T. Schreiber** (1998). Human ecg: nonlinear deterministic versus stochastic aspects. *IEE Proceedings-Science, Measurement and Technology*, **145**(6), 279–284.

129. **Karmarkar, A.**, **A. Tyagi**, **S. Hemchandra**, and **J. O'Connor** (2021). Impact of turbulence on the coherent flame dynamics in a bluff-body stabilized flame. *Proceedings of the Combustion Institute*, **38**(2), 3067–3075.

130. **Kasthuri, P.**, **V. R. Unni**, and **R. I. Sujith** (2019). Bursting and mixed mode oscillations during the transition to limit cycle oscillations in a matrix burner. *Chaos*, **29**(4), 043117.

131. **Katorgin, B.**, **V. Chvanov**, **F. Chelkis**, **I. Lozino-Lozinskaya**, and **L. Tanner** (1995). Oxidizer-rich staged combustion rocket engines use and development in russia. *In Space Programs and Technologies Conference*.

132. **Kheirkhah, S.**, **J. M. Cirtwill**, **P. Saini**, **K. Venkatesan**, and **A. M. Steinberg** (2017). Dynamics and mechanisms of pressure, heat release rate, and fuel spray coupling during intermittent thermoacoustic oscillations in a model aeronautical combustor at elevated pressure. *Combustion and Flame*, **185**, 319–334.

133. **Kitsche, W.** (2010). *Operation of a Cryogenic Rocket Engine: An Outline with Down-to-Earth and Up-to-Space Remarks*. Springer Science & Business Media.

134. **Kivelä, M.**, **A. Arenas**, **M. Barthelemy**, **J. P. Gleeson**, **Y. Moreno**, and **M. A. Porter** (2014). Multilayer networks. *Journal of Complex Networks*, **2**(3), 203–271.

135. **Kline, S.** and **F. McClintock** (1953). Describing Uncertainties in Single-Sample Experiments. *Mechanical Engineering*, **75**(January), 3–8.

136. **Knapp, B.**, **Z. Farago**, and **M. Oschwald** (2007). Interaction of LOx/GH$_2$ spray-combustion with acoustics. *In 45th AIAA Aerospace Sciences Meeting and Exhibit*. Reno, Nevada, USA, `doi:10.2514/6.2007-572`. Paper 572.

137. **Kobayashi, T.**, **S. Murayama**, **T. Hachijo**, and **H. Gotoda** (2019). Early detection of thermoacoustic combustion instability using a methodology combining complex networks and machine learning. *Physical Review Applied*, **11**(6), 064034.

138. **Kraemer, K. H.**, **R. V. Donner**, **J. Heitzig**, and **N. Marwan** (2018). Recurrence threshold selection for obtaining robust recurrence characteristics in different embedding dimensions. *Chaos*, **28**(8), 085720.

139. **Kraemer, K. H.** and **N. Marwan** (2019). Border effect corrections for diagonal line based recurrence quantification analysis measures. *Physics Letters A*, 125977.

140. **Krishnan, A.**, **R. Manikandan**, **P. Midhun**, **K. Reeja**, **V. Unni**, **R. I. Sujith**, **N. Marwan**, and **J. Kurths** (2019*a*). Mitigation of oscillatory instability in turbulent reactive flows: A novel approach using complex networks. *EPL (Europhysics Letters)*, **128**(1), 14003.

141. **Krishnan, A.**, **R. I. Sujith**, **N. Marwan**, and **J. Kurths** (2019*b*). On the emergence of large clusters of acoustic power sources at the onset of thermoacoustic instability in a turbulent combustor. *Journal of Fluid Mechanics*, **874**, 455–482.

142. **Krishnan, A.**, **R. I. Sujith**, **N. Marwan**, and **J. Kurths** (2021). Suppression of thermoacoustic instability by targeting the hubs of the turbulent networks in a bluff body stabilized combustor. *Journal of Fluid Mechanics*, **916**.

143. **Kuehn, C.** (2015). *Multiple time scale dynamics*, volume 191. Springer.

144. **Lakshmanan, M.** and **D. V. Senthilkumar** (2011). *Dynamics of nonlinear time-delay systems*. Springer Science & Business Media.

145. **Langel, G.**, **E. Laudien**, **R. Pongratz**, **M. Habiballah**, **S. Grand-Perret**, **L. Vingert**, and **.-C. F. Office National d'Etudes et de Recherches Aerospatiales (ONERA)** (1991). Combustion stability characteristics of the ariane 5 l7 engine. *In 42nd Congress of the International Astronautical Federation, Paper Number: IAF-91-250, Montreal, Canada*.

146. **Lazer, A. C.** and **P. McKenna** (1990). Large-amplitude periodic oscillations in suspension bridges: some new connections with nonlinear analysis. *Siam Review*, **32**(4), 537–578.

147. **Leeman, J.**, **D. Saffer**, **M. Scuderi**, and **C. Marone** (2016). Laboratory observations of slow earthquakes and the spectrum of tectonic fault slip modes. *Nature communications*, **7**, 11104.

148. **Lieuwen, T. C.** (2002). Experimental investigation of limit-cycle oscillations in an unstable gas turbine combustor. *Journal of Propulsion and Power*, **18**(1), 61–67.

149. **Lieuwen, T. C.** (2012). *Unsteady combustor physics*. Cambridge University Press, `doi:10.1017/CBO9781139059961`.

150. **Lieuwen, T. C.** and **V. Yang** (2005). *Combustion instabilities in gas turbine engines: operational experience, fundamental mechanisms, and modeling*. American Institute of Aeronautics and Astronautics.

151. **Lordon, F.** (1997). Endogenous structural change and crisis in a multiple time-scales growth model. *Journal of Evolutionary Economics*, **7**(1), 1–21.

152. **Lorente, A. P.**, **T. Fuller**, **S. V. Sardeshmukh**, and **W. E. Anderson** (2018). Analysis of the interactions between acoustics and unsteady heat release in a self-excited single element combustor. *In 2018 Joint Propulsion Conference*.

153. **Mandelbrot, B.** (1967). How long is the coast of britain? statistical self-similarity and fractional dimension. *science*, **156**(3775), 636–638.

154. **Mandelbrot, B. B.** (1983). *The fractal geometry of nature*, volume 173. WH Freeman New York.

155. **Manski, D.**, **C. Goertz**, **H.-D. Saßnick**, **J. R. Hulka**, **B. D. Goracke**, and **D. J. Levack** (1998). Cycles for earth-to-orbit propulsion. *Journal of Propulsion and Power*, **14**(5), 588–604.

156. **Marble, F. E.** and **D. W. Cox Jr** (1953). Servo-stabilization of low-frequency oscillations in a liquid bipropellant rocket motor. *Journal of the American Rocket Society*, **23**(2), 63–74.

157. **Martin, J.**, **W. Armbruster**, **J. S. Hardi**, **D. Suslov**, and **M. Oschwald** (2021). Experimental investigation of self-excited combustion instabilities in a lox/lng rocket combustor. *Journal of Propulsion and Power*, 1–8.

158. **Marwan, N.** (2003). *Encounters with neighbours: current developments of concepts based on recurrence plots and their applications*. Doctoral thesis, University of Potsdam.

159. **Marwan, N.** (2008). A historical review of recurrence plots. *The European Physical Journal Special Topics*, **164**(1), 3–12.

160. **Marwan, N.**, **J. F. Donges**, **Y. Zou**, **R. V. Donner**, and **J. Kurths** (2009). Complex network approach for recurrence analysis of time series. *Physics Letters A*, **373**(46), 4246–4254.

161. **Marwan, N.**, **M. C. Romano**, **M. Thiel**, and **J. Kurths** (2007). Recurrence plots for the analysis of complex systems. *Physics Reports*, **438**, 237–329.

162. **Matsuyama, S.**, **D. Hori**, **T. Shimizu**, **S. Tachibana**, **S. Yoshida**, and **Y. Mizobuchi** (2016). Large-eddy simulation of high-frequency combustion instability in a single-element atmospheric combustor. *Journal of Propulsion and Power*, **32**(3), 628–645.

163. **Méry, Y.** (2017). Impact of heat release global fluctuations and flame motion on transverse acoustic wave stability. *Proceedings of the Combustion Institute*, **36**, 3889–3898.

164. **Méry, Y.**, **L. Hakim**, **P. Scouflaire**, **L. Vingert**, **S. Ducruix**, and **S. Candel** (2013). Experimental investigation of cryogenic flame dynamics under transverse acoustic modulations. *Comptes Rendus Mécanique*, **341**(1-2), 100–109.

165. **Messineo, J.**, **J.-Y. Lestrade**, **J. Hijlkema**, and **J. Anthoine** (2016). Vortex shedding influence on hybrid rocket pressure oscillations and combustion efficiency. *Journal of Propulsion and Power*, **32**(6), 1386–1394.

166. **Miller, K.**, **J. Sisco**, **N. Nugent**, and **W. Anderson** (2007). Combustion instability with a single-element swirl injector. *Journal of Propulsion and Power*, **23**(5), 1102–1112.

167. **Millman, J.** (2010). *Integrated electronics*. Tata McGraw Hill.

168. **Mitchell, C.**, **L. Crocco**, and **W. Sirignano** (1969). Nonlinear longitudinal instability in rocket motors with concentrated combustion. *Combustion Science and Technology*, **1**(1), 35–64.

169. **Mondal, S.**, **S. Pawar**, and **R. I. Sujith** (2017*a*). Synchronous behaviour of two interacting oscillatory systems undergoing quasiperiodic route to chaos. *Chaos*, **27**(10), 103119.

170. **Mondal, S.**, **V. R. Unni**, and **R. I. Sujith** (2017*b*). Onset of thermoacoustic instability in turbulent combustors: an emergence of synchronized periodicity through formation of chimera-like states. *Journal of Fluid Mechanics*, **811**, 659–681.

171. **Morea, S.** and **S. Johnson** (2012). NASA MSFC Oral History Interview Steve Johnson Interviews – Apollo/Saturn Program. URL https://www.nasa.gov/sites/default/files/atoms/files/smorea.pdf.

172. **Morfey, C.** (1971). Acoustic energy in non-uniform flows. *Journal of Sound and Vibration*, **14**(2), 159–170.

173. **Morgan, C. J.**, **K. J. Shipley**, and **W. E. Anderson** (2015). Comparative evaluation between experiment and simulation for a transverse instability. *Journal of Propulsion and Power*, **31**, 1696–1706.

174. **Murayama, S.** and **H. Gotoda** (2019). Attenuation behavior of thermoacoustic combustion instability analyzed by a complex-network-and synchronization-based approach. *Physical Review E*, **99**(5), 052222.

175. **Murugesan, M.** and **R. I. Sujith** (2015). Combustion noise is scale-free: transition from scale-free to order at the onset of thermoacoustic instability. *Journal of Fluid Mechanics*, **772**, 225–245.

176. **Myers, M. K.** (1991). Transport of energy by disturbances in arbitrary steady flows. *Journal of Fluid Mechanics*, **226**, 383–400.

177. **Nair, V.** and **R. I. Sujith** (2014). Multifractality in combustion noise: predicting an impending combustion instability. *Journal of Fluid Mechanics*, **747**, 635–655.

178. **Nair, V.**, **G. Thampi**, **S. Karuppusamy**, **S. Gopalan**, and **R. I. Sujith** (2013). Loss of chaos in combustion noise as a precursor of impending combustion instability. *International journal of spray and combustion dynamics*, **5**(4), 273–290.

179. **Nair, V.**, **G. Thampi**, and **R. I. Sujith** (2014). Intermittency route to thermoacoustic instability in turbulent combustors. *Journal of Fluid Mechanics*, **756**, 470–487.

180. **NASA's Marshall Space Flight Center** (2019). Marshall Remembers Apollo: Saverio "Sonny" Morea. URL `https://www.youtube.com/watch?v=nw3w-KvQgY4`.

181. **Natanzon, M. S.** (2008). *Combustion instability*. American Institute of Aeronautics and Astronautics.

182. **Nayfeh, A. H.** and **B. Balachandran** (2008). *Applied nonlinear dynamics: analytical, computational, and experimental methods*. John Wiley & Sons.

183. **Newman, M.** (2018). *Networks*. Oxford university press.

184. **Newman, M. E.** (2002). Assortative mixing in networks. *Physical review letters*, **89**(20), 208701.

185. **Nicoud, F.** and **T. Poinsot** (2005). Thermoacoustic instabilities: Should the rayleigh criterion be extended to include entropy changes? *Combustion and Flame*, **142**(1-2), 153–159.

186. **Nikulin, V. V.** and **T. Brismar** (2006). Phase synchronization between alpha and beta oscillations in the human electroencephalogram. *Neuroscience*, **137**(2), 647–657.

187. **Nunome, Y.**, **T. Onodera**, **M. Sasaki**, **T. Tomita**, **K. Kobayashi**, and **Y. Daimon** (2011). Combustion instability phenomena observed during cryogenic hydrogen injection temperature ramping tests for single coaxial injector elements. *In 47th AIAA/ASME/SAE/ASEE Joint Propulsion Conference & Exhibit*.

188. **O'Connor, J.**, **V. Acharya**, and **T. Lieuwen** (2015). Transverse combustion instabilities: Acoustic, fluid mechanic, and flame processes. *Progress in Energy and Combustion Science*, **49**, 1–39.

189. **Oefelein, J. C.** and **V. Yang** (1993). Comprehensive review of liquid-propellant combustion instabilities in F-1 engines. *Journal of Propulsion and Power*, **9**(5), 657–677.

190. **Okuno, Y.**, **M. Small**, and **H. Gotoda** (2015). Dynamics of self-excited thermoacoustic instability in a combustion system: Pseudo-periodic and high-dimensional nature. *Chaos*, **25**(4), 043107.

191. **Orth, M. R.**, **C. Vodney**, **T. Liu**, **W. Z. Hallum**, **T. L. Pourpoint**, and **W. E. Anderson** (2018). Measurement of linear growth of self-excited instabilities in an idealized rocket combustor. *In 2018 AIAA Aerospace Sciences Meeting*. Kissimmee, Florida, USA, `doi:10.2514/6.2018-1185`. Paper 1185.

192. **Oschwald, M.** and **B. Knapp** (2009). Investigation of combustion chamber acoustics and its interaction with LOX/H$_2$ spray flames. *Progress in Propulsion Physics*, **1**, 205–224.

193. **Pant, T.**, **C. Han**, and **H. Wang** (2019). Computational investigations of the coupling between transient flame dynamics and thermo-acoustic instability in a self-excited resonance combustor. *Combustion Theory and Modelling*, **23**, 854–884.

194. **Pastor-Satorras, R.**, **A. Vázquez**, and **A. Vespignani** (2001). Dynamical and correlation properties of the internet. *Physical Review Letters*, **87**(25), 258701.

195. **Pavithran, I.**, **V. R. Unni**, and **R. I. Sujith** (2021). Critical transitions and their early warning signals in thermoacoustic systems. *The European Physical Journal Special Topics*, 1–22, `doi:10.1140/epjs/s11734-021-00214-w`.

196. **Pawar, S. A.**, **S. Mondal**, **N. B. George**, and **R. I. Sujith** (2018). Temporal and spatiotemporal analyses of synchronization transition in a swirl-stabilized combustor. *AIAA Journal*, **57**, 836–847.

197. **Pawar, S. A.**, **A. Seshadri**, **V. R. Unni**, and **R. I. Sujith** (2017). Thermoacoustic instability as mutual synchronization between the acoustic field of the confinement and turbulent reactive flow. *Journal of Fluid Mechanics*, **827**, 664–693.

198. **Pawar, S. A.** and **R. I. Sujith** (2018). Intermittency: A state that precedes thermoacoustic instability. *In Droplets and Sprays*, 403–430. Springer.

199. **Pawar, S. A.**, **R. Vishnu**, **M. Vadivukkarasan**, **M. Panchagnula**, and **R. I. Sujith** (2016). Intermittency route to combustion instability in a laboratory spray combustor. *Journal of Engineering for Gas Turbines and Power*, **138**(4), 041505.

200. **Pecora, L. M.** and **T. L. Carroll** (2015). Synchronization of chaotic systems. *Chaos*, **25**(9), 097611.

201. **Peracchio, A. A.** and **W. M. Proscia** (1999). Nonlinear heat-release/acoustic model for thermoacoustic instability in lean premixed combustors. *Journal of Engineering for Gas Turbines and Power*, **121**(3), 415–421.

202. **Percival, D. B.** and **A. T. Walden** (2000). *Wavelet methods for time series analysis*, volume 4. Cambridge university press.

203. **Pikovsky, A.**, **M. Rosenblum**, **J. Kurths**, and **J. Kurths** (2003). *Synchronization: a universal concept in nonlinear sciences*, volume 12. Cambridge university press.

204. **Poinsot, T.** (2017). Prediction and control of combustion instabilities in real engines. *Proceedings of the Combustion Institute*, **36**(1), 1–28.

205. **Poinsot, T. J.**, **A. C. Trouve**, **D. P. Veynante**, **S. M. Candel**, and **E. J. Esposito** (1987). Vortex-driven acoustically coupled combustion instabilities. *Journal of Fluid Mechanics*, **177**, 265–292.

206. **Pomeroy, B.** and **W. Anderson** (2016). Transverse instability studies in a subscale chamber. *Journal of Propulsion and Power*, **32**(4), 939–947, `doi:10.2514/1.B35763`.

207. **Popov, P. P.** and **W. A. Sirignano** (2016). Transverse combustion instability in a rectangular rocket motor. *Journal of Propulsion and Power*, **32**(1), 620–627, `doi:10.2514/1.B35868`.

208. **Price, E.** (1984). Experimental observations of combustion instability. *Fundamentals of Solid-Propellant Combustion*, **90**, 733–790.

209. **Putnam, A. A.** and **W. R. Dennis** (1956). Survey of organ-pipe oscillations in combustion systems. *The Journal of the Acoustical Society of America*, **28**(2), 246–259.

210. **Rayleigh, J. W. S.** (1878). The explanation of certain acoustical phenomena. *Nature*, **18**, 319–321.

211. **Reardon, F.**, **L. Crocco**, and **D. Harrje** (1964). Velocity effects in transverse mode liquid propellant rocket combustion instability. *AIAA Journal*, **2**(9), 1631–1641.

212. **Rey, C.**, **S. Ducruix**, **P. Scouflaire**, **F. Richecoeur**, **L. Vingert**, and **S. Candel** (2004). High frequency combustion instabilities associated with collective interactions in liquid propulsion. *In 40th AIAA/ASME/SAE/ASEE Joint Propulsion Conference and Exhibit*. Fort Lauderdale, Florida, USA, `doi:10.2514/6.2004-3518`. Paper 3518.

213. **Richecoeur, F.**, **P. Scouflaire**, **S. Ducruix**, and **S. Candel** (2006). High-frequency transverse acoustic coupling in a multiple-injector cryogenic combustor. *Journal of Propulsion and Power*, **22**, 790–799, `doi:10.2514/1.18539`.

214. **Rogers, D. E.** and **F. E. Marble** (1956). A mechanism for high-frequency oscillation in ramjet combustors and afterburners. *Journal of Jet Propulsion*, **26**(6), 456–462.

215. **Rohit, G.**, **M. Kanthasamy**, **G. Remesh**, **V. Narayanan**, **R. P. Thomas**, and **N. Kartha** (2013). Design, development and testing ofinjector for subsystem development of semi cryogenic engine thrust chamber. *International Journal of Innovative Research in Science, Engineering and Technology*.

216. **Romano, M. C.**, **M. Thiel**, **J. Kurths**, **I. Z. Kiss**, and **J. Hudson** (2005). Detection of synchronization for non-phase-coherent and non-stationary data. *EPL (Europhysics Letters)*, **71**, 466–472.

217. **Roy, A.**, **S. Mondal**, **S. A. Pawar**, and **R. I. Sujith** (2020). On the mechanism of open-loop control of thermoacoustic instability in a laminar premixed combustor. *Journal of Fluid Mechanics*, **884**.

218. **Rubin, S.** (1966). Longitudinal instability of liquid rockets due to propulsion feedback/pogo/. *Journal of Spacecraft and Rockets*, **3**(8), 1188–1195.

219. **Ruiz, E. A.**, **V. R. Unni**, **I. Pavithran**, **R. Sujith**, and **A. Saha** (2021). Convolutional neural networks to predict the onset of oscillatory instabilities in turbulent systems. *Chaos*, **31**(9), 093131.

220. **Saenger, R. A.** and **G. E. Hudson** (1960). Periodic shock waves in resonating gas columns. *The Journal of Acoustical Society of America*, **32**, 961–970.

221. **Sahay, A.**, **A. Roy**, **S. A. Pawar**, and **R. I. Sujith** (2021). Dynamics of coupled thermoacoustic oscillators under asymmetric forcing. *Physical Review Applied*, **15**(4), 044011.

222. **Sardeshmukh, S.**, **M. Bedard**, and **W. Anderson** (2017). The use of OH* and CH* as heat release markers in combustion dynamics. *International Journal of Spray and Combustion Dynamics*, **9**(4), 409–423.

223. **Sardeshmukh, S.**, **C. Huang**, **R. Gejji**, **M. Bedard**, **Z. Hallum**, **R. Lucht**, and **W. Anderson** (2020). High-pressure experiments relevant to rocket propulsion. *In High-Pressure Flows for Propulsion Applications*, 183–232. American Institute of Aeronautics and Astronautics.

224. **Sardeshmukh, S.**, **C. Huang**, **R. Gejji**, **M. Bedard**, **Z. Hallum**, **R. Lucht**, and **W. E. Anderson** (2019). High-pressure experiments relevant to rocket propulsion. *High Pressure Flows for Propulsion Applications*, 183–232.

225. **Sardeshmukh, S. V.**, **S. D. Heister**, and **W. E. Anderson** (2015). Prediction of combustion instability with detailed chemical kinetics. *In 53rd AIAA Aerospace Sciences Meeting*.

226. **Schäfer, C.**, **M. G. Rosenblum**, **H.-H. Abel**, and **J. Kurths** (1999). Synchronization in the human cardiorespiratory system. *Physical Review E*, **60**(1), 857.

227. **Scherer, K. R.** (2000). *Emotion, Development, and Self-Organization: Dynamic Systems Approaches to Emotional Development*, chapter Emotions as Episodes of Subsystem Synchronization Driven by Nonlinear Appraisal Processes, 70–99. Cambridge Studies in Social and Emotional Development. Cambridge University Press.

228. **Schumacher, R. T.**, **S. Garoff**, and **J. Woodhouse** (2005). Probing the physics of slip–stick friction using a bowed string. *The Journal of Adhesion*, **81**(7-8), 723–750.

229. **Schwabacher, M.** (2005). Machine learning for rocket propulsion health monitoring. *SAE transactions*, 1192–1197.

230. **Selle, L.**, **R. Blouquin**, **M. Théron**, **L.-H. Dorey**, **M. Schmid**, and **W. Anderson** (2014). Prediction and analysis of combustion instabilities in a model rocket engine. *Journal of Propulsion and Power*, **30**(4), 978–990.

231. **Sengupta, U.**, **G. Waxenegger-Wilfing**, **J. Hardi**, and **M. P. Juniper** (2021). Forecasting thermoacoustic instabilities in liquid propellant rocket engines using multimodal bayesian deep learning. *arXiv preprint arXiv:2107.06396*.

232. **Seshadri, A.**, **V. Nair**, and **R. I. Sujith** (2016). A reduced-order deterministic model describing an intermittency route to combustion instability. *Combustion Theory and Modelling*, **20**(3), 441–456.

233. **Shanbhogue, S.**, **D.-H. Shin**, **S. Hemchandra**, **D. Plaks**, and **T. Lieuwen** (2009). Flame-sheet dynamics of bluff-body stabilized flames during longitudinal acoustic forcing. *Proceedings of the Combustion Institute*, **32**(2), 1787–1794.

234. **Shima, S.**, **K. Nakamura**, **H. Gotoda**, **Y. Ohmichi**, and **S. Matsuyama** (2021). Formation mechanism of high-frequency combustion oscillations in a model rocket engine combustor. *Physics of Fluids*, **33**(6), 064108.

235. **Siapas, A. G.**, **E. V. Lubenov**, and **M. A. Wilson** (2005). Prefrontal phase locking to hippocampal theta oscillations. *Neuron*, **46**(1), 141–151.

236. **Sirignano, W. A.** (1964). *A theoretical study of nonlinear combustion instability: longitudinal mode*. Doctoral thesis, Princeton University.

237. **Sirignano, W. A.** (2015). Driving mechanisms for combustion instability. *Combustion Science and Technology*, **187**, 162–205.

238. **Sisco, J. C.**, **Y. Yu**, **V. Sankaran**, and **W. E. Anderson** (2011). Examination of mode shapes in an unstable model combustor. *Journal of Sound and Vibration*, **330**(1), 61–74.

239. **Sliphorst, M.**, **G. Stefan**, **B. Knapp**, and **M. Oschwald** (2011). Combustion instability coupling mechanisms between acoustics and lox/ch4 spray flames. *In 49th AIAA Aerospace Sciences Meeting including the New Horizons Forum and Aerospace Exposition*.

240. **Sohn, C. H.**, **W. S. Seol**, **A. A. Shibanov**, and **V. P. Pikalov** (2007). Combustion stability boundaries of the subscale rocket chamber with impinging jet injectors. *Journal of Propulsion and Power*, **23**(1), 131–139.

241. **Souchier, A.**, **C. Rothmund**, **P. Leven**, and **J. Hagberg** (1999). The development of the viking engine. *In 35th Joint Propulsion Conference and Exhibit*.

242. **Sterling, J. D.** (1993). Nonlinear analysis and modelling of combustion instabilities in a laboratory combustor. *Combustion Science and Technology*, **89**(1-4), 167–179.

243. **Strogatz, S. H.** (2018). *Nonlinear dynamics and chaos: with applications to physics, biology, chemistry, and engineering*. CRC Press.

244. **Sujith, R.**, **G. Waldherr**, and **B. Zinn** (1995). An exact solution for one-dimensional acoustic fields in ducts with an axial temperature gradient. *Journal of Sound and Vibration*, **184**(3), 389–402.

245. **Sujith, R. I.** and **S. A. Pawar** (2021). *Thermoacoustic Instability: A Complex Systems Perspective*. Springer Nature.

246. **Sujith, R. I.** and **V. R. Unni** (2020*a*). Complex system approach to investigate and mitigate thermoacoustic instability in turbulent combustors. *Physics of Fluids*, **32**(6), 061401, doi:10.1063/5.0003702.

247. **Sujith, R. I.** and **V. R. Unni** (2020*b*). Dynamical systems and complex systems theory to study unsteady combustion. *Proceedings of the Combustion Institute*, `doi:10.1016/j.proci.2020.07.081`.

248. **Summerfield, M.** (1951). A theory of unstable combustion in liquid propellant rocket systems. *Journal of the American Rocket Society*, **21**(5), 108–114.

249. **Suresh, M.** (2021). Development of turbopump systems for cryogenic and semicryogenic propulsion systems of isro. *Transactions of the Indian National Academy of Engineering*, **6**(2), 229–241.

250. **Suresha, S.**, **R. I. Sujith**, **B. Emerson**, and **T. Lieuwen** (2016). Nonlinear dynamics and intermittency in a turbulent reacting wake with density ratio as bifurcation parameter. *Physical Review E*, **94**(4), 042206.

251. **Sutton, G. P.** (2005). *History of liquid propellant rocket engines*. American Institute of Aeronautics and Astronautics.

252. **Sutton, G. P.** and **O. Biblarz** (2016). *Rocket propulsion elements*. John Wiley & Sons.

253. **Suyal, V.**, **A. Prasad**, and **H. P. Singh** (2009). Nonlinear time series analysis of sunspot data. *Solar Physics*, **260**(2), 441–449.

254. **Takens, F.** (1981). Detecting strange attractors in turbulence. *In Dynamical systems and turbulence*, 366–381. Springer.

255. **Tandon, S.** and **R. I. Sujith** (2021). Condensation in the phase space and network topology during transition from chaos to order in turbulent thermoacoustic systems. *Chaos*, **31**(4), 043126.

256. **Thannickal, V. M.**, **T. J. Tharakan**, and **S. R. Chakravarthy** (2021). Active control of combustion noise by a twin resonator trim adjustment system. *Combustion Science and Technology*, 1–24.

257. **Tony, J.**, **E. Gopalakrishnan**, **E. Sreelekha**, and **R. I. Sujith** (2015). Detecting deterministic nature of pressure measurements from a turbulent combustor. *Physical Review E*, **92**(6), 062902.

258. **Tsien, H.** (1952). Servo-stabilization of combustion in rocket motors. *Journal of the American Rocket Society*, **22**(5), 256–262.

259. **Tyagi, M.** and **R. I. Sujith** (2003*a*). Nonlinear distortion of travelling waves in variable-area ducts with entropy gradients. *Journal of Fluid Mechanics*, **492**, 1–22.

260. **Tyagi, M.** and **R. I. Sujith** (2003*b*). Resonant standing waves in oscillating closed horns. *In 9th AIAA/CEAS Aeroacoustics Conference and Exhibit*.

261. **Unni, V. R.**, **A. Krishnan**, **R. Manikandan**, **N. B. George**, **R. I. Sujith**, **N. Marwan**, and **J. Kurths** (2018). On the emergence of critical regions at the onset of thermoacoustic instability in a turbulent combustor. *Chaos*, **28**(6), 063125.

262. **Unni, V. R.** and **R. I. Sujith** (2016). Precursors to blowout in a turbulent combustor based on recurrence quantification. *In 52nd AIAA/SAE/ASEE Joint Propulsion Conference*.

263. **Unni, V. R.** and **R. I. Sujith** (2017). Flame dynamics during intermittency in a turbulent combustor. *Proceedings of the Combustion Institute*, **36**(3), 3791–3798.

264. **Urbano, A.**, **Q. Douasbin**, **L. Selle**, **G. Staffelbach**, **B. Cuenot**, **T. Schmitt**, **S. Ducruix**, and **S. Candel** (2017). Study of flame response to transverse acoustic modes from the les of a 42-injector rocket engine. *Proceedings of the Combustion Institute*, **36**(2), 2633–2639.

265. **Urbano, A.**, **L. Selle**, **G. Staffelbach**, **B. Cuenot**, **T. Schmitt**, **S. Ducruix**, and **S. Candel** (2016). Exploration of combustion instability triggering using large eddy simulation of a multiple injector liquid rocket engine. *Combustion and Flame*, **169**, 129–140, `doi:10.1016/j.combustflame.2016.03.020`.

266. **Vallaitis, T.**, **C. Koos**, **R. Bonk**, **W. Freude**, **M. Laemmlin**, **C. Meuer**, **D. Bimberg**, and **J. Leuthold** (2008). Slow and fast dynamics of gain and phase in a quantum dot semiconductor optical amplifier. *Optics express*, **16**(1), 170–178.

267. **Van der Pol, B.** (1926). Lxxxviii. on "relaxation-oscillations". *The London, Edinburgh, and Dublin Philosophical Magazine and Journal of Science*, **2**(11), 978–992.

268. **Vettoretti, G.** and **W. R. Peltier** (2018). Fast physics and slow physics in the nonlinear dansgaard–oeschger relaxation oscillation. *Journal of Climate*, **31**(9), 3423–3449.

269. **Walters, I. V.**, **C. L. Journell**, **A. Lemcherfi**, **R. M. Gejji**, **S. D. Heister**, and **C. D. Slabaugh** (2020). Operability of a natural gas–air rotating detonation engine. *Journal of Propulsion and Power*, **36**, 453–464, `doi:10.2514/1.B37735`.

270. **Wang, D.** and **D. Terman** (1995). Locally excitatory globally inhibitory oscillator networks. *IEEE transactions on neural networks*, **6**(1), 283–286.

271. **Watanabe, D.**, **H. Manako**, **T. Onga**, **T. Tamura**, **K. Ikeda**, and **M. Isono** (2016). Combustion stability improvement of LE-9 engine for booster stage of H3 launch vehicle. *Mitsubishi Heavy Industries Technical Review*, **53**(4), 28.

272. **Waxenegger-Wilfing, G.**, **K. Dresia**, **J. Deeken**, and **M. Oschwald** (2021*a*). Machine learning methods for the design and operation of liquid rocket engines–research activities at the DLR institute of space propulsion. *arXiv preprint arXiv:2102.07109*.

273. **Waxenegger-Wilfing, G.**, **U. Sengupta**, **J. Martin**, **W. Armbruster**, **J. Hardi**, **M. Juniper**, and **M. Oschwald** (2021*b*). Early detection of thermoacoustic instabilities in a cryogenic rocket thrust chamber using combustion noise features and machine learning. *Chaos*, **31**(6), 063128.

274. **Webber Jr, C.** and **J. Zbilut** (1995). Quantification of cardiac nondeterminism using recurrence plot strategies. *In Society of Neuroscience Abstracts*, volume 21.

275. **Webber Jr, C. L.** and **N. Marwan** (2015). *Recurrence quantification analysis*. Springer.

276. **Weinzierl, M.** (2018). Space, the final economic frontier. *Journal of Economic Perspectives*, **32**(2), 173–92.

277. **Williams, F. A.** (2018). *Combustion theory*. CRC Press.

278. **Xia, G.**, **M. Harvazinski**, **W. Anderson**, and **C. Merkle** (2011). Investigation of modeling and physical parameters on instability prediction in a model rocket combustor. *In 47th AIAA/ASME/SAE/ASEE Joint Propulsion Conference & Exhibit*.

279. **Yu, Y. C.**, **J. C. Sisco**, **S. Rosen**, **A. Madhav**, and **W. E. Anderson** (2012). Spontaneous longitudinal combustion instability in a continuously-variable resonance combustor. *Journal of Propulsion and Power*, **28**(5), 876–887.

280. **Zhabotinsky, A. M.** (1991). A history of chemical oscillations and waves. *Chaos*, **1**(4), 379–386.

281. **Zhao, D.**, **Z. Lu**, **H. Zhao**, **X. Li**, **B. Wang**, and **P. Liu** (2018). A review of active control approaches in stabilizing combustion systems in aerospace industry. *Progress in Aerospace Sciences*, **97**, 35–60.

282. **Zia, R. K.**, **E. F. Redish**, and **S. R. McKay** (2009). Making sense of the legendre transform. *American Journal of Physics*, **77**(7), 614–622.

283. **Zinn, B.** (1968). A theoretical study of nonlinear combustion instability in liquid-propellant rocket engines. *AIAA Journal*, **6**(10), 1966–1972.

284. **Zinn, B. T.** and **M. E. Lores** (1971). Application of the galerkin method in the solution of non-linear axial combustion instability problems in liquid rockets. *Combustion Science and Technology*, **4**(1), 269–278.

285. **Zinn, B. T.** and **E. A. Powell** (1971). Nonlinear combustion instability in liquid-propellant rocket engines. *Symposium (international) on combustion*, **13**(1), 491–503.

286. **Zou, Y.**, **R. V. Donner**, **J. F. Donges**, **N. Marwan**, and **J. Kurths** (2010). Identifying complex periodic windows in continuous-time dynamical systems using recurrence-based methods. *Chaos: An Interdisciplinary Journal of Nonlinear Science*, **20**(4), 043130.

287. **Zou, Y.**, **R. V. Donner**, **N. Marwan**, **J. F. Donges**, and **J. Kurths** (2018). Complex network approaches to nonlinear time series analysis. *Physics Reports*.

288. **Zukoski, E.** (1985). Combustion instability sustained by unsteady vortex combustion. *In 21st Joint Propulsion Conference*.

CURRICULUM VITAE

1.   **NAME**   :   K. Praveen

2.   **DATE OF BIRTH**   :   04 Dec 1994

3.   **EDUCATIONAL QUALIFICATIONS**

   2016   Bachelor of Technology (B. Tech.)

Institution	:	Amrita Vishwavidyapeetham
Specialization	:	Aerospace Engineering

   M. Tech + Doctor of Philosophy

Institution	:	Indian Institute of Technology Madras
Specialization	:	Aerospace Engineering
Registration Date	:	22 July 2016

DOCTORAL COMMITTEE

CHAIRPERSON   :   Dr. H S N Murthy

Professor and Head

Department of Aerospace Engineering

GUIDE   :   Dr. R I Sujith

D. Srinivasan Chair Professor

Department of Aerospace Engineering

MEMBERS   :   Dr. Sunetra Sarkar

Professor

Department of Aerospace Engineering

Dr. Nandan Kumar Sinha

Professor

Department of Aerospace Engineering

Dr. Niket Kaisare

Professor

Department of Chemical Engineering